

The Pennsylvania State University

The Graduate School

Department of Materials Science and Engineering

**TAILORING WELD GEOMETRY AND COMPOSITION IN FUSION WELDING  
THROUGH CONVECTIVE MASS TRANSFER CALCULATIONS**

A Thesis in

Materials Science and Engineering

by

Saurabh Mishra

Submitted in Partial Fulfillment  
of the Requirements  
for the Degree of

Doctor of Philosophy

May 2006

The thesis of Saurabh Mishra was reviewed and approved\* by the following:

Tarasankar DebRoy  
Professor of Materials Science and Engineering  
Thesis Advisor  
Chair of Committee

Kwadwo Osseo-Asare  
Distinguished Professor of Metallurgy and  
Energy and Geo-environmental Engineering

Long-Qing Chen  
Professor of Materials Science and Engineering

Judith A. Todd  
Professor of Engineering Science and Mechanics

James P. Runt  
Professor of Polymer Science  
Head for Graduate Studies of the Department of [Materials Science and Engineering](#)

\*Signatures are on file in the Graduate School

## ABSTRACT

Fusion welding is characterized by various complex physical processes where the heat source interacts with the material leading to rapid heating, formation of the weld pool, vigorous circulation of the liquid material in the pool, heat transfer in the entire weldment, and solidification of the molten material. All these physical processes have a profound impact on the mass transport in the weldment. Mass transport during fusion welding has a significant impact on various weld features like the weld pool geometry and the creation of weld defects like liquation cracking. For example, surface active elements like sulfur alter the fluid convection pattern in the weld pool, and lead to a high depth to width ratio under favorable welding conditions. Furthermore, the fluid convection pattern becomes very complex when two plates with different amounts of surface active elements such as sulfur are welded together. Similarly, during gas metal arc (GMA) welding of aluminum copper alloys, the amount of solute (copper) in the solidifying weld metal is a key factor in determining the susceptibility of the weld to liquation cracking. In the past two decades, numerical transport phenomena based models have provided useful information about the thermal cycles and weld pool geometry. However, no effort has been made to apply these concepts to design weld consumables, to study the weld bead shape on welding two plates with different sulfur contents and to tailor weld pool geometry to specified dimensions. The present research focuses on these unexplored areas. The research proposed here seeks to develop a quantitative understanding of mass transport during fusion welding, with special emphasis on the role of surface active elements and the effect of solute distribution on weld defects like liquation cracking. A comprehensive model, incorporating numerical three-dimensional calculations of temperature and velocity fields and solute distribution in the weld pool is developed for the proposed quantitative study.

The currently available numerical transport phenomena based models are faced with some major difficulties including lack of reliability of output and limited utility because of the ability to go only in the forward direction. The output of these models is not generally reliable because of the presence of some uncertain input parameters such as

arc efficiency. Furthermore, these models cannot go backwards, i.e., calculate multiple combinations of welding process variables such as current, voltage and welding speed to obtain a target weld attribute such as weld pool geometry. Also, these models are complex, require specialized training to develop and test, and consume a large amount of computer time to run. These shortcomings of the numerical transport phenomena based models are addressed in the present thesis research. New methodologies are developed in the present study where the reliability of output of the numerical transport phenomena based model is enhanced by developing a computational procedure, where the uncertain input parameters of the model are optimized by combining it with a genetic algorithm optimization model and limited volume of experimental data. The resulting numerical model providing more reliable output is validated by comparing its predictions of weld pool geometry with the corresponding experimental results. In order to reduce the computation time a neural network, trained by data generated from the numerical transport phenomena based model, is developed in the present study. Next, the neural network is combined with a genetic algorithm to go backwards, i.e., find multiple combinations of welding variables to obtain a target weld geometry. Finally, this model is applied to study solute distribution in the weld pool when joining two steel plates with different sulfur contents, and to determine the copper content of the solidifying weld metal in aluminum-copper alloys welded with different copper containing filler metals. The study identifies the factors that affect the weld pool geometry on joining two plates with different sulfur contents, and predicts the susceptibility of an aluminum-copper alloy GMA weld to liquation cracking.

The specific contributions of the present thesis research include (i) development of a numerical solute transport model for fusion welding; (ii) improving the reliability of output of the numerical model; (iii) achieving computational efficiency and economy by developing a neural network trained by data generated by the numerical model; (iv) creating a bi-directional methodology where a target weld attribute like weld pool geometry can be attained via multiple combinations of input process parameters like arc current, voltage and welding speed; (v) calculating sulfur distribution during gas tungsten arc welding of stainless steel plates with different sulfur contents and predicting the

resulting weld pool geometry; and (vi) calculating copper distribution during gas metal arc welding of aluminum-copper alloys by incorporating the heat and mass addition from filler metal and a non-equilibrium solidification model, and using the copper content of the mushy zone to predict the occurrence of liquation cracking.

## TABLE OF CONTENTS

LIST OF FIGURES .....	ix
LIST OF TABLES .....	xix
ACKNOWLEDGEMENTS .....	xxi
<b>Chapter 1 INTRODUCTION</b>	<b>...1</b>
1.1 General Background	...1
1.2 Research Objectives and Methodology	...4
1.3 Thesis Structure	...8
1.4 References	...11
<b>Chapter 2 BACKGROUND</b>	<b>...14</b>
2.1 Transport Processes Occurring During Fusion Welding	...16
2.1.1 Deposition of heat energy at weld top surface	...19
2.1.1.1 Efficiency of energy absorption	...20
2.1.2 Convective heat transfer in the weld pool	...21
2.1.2.1 Electromagnetic force	...22
2.1.2.2 Marangoni shear stress and the effect of surface active elements	...24
2.1.2.3 Buoyancy force	...32
2.1.2.4 Relative importance of the driving forces	...32
2.1.3 Turbulence in weld pool	...36
2.1.4 General governing equations for transport processes	...37
2.2 Relation between Solute Distribution and Liquation Cracking in GMA Welds	...39
2.2.1 Heat transfer from metal droplets during GMA welding	...45
2.2.1.1 Calculation of volumetric heat source	...45
2.2.1.2 Calculating droplet transfer frequency and radius	...48
2.2.1.3 Calculating droplet impingement velocity	...48
2.2.1.4 How effective is the volumetric heat source model?	...51
2.2.2 Non-equilibrium solidification	...51
2.3 Enhancing the Reliability of Output and Improving Usefulness of the Numerical Transport Phenomena Based Models	...55
2.4 Development of a Neural Network Model for Fusion Welding	...58
2.5 Important Unanswered Questions	...62
2.6 References	...65
<b>Chapter 3 MOMENTUM, ENERGY AND SOLUTE TRANSPORT MODEL FOR GAS TUNGSTEN ARC WELDING – ENHANCING RELIABILITY OF ITS OUTPUT</b>	<b>...71</b>

3.1 Mathematical Formulation	...72
3.1.1 Numerical transport phenomena based model	...72
3.1.1.1 Governing equations	...72
3.1.1.2 Boundary conditions	...75
3.1.2 Genetic algorithm as an optimization model	...76
3.2 Results and Discussion	...85
3.2.1 Improving the reliability of the output of the numerical transport phenomena based model	...85
3.3 Summary and Conclusions	...90
3.4 References	...91
Chapter 4 A GENETIC ALGORITHM AND GRADIENT DESCENT BASED NEURAL NETWORK WITH THE PREDICTIVE POWER OF A NUMERICAL TRANSPORT PHENOMENA BASED MODEL FOR WELDING	...93
4.1 Neural Network Model	...94
4.2 Calculation Procedure	...107
4.2.1 Number of hidden layers in the network	...107
4.2.2 Database generation	...108
4.2.3 Normalizing inputs and outputs	...111
4.2.4 Selection of initial weights	...111
4.3 Results and Discussion	...112
4.3.1 Structure chosen for the neural networks	...112
4.3.2 Gradient descent versus hybrid training approach	...115
4.3.3 Evaluating the predicting capability of the neural networks	...122
4.4 Summary and Conclusions	...126
4.5 References	...127
Chapter 5 TAILORING WELD GEOMETRY USING A GENETIC ALGORITHM AND A NEURAL NETWORK TRAINED WITH NUMERICAL TRANSPORT PHENOMENA BASED CALCULATIONS	...130
5.1 Mathematical Model	...132
5.2 Results and Discussion	...138
5.3 Summary and Conclusions	...148
5.4 References	...150
Chapter 6 EVOLUTION OF WELD POOL GEOMETRY ON WELDING PLATES WITH SAME AND DIFFERENT SULFUR CONTENTS	...151
6.1 Experimental Procedure	...152
6.2 Mathematical Model	...154
6.2.1 The effect of surface active element, sulfur on weld pool convection	...155

6.2.2 Loss of sulfur from the top surface	...160
6.3 Results and Discussion	...164
6.3.1 Role of phosphorus as a surface active element	...164
6.3.2 Evolution of weld pool geometry on welding two plates with same sulfur contents	...164
6.3.3 Geometry of weld pool during welding of two plates with different sulfur concentrations	...170
6.4 Summary and Conclusions	...212
6.5 References	...214
 Chapter 7 PROBING LIQUATION CRACKING THROUGH MODELING OF MOMENTUM, HEAT AND SOLUTE TRANSPORT DURING GAS METAL ARC WELDING OF ALUMINUM ALLOYS	 ...216
7.1 Mathematical model	...217
7.1.1 Thermal energy conservation equation	...218
7.1.2 Solute conservation equation	...218
7.1.3 Filler metal addition	...219
7.1.4 Thermo-solutal-flow coupling - enthalpy updating	...221
7.1.5 Boundary conditions	...227
7.2 Results and Discussion	...227
7.3 Summary and Conclusions	...239
7.4 References	...240
 Chapter 8 CONCLUDING REMARKS	 ...241
8.1 Summary	...241
8.2 Conclusions	...242
8.2 Future Work	...243

## LIST OF FIGURES

Fig. 1.1. List of tasks in the present thesis research.	...7
Fig. 2.1. Schematic plot depicting the fusion welding process. HAZ stands for Heat-Affected Zone.	...17
Fig. 2.2. Various driving forces and the resulting liquid convection in the weld pool [7,33]: (a) electromagnetic force, (b) surface tension gradient force with negative $\partial\gamma/\partial T$ , (c) surface tension gradient force with positive $\partial\gamma/\partial T$ , and (d) buoyancy force. $\partial\gamma/\partial T$ is the temperature coefficient of surface tension.	...23
Fig. 2.3. Variation of (a) surface tension of Fe-S as a function of temperature and sulfur activity; (b) $d\gamma/dT$ of Fe-S as a function of temperature for samples containing 20, 40 and 150 ppm sulfur [34].	...29
Fig. 2.4. Comparison between the calculated and measured weld pool geometry for various sulfur contents and heat inputs [34]: (a) 20 ppm and 1.9 kW, (b) 150 ppm and 1.9 kW, (c) 20 ppm and 5.2 kW, and (d) 150 ppm and 5.2 kW.	...30
Fig. 2.5. Effect on the weld pool geometry [43] when welding two tubes with (a) same sulfur content of approximately 90 ppm (Heat A), which is relatively high; (b) same sulfur content of less than 30 ppm (Heat C), which is relatively low; and (c) different sulfur contents, i.e., welding Heat A and Heat C. Full penetration welds at the joint were desired. Welding conditions: Start current – 35 A; Finish current – 26 A; Fixture rotation speed - 4.6 revolutions/min, Outer diameter of tubing – 25 mm; Wall thickness – 2.4 mm.	...31
Fig. 2.6. PMZ microstructure of GMA weld in 2219 aluminum alloy made with 2319 aluminum filler wire [5].	...41
Fig. 2.7. Schematic plot showing the GMA welding process. The mushy zone represents the two phase solid-liquid region.	...44
Fig. 2.8. Schematic plot illustrating the cylindrical volumetric heat source in the weld pool along the longitudinal plane [33,85].	...47
Fig. 2.9. Calculated droplet characteristics [33,81,85]. (a) comparison between the fitted and measured droplet transfer frequency, and (b) comparison between calculated and measured droplet acceleration in the arc column. In part (a), the triangles represent experimental data from Rhee and Kannatey-Asibu [85], and in parts (a) and (b), circles represent experimental data from Jones et al. [86].	...49

- Fig. 2.10. Comparison of the calculated and experimental geometry of the fusion zone (FZ) and the heat-affected zone (HAZ) of GMA weld in HSLA-100 steel. Welding conditions: GMA, 405 A, 31.3 V, 5.29 mm/s [55]. ...52
- Fig. 2.11. Comparison of interface velocity versus solute partition coefficient plots obtained using Eq. (2.40) (curve 1) and a dilute continuous growth model (curve 2) with the experimental data (circles and triangles) for solidification of Si-As dilute alloy. The value of  $k_p = 0.35$  and that of  $V_D^L = 1.2$  m/s [90]. ...54
- Fig. 2.12. Typical back-propagation neural network structure. The symbols  $I_1$  to  $I_4$  represent the four input process parameters of a fusion welding process, while  $O_1$  and  $O_2$  represent the corresponding output weld attributes. ...60
- Fig. 3.1. Generalized generation gap (G3) genetic algorithm using parent centric recombination (PCX) operator [24]. ...81
- Fig. 3.2. Flow chart of the generalized generation gap (G3) model. ...82
- Fig. 3.3. Experimental weld geometry and the calculated weld geometry, (a) to (e), obtained using the optimum set of values of the unknown input parameters for the five sets of welding conditions given in Table 3.1, i.e., 1 to 5, respectively. The 1745 K isotherm is the equilibrium solidus temperature of stainless steel, which marks the weld pool boundary. ...88
- Fig. 4.1. Neural network architecture used in the present study. The input layer has 17 input variables and the output layer has one of the six output variables,  $O$ , i.e., weld pool depth, weld pool width, weld pool length, peak temperature, cooling time from 800°C to 500°C or maximum liquid velocity in the weld pool. Each connection to a node,  $j$ , from a node in the previous layer,  $i$ , has an adjustable weight,  $w_{ij}$ , associated with it. The weights embody the non-linear relationship between the input and the output variables. Each node in the hidden and the output layers is given an extra input, which always has a value of 1. The weight,  $w_0$ , of this extra input is called the bias. The net input,  $v_j$ , for a node,  $j$ , is described in Eq. (4.1) and  $y_i$  is the output of node,  $i$ . ...96
- Fig. 4.2. The minimization of the generalized Rosenbrock function,  $F_{Ros}$ , given in Eq. (4.7), with iterations. Random search involved random initial guess, while guided search included an initial guess, which was close to the actual solution. ...101
- Fig. 4.3. Generalized generation gap (G3) genetic algorithm using parent centric recombination (PCX) operator. ...104
- Fig. 4.4. Flow chart of the generalized generation gap (G3) model. ...105

- Fig. 4.5. The ranges of values of the input variables in the training and testing datasets. The normalized values of the variables were obtained using Eq. (4.25) and corresponding minimum and maximum values listed in Table 4.1. ...110
- Fig. 4.6. Flowchart for training the neural network. ...113
- Fig. 4.7. Comparison of mean square error (MSE), defined by Eq. (4.4), for different number of nodes in the hidden layer. For each output variable the results are an average of five runs, with different sets of initial random weights, using the gradient descent training method. The number of iteration for each run were 5000. ...114
- Fig. 4.8. Mean square error (MSE), defined by Eq. (4.4), versus number of iterations for the gradient descent training method. For each output variable five runs were conducted with different sets of initial random weights. The error bars show the variation of MSE values over the five runs. ...116
- Fig. 4.9. Absolute value of the difference between (a) the weld pool width in the training data and that calculated from neural network (NN); (b) the weld pool width in the testing data and that calculated from neural network (NN); (c) the peak temperature in the training data and that calculated from neural network (NN); and (d) the peak temperature in the testing data and that calculated from neural network (NN). The results are for the five sets of weights calculated by gradient descent (GD) method, and the global set of weight calculated by the hybrid approach. ...119
- Fig. 4.10. Comparison of the values of weights for the gradient descent and hybrid training approaches for (a) weld pool depth, and (b) maximum liquid velocity in the weld pool. Cases 01 to 05 are for the five sets of weights obtained from gradient descent method when using five different sets of initial random weights. ...121
- Fig. 4.11. Comparison of weld pool (a) and (b) depth, (c) and (d) width and (e) and (f) length calculated by the respective neural networks and those given in the training and the testing datasets, respectively. ...124
- Fig. 4.12. Comparison of (a) and (b) peak temperature, (c) and (d) cooling time between 800°C and 500°C and (e) and (f) maximum liquid velocity in the weld pool calculated by the respective neural networks and those given in the training and the testing datasets, respectively. ...125
- Fig. 5.1. Generalized generation gap (G3) genetic algorithm using parent centric recombination (PCX) operator. ...135
- Fig. 5.2. Flow chart of the generalized generation gap (G3) model. ...136

- Fig. 5.3: Initial values of individual welding variable sets and their objective functions. (a) A large space of variables was searched to find optimum solutions as shown by 120 randomly selected initial welding variable sets. (b) The low values of the objective functions of several individuals in the initial population indicate the possibility of existence of multiple optimal solutions. ...141
- Fig. 5.4: Several fairly diverse welding variable sets could produce low values of the objective function indicating the existence of alternate paths to obtain the target weld geometry. The plots show the welding variable sets that produced low values of the objective function,  $O(f)$ , with iterations. (a) individuals after 1st iteration with  $O(f)$  less than 0.1, (b) individuals after 10th iteration with  $O(f)$  less than 0.01, and (c) individuals after 25th iteration with  $O(f)$  less than 0.001. ...143
- Fig. 5.5: Comparison of the experimental target weld geometry with those calculated from the numerical transport phenomena based model for GTA welding described in Chapter 3. Calculated weld geometries in cases (a) to (h) correspond to the eight solutions, i.e., sets of current, voltage and welding speed listed in Table 5.1. In the calculated results the weld pool boundary is marked by the 1745 K isotherm, which is the solidus temperature of stainless steel. ...146
- Fig. 6.1. Liquid convection in the weld pool for two cases: (a)  $\partial\gamma/\partial T$  is negative, which is generally the case when surface active element like sulfur is absent. (b)  $\partial\gamma/\partial T$  is positive, which is generally the case when surface active element like sulfur is present. Symbol  $\gamma$  is the surface tension,  $\partial\gamma/\partial T$  is the temperature coefficient of surface tension,  $T$  is the temperature,  $x$  and  $z$  are two locations in the weld pool, and  $F$  is the driving force. ...156
- Fig. 6.2. Temperature coefficient of surface tension,  $d\gamma/dT$ , as a function of temperature for stainless steel specimens containing 0.003 wt%, 0.007 wt%, 0.012 wt%, 0.03 wt%, 0.04 wt% , 0.06 wt% and 0.3 wt% sulfur. ...159
- Fig. 6.3. Desulphurization of Fe-S alloys at 1600 °C [19].  $V$  is equal to  $V_0 - vt$ , where  $V_0$  is the initial volume of the melt in  $\text{cm}^3$ ,  $v$  is the volume change of the melt in  $\text{cm}^3/\text{s}$ , and  $t$  is time in s. Initial sulfur contents of the four alloys were: 6510-13 had 0.18 wt%, 6505-8 had 0.26 wt%, 6510-12 had 0.35 wt% and 6510-11 had 0.42 wt%. The data points for each alloy correspond to keeping the heated alloys under vacuum for 0, 5, 10 and 15 minutes, respectively. ...163
- Fig. 6.4. Surface tension versus atom% for solutions of C, P, N, O, S and Se in liquid iron at 1823 K [22]. After P. Kozakevitch, in "Surface Phenomena of Metals", Society of Chemical Industry Monograph 28 (1968) p. 223. ...165
- Fig. 6.5. Experimental and calculated weld pool geometry, (a) to (f), for the six sets of welding conditions given in cases 1 to 6 of Table 6.4, respectively. The 1745 K

isotherm is the equilibrium solidus temperature of stainless steel, which marks the weld pool boundary. ...168

Fig. 6.6. Weld pool geometry when welding a stainless steel plate having low sulfur content (0.003 wt%) with a plate having very high sulfur content (0.293 wt%). The white line at location 'A' indicates the joint of the two plates. Location 'C' indicates the point of maximum penetration. Line 'AB' denotes the shift of the point of maximum penetration from the joint of the two plates. The length of line 'AB' is called the center line shift (CLS). Welding conditions: 100 A, 9.8 V, welding speed is 1.7 mm/s. ...172

Fig. 6.7. An experiment to demonstrate the shifting of the arc towards the low sulfur side. Looking from the left side of the setup, first a low sulfur plate (304L – 0.003 wt% sulfur) on the right was welded to a high sulfur plate (304RL – 0.024 wt% sulfur) on the left. After half way the plates were reversed as shown in the figure. ...173

Fig. 6.8. The shifting of the arc towards the low sulfur side. The pictures of the arc were taken from the left side of the setup shown in Fig. 6.7. The vertical dotted line shows the center line of the weld. (a) The arc can be seen shifted towards right, i.e., towards the low sulfur side (304L plate). (b) The arc is seen shifted towards left because after halfway the low sulfur plate (304L) is kept on the left side as shown in Fig. 6.7. ...174

Fig. 6.9. The degree of ionization (logarithmic scale) versus temperature for some gases and metal vapors [25]. ...179

Fig. 6.10. Relation between the center line shift (CLS) and the two factors affecting it, i.e., absolute value of difference in sulfur content of the two plates and the energy input per unit length. The symbols represent the experimentally measured data while the line represents the linear fit to the experimental data. The symbol  $C_L$  is the sulfur content of the left plate (wt%),  $C_R$  is the sulfur content of the right plate (wt%),  $I$  is current (A),  $V$  is voltage (V) and  $U$  is the welding speed (mm/s). ...180

Fig. 6.11. Variation of center line shift (CLS) with sulfur content when subject tubes were welded to: (a) low sulfur standard, i.e., 15 ppm (0.0015 wt%) sulfur, (b) high sulfur standard, i.e., 133 ppm (0.0133 wt%) sulfur [12]. The solid circles represent the results for cases where the two tubes had different sulfur contents. The crosses represent the cases where the two tubes had the same sulfur content. Welding conditions: Start current – 35 A; Finish current – 26 A; Fixture rotation speed – 4.6 revolutions/min, Outer diameter of tubing – 9.5 mm. Unit conversion: 1 ppm =  $10^{-4}$  wt%. ...181

Fig. 6.12. Results for case 1 in Table 6.6. (a) Experimental weld pool geometry. The vertical line shows the joint of the two plates. (b) Calculated temperature and

velocity fields in the weld pool. The contours represent the temperatures in degree Kelvin and the vectors represent the liquid velocity. The 1745 K isotherm is the solidus temperature of stainless steel used and marks the weld pool boundary. (c) Calculated concentration of sulfur in the weld pool. The contours represent sulfur concentration in wt%. The sulfur concentration on the top surface and the bulk of the weld pool was about 0.026 wt%. Welding conditions: 150 A, 10.5 V, welding speed is 1.7 mm/s. ...183

Fig. 6.13. Results for case 2 in Table 6.6. (a) Experimental weld pool geometry. The vertical line shows the joint of the two plates. (b) Calculated temperature and velocity fields in the weld pool. The contours represent the temperatures in degree Kelvin and the vectors represent the liquid velocity. The 1745 K isotherm is the solidus temperature of stainless steel used and marks the weld pool boundary. (c) Calculated concentration of sulfur in the weld pool. The contours represent sulfur concentration in wt%. The sulfur concentration on the top surface and the bulk of the weld pool was about 0.041 wt%. Welding conditions: 150 A, 10.8 V, welding speed is 1.7 mm/s. ...184

Fig. 6.14. Results for case 3 in Table 6.6. (a) Experimental weld pool geometry. The vertical line shows the joint of the two plates. (b) Calculated temperature and velocity fields in the weld pool. The contours represent the temperatures in degree Kelvin and the vectors represent the liquid velocity. The 1745 K isotherm is the solidus temperature of stainless steel used and marks the weld pool boundary. (c) Calculated concentration of sulfur in the weld pool. The contours represent sulfur concentration in wt%. The sulfur concentration on the top surface and the bulk of the weld pool was about 0.008 wt%. Welding conditions: 150 A, 10.5 V, welding speed is 1.7 mm/s. ...185

Fig. 6.15. Results for case 4 in Table 6.6. (a) Experimental weld pool geometry. The vertical line shows the joint of the two plates. (b) Calculated temperature and velocity fields in the weld pool. The contours represent the temperatures in degree Kelvin and the vectors represent the liquid velocity. The 1745 K isotherm is the solidus temperature of stainless steel used and marks the weld pool boundary. (c) Calculated concentration of sulfur in the weld pool. The contours represent sulfur concentration in wt%. The sulfur concentration on the top surface and the bulk of the weld pool was about 0.018 wt%. Welding conditions: 150 A, 10.8 V, welding speed is 3.4 mm/s. ...186

Fig. 6.16. Results for case 5 in Table 6.6. (a) Experimental weld pool geometry. The vertical line shows the joint of the two plates. (b) Calculated temperature and velocity fields in the weld pool. The contours represent the temperatures in degree Kelvin and the vectors represent the liquid velocity. The 1745 K isotherm is the solidus temperature of stainless steel used and marks the weld pool boundary. (c) Calculated concentration of sulfur in the weld pool. The contours represent sulfur concentration in wt%. The sulfur concentration on the top surface and the bulk of

the weld pool was about 0.035 wt%. Welding conditions: 150 A, 10.9 V, welding speed is 3.4 mm/s. ...187

Fig. 6.17. Results for case 6 in Table 6.6. (a) Experimental weld pool geometry. The vertical line shows the joint of the two plates. (b) Calculated temperature and velocity fields in the weld pool. The contours represent the temperatures in degree Kelvin and the vectors represent the liquid velocity. The 1745 K isotherm is the solidus temperature of stainless steel used and marks the weld pool boundary. (c) Calculated concentration of sulfur in the weld pool. The contours represent sulfur concentration in wt%. The sulfur concentration on the top surface and the bulk of the weld pool was about 0.007 wt%. Welding conditions: 150 A, 10.7 V, welding speed is 3.4 mm/s. ...188

Fig. 6.18. Results for case 7 in Table 6.6. (a) Experimental weld pool geometry. The vertical line shows the joint of the two plates. (b) Calculated temperature and velocity fields in the weld pool. The contours represent the temperatures in degree Kelvin and the vectors represent the liquid velocity. The 1745 K isotherm is the solidus temperature of stainless steel used and marks the weld pool boundary. (c) Calculated concentration of sulfur in the weld pool. The contours represent sulfur concentration in wt%. The sulfur concentration on the top surface and the bulk of the weld pool was about 0.016 wt%. Welding conditions: 100 A, 9.8 V, welding speed is 1.7 mm/s. ...189

Fig. 6.19. Results for case 8 in Table 6.6. (a) Experimental weld pool geometry. The vertical line shows the joint of the two plates. (b) Calculated temperature and velocity fields in the weld pool. The contours represent the temperatures in degree Kelvin and the vectors represent the liquid velocity. The 1745 K isotherm is the solidus temperature of stainless steel used and marks the weld pool boundary. (c) Calculated concentration of sulfur in the weld pool. The contours represent sulfur concentration in wt%. The sulfur concentration on the top surface and the bulk of the weld pool was about 0.067 wt%. Welding conditions: 100 A, 10.0 V, welding speed is 1.7 mm/s. ...190

Fig. 6.20. Results for case 9 in Table 6.6. (a) Experimental weld pool geometry. The vertical line shows the joint of the two plates. (b) Calculated temperature and velocity fields in the weld pool. The contours represent the temperatures in degree Kelvin and the vectors represent the liquid velocity. The 1745 K isotherm is the solidus temperature of stainless steel used and marks the weld pool boundary. (c) Calculated concentration of sulfur in the weld pool. The contours represent sulfur concentration in wt%. The sulfur concentration on the top surface and the bulk of the weld pool was about 0.009 wt%. Welding conditions: 100 A, 9.9 V, welding speed is 1.7 mm/s. ...191

Fig. 6.21. Results for case 10 in Table 6.6. (a) Experimental weld pool geometry. The vertical line shows the joint of the two plates. (b) Calculated temperature and velocity fields in the weld pool. The contours represent the temperatures in degree

Kelvin and the vectors represent the liquid velocity. The 1745 K isotherm is the solidus temperature of stainless steel used and marks the weld pool boundary. (c) Calculated concentration of sulfur in the weld pool. The contours represent sulfur concentration in wt%. The sulfur concentration on the top surface and the bulk of the weld pool was about 0.019 wt%. Welding conditions: 100 A, 10.2 V, welding speed is 3.4 mm/s. ...192

Fig. 6.22. Results for case 11 in Table 6.6. (a) Experimental weld pool geometry. The vertical line shows the joint of the two plates. (b) Calculated temperature and velocity fields in the weld pool. The contours represent the temperatures in degree Kelvin and the vectors represent the liquid velocity. The 1745 K isotherm is the solidus temperature of stainless steel used and marks the weld pool boundary. (c) Calculated concentration of sulfur in the weld pool. The contours represent sulfur concentration in wt%. The sulfur concentration on the top surface and the bulk of the weld pool was about 0.041 wt%. Welding conditions: 100 A, 10.2 V, welding speed is 3.4 mm/s. ...193

Fig. 6.23. Results for case 12 in Table 6.6. (a) Experimental weld pool geometry. The vertical line shows the joint of the two plates. (b) Calculated temperature and velocity fields in the weld pool. The contours represent the temperatures in degree Kelvin and the vectors represent the liquid velocity. The 1745 K isotherm is the solidus temperature of stainless steel used and marks the weld pool boundary. (c) Calculated concentration of sulfur in the weld pool. The contours represent sulfur concentration in wt%. The sulfur concentration on the top surface and the bulk of the weld pool was about 0.008 wt%. Welding conditions: 100 A, 10.0 V, welding speed is 3.4 mm/s. ...194

Fig. 6.24. Distribution of manganese-sulfide (MnS) precipitates (dark spots and discs) in 303 stainless steel (SS) base metal. ...197

Fig. 6.25. Distribution of manganese-sulfide (MnS) precipitates (dark spots and discs) in 304RL stainless steel (SS) base metal. ...198

Fig. 6.26. Distribution of manganese-sulfide (MnS) precipitates (dark spots) in 304L stainless steel (SS) base metal. ...199

Fig. 6.27. Distribution of manganese-sulfide (MnS) precipitates (dark spots) in the weld pool for case 2 of Table 6.6. Welding conditions: 150 A, 10.8 V, welding speed is 1.7 mm/s. 304RL stainless steel has 0.024 wt% sulfur while 303 stainless steel has 0.293 wt% sulfur. ...200

Fig. 6.28. The EPMA measurements of sulfur and phosphorus concentrations were done along the dotted lines. ...203

Fig. 6.29. Experimental and calculated sulfur concentrations along the horizontal dotted line shown in Fig. 6.28 for (a) case 1, (b) case 2, and (c) case 3 of Table 6.6. The

- symbols represent the experimental data and the solid line represents the calculated results. ...204
- Fig. 6.30. Experimental and calculated sulfur concentrations along the vertical dotted line shown in Fig. 6.28 for (a) case 1, (b) case 2, and (c) case 3 of Table 6.6. The symbols represent the experimental data and the solid line represents the calculated results. ...205
- Fig. 6.31. Experimentally measured phosphorus concentrations along the horizontal dotted line shown in Fig. 6.24 for (a) case 1, (b) case 2, and (c) case 3 of Table 6.6. ...206
- Fig. 6.32. Experimentally measured phosphorus concentrations along the vertical dotted line shown in Fig. 6.28 for (a) case 1, (b) case 2, and (c) case 3 of Table 6.6. ...207
- Fig. 6.33. Variation of weld pool penetration with energy input per unit length for 12 cases given in Table 6.6. The three stainless steel combinations welded together are: 304L welded to 303, 304RL welded to 303, and 304L welded to 304RL. The sulfur contents of the three kinds of stainless steels used are: 304L (0.003 wt%), 304RL (0.024 wt%) and 303 (0.293 wt%). ...210
- Fig. 6.34. Variation of weld pool width with energy input per unit length for 12 cases given in Table 6.6. The three stainless steel combinations welded together are: 304L welded to 303, 304RL welded to 303, and 304L welded to 304RL. The sulfur contents of the three kinds of stainless steels used are: 304L (0.003 wt%), 304RL (0.024 wt%) and 303 (0.293 wt%). ...211
- Fig. 7.1. Effect of interface speed on local interfacial partitioning. ...224
- Fig. 7.2. Effect of interface speed on solidus and liquidus line slopes (an equilibrium liquidus slope of  $-3.37$  K/wt%, and an equilibrium partition coefficient of 0.16 were chosen for this specific demonstration). ...225
- Fig. 7.3. Velocity and temperature fields in the weld pool for the welding conditions indicated in Table 7.1. The filler metal composition was 0.08 wt% copper. All the temperatures are in degree Kelvin. ...229
- Fig. 7.4. Concentration field (wt% Cu) in the weld pool. The filler metal compositions were (a) 0.08 wt% Cu, (b) 2.0 wt% Cu, (c) 4.0 wt% Cu, and (d) 9.0 wt% Cu. ...232
- Fig. 7.5. The concentration of copper in the weld metal for different filler metal compositions. The concentration of copper in the base metal was 6.3 wt%. The safe and susceptible regions are indicated for equilibrium solidification. ...234

- Fig. 7.6. Variation of equilibrium partition coefficient ( $k_p^*$ ) (dotted line) and non-equilibrium partition coefficient ( $k_p$ ) (solid line) with temperature. ...235
- Fig. 7.7. Solid fraction versus temperature for alloy composition of 6.3 wt% copper. The solid line curve was obtained from the equilibrium phase diagram and the dotted line curve was obtained using the modified non-equilibrium solidus and liquidus lines. ...236
- Fig. 7.8. Solid fraction versus temperature calculated using modified non-equilibrium solidus and liquidus lines for different alloy compositions. The PMZ composition was 6.3 wt% Cu (dash-dot line in the center). The calculated mushy zone compositions, or the solidifying weld metal compositions, of 2.16 wt% Cu (dotted line above the central line) and 8.91 wt% Cu (solid line below the central line) correspond to the filler metal compositions of 2.0 wt% Cu and 9.0 wt% Cu, respectively. ...238

## LIST OF TABLES

Table 2.1. Welding conditions, material properties and other data of AISI 1005 steel welds used by Zhang [33] for calculating the values of dimensionless numbers.	...35
Table 2.2. Dimensionless numbers in the GTA weld pool of 1005 steel [33]. The data used by Zhang [33] in the calculations are given in Table 2.1.	...35
Table 3.1. Welding variables and experimentally measured weld pool penetration and width. The experimental data was provided by Dr. T. J. Lienert and Dr. M. Johnson of Los Alamos National Laboratory.	...77
Table 3.2. Data used in the calculations [5].	...78
Table 3.3: Terminology used in genetic algorithm.	...80
Table 3.4. Optimized values of the five unknown input parameters of the numerical transport phenomena based model.	...85
Table 4.1. The input variables and their ranges of values considered in the training datasets.	...109
Table 4.2. Comparison of the mean square error (MSE), defined in Eq. (4.4), for the gradient descent method and the hybrid training approach. The results for the gradient descent method were taken after 5000 iterations.	...115
Table 4.3. The mean square error (MSE), defined in Eq. (4.4), and mean error (ME), defined in Eq. (4.26), for the results of the neural network for the weld pool geometry, peak temperature, cooling time between 800°C and 500°C and maximum liquid velocity in the weld pool. The results were obtained using the hybrid training approach.	...123
Table 5.1: Various combinations of welding variables, i.e., arc current (I), voltage (V) and welding speed (U) obtained using neural network model to achieve the following target weld dimensions: penetration = 1.39 mm and width = 4.05 mm. The target weld geometry was obtained experimentally using the following welding variables: I = 101.0 A, V= 9.9 V and U = 3.4 mm/s for GTA welding of 303 stainless steel (0.293 wt% sulfur).	...144
Table 5.2: Various combinations of welding variables, i.e., arc current (I), voltage (V) and welding speed (U) obtained using neural network model to achieve the following target weld dimensions: penetration = 1.94 mm and width = 4.39 mm. The target weld geometry was obtained using the welding conditions listed in (a).	...148

Table 6.1. Compositions of the three grades of stainless steels (SS) used in the present study.	...153
Table 6.2. Welding conditions used in the present study. Case numbers 1 to 6 list the cases where the two welded specimens contained the same amount of sulfur. The remaining entries are for the cases where the two welded specimens contained different amounts of sulfur.	...154
Table 6.3. Data used in the calculations.	...162
Table 6.4. Welding variables and experimentally measured weld pool penetration and width. The experimental data was provided by Dr. T. J. Lienert and Dr. M. Johnson of Los Alamos National Laboratory. 'Exp' stands for experimental results while 'Cal' stands for calculated results.	...167
Table 6.5. The values of Peclet numbers ( $Pe_h$ ) for heat transfer for the six cases listed in Table 6.4 and shown in Fig. 6.5.	...167
Table 6.6. The center line shift (CLS) of all the experimental results for welding of plates with different sulfur contents. SS stands for stainless steel. $C_L$ is the sulfur concentration in wt% in the left piece while $C_R$ is the sulfur concentration in wt% in the right piece. The value of energy input (J/mm) is given by (Current×Voltage/Welding speed).	...178
Table 7.1. Data used in the calculations [25].	...228

## ACKNOWLEDGEMENTS

Over the course of my study at Penn State, I have met many people that have helped to make the undertaking of this magnitude possible. I would first like to express my sincere gratitude and deep appreciation to my advisor, Dr. Tarasankar DebRoy. His guidance of the research effort, professional expertise, demand for excellence and encouragement brought the best from all involved. He gave me many opportunities to advance my research as well as my professional development.

I would like to acknowledge Drs. Long-Qing Chen, Kwadwo Osseo-Asare and Judith A. Todd for their valuable advice and suggestions on my work while serving on my thesis committee. I really appreciate them for giving their time to review and comment on this thesis.

I am grateful to Dr. T. J. Lienert and Dr. M. Johnson of Los Alamos National Laboratory for providing experimental results and for his helpful discussions. I would also like to express my thanks to Dr. J. W. Elmer of Lawrence Livermore National Laboratory for his valuable suggestions.

Many thanks to my colleagues, Drs. Tao Hong, Hailiang Zhao, Amitava De, Gaur Gopal Roy, Suman Chakraborty, Cheolhee Kim, Wei Zhang, Xiuli He, Mr. Sarangapani Sista, Mr. Amit Kumar, Mr. Rohit Rai, Mr. Rituraj Nandan and Mr. Brandon Ribic, for their outstanding research and great help. They have made my study at Penn State a rewarding and memorable experience.

I am grateful to my family members and friends for their love and support.

Finally, I would like to acknowledge a grant from the U.S. Department of Energy, Office of Basic Energy Sciences, Division of Materials Sciences, for supporting this research work, under grant number DE-FGO2-01ER45900.

# Chapter 1

## Introduction

### 1.1 General Background

In the last two decades, the application of numerical transport phenomena has provided useful information about the thermal cycles and weld pool geometry in both linear and spot welding [1-19]. The fluid flow pattern in the weld pool as well as important variables like temperature field, cooling rate, solidification rate, mode of solidification and temperature gradients have been well understood [13]. Computed temperatures have been used to understand the evolution of phase composition [5,16], grain structure [7,8], inclusion structure [17], and weld metal composition change owing to both the evaporation of alloying elements and the dissolution of gases [9,14]. In contrast, very little has been done to understand solute transport in the weld pool. In many cases the final solute distribution in the weldment has a significant impact on its properties. For example, when stainless steel containing surface active elements like sulfur is welded, the temperature coefficient of surface tension,  $dy/dT$ , often becomes positive, causing the liquid metal to flow from the periphery to the center of the weld pool. This fluid motion brings more heat to the center of the weld pool resulting in a deep and narrow weld bead. This property of sulfur containing stainless steels has been widely used to achieve good weldability with higher depth to width (D/W) ratios. This phenomenon has been addressed in the literature, both by conducting experiments and using mathematical models, for welding of two plates with same sulfur content [20-31].

An important question that follows the above example is what would happen if two plates being welded have different sulfur contents. The available models cannot address these problems. Such situations are common in the nuclear waste management industry where stabilization, packaging and storage of plutonium-bearing materials involve closure welding of 316 stainless steel (SS) container (0.03 wt% sulfur) with 416 SS lid (>0.15 wt% sulfur) [32]. The final closure of the container must be leak-tight and structurally sound [32-34]. Another example is the tungsten inert gas (TIG) welding of small diameter stainless steel tubing for instrumentation systems in CANDU (Canadian

Deuterium Uranium) nuclear reactors [31]. Experiments have shown that during welding of two stainless steel plates with different sulfur contents the point of maximum penetration shifts towards the plate with lower sulfur content [29,31]. The weld bead shift is sometimes so severe that there is very little melting of the piece with higher sulfur content, i.e., lack-of-fusion defect occurs at the interface, resulting in improper joining of the two pieces [31]. Since many of the instrumentation systems in a nuclear reactor contain the primary coolant, insufficient fusion of the interface is unacceptable [31].

Heiple et al. [24] gave a qualitative explanation for the shifting of the weld bead based on their surface tension driven fluid flow model. They stated that the plate with lower sulfur content has relatively higher surface tension than the one with higher sulfur content. The result is a net surface tension gradient across the weld pool leading to surface fluid flow toward the side of the plate with less sulfur. This flow pattern causes maximum penetration in the plates containing less sulfur. However, once the weld pool is formed, liquid metal in the weld pool circulates vigorously causing mixing of sulfur from the two plates. Actual surface tension gradient should depend on the final sulfur distribution in the weld pool. Furthermore, quantitative modeling of the process is necessary to predict the actual location of the weld bead when welding two plates with different sulfur contents.

Another example illustrating the importance of solute transport in the weld pool is observed during gas metal arc (GMA) welding of aluminum-copper alloys using filler metals with different copper contents. Here, the distribution of copper in the weld pool is affected by several factors including mixing of the base metal with the filler metal, non-equilibrium solute partitioning during solidification and convective solute transport. The copper distribution in the weld pool decides the solid fraction of the solidifying weld metal, which is a key factor governing the occurrence of liquation cracking [35-45] in aluminum-copper alloy welds. Huang and Kou [35] found that the partially melted zone (PMZ) of the aluminum alloys becomes prone to liquation cracking when its solid fraction becomes lower than that of the solidifying weld metal. They [35] argued that lower solid fraction in the PMZ makes this region weaker than the weld metal, making the PMZ vulnerable to liquation cracking. Accurate prediction of liquation cracking

susceptibility in aluminum-copper alloys requires thorough investigation of the complex coupling of momentum, heat and solute transport under non-equilibrium conditions during GMA welding.

Though numerical transport phenomena based models have provided significant insights into the welding process in the past two decades, the temperature fields (and therefore, fusion zone geometry) and thermal cycles predicted by these models are not always reliable, i.e., they do not always agree with the experimental results. The disagreement between the computed and experimentally determined temperature fields can be primarily attributed to the uncertainty of the values of some of the input parameters, which cannot be prescribed based on either scientific principles or welding conditions. In general there are five uncertain input parameters, i.e., arc efficiency, arc radius, power distribution factor, and the effective thermal conductivity and viscosity of the liquid metal. Although the values of arc efficiency have been experimentally measured for many welding conditions, the reported values vary significantly, even for apparently similar welding conditions. Measured values of the arc radius and power distribution factor depend on welding conditions and, as a result, their values cannot be accurately specified except for certain narrow windows of welding conditions. Values of the effective thermal conductivity and viscosity are important, since they allow accurate modeling of the high rates of transport of heat and mass in systems with strong fluctuating velocities, such as small weld pools with very strong convection currents. The values of effective conductivity and viscosity are properties of the specific welding system, and not the inherent physical properties of the liquid metal [14], and the values of these parameters significantly affect the results of numerical calculations. A systematic global search for the uncertain input parameters is needed so that the computed temperature profiles always agree with the corresponding experimentally determined values. Genetic algorithm (GA) is a powerful optimization technique that can search for global optimal solution independent of the initial guessed values [46-49]. Therefore, GA can be used to estimate the uncertain input parameters.

Another shortcoming of the current generation of numerical transport phenomena based models is that they cannot determine alternative pathways to achieve a target weld

attribute. The desired depth and width of the weld pool and the cooling rate are often specified to achieve a structurally sound and reliable welded joint. Therefore, an important requirement is to determine the values of the welding variables necessary for achieving a given weld attribute, such as the weld geometry. In practice a particular weld attribute may be obtained through multiple combinations of welding variables. The forward numerical model for the calculation of temperature and velocity fields and solute distribution needs to be systematically interrogated to estimate the optimized values of welding variable sets that can produce a specified weld geometry. However, this investigation is very time consuming as it involves multiple runs of the numerical model. The numerical transport phenomena based calculations are complex, and are unsuitable in situations where rapid calculations are desired. A practical solution to this problem is to develop a neural network that is trained with the data generated by a numerical transport phenomena based model. Neural network models are powerful non-linear regression analysis methods [50-54] that can relate input variables like welding process parameters and material properties with weld characteristics such as weld pool geometry, and provide high computational speed.

In summary, the solute distribution in a weld has significant impact on its properties such as weld pool geometry and occurrence of weld defects like liquation cracking. A comprehensive transport phenomena based model is needed to accurately predict solute distribution in the weld, which can be applied to design weld consumables, to study the weld bead shape on welding two plates with different sulfur contents and to tailor weld pool geometry to specified dimensions. Furthermore, new methodologies need to be developed where the reliability of the output of the transport phenomena based models is increased by combining these models with genetic algorithm based optimization routines.

## **1.2 Research Objectives and Methodology**

This doctoral research focuses on studying mass transport during fusion welding to determine the distribution of solutes in the weld, and their impact on the weld pool

geometry and consumable design to avoid occurrence of weld defects like liquation cracking. In order to achieve this goal, the specific tasks undertaken and the methodology used in the present thesis research are shown in Fig. 1.1. In short, the figure shows the following specific accomplishments:

1. Integrating three-dimensional solute transport equations with an already existing three-dimensional numerical heat transfer and fluid flow model, in our research group at Penn State, to understand the complex coupling of momentum, heat and solute transport during gas tungsten arc (GTA) fusion welding. This model provides temperature field, velocity fields and solute distribution in the entire GTA weld.

2. Improving the reliability of the output of the numerical transport phenomena based models by estimating the values of five uncertain input parameters, i.e., arc efficiency, arc radius, arc power distribution factor, effective thermal conductivity and viscosity of liquid by using a real number based genetic algorithm (GA) and a limited volume of experimental data. The ability of the GA to find the global optimal solution independent of the initial guessed values [46-49] makes it appropriate for estimating these uncertain input parameters.

3. Developing a computational procedure using GA to systematically search for multiple sets of welding variables of arc current, voltage and welding speed to obtain a specified weld geometry. The property of GA to provide a population of solutions makes such a systematic search possible [46-49]. Several neural networks have been developed that are trained with the data generated by the numerical transport phenomena based model. Replacing the forward numerical model in this computational procedure by these neural networks has led to significant computational economy.

The numerical transport phenomena based model should be flexible and readily modifiable for application in different welding conditions and materials. The model has been tested on two systems in the present study, which include:

4. Evolution of weld pool geometry during GTA welding of stainless steel plates having same and different sulfur contents.

5. Adapting the numerical transport phenomena based model to gas metal arc (GMA) welding, by considering heat and solute intake due to filler metal addition, and

integrating a non-equilibrium solidification model. This model provides the non-equilibrium solute distribution in the solidifying weld metal, which is used for the design of consumables to avoid liquation cracking during GMA welding of Al-6.3%Cu alloy using filler metals with different copper content.

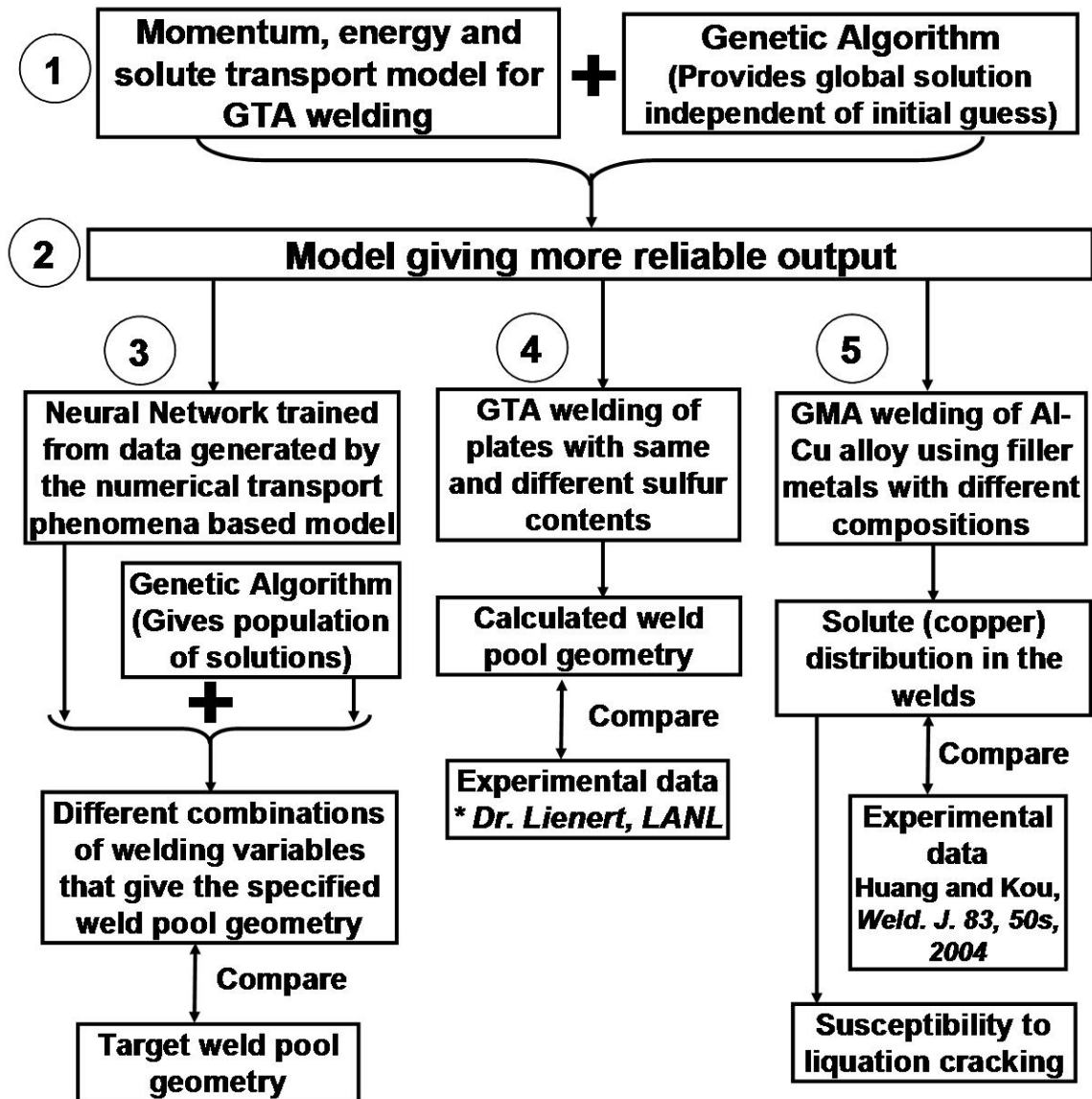


Fig. 1.1. List of tasks in the present thesis research.

### 1.3 Thesis Structure

The thesis consists of eight chapters. Chapter 1 describes the overall subject matter, outlines of the research objectives and methodology, and the thesis contents.

The available knowledge for simulating convective solute transport in fusion welding is reviewed in chapter 2. At first, the current understanding of transport processes including energy absorption, liquid convection and driving forces, turbulence is examined, and the effect of surface active elements on weld pool convection is reviewed. Secondly, the factors contributing to solute transport during GMA welding, and the relation between the resulting solute distribution and liquation cracking, are reviewed. Next, the resources available for enhancing the reliability of output of the numerical transport phenomena based models are presented, and the techniques that can make these models go backwards are reviewed. Finally, the possibility of developing a neural network model for fusion welding is explored in order to reduce the time of calculations.

In chapter 3 three-dimensional solute transport equations are integrated with an already existing three-dimensional numerical heat transfer and fluid flow model, to understand the complex coupling of momentum, heat and solute transport during gas tungsten arc (GTA) fusion welding. This model provides the temperature field, velocity fields and solute distribution in the entire GTA weld. Next, a computational procedure is developed where the transport phenomena based model is combined with a genetic algorithm (GA) and a limited volume of experimental data. This computational procedure is used to improve the reliability of output of the transport phenomena based model, by optimizing the values of its uncertain input parameters. The calculated and experimental weld pool geometry for GTA welding of stainless steel is compared to examine the reliability of the computational procedure.

In chapter 4, six neural networks have been developed for the GTA welding of stainless steel, in order to achieve computational economy in conducting calculations for fusion welding. The neural networks relate 17 input variables, which include welding process parameters and important material properties, with important output parameters such as weld pool geometry and peak temperature. A hybrid optimization scheme, including a gradient descent method and a genetic algorithm, is found to be very effective

in proper training of the networks. The accuracy of neural networks is ascertained by comparing their predictions with the corresponding results from the numerical transport phenomena based model.

In chapter 5, a computational procedure has been developed using a genetic algorithm and the neural networks to go backwards, i.e., systematically search for multiple sets of welding variables of arc current, voltage and welding speed to obtain a specified weld geometry. The use of neural networks in place of a heat transfer and fluid flow model significantly expedites the computational task. Several sets of welding variables with significantly different values of current, voltage and welding speed are found for a target weld geometry. Good agreement between the model predictions and the experimental data of weld pool penetration and width for various welding conditions shows that this approach is promising.

In chapter 6, the effect of surface active element, sulfur, on the evolution of weld pool geometry in stainless steel GTA welds is examined. The numerical transport phenomena based model is used to calculate the weld pool geometry when joining two plates with same and different sulfur contents. The influence of weld pool top surface sulfur distribution on weld pool convection and the shifting of the welding arc are identified as the two main factors contributing to the evolution of weld pool geometry when joining two plates with different sulfur contents. The calculated weld pool geometry is in fairly good agreement with the corresponding experimental results in all the cases.

In chapter 7, the numerical transport phenomena based model has been adapted to calculate solute transport during GMA welding, by considering heat and solute intake due to filler metal addition, and integrating a non-equilibrium solidification model. This model provides the non-equilibrium solute distribution in the solidifying weld metal, which is used for the design of consumables, to avoid liquation cracking during GMA welding of Al-6.3wt%Cu alloy, using filler metals with different copper contents. The model predictions of liquation cracking susceptibility in Al-Cu alloy weldments are confirmed by independent experiments for various filler metal compositions.

Summary and conclusions of the present study are presented in chapter 8. The results presented in this thesis indicate that the solute distribution in fusion welds, and its impact on weld pool geometry and occurrence of weld defects like liquation cracking, can be quantitatively predicted by a numerical transport phenomena based model. Furthermore, new methodologies are developed where the reliability of output of the transport phenomena based models is increased, the speed of computation has been significantly enhanced by developing neural networks, and the weld pool can be tailored to specified dimensions.

#### 1.4 References

1. H. Zhao, and T. DebRoy, *J. Appl. Phys.* 93, 10089 (2003).
2. W. Zhang, C.-H. Kim, and T. DebRoy, *J. Appl. Phys.* 95, 5210 (2004).
3. W. Zhang, C.-H. Kim, and T. DebRoy, *J. Appl. Phys.* 95, 5220 (2004).
4. A. De, and T. DebRoy, *J. Appl. Phys.* 95, 5230 (2004).
5. J. W. Elmer, T. A. Palmer, S. S. Babu, W. Zhang and T. DebRoy, *J. Appl. Phys.* 95, 8327 (2004).
6. A. De, and T. DebRoy, *J. Phys. D: Appl. Phys.* 37, 140 (2004).
7. S. Mishra, and T. DebRoy, *J. Phys. D: Appl. Phys.* 37, 2191 (2004).
8. S. Mishra, and T. DebRoy, *Acta Mater.* 52, 1183 (2004).
9. X. He, P. Fuerschbach, and T. DebRoy, *J. Appl. Phys.* 94, 6949 (2003).
10. C.-H. Kim, W. Zhang, and T. DebRoy, *J. Appl. Phys.* 94, 2667 (2003).
11. A. Kumar, and T. DebRoy, *J. Appl. Phys.* 94, 1267 (2003).
12. S. A. David, R. Trivedi, M. E. Eshelman, J. M. Vitek, S. S. Babu, T. Hong, and T. DebRoy, *J. Appl. Phys.* 93, 4885 (2003).
13. W. Zhang, G. G. Roy, J. Elmer, and T. DebRoy, *J. Appl. Phys.* 93, 3022 (2003).
14. X. He, P. Fuerschbach, and T. DebRoy, *J. Phys. D: Appl. Phys.* 36, 3079 (2003).
15. X. He, P. W. Fuerschbach, and T. DebRoy, *J. Phys. D: Appl. Phys.* 36, 1388 (2003).
16. J. W. Elmer, T. A. Palmer, W. Zhang, B. Wood, and T. DebRoy, *Acta Mater.* 51, 3333 (2003).
17. T. Hong, and T. DebRoy, *Metall. Mater. Trans. B* 34, 267 (2003).
18. K. Mundra, T. DebRoy, and K. Kelkar, *Numerical Heat Transfer A* 29, 115 (1996).
19. A. Kumar, and T. DebRoy, *Int. J. Heat Mass Transfer.* 47, 5793 (2004).
20. W. Pitscheneder, T. DebRoy, K. Mundra and R. Ebner, *Weld. J.* 75, 71s (1996).
21. P. Sahoo, T. DebRoy and M. J. McNallan, *Met. Trans. B* 19, 483 (1988).
22. C. R. Heiple and J. R. Roper, *Weld. J.* 61, 97s (1982).
23. C. R. Heiple, J. R. Roper, R. T. Stagner and J. J. Alden, *Weld. J.* 62, 72s (1983).
24. C. R. Heiple, P. Burgardt, J. R. Roper, J. L. Long: *Proc. Int. Conf. on the Effects of Residual, Trace and Micro-alloying Elements on Weldability and Weld Properties*, TWI, Cambridge, 1984, 36.

25. S. W. Pierce, P. Purgardt and D. L. Olson, *Weld. J.* 78, 45s (1999).
26. B. J. Keene, K. C. Mills, J. L. Robinson and M. H. Rodwell: *Proc. Int. Conf. on the Effects of Residual, Trace and Micro-alloying Elements on Weldability and Weld Properties*, TWI, Cambridge, 1984, 45.
27. J. Leinonen and L. P. Karjalainen: *Proc. Int. Conf. on the Effects of Residual, Trace and Micro-alloying Elements on Weldability and Weld Properties*, TWI, Cambridge, 1984, 4.
28. J. Autio, J. Makio, K. Makela, E. Minni and P. Kettunen: *Proc. Int. Conf. on the Effects of Residual, Trace and Micro-alloying Elements on Weldability and Weld Properties*, TWI, Cambridge, 1984, 18.
29. A. F. Rollin and M. J. Bentley: *Proc. Int. Conf. on the Effects of Residual, Trace and Micro-alloying Elements on Weldability and Weld Properties*, TWI, Cambridge, 1984, 9.
30. K. J. Rodgers: *Proc. Int. Conf. on the Effects of Residual, Trace and Micro-alloying Elements on Weldability and Weld Properties*, TWI, Cambridge, 1984, 2.
31. M. J. Tinkler, I. Grant, G. Mizuno and C. Gluck: *Proc. Int. Conf. on the Effects of Residual, Trace and Micro-alloying Elements on Weldability and Weld Properties*, TWI, Cambridge, 1984, 29.
32. D. G. Kolman, Report on 'Assessment of the corrosion, stress corrosion cracking and embrittlement susceptibility of 30313 storage containers' available at <http://public.lanl.gov/MCEL/PDF-Publications/CorrSCC3013.pdf>.
33. G. R. Cannell, W. L. Daugherty and M. W. Stokes, Report on 'Closure welding of plutonium bearing storage containers' available at <http://sti.srs.gov/fulltext/ms2002053/ms2002053.pdf>.
34. DOE-STD-3013-96, 'Criteria for preparing and packaging plutonium metals and oxides for long-term storage' available at <http://www.eh.doe.gov/techstds/standard/std3013/s963013.pdf>.
35. C. Huang, and S. Kou, *Weld. J.* 83, 50s (2004).
36. H. Zhao and T. DebRoy, *Metall. Mater. Trans. B* 32, 163 (2001).
37. H. W. Kerr, and M. Katoh, *Weld. J.* 66, 251s (1987).

38. M. Miyazaki, K. Nishio, M. Katoh, S. Mukae, and H. W. Kerr, *Weld. J.* 69, 362s (1990).
39. C. Huang, and S. Kou, *Weld. J.* 79, 113s (2000).
40. C. Huang, and S. Kou, *Weld. J.* 80, 9s (2001).
41. C. Huang, and S. Kou, *Weld. J.* 80, 46s (2001).
42. C. Huang, and S. Kou, *Weld. J.* 81, 211s (2002).
43. C. Huang, and S. Kou, *Weld. J.* 82, 184s (2003).
44. C. Huang, and S. Kou, *Weld. J.* 83, 111s (2004).
45. S. Kou, and Y. H. Wang, *Metall. Trans. A* 17, 2271 (1986).
46. D. E. Goldberg, *Genetic Algorithm in Search, Optimization and Machine Learning* (Addison-Wesley, MA, 1989).
47. *Handbook of Evolutionary Computations*, edited by T. Back, D. B. Fogel and Z. Michalewicz (IOP Publishing Ltd., Oxford University Press, 2000).
48. K. Deb, A. Anand, and D. Joshi, *Evolutionary Computation* 10, 371 (2002).
49. K. Deb, *Multi-objective optimization using evolutionary algorithms – Edition 1* (Wiley, New York, 2001).
50. J. M. Vitek, Y. S. Iskander and E. M. Oblow, *Weld. J.* 79 33s (2000).
51. J. M. Vitek, Y. S. Iskander and E. M. Oblow, *Weld. J.* 79, 41s-50s (2000).
52. D. E. Rumelhart, G. E. Hinton and R. J. Williams, *Nature* 323, 533-536 (1986).
53. L. Burke and J. P. Ignizio, *J. Intelligent Manufacturing* 8, 157 (1997).
54. L. Fausett, *Fundamentals of Neural Networks* (Prentice-Hall, NJ, 1994).

## Chapter 2

### Background

This doctoral research focuses on studying mass transport during fusion welding to determine the distribution of solutes in the weld, and their impact on the weld pool geometry and consumable design to avoid occurrence of weld defects like liquation cracking. In particular, solute transport equations are introduced into an existing numerical heat and fluid flow to study the distribution of solute in the weld pool. This transport phenomena based model is used to understand the evolution of weld pool geometry during gas tungsten arc (GTA) welding of stainless steel plates having same and different sulfur contents, and the design of consumables to avoid liquation cracking during gas metal arc (GMA) welding of Al-6.3wt%Cu alloy using filler metals with different copper contents. Furthermore, new methodologies are developed in order to address some major problems associated with the currently available numerical transport phenomena based models. Firstly, the reliability of the output of the numerical transport phenomena based model is increased by combining this model with a genetic algorithm based optimization routine and a limited volume of experimental data. Secondly, a neural network, trained by data generated from the numerical transport phenomena based model, is developed in order to obtain the results in a reasonable time frame. Finally, the neural network is combined with a genetic algorithm to go backwards, i.e., find multiple combinations of welding variables to obtain a specific weld geometry. The following important problems and issues pertinent to the subject of this study are critically reviewed in this chapter.

(1) Solute transport and distribution during fusion welding has a profound effect on the weld characteristics such as weld pool geometry and creation of weld defects like liquation cracking. However, not much attention has been paid in the literature to this important topic. Most of the studies to date are focused on understanding heat and fluid flow during welding, due to their importance in accurately calculating temperature and velocity fields in the weld. This section reviews the current understanding of heat and fluid flow during fusion welding, and the effect of surface active elements on weld pool

convection. This review is important as it presents the importance of convective heat transport in the weld pool, and prepares the basic foundation for conducting convective solute transport calculations in the present thesis research. The calculation procedure described in this section is readily applicable to GTA welding.

(2) The GMA welding process is slightly more complex, due to the addition of a consumable electrode. The heated metal droplets from the electrode make a significant contribution to both the heat and solute transport in the weldment, and the resulting solute distribution plays a major role in the occurrence of weld defects like liquation cracking. This section reviews the factors contributing to solute transport during GMA welding, and the relation between solute distribution and liquation cracking.

(3) Before a numerical transport phenomena based model is used to calculate mass transport during fusion welding, some major limitations of these models need to be addressed. The output of the currently available numerical transport phenomena based models is often not reliable mainly because of the uncertainty in the values of some of the input parameters like arc efficiency, arc radius, arc power distribution factor, effective thermal conductivity and effective viscosity of the liquid. A recourse to this problem is to calculate the optimized values of these parameters using some optimization routine and experimental data. Also, the current generation of numerical transport phenomena based models cannot go backwards, i.e., they cannot provide the welding process parameters such as current, voltage and welding speed, to obtain a target weld geometry. Genetic algorithms (GAs) are powerful optimization routines that can find the global optimal solution of a problem independent of the initial guessed values. The capabilities of GAs and their possible applications for solving the above mentioned problems of transport phenomena based models for fusion welding are reviewed in this chapter.

(4) Another shortcoming of the numerical transport phenomena based models for fusion welding, which severely limits their use in the welding industry, is that they are complex, require specialized training to develop and test, and consume a large amount of computer time to run. A practical solution to this problem is to develop a neural network, which can relate input variables like welding process parameters and material properties with weld characteristics such as weld pool geometry, and at the same time provide high

computational speed. This chapter reviews the previous work done in this regard, and the problems and issues involved in developing a neural network for a complex problem like fusion welding.

At the end of this chapter, several important unanswered questions pertinent to the present research are identified. Solving these unanswered questions is an important goal of the present thesis study, and details of the solution are presented in subsequent chapters.

## **2.1 Transport Processes Occurring During Fusion Welding**

The fusion welding process is schematically illustrated in Fig. 2.1 [1-6]. Three distinct regions of the weld can be seen in this figure: the fusion zone (FZ), the heat affected zone (HAZ) and the base metal. During fusion welding, the heat source interacts with the base metal leading to a series of complex physical processes [1-6]. The FZ undergoes melting and solidification. In the weld pool, the liquid metal circulates vigorously under the influence of electromagnetic, surface tension gradient and buoyancy forces. The spatial variation of surface tension due to temperature and composition gradients at the weld pool top surface often provides the main driving force for the convective flow, known as the Marangoni flow [3]. Surface active elements like sulfur significantly alter the spatial variation of surface tension and the resulting liquid convection pattern. It is well known that the convective heat flow affects the FZ geometry and the temperature distribution in the HAZ. However, the influence of convection on solute distribution in the weld pool has not been studied yet.

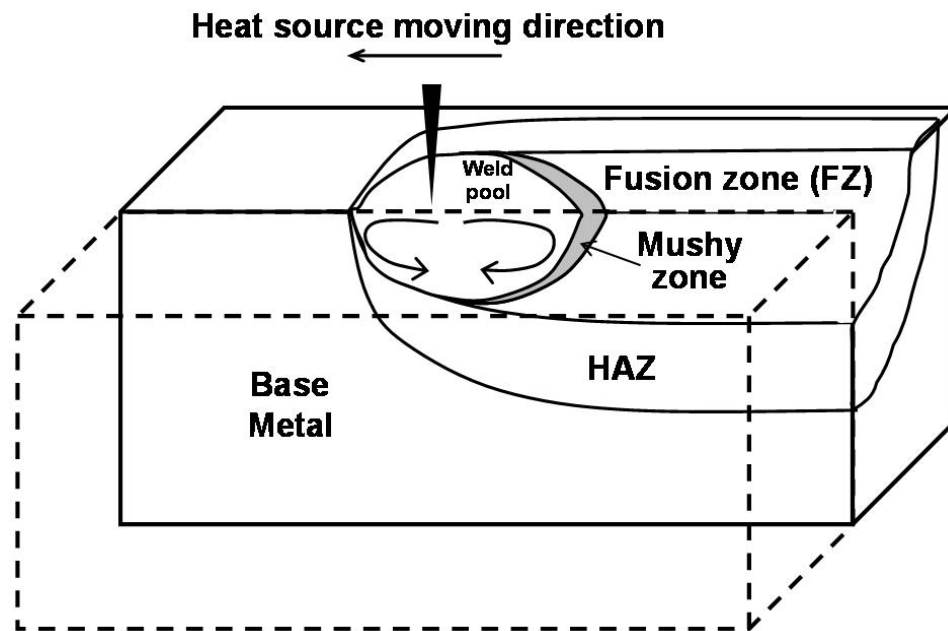


Fig. 2.1. Schematic plot depicting the fusion welding process. HAZ stands for Heat-Affected Zone.

Various solid-state transformations can take place in the HAZ, which experiences significant thermal exposure during welding. Furthermore, the portions of HAZ close to the FZ may be liquated owing to the presence of low temperature eutectics [5]. This leads to the formation of a partially melted zone (PMZ), which plays a major role in the occurrence of weld defects like liquation cracking [5]. The base metal is unaffected by the welding process. During fusion welding, the complex physical processes take place in a very small area, usually of the order of a few millimeters. Since a large number of physical processes occur simultaneously during welding, it is often necessary to divide the complex welding process into a number of simple constituent parts. These parts include the interaction of the heat source and the weld pool, the heat transfer, fluid flow and solute transport in the weld pool, the evolution of FZ and HAZ microstructure, and the development of residual stress and distortion in the welds. The heat transfer, fluid flow and solute transport is of particular interest, since it provides the knowledge of temperature fields, velocity fields and solute distribution in the weldment, which is essential for understanding other physical processes such as the evolution of weld pool geometry, occurrence of weld defects, microstructural evolution and residual stress [1-6].

Experimental observation of heat transfer, fluid flow and solute transport in the weld pool is very difficult. The measurement of temperatures in the weld pool by placing thermocouples is tough and inaccurate because of the small size of the weld pool and very high liquid temperatures [7-14]. Indirect measurement methods such as infrared thermographic cameras [9,13] are also not very accurate because many assumptions need to be made with respect to the dependence of emissivity on temperature, the associated angle, and the wavelength [11,12]. In addition, during arc welding process the intense arc and plasma environment create additional complexity. As of now, there is no technique available that can reliably measure temperature within the molten pool. The measurement of liquid flow velocities and solute composition in the small and intensely heated weld pool is also difficult. Very few data have been reported on the measurement of liquid flow velocities in the weld pool [13,15,16] and almost all the available data on weld pool composition is for post-welded samples. Therefore, a practical recourse is to use

quantitative calculations to gain insights into the phenomena of heat transfer, fluid flow and solute transport during welding [14].

This section examines the current understanding of heat transfer, fluid flow and solute transport in the weld pool. Only a fraction of heat energy is actually absorbed by the base metal during fusion welding. The efficiency of energy absorption is an important parameter. Thus, the factors affecting the efficiency of energy absorption are discussed first. In the weld pool, the absorbed heat is transported both by convection and conduction. Therefore, the liquid convection and the forces driving it are also discussed. The turbulence in the weld pool is also reviewed because it may affect weld pool heat transfer. The conservation equations governing heat transfer, fluid flow and solute transport are then presented. Next, the numerical solution of these conservation equations using the control volume/finite difference method [17-19] is discussed. At the end of this section, a summary of the previous work in the field of transport phenomena in simple systems is presented.

### 2.1.1 Deposition of heat energy at weld top surface

Since the distribution of heat input has a direct influence on the weld pool geometry, it is important to know how the heat energy is distributed on the weld top surface. For GTA welding, the following Gaussian distribution is widely used to account for the heat flux at the weld top surface [20-22].

$$q(r) = \frac{dVI\eta}{\pi r_b^2} \exp\left(-d \frac{r^2}{r_b^2}\right) \quad (2.1)$$

where  $q$  is the heat flux at a given location at the weld top surface,  $r$  is the distance between the heat source and the specific location,  $d$  is a distribution factor,  $I$  and  $V$  are welding current and voltage, respectively,  $\eta$  is the arc efficiency and  $r_b$  is a characteristic energy distribution parameter. Two typical values of  $d$  have been reported in the literature, i.e., 3.0 and 0.5. The  $d$  value of 0.5 was proposed by Tsai et al. [23] and Smartt et al. [24] based on experimental measurements. On the other hand, several weld models [20-22,25-27] used the  $d$  value of 3.0. Depending on the arc length, electrode tip angle, and current, the distribution parameter ( $r_b$ ) is reported to vary in the range between 1.0

and 4.0 mm [23,24]. Equation (2.1) indicates that if the values of  $d$ ,  $\eta$  and  $r_b$  are known, the heat flux at the weld top surface can be computed. The knowledge of the input heat flux is a necessary in order to calculate the heat dissipation in the weldment.

It is noteworthy that although Eq. (2.1) was originally proposed for GTA welding, similar expressions have also been used to describe the heat flux at the weld top surface for GMA [28,29] welding.

### 2.1.1.1 Efficiency of energy absorption

Only a fraction of energy is transferred from the heat source to the workpiece during welding,. The amount of energy transferred is important since it directly affects the weld pool geometry. The physical phenomena that influence the absorption of energy are unique to each welding process [27].

For arc welding, the fraction of the arc energy that is transferred to the workpiece is defined by arc efficiency ( $\eta$ ), which is given as [2]:

$$\eta = 1 - \frac{q_e + (1 - n)q_p + mq_w}{VI} \quad (2.2)$$

where  $q_e$  is the rate of heat transferred to the electrode from the welding arc,  $n$  is the proportion of heat output from the arc column that is transferred into the workpiece,  $q_p$  is the rate of heat loss by radiation and convection from the arc column,  $m$  is the fraction of absorbed energy that is radiated away and lost,  $q_w$  is the rate of heat absorbed by the workpiece, and  $I$  and  $V$  are welding current and voltage, respectively.

In cases where a consumable electrode is used, such as in gas metal arc (GMA) welding,  $q_e$  is also transferred to the workpiece and as a result, arc efficiency is given as [2]:

$$\eta = 1 - \frac{(1 - n)q_p + mq_w}{VI} \quad (2.3)$$

It is noteworthy that although Eqs. (2.2) and (2.3) are useful in explaining the manner in which various types of heat loss affect arc efficiency, it is very difficult to evaluate the values of  $q_e$ ,  $q_p$ ,  $q_w$ ,  $n$  and  $m$  from theoretical considerations. Therefore, commonly the value of arc efficiency is determined experimentally under various welding conditions. In

the literature, experimentally measured arc efficiency values are available for various arc welding processes including submerged arc welding (SAW), gas tungsten arc welding (GTAW) and gas metal arc welding (GMAW). Depending on the welding process used, the measured arc efficiency values vary from 20% to over 95% [7,14].

Tsai and Eagar [23] experimentally measured the arc efficiency and the distribution of heat flux as a function of various welding parameters for a gas tungsten arc. These welding parameters included the welding current, electrode tip angle, arc length, and shielding gas. In their experiments, the current changed from 100 to 280 A, the electrode tip angle changed from 30° to 120°, the arc length varied from 2 to 9 mm, and three different shielding gases were used: pure argon, 25% of helium + 75% of argon, and 50% of helium + 50% of argon. They found that the arc energy distribution parameter,  $r_b$ , had strong dependence on the welding current, shielding gas and arc length, but did not change much with the electrode tip angle. For the welding conditions used in their experiments, the value of  $r_b$  varied from 1.5 to 3.6 mm.

The arc efficiency for GMAW is usually higher than that for GTAW, since a fraction of energy lost to the electrode is transferred into the workpiece in the form of superheated metal droplets. The droplet transfer is a unique feature in GMAW, and it is often responsible for the finger penetration observed in the GMA welds. The droplet heat transfer will be reviewed in a later section.

The aforementioned discussion reveals that no unique value can be found in the literature for the three important input parameters of  $d$ ,  $\eta$  and  $r_b$  for a given welding system. Therefore, these three parameters can be regarded as uncertain input parameters in numerical transport phenomena based calculations of fusion welding. Appropriate values of these parameters need to be known for the reliable calculation of input heat flux during welding.

### **2.1.2 Convective heat transfer in the weld pool**

Convective heat transfer is very important because in many cases it has a profound impact on the shape and size of the weld pool and the temperature distribution in the entire weld [2,4-7]. The liquid convection is driven by the surface tension gradient,

buoyancy, and when electric current is used, electromagnetic forces [2,4-7]. Since the calculation of convective heat transfer requires the solution of the equations of conservation of mass, momentum, heat and solute and is highly complicated, numerical solution is often utilized. In order to accurately predict the convective heat transfer in the weld pool, the effect of various driving forces must be properly incorporated into the momentum equation.

### 2.1.2.1 Electromagnetic force

Fig. 2.2 is a schematic plot that shows the important driving forces in the weld pool and the resulting liquid flow pattern. The electromagnetic force, also called Lorentz Force, is caused by the electric current field together with the magnetic field induced by it in the metal workpiece. As shown in Fig. 2.2(a), the direction of the electromagnetic force is downward and inward. As a result, at the top surface of the weld pool the melt flows from the periphery to the center, and at the center the liquid metal is driven downwards, leading to a deep and narrow weld pool. The electromagnetic force ( $\vec{F}_{emf}$ ) can be expressed as [30-32]:

$$\vec{F}_{emf} = \vec{J} \times \vec{B} \quad (2.4)$$

where  $\vec{B}$  is the magnetic flux vector and  $\vec{J}$  is the current density vector in the weld pool.

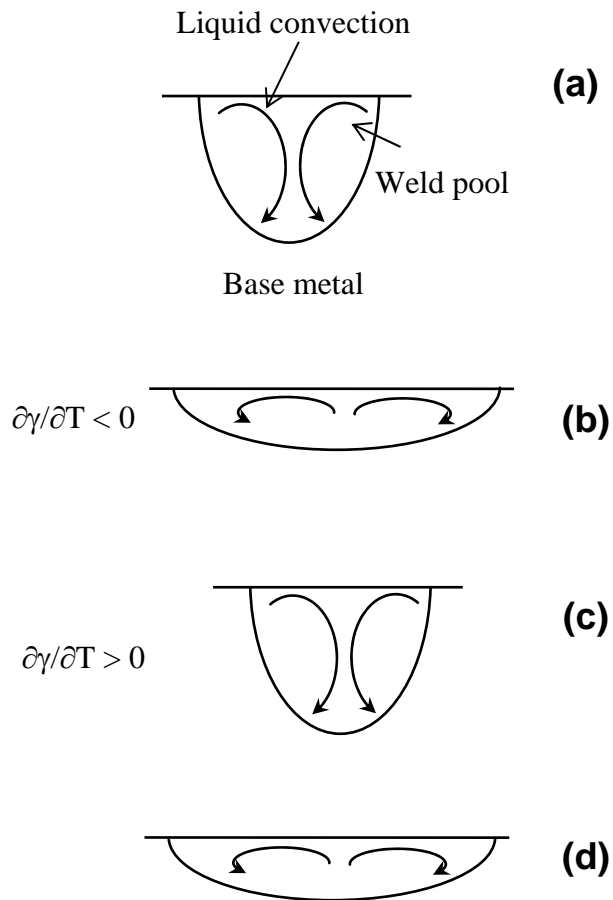


Fig. 2.2. Various driving forces and the resulting liquid convection in the weld pool [7,33]: (a) electromagnetic force, (b) surface tension gradient force with negative  $\partial\gamma/\partial T$ , (c) surface tension gradient force with positive  $\partial\gamma/\partial T$ , and (d) buoyancy force.  $\partial\gamma/\partial T$  is the temperature coefficient of surface tension.

Comprehensive three-dimensional calculations of  $\vec{J}$  and  $\vec{B}$  fields are needed for accurate determination of the electromagnetic force in the weld pool. Kou and Sun [31] obtained the following analytical expressions for  $\vec{J}$  and  $\vec{B}$  fields by solving Maxwell's equations in an axis-symmetric system with Magneto-hydrodynamics (MHD) approximation.

$$J_z = \frac{I}{2\pi_0} \int_0^\infty \lambda J_0(\lambda r) \exp(-\lambda^2 \sigma_j^2 / 12) \frac{\sinh[\lambda(c-z)]}{\sinh(\lambda c)} d\lambda \quad (2.5)$$

$$J_r = \frac{I}{2\pi_0} \int_0^\infty \lambda J_1(\lambda r) \exp(-\lambda^2 \sigma_j^2 / 12) \frac{\cosh[\lambda(c-z)]}{\sinh(\lambda c)} d\lambda \quad (2.6)$$

$$B_\theta = \frac{\mu_m I}{2\pi} \int_0^\infty J_1(\lambda r) \exp(-\lambda^2 \sigma_j^2 / 12) \frac{\sinh[\lambda(c-z)]}{\sinh(\lambda c)} d\lambda \quad (2.7)$$

where  $J_z$  is the vertical component of the current density,  $r$  is the radial distance from the arc center,  $I$  is the current,  $\sigma_j$  is the effective current radius of the arc,  $J_0$  is the Bessel function of zero order and first kind,  $z$  is the vertical distance from the top surface,  $c$  is the thickness of the workpiece,  $J_r$  is the radial component of current density,  $J_1$  is the first kind of Bessel function of first order,  $B_\theta$  is the angular component of the magnetic field, and  $\mu_m$  is the magnetic permeability of the material. The radial and the axial components of the magnetic flux,  $B_r$  and  $B_z$ , are assumed to be zero. Once the  $\vec{J}$  and  $\vec{B}$  fields are known, the electromagnetic force in the weld pool can be computed using Eq. (2.4).

### 2.1.2.2 Marangoni shear stress and the effect of surface active elements

Surface tension ( $\gamma$ ) is a thermo-physical property of liquid metal. The spatial gradient of surface tension is a stress known as the Marangoni shear stress. This stress arises due to spatial variation of temperature and composition, which can be expressed as:

$$\tau = \frac{\partial \gamma}{\partial T} \frac{\partial T}{\partial r} + \frac{\partial \gamma}{\partial C} \frac{\partial C}{\partial r} \quad (2.8)$$

where  $\tau$  is the shear stress due to surface tension,  $T$  is the temperature,  $r$  is the distance along the surface from the heat source, and  $C$  is the concentration of surface active element. When the materials being welded either have no surface active element or have

the same composition of surface active element throughout, then the concentration gradient,  $\partial C/\partial r$ , is zero, and the difference in surface tension is due to the spatial temperature variation alone. In other words, the shear stress depends only on  $\partial\gamma/\partial T$  and the spatial temperature gradient  $\partial T/\partial r$  at the pool surface.

In the absence of a surface active element, the temperature coefficient of surface tension,  $\partial\gamma/\partial T$ , for many materials is less than zero, i.e., the higher the temperature, the lower the surface tension. Hence, at the weld pool top surface, the liquid metal is pulled radially outward by the higher surface tension liquid metal at the pool edge [7,33-39]. This leads to a wide and shallow weld pool, as shown in Fig. 2.2(b). If some surface active elements such as sulfur and oxygen are present in the weld pool in a small yet significant amounts, then the value of  $\partial\gamma/\partial T$  can become positive [7, 33-39]. For liquid metal with a positive value of  $\partial\gamma/\partial T$ , the liquid is pulled radially inwards by the high surface tension liquid at the center of the weld pool. This leads to a deep and narrow weld pool as shown in Fig. 2.2(c).

Sahoo et al. [35] determined surface tension,  $\gamma$ , as a function of both temperature and activity of surface active element as:

$$\gamma = \gamma_m - A[T - T_m] - RT\Gamma_s \ln[1 + Ka_i] \quad (2.9)$$

$$K = k_1 \exp\left(-\frac{\Delta H^0}{RT}\right) \quad (2.10)$$

where  $\gamma_m$  is the surface tension of the pure metal at melting point,  $T_m$  is the melting point of the material,  $a_i$  is the activity of the surface active element,  $i$ ,  $A$  is negative of  $d\gamma/dT$  for pure metal,  $\Gamma_s$  is the surface excess at saturation,  $k_1$  is the entropy factor, and  $\Delta H^0$  is the standard enthalpy of adsorption. By differentiating Eq. (2.9) with respect to temperature, they [35] obtained the expression for  $d\gamma/dT$  as a function of both temperature and activity of surface active element as:

$$\frac{d\gamma}{dT} = -A - R\Gamma_s \ln[1 + Ka_i] - \frac{Ka_i}{1 + Ka_i} \Gamma_s (\Delta H^0 - \Delta \bar{H}_i^m) \quad (2.11)$$

where  $\Delta \bar{H}_i^m$  is the partial molar enthalpy of mixing of surface active element,  $i$ , in the solution.

Pitscheneder et al. [34] used Eqs. (2.9) and (2.11) to analyze the variation of surface tension,  $\gamma$ , and  $d\gamma/dT$ , respectively, with both temperature and activity of surface active element sulfur, in iron-sulfur (Fe-S) system. The variation of surface tension of the alloy with temperature and sulfur activity is shown in Fig. 2.3(a). It can be seen that the surface tension of the alloy is a strong function of both the factors. The surface tension decreases with increase in sulfur activity for a given temperature. For a given sulfur activity having a value close to zero, the surface tension decreases continuously with increase in temperature, leading to a negative slope, i.e., negative  $d\gamma/dT$ . However, at significantly high values of sulfur activity, surface tension first increases and then decreases with temperature, leading to a change in the value of  $d\gamma/dT$  from positive to negative. The variation of  $d\gamma/dT$  with temperature for three different values of sulfur activity is presented in Fig. 2.3(b) [34]. The figure shows a significant difference in  $d\gamma/dT$  for the three compositions.

Pitscheneder et al. [34] used a heat transfer and fluid flow model and Eq. (2.11) to study the effect of sulfur content and heat input on the weld pool geometry. The comparison between the predicted and measured cross sections of steel welds containing 20 and 150 parts per million (ppm) of sulfur, which were laser welded under different powers is shown in Fig. 2.4. It can be seen that at a laser power of 1.9 kW, the pool geometries in two steels were similar. In contrast, when the laser power increased to 5.2 kW, the weld containing 150 ppm sulfur had a much deeper penetration than that containing 20 ppm sulfur. They [34] explained the observed results based on the direction of the convection dominant heat transport in the weld pool. At the laser power of 1.9 kW, the weld pool and the liquid velocities were small. The maximum values of the Peclet number, which gives the ratio of the convective to conductive heat transport, for the steel weld pools with 20 and 150 ppm sulfur were 0.18 and 0.91, respectively. Such low Peclet number indicated that conduction was the dominant mechanism for heat dissipation in the weld pool. In other words, the direction of the liquid flow was not important in determining the weld pool shape. As a result, there were no significant differences between the weld pool geometries for steels containing 20 and 150 ppm sulfur. On the other hand, at the laser power of 5.2 kW, the values of Peclet number were greater than

200. Such high Peclet numbers indicated that convection was the dominant mode of heat transport in the weld pool. As a result, the weld pool geometry was largely determined by the direction of the liquid flow. For the sulfur content of 20 ppm, the value of  $\partial\gamma/\partial T$  was negative, which resulted in an outward flow and consequently a shallow and wide pool. For the sulfur content of 150 ppm, the value of  $\partial\gamma/\partial T$  was positive in majority of the weld pool, and the convection pattern was radially inward. Hence, the convective heat transport in the downward direction resulted in a deep weld penetration. The good agreement between the calculated and measured weld pool geometries, shown in Fig. 2.4, indicated that the role of sulfur on the weld pool geometry could be reasonably predicted using Eq. (2.11) and the heat transfer and fluid flow model.

In all the above mentioned studies, the concentration of sulfur was the same throughout the welded materials. However, when the two plates being welded have different sulfur contents, the weld geometry evolves in a very unique way. Such situations are common in the nuclear waste management industry, where stabilization, packaging and storage of plutonium-bearing materials involve closure welding of 316 stainless steel (SS) container (0.03 wt% sulfur) with 416 SS lid (>0.15 wt% sulfur) [40]. The final closure of the container must be leak-tight and structurally sound [40-42]. Another example is the tungsten inert gas (TIG) welding of small diameter 304L stainless steel tubing for instrumentation systems in CANDU (Canadian Deuterium Uranium) nuclear reactors [43]. Fig. 2.5 shows the results of one such experiment, where full penetration welds were desired when joining two tubes with same and different sulfur contents [43]. The results in Fig. 2.5(a) and (b) are consistent with the aforementioned discussion, i.e., higher penetration is obtained in high sulfur containing materials. Furthermore, Fig. 2.5(a) was acceptable as full-penetration weld was obtained, and Fig. 2.5(b) was unacceptable because full penetration weld was not formed. Thus, an optimum level of sulfur content was required in order to get an acceptable full penetration weld as shown in Fig. 2.5(a). However, there were some situations where the materials in Fig. 2.5(a) and Fig. 2.5(b) needed to be welded together, as shown in Fig. 2.5(c). Tinkler et al. [43] observed that when low sulfur tubing was joined to high sulfur tubing, as shown in Fig. 2.5(c), the weld shifted markedly towards the low sulfur side. As a result there was

very little melting of the piece with high sulfur content, i.e., lack-of-fusion defect occurred at the interface, resulting in improper joining of the two tubes [43] and unacceptable weld. Since many of the instrumentation systems in a nuclear reactor contain the primary coolant, insufficient fusion of the interface was unacceptable [43].

Heiple et al. [37] gave a qualitative explanation for the shifting of the weld bead based on their surface tension driven fluid flow model [35,36]. They stated that the tube with lower sulfur content has relatively higher surface tension than the one with higher sulfur content. The result is a net surface tension gradient across the weld pool leading to surface fluid flow toward the side of the tube with less sulfur. This flow pattern causes maximum penetration in the plates containing less sulfur. However, once the weld pool is formed, liquid metal in the weld pool circulates vigorously causing mixing of sulfur from the two plates. Actual surface tension gradient should depend on the final sulfur distribution in the weld pool. Also, during a similar experiment, Rollin et al. [44] observed that the welding arc was displaced towards the low sulfur side. They stated that the arc shift should also be a contributing factor to the weld bead shift, along with the surface tension driven fluid flow. A thorough quantitative modeling effort is still lacking in the literature, which can take into account all the factors affecting weld bead shift, and predict the actual location of the weld bead when joining two plates with different sulfur contents.

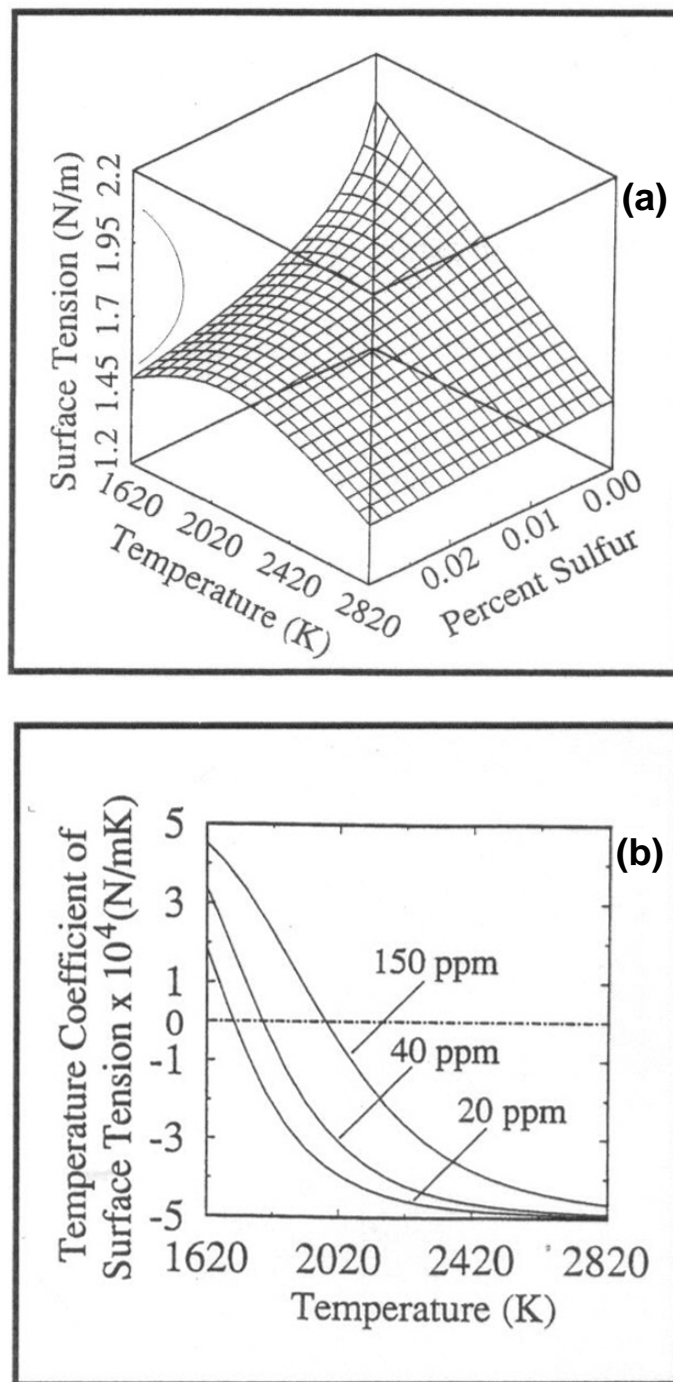


Fig. 2.3. Variation of (a) surface tension of Fe-S as a function of temperature and sulfur activity; (b)  $dy/dT$  of Fe-S as a function of temperature for samples containing 20, 40 and 150 ppm sulfur [34].

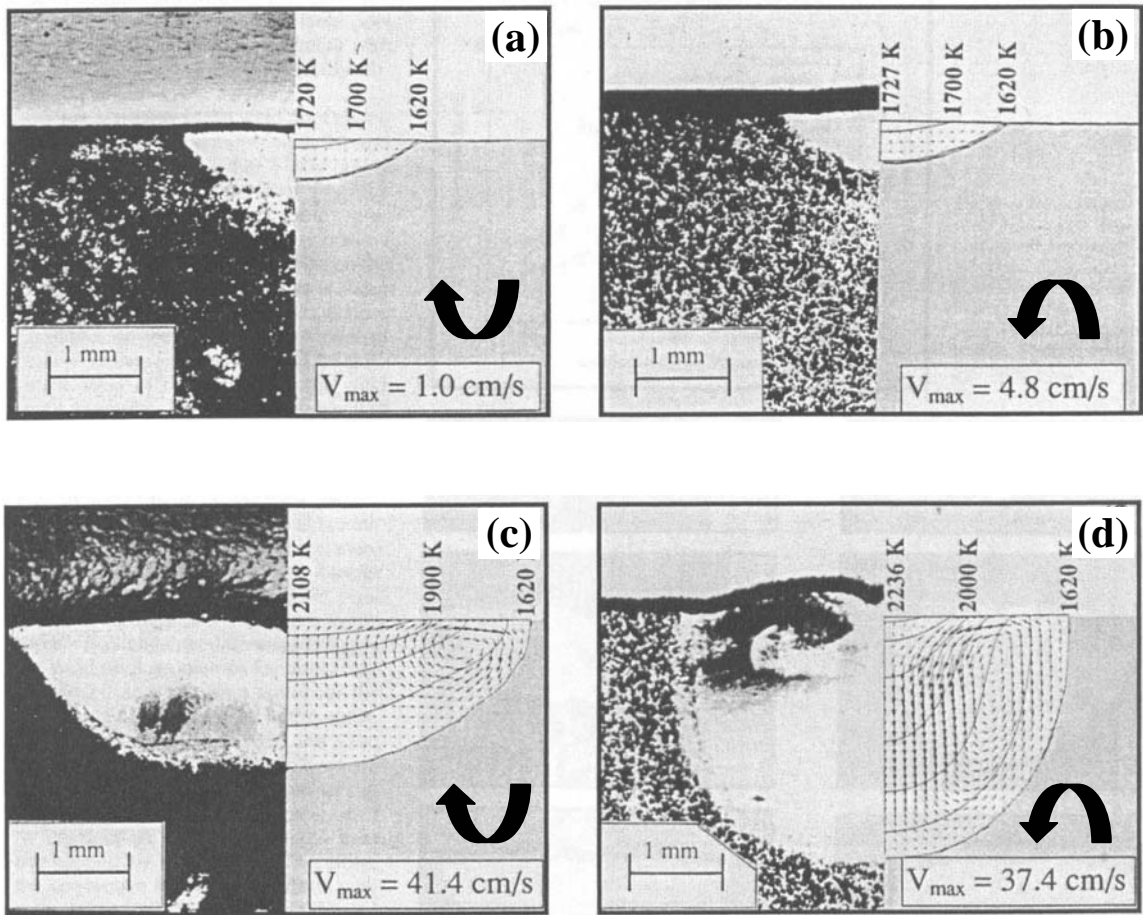


Fig. 2.4. Comparison between the calculated and measured weld pool geometry for various sulfur contents and heat inputs [34]: (a) 20 ppm and 1.9 kW, (b) 150 ppm and 1.9 kW, (c) 20 ppm and 5.2 kW, and (d) 150 ppm and 5.2 kW.

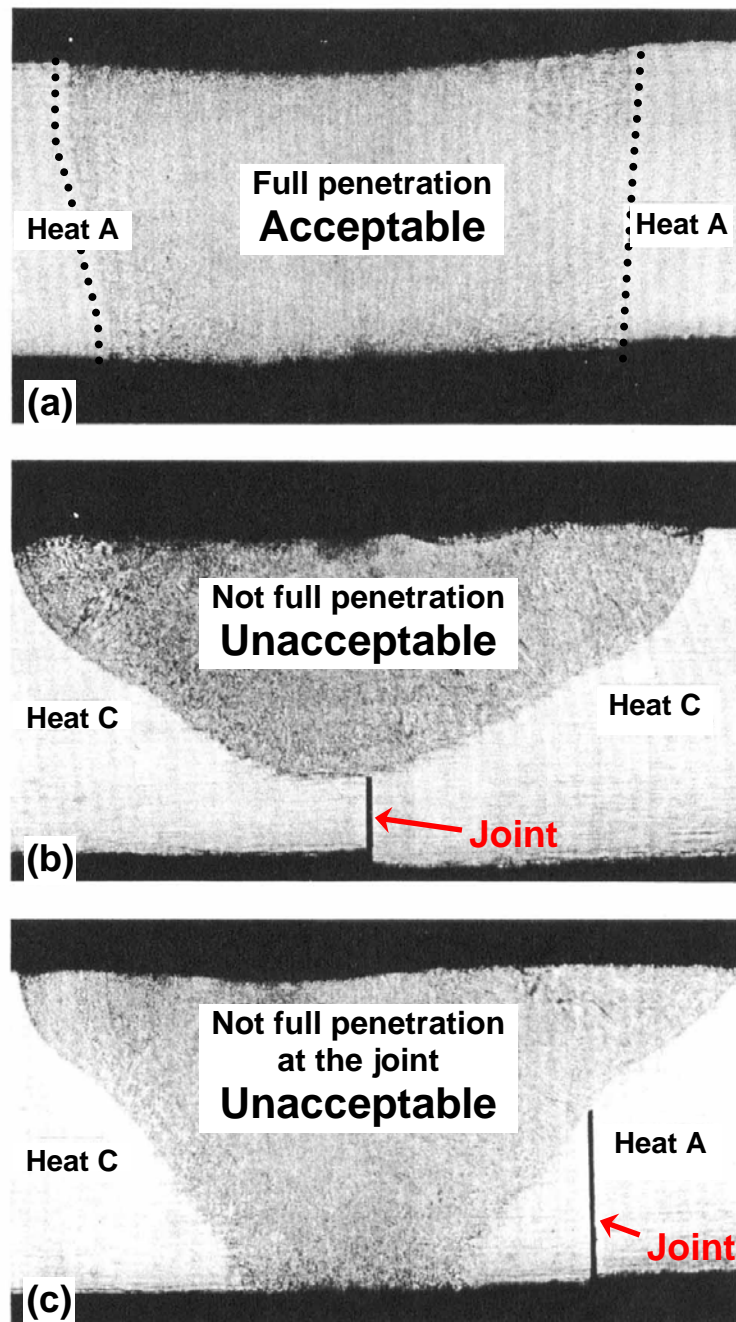


Fig. 2.5. Effect on the weld pool geometry [43] when welding two tubes with (a) same sulfur content of approximately 90 ppm (Heat A), which is relatively high; (b) same sulfur content of less than 30 ppm (Heat C), which is relatively low; and (c) different sulfur contents, i.e., welding Heat A and Heat C. Full penetration welds at the joint were desired. Welding conditions: Start current – 35 A; Finish current – 26 A; Fixture rotation speed - 4.6 revolutions/min, Outer diameter of tubing – 25 mm; Wall thickness – 2.4 mm.

### 2.1.2.3 Buoyancy force

The Boussinesq approximation is often used to calculate the buoyancy force driven flow, i.e., the variation in the density of the liquid metal is ignored, except when it gives rise to a buoyancy force, which is also termed as the gravitational force. It can be seen in Fig. 2.2(d) that the buoyancy driven convection causes the liquid metal to rise along the pool center and to fall along the pool boundary due to the local variation of density. This flow pattern is expected because the liquid metal near the heat source is at a relatively higher temperature. It moves upwards because of its relatively low density. On the other hand, the liquid metal near the pool boundary has relatively low temperature. Therefore, it flows downward because of its high density [7].

The buoyancy force is given by [45]:

$$F_b = \rho g \beta (T - T_{ref}) \quad (2.12)$$

where  $\rho$  is the density of liquid metal,  $g$  is the acceleration due to gravity,  $\beta$  is the thermal expansion coefficient,  $T$  is the temperature of the liquid metal, and  $T_{ref}$  is an arbitrarily selected reference temperature.

### 2.1.2.4 Relative importance of the driving forces

It is useful to check some dimensionless numbers in order to understand the heat transfer, fluid flow and solute transport behavior in the weld pool. These dimensionless numbers characterize the relative importance of the driving forces affecting fluid flow. Such dimensionless numbers can be used to predict the size and shape of the FZ and HAZ. For instance, if the electromagnetic force is the dominant driving force, a deep and narrow pool shape is expected. In contrast, if the surface tension gradient force with negative  $\partial\gamma/\partial T$  is mainly responsible for the liquid motion, the resulting weld pool is expected to be wide and shallow. Various dimensionless numbers are discussed as follows.

The ratio of buoyancy to viscous force is determined by Grashof number,  $Gr$  [33,46]:

$$\text{Gr} = \frac{g \beta L_B^3 \Delta T \rho^2}{\mu^2} \quad (2.13)$$

where  $g$  is the acceleration due to gravity,  $\beta$  is the thermal expansion coefficient,  $\Delta T$  is the difference between the weld pool peak temperature and the solidus temperature of the material,  $L_B$  is a characteristic length for the buoyancy force in the liquid pool, which is approximated by one eighth of the pool width, and  $\mu$  is the liquid viscosity.

Magnetic Reynolds number ( $R_m$ ) defines the ratio of electromagnetic force to viscous force, and is expressed as [33,47,48]:

$$R_m = \frac{\rho \mu_m I^2}{4\pi^2 \mu^2} \quad (2.14)$$

where  $\rho$  is the density,  $I$  is the arc current, and  $\mu_m$  is the magnetic permeability.

Surface tension Reynolds number ( $Ma$ ) is used to describe the ratio of surface tension gradient force to viscous force, and is calculated as [33,47,48]:

$$Ma = \frac{\rho L_R \Delta T |\partial\gamma / \partial T|}{\mu^2} \quad (2.15)$$

where  $L_R$  is the characteristic length of the weld pool and is assumed to be equal to a half of the weld pool width, and  $\partial\gamma / \partial T$  is the temperature coefficient of surface tension.

Once the values of  $Gr$ ,  $R_m$  and  $Ma$  are determined, the relative importance of the driving forces, i.e., surface tension gradient, electromagnetic, and buoyancy forces, can be judged by the combination of these dimensionless numbers. For example, the ratio of the electromagnetic force to the buoyancy force is given by [33]:

$$R_{M/B} = \frac{R_m}{Gr} \quad (2.16)$$

and the ratio of the surface tension gradient force to the buoyancy force is expressed as [33]:

$$R_{S/B} = \frac{Ma}{Gr} \quad (2.17)$$

Zhang [33] demonstrated the usefulness of the aforementioned approach by considering the example of GTA welding of 1005 steel. The data used by him [33] for calculations are given in Table 2.1. The values of dimensionless numbers calculated by

him [33] are summarized in Table 2.2. It can be seen from Table 2.2 that the buoyancy force is negligible compared to the electromagnetic and surface tension gradient forces. On the other hand, the surface tension gradient force plays more important role than the electromagnetic force, since  $R_{S/B}$  is greater than  $R_{M/B}$ . Therefore, a wide and shallow pool shape is expected, which was consistent with the experimental observation [8].

It should be noted that for the particular GTA welding case examined by Zhang [33], the electromagnetic force is smaller than the surface tension gradient force because of the low current (110 A) used. It has been reported that when the current is high (>250 A), the electromagnetic force becomes the dominant driving force in the weld pool convection, which can result in a weld pool with deep penetration [49,50].

The above discussion shows that the different driving forces play an important role in dissipating the heat and controlling the fluid motion in the weld pool. The driving forces also influence the temperature distribution in the weld. Therefore, to accurately simulate the weld heat transfer, fluid flow and solute transport, various driving forces need to be incorporated in the governing conservation equations and corresponding boundary conditions. Details of incorporating the driving forces in the governing equations will be presented in later sections.

Table 2.1. Welding conditions, material properties and other data of AISI 1005 steel welds used by Zhang [33] for calculating the values of dimensionless numbers.

Data	Value
Arc current, I (A)	110
Arc voltage, V (V)	17.5
Welding speed, $U_w$ (mm/s)	0.6
Arc energy distribution parameter, $r_b$ (mm)	2.7
Gravitational acceleration, $g$ ( $m/s^2$ )	9.8
Coefficient of thermal expansion, $\beta$ ( $K^{-1}$ )	$1.7 \times 10^{-6}$
Density of liquid metal, $\rho$ ( $kg/m^3$ )	$7.2 \times 10^3$
Solidus temperature, $T_s$ (K)	1779
Effective viscosity of liquid, $\mu$ (kg/m-s)	$6.3 \times 10^{-3}$
Specific heat of liquid, $C_{pl}$ (J/kg-K)	754
Effective thermal conductivity of liquid, $k_l$ (J/m-s-K)	36.4
Magnetic permeability, $\mu_m$ ( $N/A^2$ )	$1.26 \times 10^{-6}$
Temperature coefficient of surface tension $\partial\gamma/\partial T$ , (N/m-K)	$-0.49 \times 10^{-3}$
Width of the weld pool (mm)	8.8
Depth of the weld pool (mm)	1.8
Maximum velocity at the weld pool top surface (mm/s)	120
Peak temperature of the weld pool (K)	2020
Temperature variation at the pool surface, $\Delta T$ (K)	240
Thickness of the workpiece, $L_w$ (mm)	10

Table 2.2. Dimensionless numbers in the GTA weld pool of 1005 steel [33]. The data used by Zhang [33] in the calculations are given in Table 2.1.

Dimensionless number	Description	Value
Gr	Ratio of buoyancy to viscous force	30
Rm	Ratio of electromagnetic to viscous force	$7.0 \times 10^4$
Ma	Ratio of surface tension to viscous force	$9.4 \times 10^4$
$R_{M/B}$	Ratio of electromagnetic to buoyancy force	$2.3 \times 10^3$
$R_{S/B}$	Ratio of surface tension to buoyancy force	$3.1 \times 10^3$

### 2.1.3 Turbulence in weld pool

The liquid flow can be classified as laminar or turbulent flow based on its stability. In a laminar flow, the flow velocity in any location is deterministic, whereas in a turbulent flow, the flow velocity fluctuates in a random manner. Laminar flow is often observed at low flow velocity and high viscosity. The laminar flow may change to the turbulent flow as the flow velocity increases, which can greatly enhance the mixing of mass, momentum, energy and solute. The following Reynolds number is used to describe the flow behavior [46].

$$\text{Re} = \frac{\rho u_R L_R}{\nu} \quad (2.18)$$

where  $\rho$  is the liquid density,  $u_R$  and  $L_R$  are the characteristic velocity and length of the flow, respectively, and  $\nu$  is the kinematic (molecular) viscosity of the liquid. The critical transition Reynolds number from laminar to turbulent flow, for flow through pipes, is determined to be about 2100 [46].

In order to accurately simulate the heat transfer, fluid flow and solute transport in the weld pool, it is important to understand the turbulent behavior of the liquid metal. It is not yet fully clear whether the flow in the weld pool is turbulent in nature. However, several evidences suggest the existence of turbulence in the weld pool. Malinowski-Brodnicka et al. [51] measured the flow velocity in AISI 310 stainless steel weld pools and found the Reynolds number to be about 3000. Comparing this value to the critical transition Reynolds number of 2100, they [51] concluded that the flow in the weld pool was most likely turbulent. Several researchers [52,53-58] have obtained promising results by considering turbulence in the numerical heat transfer and fluid flow models for fusion welding. A widely used approach to incorporate the effect of turbulence in the numerical heat transfer and fluid flow calculations is to use effective viscosity and effective thermal conductivity of the molten metal [24,45,48,56-58]. The effective viscosity and effective thermal conductivity are often 5 to 20 times higher than their molecular values [45,56,57,59]. Such high values are necessary to account for the enhanced mixing of momentum and energy caused by turbulence. The predicted shape and size of the weld pool by adopting appropriate effective viscosity and effective thermal conductivity values

have been found to be quite close to experimental results [48,56,57]. However, in these calculations the values of the effective viscosity and thermal conductivity were often taken based on experience and not from fundamental principles. The values of effective thermal conductivity and effective viscosity are properties of the specific welding system, and not the inherent physical properties of the liquid metal [48,56]. Thus, effective thermal conductivity and effective viscosity are important uncertain input parameters in numerical transport phenomena based models, which significantly affect the results of numerical calculations. Reliable values of these uncertain input parameters are needed in order to perform accurate numerical calculations.

#### 2.1.4 General governing equations for transport processes

The following governing conservation equations describe the heat transfer and fluid flow in the weld pool [17,45,48]. An incompressible, laminar and Newtonian liquid flow is assumed in the weld pool. Thus, the circulation of liquid metal in the weld pool can be represented by the following momentum equation [45,48]:

$$\rho \frac{\partial u_j}{\partial t} + \rho \frac{\partial (u_i u_j)}{\partial x_i} = \frac{\partial}{\partial x_i} \left( \mu \frac{\partial u_j}{\partial x_i} \right) + S_j \quad (2.19)$$

where  $\rho$  is the density,  $t$  is the time,  $x_i$  is the distance along the  $i$  ( $i = 1, 2$  and  $3$ ) direction,  $u_j$  is the velocity component along the  $j$  direction,  $\mu$  is the viscosity, and  $S_j$  is the source term for the  $j$ th momentum equation and is given as [45,48]:

$$S_j = -\frac{\partial p}{\partial x_j} + \frac{\partial}{\partial x_i} \left( \mu \frac{\partial u_i}{\partial x_j} \right) - C \left( \frac{(1-f_L)^2}{f_L^3 + B} \right) u_j + S_{e_j} + S_{b_j} \quad (2.20)$$

where  $p$  is the pressure,  $f_L$  is the liquid fraction,  $B$  is a constant introduced to avoid division by zero,  $C$  ( $= 1.6 \times 10^4$ ) is a constant that takes into account solid-liquid mushy zone morphology,  $U$  is the welding speed and  $S_{b_j}$  represents both the electromagnetic and buoyancy source terms, which are calculated on the basis of Eqs. (2.4) and (2.12), respectively. In Eq. (2.20), the first term on the right hand side is the pressure gradient, the second term is the viscosity term, and the third term represents the frictional

dissipation in the mushy zone according to the Carman-Kozeny equation for flow through a porous media. The pressure field can be obtained by solving the following continuity equation simultaneously with the momentum equation [45,48]:

$$\frac{\partial(\rho u_i)}{\partial x_i} = 0 \quad (2.21)$$

In order to trace the weld pool liquid/solid interface, i.e., the phase change, the total enthalpy  $H$  is represented by a sum of sensible heat  $h$  and latent heat content  $\Delta H$ , i.e.,  $H = h + \Delta H$ . The sensible heat  $h$  is expressed as  $h = \int C_p dT$ , where  $C_p$  is the specific heat, and  $T$  is the temperature. The latent heat content  $\Delta H$  is given as  $\Delta H = f_L L$ , where  $L$  is the latent heat of fusion. The liquid fraction  $f_L$  is assumed to vary linearly with temperature [45,48]:

$$f_L = \begin{cases} 1 & T > T_L \\ \frac{T - T_s}{T_L - T_s} & T_s \leq T \leq T_L \\ 0 & T < T_s \end{cases} \quad (2.22)$$

where  $T_L$  and  $T_s$  are the liquidus and solidus temperature, respectively. Thus, the thermal energy transportation in the weld workpiece can be expressed by the following energy equation [45,48]:

$$\rho \frac{\partial h}{\partial t} + \rho \frac{\partial(u_i h)}{\partial x_i} = \frac{\partial}{\partial x_i} \left( \frac{k}{C_p} \frac{\partial h}{\partial x_i} \right) + S_h \quad (2.23)$$

where  $k$  is the thermal conductivity. The source term  $S_h$  is due to the latent heat content and is given as [45,48]:

$$S_h = -\rho \frac{\partial(\Delta H)}{\partial t} - \rho \frac{\partial(u_i \Delta H)}{\partial x_i} \quad (2.24)$$

When knowledge of solute concentration distribution is desired then the solute conservation equation is also required, which is given as [46]:

$$\frac{\partial(\rho C)}{\partial t} + \frac{\partial(\rho u_j C)}{\partial x_j} = \frac{\partial}{\partial x_j} \left( \rho D \frac{\partial C}{\partial x_j} \right) - \rho U \frac{\partial C}{\partial x_j} \quad (2.25)$$

where  $C$  is the solute concentration,  $D$  is the mass diffusivity of the solute and  $U$  is the welding speed. However, not much attention has been paid in the literature for calculating solute distribution in the weld pool. Since these governing equations are very complex, they need to be solved numerically.

Control volume (CV) / finite difference (FD) method [17-19] is commonly used for solving the governing conservation equations in computational fluid dynamics problems, such as the heat transfer and fluid flow during fusion welding. Detailed description of this method is available in the literature [17-19], and is not repeated here.

In summary, this section examines the current issues and problems in modeling transport processes in fusion welds. In particular, the liquid convection and driving forces, turbulence and governing conservation equations are discussed. This section demonstrates that accurate prediction of temperature and velocity fields, weld bead geometry, and thermal cycles in the weld needs to consider convective heat transfer in the weld pool. Appropriate modeling of liquid metal convection in the weld pool needs to account for the combination of driving forces such as surface tension gradient, electromagnetic, and buoyancy forces. Since convection plays such an important role in the transport processes during welding, analysis of its effect on solute transport during welding is a must, as is done in the present thesis research.

The topics covered in this section are readily applicable to the GTA welding process. However, for the GMA welding process, additional heat and mass is added into the weld pool by the heated metal droplets from the consumable electrode. The next section discusses solute transport in GMA welds, the resulting solute distribution and its role in the occurrence of weld defects like liquation cracking.

## **2.2 Relation between Solute Distribution and Liquation Cracking in GMA Welds**

Liquation cracking, also known as heat-affected zone (HAZ) cracking, is a common problem during GMA welding of aluminum alloys [5,60-68]. It occurs in the

HAZ when low melting point region, i.e., partially melted zone (PMZ), is formed during welding. The PMZ is the area immediately outside the weld metal, as shown in Fig. 2.6, where liquation occurs during welding because of overheating above the solidus temperature [5,60]. The evidence of liquation in the PMZ can be seen in Fig. 2.6, which shows the PMZ microstructure in alloy 2219, i.e., Al-6.3wt%Cu [5]. The liquated and re-solidified material can be seen along the grain boundaries (GB), which contain a dark-etching GB-eutectic phase and a light-etching solute depleted phase. Since the grain boundaries are liquated, inter-granular cracking can occur under the tensile strains induced by welding. Significant tensile strains are induced in the workpiece when it is restrained and unable to contract freely upon cooling due to solidification shrinkage [60].

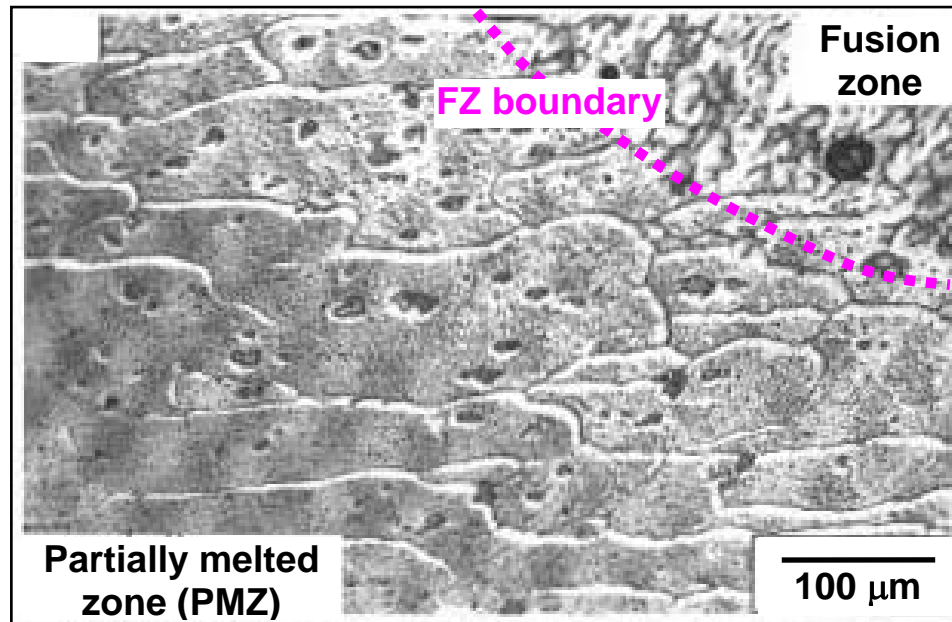


Fig. 2.6. PMZ microstructure of GMA weld in 2219 aluminum alloy made with 2319 aluminum filler wire [5].

Liquation cracking in aluminum alloy welds has been a subject of great interest in the literature [5,60-74]. Metzger [69] observed liquation cracking in full-penetration GTA welds of Alloy 6061 made with Al-Mg filler metals at high dilution ratios, but not in similar welds made with Al-Si filler metals at any dilution ratios. This was confirmed by subsequent studies on 6061 and similar alloys such as 6063 and 6082 [70-74]. Gittos and Scott [70] used the circular-patch test, described in Ref. [75], to study liquation cracking in an aluminum alloy close to Alloy 6082 in composition. Liquation cracking occurred in full-penetration GTA welds made with the Al-5Mg filler metal at high-dilution ratios (about 80%), but not with the Al-5Si filler metal at any dilution ratios. They [70] proposed that liquation cracking occurs when the base metal equilibrium solidus temperature is below the weld metal equilibrium solidus temperature. Katoh and Kerr [71], Kerr and Katoh [72] and Miyazaki et al. [73] used the V-restraint test, described in Refs. [76,77], to study liquation cracking in GTA and GMA partial penetration welds in 6000 series aluminum alloys. Their results contradicted the cracking condition of Gittos and Scott [70].

Huang and Kou [60] used the circular-patch test to investigate liquation cracking in full-penetration GMA welds in 2219 aluminum-copper (Al-Cu) alloy. They [60] used different composition filler metals in order to vary the weld-metal composition over a wide range. They [60] found that liquation cracking is severe when the weld-metal solute (copper) content is significantly lower than that of the base-metal solute content, and it decreases as the weld-metal solute content increases. Using the Scheil equation [5] and the solute content of the PMZ (equal to the base metal solute content) and the weld metal, Huang and Kou [60] calculated the curves of temperature (T) versus solid fraction ( $f_s$ ) for both the weld metal and the PMZ. The Scheil equation represents the simplest case of non-equilibrium solidification, assuming complete liquid diffusion and no solid diffusion of the solute, and is given as [5]:

$$f_s = 1 - \left( \frac{(-m_L)C_0}{T_m - T} \right)^{\frac{1}{1-k}} \quad (2.26)$$

where  $m_L$  ( $< 0$ ) is the slope of the liquidus line in the aluminum-copper phase diagram,  $T_m$  is the melting point of pure aluminum,  $C_0$  is the solute content of the alloy and  $k$  is the

equilibrium partition ratio, i.e., the ratio of the compositions of solid and liquid at the solid/liquid interface. Huang and Kou [60] used the  $T$  versus  $f_s$  curves to analyze the competition between the solidifying weld metal and the solidifying PMZ. The  $T$  vs.  $f_s$  curves showed that liquation cracking took place only when the weld-metal solid fraction exceeded the PMZ solid fraction, throughout PMZ solidification. They [60] argued that lower solid fraction in the PMZ makes this region weaker than the weld metal, making the PMZ vulnerable to liquation cracking.

Since the solid fraction of the solidifying weld metal is decided by the solute distribution in the weld pool, accurate prediction of liquation cracking susceptibility in aluminum-copper alloy welds requires thorough investigation of non-equilibrium solute distribution during GMA welding. The solute distribution in GMA welds is affected by weld pool convection, as described in the previous section, as well as by other factors including mixing of the filler metal with the base metal, dissolution of the base metal at the melting front, non-equilibrium solidification and solute rejection at the solidification front. The existing literature on numerical calculations for the GMA welding process largely deals with the heat and fluid flow calculations in order to predict the weld bead geometry. Not much attention has been paid to modeling solute distribution in the weld. Still, some guidance can be obtained from the literature about heat transfer from the filler metal and non-equilibrium solidification modeling.

Fig. 2.7 shows a schematic plot of the GMA welding process. The heat is transported from the arc to the workpiece, and superheated liquid metal droplets formed from the consumable electrode wire also carry heat and mass into the weld pool [2,78-81]. The welding parameters affect droplet diameter, transfer frequency, acceleration and impingement velocity. The heat transfer from the metal droplets is described as follows.

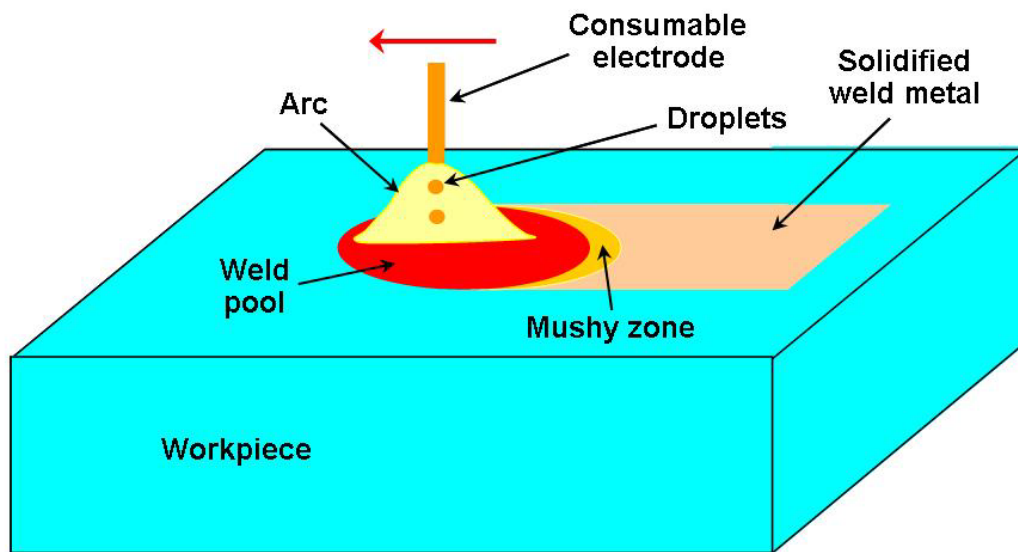


Fig. 2.7. Schematic plot showing the GMA welding process. The mushy zone represents the two phase solid-liquid region.

## 2.2.1 Heat transfer from metal droplets during GMA welding

Molten droplet transfer is an important characteristic of GMA welding, which makes the welding process highly productive [33]. The molten metal at the feeding wire tip is transferred to the weld pool through three basic modes, i.e., globular, spray, and short-circuiting [1,5,33]. Spray transfer mode is often observed at medium and high currents. In this mode, small discrete metal droplets travel across the arc gap at high speed and frequency, which enables highly stable metal transfer and less spatter [33]. Spray transfer mode is often preferred for GMA welding of thick workpiece because of its stability and efficiency [33].

For the spray transfer mode, earlier research work in butt [55,82] and fillet welding [33,79-81] has shown that the droplet heat transfer can be effectively simulated by incorporating a time-averaged volumetric heat source term ( $S_v$ ) in the energy conservation equation.

### 2.2.1.1 Calculation of volumetric heat source

As shown in Fig. 2.8, the volumetric heat source is characterized by its radius ( $R_v$ ), height ( $d$ ) and power density ( $S_v$ ). The height is calculated by using the following equation based on kinetic energy balance [1,33,82]:

$$d = h_v - x_v + D_d \quad (2.27)$$

where  $h_v$  is the estimated height of cavity by the impact of metal droplets,  $x_v$  is the distance traveled by the center of the slug between the impingement of two successive droplets, and  $D_d$  is the droplet diameter. The values of  $h_v$  and  $x_v$  in Eq. (2.27) are determined as follows [1,33,82]:

$$h_v = \left( -\frac{2\gamma}{D_d \rho g} + \sqrt{\left[ \left( \frac{2\gamma}{D_d \rho g} \right)^2 + \frac{D_d v_d^2}{6g} \right]} \right) \quad (2.28)$$

$$x_v = \left( h_v + \frac{2\gamma}{D_d \rho g} \right) \left\{ 1 - \cos \left[ \left( \frac{g}{h_v} \right)^{1/2} \Delta t \right] \right\} \quad (2.29)$$

where  $\gamma$  is the surface tension of the molten metal,  $g$  is the gravitational constant,  $v_d$  is the droplet impingement velocity, and  $\Delta t$  is the interval between two successive drops ( $\Delta t = 1/f$ , where  $f$  is the droplet transfer frequency). The radius of the volumetric heat source was assumed to be twice as the droplet radius [1,33,82]. In a more recent study, Kumar and DebRoy [83] calculated the optimized value of the radius of the volumetric heat source as 2.7 times the droplet radius.

The total sensible heat input from the metal droplets,  $Q_t$ , is given as [33,79]:

$$Q_t = \rho \pi r_w^2 w_f H_d \quad (2.30)$$

where  $\rho$  is the density,  $r_w$  is the radius of the wire,  $w_f$  is the wire feeding rate, and  $H_d$  is the total enthalpy of the droplets. Since a portion of  $Q_t$  is used to heat the additional metal from the droplets up to the liquidus temperature, the effective heat ( $Q_d$ ) that the droplets carry into the weld pool is given as [33,79,81]:

$$Q_d = \rho \pi r_w^2 w_f C_{pl} (T_d - T_l) \quad (2.31)$$

where  $C_{pl}$  is the specific heat of the liquid metal,  $T_d$  is the droplet temperature, which is assumed to be 2673 K [84], and  $T_l$  is the liquidus temperature. The time-averaged power density of the volumetric heat source,  $S_v$ , is calculated from the computed values of  $Q_d$ ,  $D_d$  and  $d$  as [33,79]:

$$S_v = \frac{Q_d}{\pi D_d^2 d} \quad (2.32)$$

It is noteworthy that  $S_v$  only applies to grid points within the cylindrical heat source, and the power density is zero outside the cylinder. In the present study, the solute addition from the filler metal will also be considered in a similar manner, by incorporating a time-averaged volumetric mass source term in the solute conservation equation.

As shown in Eqs. (2.27) to (2.29), the calculation of the dimensions of the volumetric heat source requires the knowledge of the droplet transfer frequency, radius and impingement velocity. These parameters are determined from the literature for given welding conditions [33,79].

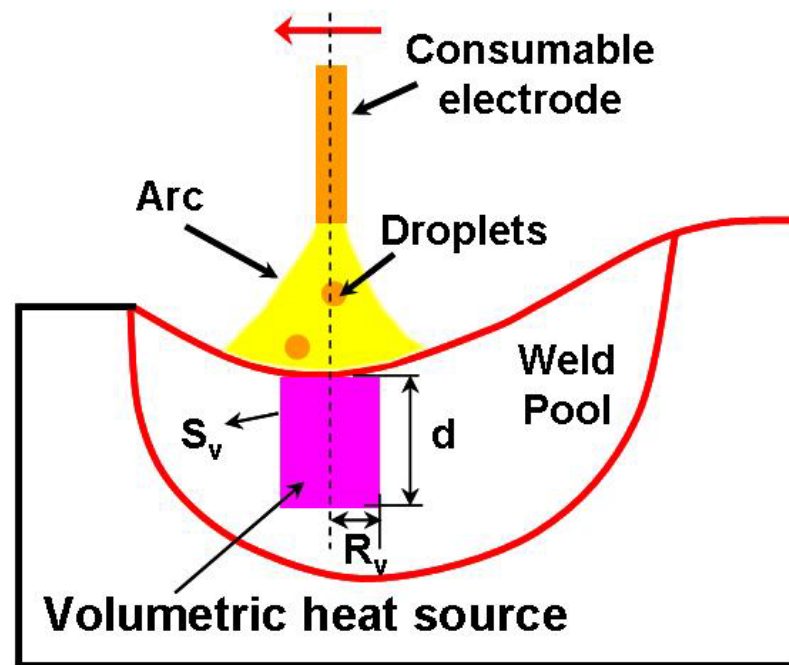


Fig. 2.8. Schematic plot illustrating the cylindrical volumetric heat source in the weld pool along the longitudinal plane [33,85].

### 2.2.1.2 Calculating droplet transfer frequency and radius

Rhee and Kannatey-Asibu [85] and Jones et al. [86] found that the welding current strongly affects the droplet frequency. Kim et al. [81] calculated the droplet transfer frequency by fitting the experimental results of Rhee and Kannatey-Asibu [85] and Jones et al. [86] into a sigmoid function combined with a quadratic function, as shown in Fig. 2.9(a). The resulting equation is given as [81,85]:

$$f = \frac{-243.44}{1 + \exp\left(\frac{I - 291.086}{6.06437}\right)} + 323.506 - 0.874 \times I + 0.0025 \times I^2 \text{ (Hz)} \quad (2.33)$$

where  $I$  is the welding current in ampere.

With the knowledge of the droplet transfer frequency and assuming that the droplets are spherical, the droplet radius  $r_d$  is given by [81,85]:

$$r_d = \sqrt[3]{\frac{3}{4} r_w^2 w_f / f} \quad (2.34)$$

where  $r_w$  is the radius of the fed wire, and  $w_f$  is the wire feeding rate.

### 2.2.1.3 Calculating droplet impingement velocity

The molten droplets detached from electrode wire are accelerated in the arc column mainly by plasma drag force and gravity [33,81,85]. If a constant acceleration is assumed, the velocity of droplets impinging the weld pool is given as [33,81,85]:

$$v_d = \sqrt{v_0^2 + 2a_d L_a} \quad (2.35)$$

where  $v_0$  is the initial droplet velocity,  $a_d$  is the droplet acceleration and  $L_a$  is the arc length. Equation (2.35) indicates that the values of  $v_0$ ,  $a_d$  and  $L_a$  are needed to calculate the droplet impingement velocity. Kim et al. [81] estimated the initial velocity of the droplets by fitting the experimental results of Lin et al. [87] in the following equation [33,85]:

$$v_0 = \sqrt{-0.33692 + 0.00854(I/D_d)} \text{ (m/s)} \quad (2.36)$$

where  $I$  is the arc current in ampere, and  $D_d$  is the droplet diameter in meter.

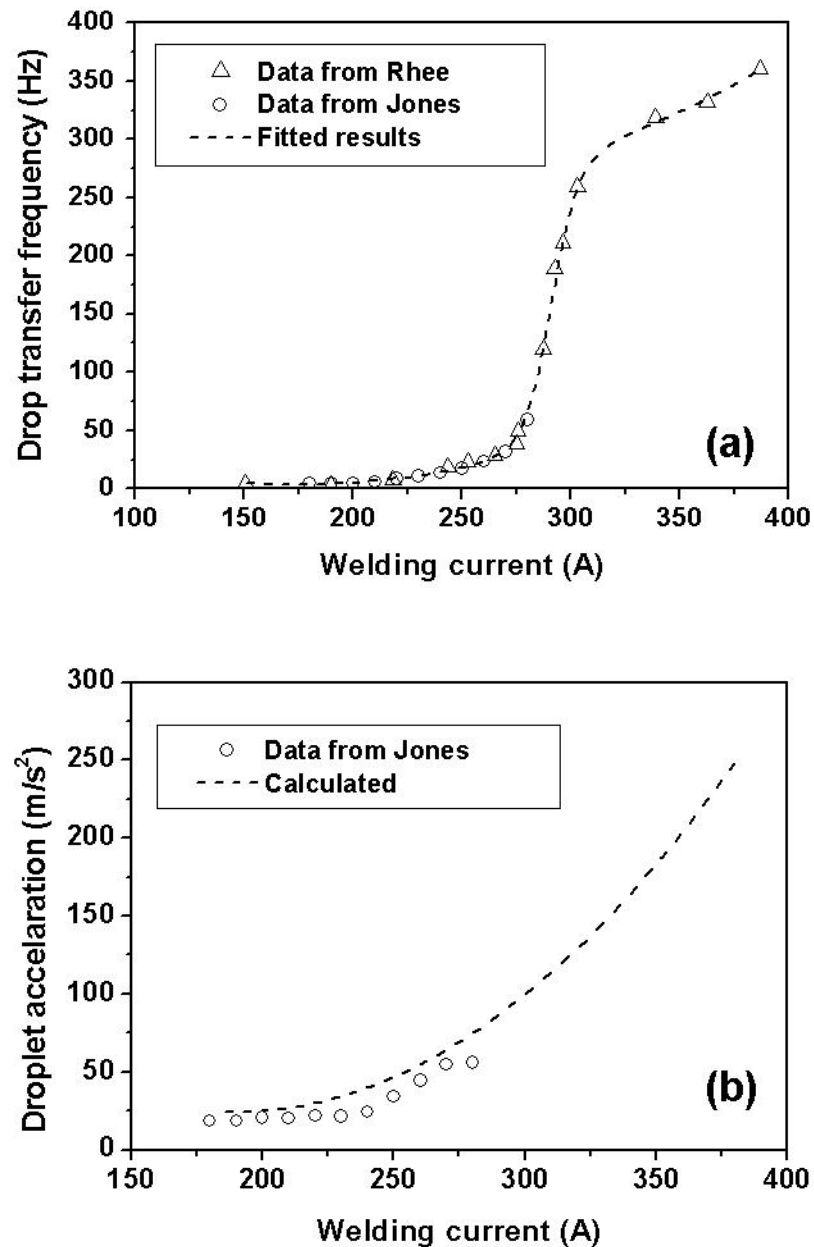


Fig. 2.9. Calculated droplet characteristics [33,81,85]. (a) comparison between the fitted and measured droplet transfer frequency, and (b) comparison between calculated and measured droplet acceleration in the arc column. In part (a), the triangles represent experimental data from Rhee and Kannatey-Asibu [85], and in parts (a) and (b), circles represent experimental data from Jones et al. [86].

In the arc column, the arc plasma travels from the electrode to the workpiece at high speeds [1]. Hence, the viscous plasma flow pushes the droplet in the arc column. The gravity force further accelerates the droplet. By considering the interaction between the arc plasma and the droplet, the acceleration,  $a_d$ , due to the plasma drag and gravity forces is given as [33,81,85,88]:

$$a_d = \frac{3 v_g^2 \rho_g}{8 r_d \rho_m} C_d + g \quad (2.37)$$

where  $v_g$  and  $\rho_g$  are the velocity and density of argon plasma, respectively,  $r_d$  is the radius of droplet,  $C_d$  is the drag coefficient,  $\rho_m$  is the density of droplet and  $g$  is the gravitational constant. The velocity of argon plasma is calculated using the following equation [1,33,81,85]:

$$v_g = k_1 \times I \quad (\text{m/s}) \quad (2.38)$$

where  $k_1$  is a constant whose value is taken to be 1/4 [81,85]. The other parameters in Eq. (2.37) were calculated by Kim et al. [81] using the relationship and data available in the literature. The acceleration,  $a_d$ , calculated by Kim et al. [81] using Eq. (2.37) was in good agreement with the corresponding experimental data as shown in Fig. 2.9(b).

Kim et al. [81] estimated the arc length using the equivalent circuit of GMA welding system. In a steady state, the arc length is given by the following circuit equation [33,81,85,88]:

$$V_{OC} = V_{a0} + (R_S + R_P + R_e + R_a)I + (E_{al} + E_{ai}I)L_a \quad (2.39)$$

where  $V_{OC}$  is the open-circuit voltage,  $R_S + R_P$  is the electrical resistance of the welding power source and cable,  $R_e$  is the electrical resistance over the electrode extension,  $V_{a0}$ ,  $R_a$ ,  $E_{al}$  and  $E_{ai}$  are coefficients used in Ayrton's equation [88]. Kim et al. [81] determined these parameters from the data available in the literature.

Thus, Kim et al. [81] calculated the impingement velocity using Eq. (2.35), with the estimated droplet initial velocity, acceleration and arc length. Next, they [81] used the droplet impingement velocity, transfer frequency and radius to calculate the dimensions of the cylindrical volumetric heat source, as discussed in the previous section.

#### **2.2.1.4 How effective is the volumetric heat source model?**

Yang and DebRoy [55] developed a three-dimensional turbulence model to study the heat transfer and fluid flow in GMA steel welds. A time-averaged volumetric heat source was used to simulate the additional heat from the superheated metal droplets. The weld top surface was assumed to be flat. Fig. 2.10 shows the comparison between the calculated and the measured FZ geometry. As shown in Fig. 2.10, their [55] model could reasonably predict the shape and size of the GMA welds, indicating that volumetric heat source is a viable approach for incorporating heat transfer by metal droplets during GMA welding. Zhang et al. [79,80] and Kim et al. [81] also used the volumetric heat source model in the simulation of the GMA fillet welding process and obtained good results. Therefore, this approach has been adopted in the present thesis research.

#### **2.2.2 Non-equilibrium solidification**

Rapid, non-equilibrium solidification is an important characteristic of fusion welding process [5]. The thermodynamics and kinetics of non-equilibrium solidification significantly affect the solute partitioning during weld solidification. Partitioning of the solute is an important contributor to the solute distribution in the weld. Many previous attempts to understand weld pool solidification considered thermal field alone [48,56] and ignored the convective solute transport in the weld pool. Chakraborty and Dutta [89] developed a solidification model for studying heat and mass transfer in a single-pass laser surface alloying process. However, they [89] assumed equilibrium at the solid-liquid interface that may not be attained when the interface speed is comparable with or faster than the diffusion speed. The well known Scheil equation for solute segregation, given by Eq. (2.26), represents a simple case of non-equilibrium solidification, assuming complete liquid diffusion and no solid diffusion of the solute [5]. It is derived assuming local equilibrium at the solid-liquid interface and a constant value of the solute partition coefficient, which are not valid during rapid solidification [90]. Both the velocity of solidification front and the undercooling must be considered to accurately represent solidification during welding.

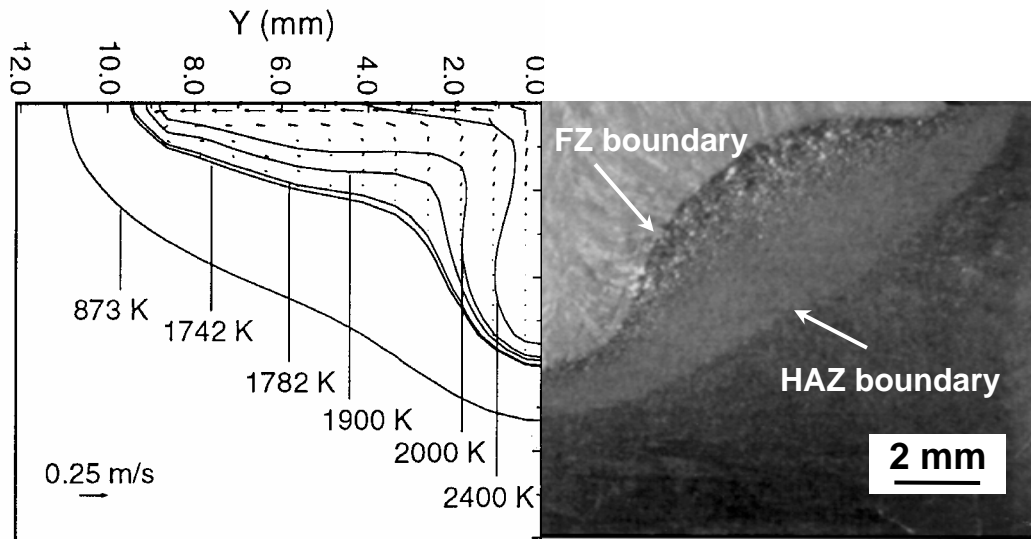


Fig. 2.10. Comparison of the calculated and experimental geometry of the fusion zone (FZ) and the heat-affected zone (HAZ) of GMA weld in HSLA-100 steel. Welding conditions: GMA, 405 A, 31.3 V, 5.29 mm/s [55].

Galenko and Sobolev [90] presented a local non-equilibrium approach to understand the solidification of undercooled alloys. They [90] took into account the relaxation to local equilibrium of the solute flux in both the solid and liquid phases, and incorporated the diffusive speed as an important parameter governing the solute concentration field. Subsequently, they [90] derived a generalized expression for the non-equilibrium solute partition coefficient,  $k_p$ , as:

$$k_p = \begin{cases} \frac{k_p^*[1 - (V/V_D^L)^2] + V/V_D^L}{1 - (V/V_D^L)^2 + V/V_D^L} & \dots \text{for } V < V_D^L \\ = 1 & \dots \text{for } V \geq V_D^L \end{cases} \quad (2.40)$$

where  $k_p^*$  is the equilibrium partition coefficient,  $V$  is the solid-liquid interface velocity and  $V_D^L$  is the diffusive speed in the liquid, which can be calculated as [90]:

$$V_D^L = (D_1^* / \tau_D^L)^{0.5} \quad (2.41)$$

where  $\tau_D^L$  refers to the time of diffusional relaxation of collective atoms (molecules, particles) to their equilibrium state in a local volume of alloy and  $D_1^*$  is the diffusion coefficient in the liquid under the conditions of interfacial equilibrium. Galenko and Sobolev [90] used Eq. (2.40) to calculate the non-equilibrium partition coefficient as a function of the interface velocity for the solidification of Si-As dilute alloy, as shown in Fig. 2.11. In this figure, they [90] compared results of their model, which takes into account both the finite speed of solute diffusion in the bulk liquid and the deviation from equilibrium at the solidification front, with independent experimental results [91] and the results from another model which only takes into account the deviation from equilibrium at the solidification front. The reasonable agreement between the results for their model and the experimental results ensured the validity of Eq. (2.40). In the present thesis research, Eq. (2.40) will be used to calculate the non-equilibrium solute partitioning during weld solidification.

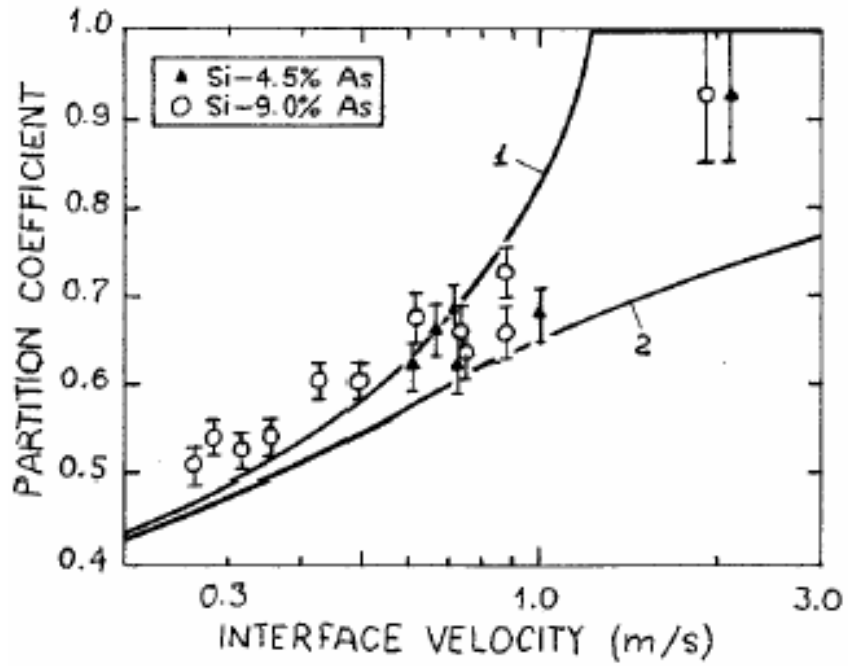


Fig. 2.11. Comparison of interface velocity versus solute partition coefficient plots obtained using Eq. (2.40) (curve 1) and a dilute continuous growth model (curve 2) with the experimental data (circles and triangles) for solidification of Si-As dilute alloy. The value of  $k_p = 0.35$  and that of  $V_D^L = 1.2$  m/s [90].

In summary, although significant progress has been made in modeling of heat transfer during GMA welding, not much effort has been devoted to understanding the solute distribution in the weld. The available models for non-equilibrium solute partitioning need to be incorporated in a numerical model for GMA welding to accurately model solute distribution in the weld. Furthermore, the complex coupling of momentum, heat and solute transport under non-equilibrium conditions during GMA welding are yet to be investigated. All these issues will be incorporated in the present thesis research for the accurate calculation of the evolution of solute distribution in GMA welds.

The next two sections highlight some of the major limitations of the presently available numerical transport phenomena based models, and their possible remedies.

### **2.3 Enhancing the Reliability of Output and Improving Usefulness of the Numerical Transport Phenomena Based Models**

Currently the numerical transport phenomena based models for fusion welding are used mostly as a research tool rather than as a tool for designing and manufacturing in industry. There are several reasons for the restricted use of these advanced tools. First, the weld attributes predicted by the numerical transport phenomena based models such as weld geometry and cooling rate do not always agree with the experimental results. Second, the fusion welding system is highly complex and involves the non-linear interaction of several welding variables. As a result, a particular weld attribute, such as the weld geometry, can be obtained through the use of various sets of welding variables. The current generation of numerical transport phenomena based models cannot determine alternative pathways to achieve a target weld attribute.

A primary reason for the disagreement between the computed and experimentally determined weld attribute such as weld geometry is the uncertainty of the values of some of the input parameters because they cannot be prescribed based on either scientific principles or welding conditions. The models for the gas tungsten arc (GTA) welding process have five uncertain input parameters, i.e., arc efficiency, arc radius, power distribution factor, and the effective thermal conductivity and viscosity of the liquid metal [83,92]. Although the values of arc efficiency have been experimentally measured

for many welding conditions, the reported values vary significantly, even for apparently similar welding conditions. Measured values of the arc radius and power distribution factor depend on welding conditions and, as a result, their values cannot be accurately specified except for certain narrow windows of welding conditions. Values of the effective thermal conductivity and viscosity are important, since they allow accurate modeling of the high rates of transport of heat and mass in systems with strong fluctuating velocities, such as small weld pools with very strong convection currents. The values of effective conductivity and viscosity are properties of the specific welding system, and not the inherent physical properties of the liquid metal [48,83,92] and the values of these parameters significantly affect the results of numerical transport phenomena based calculations. A systematic global search for the uncertain input parameters is needed so that the computed weld attributes such as weld geometry always agree with the corresponding experimentally determined values.

The desired depth and width of the weld pool and the cooling rate are often specified to achieve a structurally sound and reliable welded joint. Therefore, an important requirement is to determine the values of the welding variables necessary for achieving a given weld attribute, such as the weld geometry. In practice a particular weld attribute may be obtained through multiple combinations of welding variables. The forward numerical transport phenomena based model needs to be systematically interrogated to estimate the optimized values of welding variable sets that can produce a specified weld geometry.

De and DebRoy [92] and Kumar and DebRoy [83] recently developed inverse models to calculate various unknown input parameters such as the arc efficiency, effective thermal conductivity and effective viscosity for numerical transport phenomena based modeling of the welding processes using derivative based optimization techniques. A drawback of derivative based optimization techniques is their occasional convergence to a local solution [93]. Furthermore, appropriate initial guess of the uncertain input variables is needed to achieve the global optimal solution [93]. Genetic algorithm (GA) is a stochastic, population based optimization technique that can find the global optimal solution independent of the initial guessed values [94-96].

Genetic algorithms work with a set of "individuals" - a population, where each individual is a solution of a given problem [93]. The initial population defines the possible solutions of the optimization problem, i.e., sets of variables that need to be optimized. There are two popular ways of representing the variables in the population in GA: binary and real numbers. Generally binary representation of variables converges slowly compared to the real representations [94,95]. In addition, since the binary genetic algorithm has its precision limited by the binary representation of variables, using real numbers allows representation to the machine precision in continuous search space [94,95]. The real coded genetic algorithm also has the advantage of requiring less storage than the binary GA because a single floating point number represents a variable instead of many integers having values 0 and 1 [94,95].

A number of real parameter genetic algorithms have been developed recently with an aim to solve real-world optimization problems. Deb et al. [94] developed an efficient real coded GA, called the generalized generation gap (G3) model using parent centric recombination (PCX) operator. The generic G3 model using the PCX operator is an elite-preserving, scalable, and computationally fast population-alteration model [94]. Deb et al. [94] showed that this model converged at a much faster rate on standard test functions as compared to other real-parameter GAs as well as classical optimization algorithms. Also, this model required the least number of calculations of the test function in finding the global optimal solution [94]. Keeping the number of function evaluations to a minimum is very important in an optimization problem involving repeated runs of numerical transport phenomena based models, because these models are complex and consume a large amount of computer time.

Kumar et al. [96] used the PCX based G3 GA and a limited volume of experimental data to find the optimized values of three unknown parameters in the non-isothermal Johnson-Mehl-Avrami (JMA) equation, i.e., activation energy, pre-exponential factor and exponent in the non-isothermal JMA equation. The non-isothermal JMA equation is often used to represent phase transformation behavior in many systems involving nucleation and growth such as the  $\alpha$ -ferrite to  $\gamma$ -austenite transformation in C-Mn steels during heating [96]. They [96] reported that the GA based determination of the

three JMA equation parameters resulted in better agreement between the calculated and the experimentally determined austenite phase fractions than was previously achieved. Thus, PCX based G3 GA holds significant promise in finding the optimized values of the uncertain input parameters of the numerical transport phenomena based models.

The problem of finding multiple combinations of welding variables to achieve a target weld attribute like weld geometry cannot be approached using classical gradient-based search and optimization methods, because they produce a single optimum solution. These methods use a point-by-point approach, where one relatively imperfect solution in each iteration is modified to a different more appropriate solution [93,95]. Therefore, a combination of a classical optimization method with a phenomenological model can provide only a single local optimum solution in situations where multiple solutions exist. In contrast, genetic algorithms can obtain a population of optimal solutions [93-95]. Therefore, GA can be combined with a numerical transport phenomena based model to find multiple combinations of welding variables to obtain a target weld geometry. However, such a method would require multiple runs of the numerical model and would be highly time consuming. Unless a model can do calculations in a reasonable time frame, it is unlikely to find widespread practical applications. A practical solution to this problem is to develop a neural network that is capable of providing high computational speed. The following section discusses the current state of understanding about the development of a neural network for the fusion welding process.

## **2.4 Development of a Neural Network Model for Fusion Welding**

Neural network models are powerful non-linear regression analysis methods [97-101] that can relate input variables like welding process parameters and material properties with weld characteristics such as weld pool geometry. Fig. 2.12 shows typical neural network architecture. Input nodes, at the bottom of the figure, receive problem attributes for a particular input/output pair, and transmit that information to adjacent nodes through the connections between them [100]. Output nodes, at the top of the figure, display the neural network's response to the particular input pattern [100]. Connections between nodes have associated weights, such as  $w_1$ ,  $w_2$  shown in Fig. 2.12. Hidden nodes

perform non-linear transformations that are central to the modeling capability of the network. For a fusion welding experiment, an input/output pair can consist of the input process parameters as arc current, voltage, welding speed and wire speed, and the corresponding output weld attributes as weld pool depth and width, as shown in Fig. 2.12. The approach would then be to collect many such measurements, and repeatedly present the input vectors to the network [100]. The network, whose weights are (usually) initially random values, will give meaningless outputs at first. Here comes the concept of training the algorithm, which essentially implies finding a set of weights that minimize the error between the desired output and the output calculated by the neural network. A backpropagation algorithm [97,99,100,102] is commonly used for training the neural network. The backpropagation algorithm adjusts the weights of the network as the training progresses, by calculating an error between the desired output and the output calculated by the network [100]. The error,  $E$ , is given as [100]:

$$E = \sum_{j=1}^n (t_j - a_j)^2 \quad (2.42)$$

where  $n$  is the number of input/output pairs used for training,  $t_j$  is the target output for the input/output pair  $j$  and  $a_j$  is the corresponding output calculated by the neural network. Then the sum squared error over the entire training set is the error term which drives the weight change as follows [100]:

$$\Delta w_i = \frac{\delta E}{\delta w_i} \quad (2.43)$$

where  $w_i$  is the weight on the connection  $i$ . This approach is essentially a gradient descent search method for minimizing a non-linear function. Once the error is minimized to the required level, the trained neural network is tested on new input/output pairs.

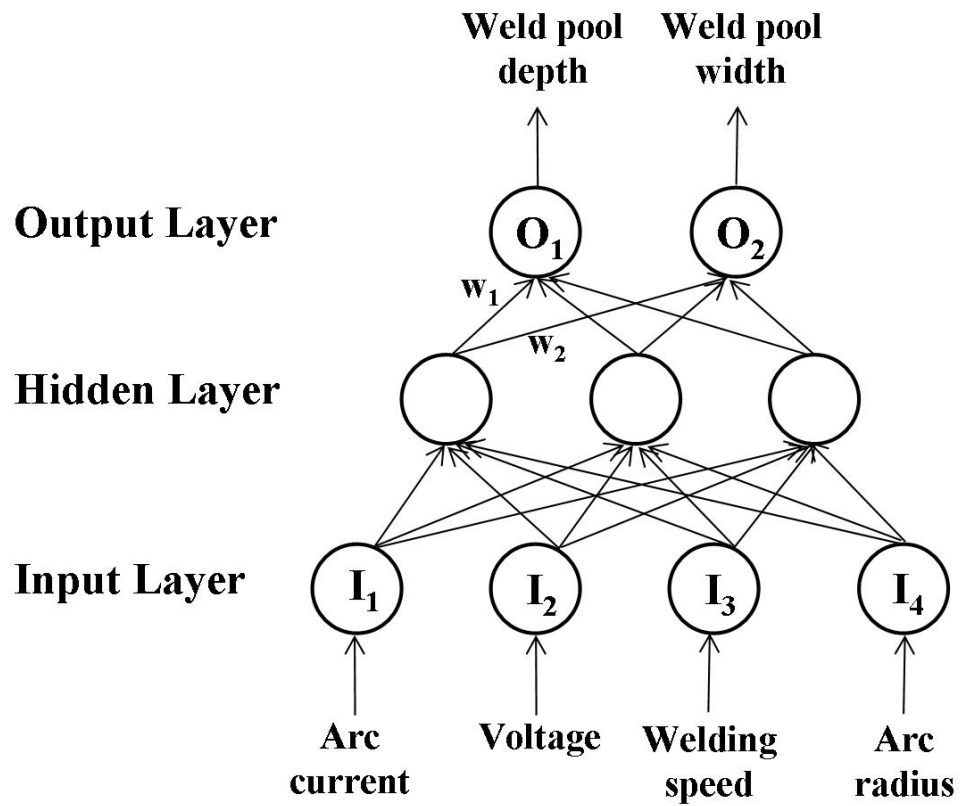


Fig. 2.12. Typical back-propagation neural network structure. The symbols  $I_1$  to  $I_4$  represent the four input process parameters of a fusion welding process, while  $O_1$  and  $O_2$  represent the corresponding output weld attributes.

As mentioned above, the most common backpropagation algorithm uses a gradient descent search method. During the training of the neural network, the gradient descent search method decreases the error very rapidly. However, the final result depends on the initial random weights, which is a common problem with the gradient descent based optimization techniques [100,103,104]. Furthermore, for simple two-layer networks (without a hidden layer), the error surface is bowl shaped and using gradient-descent techniques to minimize the error is not a problem. However, the addition of a hidden layer, used to solve more difficult problems like fusion welding process, increases the possibility for complex error surfaces which contain many minima. The gradient based methods can easily get trapped in such local minima. Stochastic optimization techniques like genetic algorithm are capable of finding the global minima and avoiding local minima [94-96]. Therefore, a hybrid training approach can be a good option for training a neural network, where the initial guidance is provided by the gradient descent method and the global minima is found by a genetic algorithm.

In recent decades, many researchers have attempted systematic correlations between welding variables and weld characteristics using neural networks [97,98,105-123]. The previous efforts to model the GTA welding process using neural network were based on training the network with experimental data [102,105,106]. Since the volume of experimental data required to train a neural network depends on the number of input and output variables, most previous efforts considered only few input parameters to keep the necessary volume of experimental data tractable [102,105,106]. For example, Tarng et al. [105], Andersen et al. [102] and Juang et al. [106] developed neural network models of GTA welding process, which considered the effects of input process parameters like welding speed, arc current and voltage on the weld pool geometry. These neural network models were developed using a limited volume of experimental data, and they could not determine the effect of important material properties like thermal conductivity, specific heat, etc. on weld pool geometry. Furthermore, the existing neural network models [102,105,106] do not provide any information about some of the other important output parameters such as the cooling rate and peak temperature. A neural network can only be used as a substitute for numerical transport phenomena based models if it can incorporate

the effects of the important input welding process parameters and material properties on the weld pool geometry, cooling rate and peak temperature. Such a neural network can be produced by training it with the results of a well tested numerical transport phenomena based model providing reliable output.

## **2.5 Important Unanswered Questions**

The current generation of numerical transport phenomena based models suffers from two major limitations, i.e., lack of reliability of the output and absence of bidirectional capability. These problems seriously limit the usefulness of these models. New methodologies need to be developed by coupling numerical transport phenomena based models, stochastic optimization algorithms and neural networks in order to address these limitations. Once the reliability and utility issues are addressed, the next step is to enhance the model capabilities. Mass transport during fusion welding and the resulting solute distribution in the weld have a significant impact on the weld pool geometry and consumable design to avoid occurrence of weld defects like liquation cracking. The transport phenomena based models can be applied to calculate the solute transport in the weld and study its effect on weld properties. The aforementioned approach involves development of several new methodologies leading to a number of unanswered questions. Following is a selection of important unanswered questions that are addressed in the present thesis study.

The output of the currently available numerical transport phenomena based models is often not reliable mainly because of some uncertain input parameters. Furthermore, the numerical transport phenomena based models cannot go backwards, i.e., they cannot provide the welding process parameters such as current, voltage and welding speed, to obtain a target weld attribute such as weld pool geometry. In practice a particular weld attribute may be obtained through multiple combinations of welding variables. In the present thesis study, a new methodology will be developed where the numerical transport phenomena based model will be coupled with a genetic algorithm based optimization routine and a limited volume of experimental data to optimize the

values of the uncertain input parameter. Do these optimized values of the uncertain input parameters provide reliable output? This question will be answered by comparing the computed weld pool shape and size with the corresponding experimental results.

The same methodology as above can in principle be applied to find multiple combinations of welding process parameters to obtain a target weld attribute like weld pool geometry. However, this method is computationally very expensive because it requires multiple runs of the numerical model, which is complex, requires specialized training to develop and test, and consumes a large amount of computer time to run. How can this procedure be made computationally economical? A practical solution to this problem is to develop a neural network, which can relate input variables like welding process parameters and material properties with weld characteristics such as weld pool geometry, and at the same time provide high computational speed. The outstanding issues associated with the development of a neural network for the fusion welding process are as follows: (1) How does a hybrid training approach compare with the conventional gradient descent training approach? (2) Is the neural network well trained? (3) Do the results of the neural network comply with the phenomenological laws of welding physics? These questions will be answered in the present thesis research by developing a neural network trained with the results of the numerical transport phenomena based model. A hybrid training approach will be used, which includes the gradient descent method and a genetic algorithm. The performance of the neural network will be tested on independent set of results generated by the numerical transport phenomena base model. Once the neural network is used in the above methodology, computational efficiency is achieved and multiple sets of welding process parameters are obtained, the question that arises is, “Do the multiple combinations of welding process parameters lead to the same weld pool geometry”? This question will be answered by comparing the weld pool geometry calculated using each set of welding process parameters with the target experimental weld pool geometry.

Solute transport and distribution during fusion welding has a profound effect on the weld characteristics such as weld pool geometry and creation of weld defects like liquation cracking. It is important to understand the following questions: (1) How does

weld pool convection affect solute transport? (2) How does the distribution of surface active element sulfur affect weld pool geometry? (3) What other factors affect the weld pool geometry in GTA welds when welding two plates with different sulfur contents? (4) What factors affect solute transport during GMA welding? (5) How is the heat and solute transport from filler metal during GMA welding incorporated? (6) During GMA welding, what is the mushy zone solute content for different filler metal compositions? In order to address these questions solute transport equations will be introduced into an already existing numerical heat transfer and fluid flow model to study the distribution of solute in the weld pool. The usefulness and reliability of output of this model will be enhanced by the computational procedures described above. This transport phenomena based model will be used to understand the evolution of weld pool geometry during GTA welding of stainless steel plates having same and different sulfur contents. Next, the numerical model will be adapted to the GMA welding process by using time-averaged volumetric heat and mass source to incorporate the heat and solute intake from the filler metal, and a non-equilibrium solidification model. The numerical model will then used for the design of consumables to avoid liquation cracking during GMA welding of Al-6.3wt%Cu alloy using filler metals with different copper contents.

## 2.6 References

1. J. F. Lancaster, *The Physics of Welding - 2nd Edition* (Pergamon, Oxford, 1986).
2. K. Easterling, *Introduction to the Physical Metallurgy of Welding - 2nd Edition* (Butterworth-Heinemann, Oxford, 1992).
3. S. A. David and T. DebRoy, *Science* 257, 497 (1992).
4. T. DebRoy and S. A. David, *Rev. Mod. Phys.* 67, 85 (1995).
5. S. Kou, *Welding Metallurgy - 2nd Edition* (John Wiley & Sons, Hoboken, New Jersey, 2003).
6. Ø. Grong, *Metallurgical Modeling of Welding - 2nd Edition* (The Institute of Materials, London, 1997).
7. D. A. Schauer, W. H. Giedt and S. M. Shintaku, *Weld. J.* 57, 127s (1978).
8. W. H. Giedt, X. Wei and S. Wei, *Weld. J.* 63, 376s (1984).
9. W. E. Lukens and R. A. Morris, *Weld. J.* 61, 27s (1982).
10. J. D. Boillot, P. Cielo, G. Begin, C. Michel and M. Lessard, *Weld. J.* 64, 209s (1985).
11. H. G. Kraus, *Weld. J.* 66, 353s (1987).
12. H. G. Kraus, *Weld. J.* 68, 84s (1989).
13. W. Pitscheneder, R. Ebner, T. Hong, T. DebRoy, K. Mundra and R. Benes, in *Mathematical Modelling of Weld Phenomena 4*, edited by H. Cerjak, p. 3, 1998.
14. T. DebRoy and S. Kou, *Heat Flow in Welding*, Chapter 3, *Welding Handbook*, vol. 1, 9<sup>th</sup> Edition, American Welding Society, p. 87, 2001.
15. C. R. Heiple and J. R. Roper, *Weld. J.* 60, 143s (1981).
16. C. R. Heiple and J. R. Roper, *Weld. J.* 61, 97s (1982).
17. S. V. Patankar: *Numerical Heat Transfer and Fluid Flow* (Hemisphere Publishing Corp., New York, 1982).
18. H. K. Versteeg and W. Malalasekera, *An Introduction to Computational Fluid Dynamics: The Finite Volume Method* (Addison-Wesley, New York, 1996).
19. W. Shyy, H. Ouyang, E. Blosch, S. S. Thakur and J. Liu, *Computational Techniques for Complex Transport Phenomena* (Cambridge University Press, London, 1997).
20. M. C. Tsai and S. Kou, *Numer. Heat Transfer A* 17, 73 (1990).
21. M. C. Tsai and S. Kou, *Weld. J.* 69, 241s (1990).

22. M. C. Tsai and S. Kou, *Int. J. Numer. Meth. Fl.* 9, 1503 (1989).
23. N. S. Tsai and T. W. Eager, *Metall. Trans. B* 16, 841 (1985).
24. H. B. Smartt, J. A. Stewart and C. J. Einerson, in *85 ASM International Welding Congress*, edited by E. F. Nippes et al., paper no. 8511-011, ASM International, Materials Park, OH, 1985.
25. S. Kou and Y. H. Wang, *Metall. Trans. B* 17, 2271 (1986).
26. T. Zacharia, S. A. David, J. M. Vitek and T. DebRoy, *Weld. J.* 68, 499s (1989).
27. K. Mundra, T. DebRoy, T. Zacharia and S. A. David, *Weld. J.* 71, 313s (1992).
28. C. S. Wu and L. Dorn, *Comput. Mater. Sci.* 2, 341 (1994).
29. J. W. Kim and S. J. Na, *Weld. J.* 74, 141s (1995).
30. J. D. Jackson, *Classical Electrodynamics - 3rd Edition* (Wiley, New York, 1998).
31. S. Kou and D. K. Sun, *Metall. Trans. A* 16, 203 (1985).
32. A. Kumar and T. DebRoy, *J. Appl. Phys.* 94, 1267 (2003).
33. W. Zhang, *Probing Heat Transfer, Fluid Flow and Microstructural Evolution During Fusion Welding of Alloys*, Ph.D. Thesis, The Pennsylvania State University, USA, May, 2004.
34. W. Pitscheneder, T. DebRoy, K. Mundra and R. Ebner, *Welding J.* 75, 71s (1996).
35. P. Sahoo, T. DebRoy and M. J. McNallan, *Metall. Trans. B* 19, 483 (1988).
36. C. R. Heiple, J. R. Roper, R. T. Stagner and J. J. Alden, *Weld. J.* 62, 72s (1983).
37. C. R. Heiple, P. Burgardt, J. R. Roper and J. L. Long, in *Proc. Int. Conf. on the Effects of Residual, Trace and Micro-alloying Elements on Weldability and Weld Properties*, TWI, Cambridge, 1984, p. 36.
38. C. Limmaneevichitr and S. Kou, *Weld. J.* 79, 126s (2000).
39. C. Limmaneevichitr and S. Kou, *Weld. J.* 79, 324s (2000).
40. D. G. Kolman, Report on 'Assessment of the corrosion, stress corrosion cracking and embrittlement susceptibility of 30313 storage containers', available at <http://public.lanl.gov/MCEL/PDF-Publications/CorrSCC3013.pdf>.
41. G. R. Cannell, W. L. Daugherty and M. W. Stokes, Report on 'Closure welding of plutonium bearing storage containers', available at <http://sti.srs.gov/fulltext/ms2002053/ms2002053.pdf>.

42. DOE-STD-3013-96, 'Criteria for preparing and packaging plutonium metals and oxides for long-term storage', available at <http://www.eh.doe.gov/techstds/standard/std3013/s963013.pdf>.
43. M. J. Tinkler, I. Grant, G. Mizuno and C. Gluck, *Proc. Int. Conf. on the Effects of Residual, Trace and Micro-alloying Elements on Weldability and Weld Properties*, TWI, Cambridge, 1984, p. 29.
44. A. F. Rollin and M. J. Bentley, *Proc. Int. Conf. on the Effects of Residual, Trace and Micro-alloying Elements on Weldability and Weld Properties*, TWI, Cambridge, 1984, p. 9.
45. K. Mundra, T. DebRoy and K. Kelkar, *Numer. Heat Transfer A* 29, 115 (1996).
46. R. B. Bird, W. E. Stewart and E. N. Lightfoot, *Transport Phenomena* (John Wiley & Sons, New York, 1960).
47. G. M. Oreper and J. Szekely, *Metall. Trans. A* 18, 1325 (1987).
48. W. Zhang, G. G. Roy, J. W. Elmer and T. DebRoy, *J. Appl. Phys.* 93, 3022 (2003).
49. W. G. Essers and R. Walter, *Weld. J.* 60, 38s (1981).
50. R. T. C. Choo, J. Szekely and R. C. Westhoff, *Weld. J.* 69, 360s (1990).
51. M. Malinowski-Brodnicka, G. denOuden and W. J. P. Vink, *Weld. J.* 69, 52s (1990).
52. R. T. C. Choo and J. Szekely, *Weld. J.* 73, 25s (1994).
53. K. Hong, D. C. Weckman and A. B. Strong, in *Trends in Weld. Res.*, edited by H. B. Smartt et al., ASM International, Materials Park, OH, 1996, p. 399.
54. K. Hong, D. D. Weckman, A. B. Strong and W. Zheng, *Sci. Technol. Weld. Joining* 3, 125 (2002).
55. Z. Yang and T. DebRoy, *Metall. Mater. Trans. B* 30, 483 (1999).
56. X. He, P. W. Fuerschbach and T. DebRoy, *J. Phys. D: Appl. Phys.* 36, 1388 (2003).
57. X. He, T. DebRoy and P. W. Fuerschbach, *J. Appl. Phys.* 94, 6949 (2003).
58. K. Mundra, J. M. Blackburn and T. DebRoy, *Sci. Technol. Weld. Joining* 2, 174 (1997).
59. H. Davis, *Numerical Modelling of Weld Pool Convection in Gas Metal Arc Welding*, Ph.D. Thesis, University of Adelaide, Australia, September, 1995.
60. C. Huang and S. Kou, *Weld. J.* 83, 50s (2004).

61. H. Zhao and T. DebRoy, *Metall. Mater. Trans. B* 32, 163 (2001).
62. M. Miyazaki, K. Nishio, M. Katoh, S. Mukae and H. W. Kerr, *Weld. J.* 69, 362s (1990).
63. C. Huang and S. Kou, *Weld. J.* 79, 113s (2000).
64. C. Huang and S. Kou, *Weld. J.* 80, 9s (2001).
65. C. Huang and S. Kou, *Weld. J.* 80, 46s (2001).
66. C. Huang and S. Kou, *Weld. J.* 81, 211s (2002).
67. C. Huang and S. Kou, *Weld. J.* 82, 184s (2003).
68. C. Huang and S. Kou, *Weld. J.* 83, 111s (2004).
69. G. E. Metzger, *Weld. J.* 46, 457s (1967).
70. N. F. Gittos and M. H. Scott, *Weld. J.* 60, 95s (1981).
71. M. Katoh and H. W. Kerr, *Weld. J.* 66, 360s (1987).
72. H. W. Kerr and M. Katoh, *Weld. J.* 66, 251s (1987).
73. M. Miyazaki, K. Nishio, M. Katoh, S. Mukae and H. W. Kerr, *Weld. J.* 69, 362s (1990).
74. M. B. D. Ellis, M. F. Gittos and I. Hadley, *The Weld. Ins. J. (U.K.)* 6, 213 (1997).
75. J. C. Borland and J. H. Rogerson, *British Weld. J.* 8, 494 (1963).
76. W. F. Savage and C. D. Lundin, *Weld. J.* 44, 433s (1965).
77. W. F. Savage and C. D. Lundin, *Weld. J.* 45, 497s (1966).
78. *ASM Handbook: Welding, Brazing and Soldering*, vol. 6, ASM International, Materials Park, OH, 1993.
79. W. Zhang, C.-H. Kim and T. DebRoy, *J. Appl. Phys.* 95, 5210 (2004).
80. W. Zhang, C.-H. Kim and T. DebRoy, *J. Appl. Phys.* 95, 5220 (2004).
81. C.-H. Kim, W. Zhang and T. DebRoy, *J. Appl. Phys.* 94, 2667 (2003).
82. S. Kumar and S. C. Bhaduri, *Metall. Mater. Trans. B* 25, 435 (1994).
83. A. Kumar and T. DebRoy, *Int. J. Heat Mass Transfer.* 47, 5793 (2004).
84. G. Jelmorini, G. W. Tichelaar and G. J. P. M. Van den Heuvel, *IIW Document 212-411-77*, International Institute of Welding, London, 1977.
85. S. Rhee and E. Kannatey-Asibu, Jr., *Weld. J.* 71, 381s (1992).
86. L. A. Jones, T. W. Eagar and J. H. Lang, *J. Phys. D: Appl. Phys.* 31, 107 (1998).

87. Q. Lin, X. Li and S. W. Simpson, *J. Phys. D: Appl. Phys.* 34, 347 (2001).
88. C.-H. Kim and S.-J. Na, *Proc. Instn. Mech. Engrs.* 215B, 1270 (2001).
89. S. Chakraborty and P. Dutta, *Mat. Manuf. Processes* 17, 455 (2002).
90. P. Galenko and S. Sobolev, *Phys. Rev. E* 55, 343 (1997).
91. J. A. Kittl, M. J. Aziz, D. P. Brunco and M. O. Thompson, *J. Cryst. Growth* 148, 172 (1995).
92. A. De and T. DebRoy, *J. Phys. D: Appl. Phys.* 37, 140 (2004).
93. D. E. Goldberg, *Genetic Algorithm in Search, Optimization and Machine Learning* (Addison-Wesley, MA, 1989).
94. K. Deb, A. Anand and D. Joshi, *Evolutionary Computation* 10, 371 (2002).
95. K. Deb, *Multi-objective optimization using evolutionary algorithms – 1st Edition* (Wiley, New York, 2001).
96. A. Kumar, S. Mishra, J. W. Elmer and T. DebRoy, *Metall. Mater. Trans. A* 36, 15 (2005).
97. J. M. Vitek, Y. S. Iskander and E. M. Oblow, *Weld. J.* 79, 33s (2000).
98. J. M. Vitek, Y. S. Iskander and E. M. Oblow, *Weld. J.* 79, 41s (2000).
99. D. E. Rumelhart, G. E. Hinton and R. J. Williams, *Nature* 323, 533 (1986).
100. L. Burke and J. P. Ignizio, *J. Intell. Manufac.* 8, 157 (1997).
101. L. Fausett, *Fundamentals of Neural Networks* (Prentice-Hall, NJ, 1994).
102. K. Andersen, G. E. Cook, G. Karsai and K. Ramaswamy, *IEEE Trans. Ind. Appl.* 26, 824 (1990).
103. P. K. D. V. Yarlagadda, *Proc. Inst. Mech. Engineers B - J. Engineering Manufacture* 215, 1465 (2001).
104. S. H. Huang and H. C. Zhang, *Computers in Industry* 26, 107 (1995).
105. Y. S. Tarn, H. L. Tsai and S. S. Yeh, *Int. J. Mach. Tools Manuf.* 39, 1427 (1999).
106. S. C. Juang, Y. S. Tarn and H. R. Lii, *J. Mat. Proc. Technol.* 75, 54 (1998).
107. I. S. Kim, J. S. Son, S. H. Lee and P. K. D. V. Yarlagadda, *Robotics Computer-Integrated Manuf.* 20, 57 (2004).
108. I. S. Kim, J. S. Son and P. K. D. V. Yarlagadda, *Robotics Computer-Integrated Manuf.* 19, 567 (2003).

109. D. S. Nagesh and G. L. Datta, *J. Mat. Process. Technol.* 123, 303 (2002).
110. H. K. D. H. Bhadeshia, D. J. Mackay and L. E. Svensson, *Mat. Sc. Technol.* 11, 1046 (1995).
111. P. Li, M. T. C. Fang and J. Lucas, *J. Mat. Process. Technol.* 71, 288 (1997).
112. J.-Y. Jeng, T.-F. Mau and S.-M. Leu, *J. Mat. Process. Technol.* 99, 207 (2000).
113. E. A. Metzbower, J. J. Deloach, S. H. Lalam and H. K. D. H. Bhadeshia, *Sc. Technol. Weld. Joining* 6, 116 (2001).
114. I. S. Kim, Y. J. Jeong, C. W. Lee and P. K. D. V. Yarlagadda, *Int. J. Advanced Manuf. Technol.* 22, 713 (2003).
115. G. E. Cook, R. J. Barnett, K. Andersen and A. M. Strauss, *IEEE Trans. Ind. Appl.* 31, 1484 (1995).
116. H. Tsuei, D. Dunne and H. Li, *Sc. Technol. Weld. Joining* 8, 205 (2003).
117. J. Gao and C. Wu, *Sc. Technol. Weld. Joining* 8, 143 (2003).
118. I. S. Kim, S. H. Lee and P. K. D. V. Yarlagadda, *Sc. Technol. Weld. Joining* 8, 347 (2003).
119. H. Demuth and M. Beale, *Neural network tool box user's guide – Version 3.0* (Mathworks, Inc., MA, 1998).
120. J. M. Vitek, S. A. David, M. W. Richey, J. Biffin, N. Blundell and C. J. Page, *Sci. Technol. Weld. Joining* 6, 305 (2001).
121. K. Eguchi, S. Yamane, H. Sugi, T. Kubota and K. Oshima, *Sci. Technol. Weld. Joining* 4, 327 (1999).
122. X. Li, S. W. Simpson and M. Rados, *Sci. Technol. Weld. Joining* 5, 71 (2000).
123. E. A. Metzbower, J. J. Deloach, S. H. Lalam and H. K. D. H. Bhadeshia, *Sci. Technol. Weld. Joining* 6, 368 (2001).

## Chapter 3

### **Momentum, Energy and Solute Transport Model for Gas Tungsten Arc Welding – Enhancing Reliability of Its Output**

In recent decades, heat transfer and fluid flow models have provided significant insights into the welding process. However, these models have not been applied to calculate solute transport during welding. Solute transport has a significant impact on the weld properties such as the evolution of weld pool geometry and occurrence of weld defects like liquation cracking. In the present study, solute transport during welding has been calculated by incorporating solute conservation equation and appropriate boundary conditions in an already existing numerical heat transfer and fluid flow model for fusion welding. The resulting solute distribution has been compared with corresponding experimental results.

One of the major problems with the existing numerical transport phenomena based models [1-18] is that the temperature fields (and therefore, fusion zone geometry) and thermal cycles predicted by these models are not always reliable, i.e., they do not always agree with the experimental results. The disagreement between the computed and experimentally determined temperature fields can be primarily attributed to the uncertainty in the values of some of the input parameters, which cannot be prescribed based on either scientific principles or welding conditions. In general there are five uncertain input parameters, i.e., arc efficiency, arc radius, power distribution factor, and effective thermal conductivity and viscosity of the liquid metal. Although the values of arc efficiency have been experimentally measured for many welding conditions, the reported values vary significantly, even for apparently similar welding conditions. Measured values of the arc radius and power distribution factor depend on welding conditions and, as a result, their values cannot be accurately specified except for certain narrow windows of welding conditions. Values of the effective thermal conductivity and viscosity are important, since they allow accurate modeling of the high rates of transport of heat and mass in systems with strong fluctuating velocities, such as small weld pools with very strong convection currents. The values of effective conductivity and viscosity

are properties of the specific welding system, and not the inherent physical properties of the liquid metal [13] and the values of these parameters significantly affect the results of numerical transport phenomena based calculations.

In the present chapter we show that the computational transport phenomena based model of GTA welding can overcome the aforementioned difficulties by combining with a genetic algorithm (GA). The reliability of the output of the numerical transport phenomena based model can be significantly improved by optimizing the values of the uncertain input parameters from a limited volume of the experimental data. A systematic global search for the values of the uncertain input parameters is conducted using GA, which is a powerful optimization technique that can search for global optimal solution independent of the initial guessed values [19-22]. This computational procedure is applied to the GTA welding of stainless steel. A comparison of the calculated and experimental geometry is undertaken to examine the reliability of the computational procedure.

### **3.1 Mathematical Formulation**

#### **3.1.1 Numerical transport phenomena based model**

The gas tungsten arc (GTA) welding process involves a heat source that moves along the negative x-direction with a constant speed,  $U$ . The welding arc heats the work-piece surface and contributes to the formation of a molten pool. The following major assumptions are made in the model:

- (i) The molten metal is considered to be Newtonian and incompressible.
- (ii) The density variation in the calculation domain is ignored except for the calculation of the buoyancy force following Boussinesq's approximation.

##### **3.1.1.1 Governing equations**

In a stationary co-ordinate system, the generalized governing equation for the transport of various quantities in the molten pool and its surroundings  $(x',y,z)$  can be written as:

$$\frac{\partial}{\partial t}(\rho\phi) + \nabla \cdot (\rho \bar{u}\phi) = \nabla \cdot (\Gamma \nabla \phi) + S_\phi \quad (3.1)$$

where  $t$  is time,  $\rho$  is the density,  $\phi$  is any dependent scalar variable per unit mass,  $\bar{u}$  is the resultant velocity vector,  $\Gamma$  is a generalised diffusion coefficient, and  $S_\phi$  is a source term. The transport phenomena inside the molten pool can be conveniently studied with respect to a co-ordinate system that moves along the  $x$ -direction with the moving heat source by considering the following coordinate transformation:

$$x = x' - (-U)t \quad (3.2)$$

where  $U$  is the welding speed along the negative  $x$ -direction, and  $x, y, z$  are co-ordinates in a frame moving with the welding torch. In the following discussion, the following notation will be followed for description of the conservation equations:

$$x_1 = x, x_2 = y, x_3 = z \quad (3.3)$$

Applying the above transformation and substituting  $\phi$  by the appropriate variables, the governing equations in the moving co-ordinate system assume the following forms.

The equivalent single-phase linear momentum conservation equation for the  $x$ -direction, with  $i = 1, 2$  and  $3$  in index notation is given by:

$$\rho \frac{\partial u_x}{\partial t} + \rho \frac{\partial u_i u_x}{\partial x_i} = -\frac{\partial p}{\partial x} + \frac{\partial}{\partial x_i} \left( \mu \frac{\partial u_x}{\partial x_i} \right) + \rho g \beta_T (T - T_r) + \rho g \beta_c (C - C_r) - \rho U \frac{\partial u_i}{\partial x_i} + S_x \quad (3.4)$$

where  $g$  is the gravitational acceleration,  $T_r$  is a reference temperature taken as the solidus temperature of the alloy,  $T_m$ , and  $C_r$  is the concentration of the solute at  $T_r$ . The terms  $\beta_T$  and  $\beta_c$  represent the thermal and solutal volumetric expansion coefficients, respectively. The source term  $S_x$  considers frictional resistance to flow experienced by the liquid metal in the two-phase solid-liquid region similar to flow in a porous medium. This resistance is calculated using Darcy's model and the Carman-Kozeny relationship [12,17,23]. The source term also includes the Lorentz force as a consequence of the electric current used in the welding. Combining these two effects, the source term can be represented as:

$$S_x = -\frac{K_m(1-f_l)^2}{f_l^3 + b}u_x + (J \times B)_x \quad (3.5)$$

where  $f_l$  is the liquid fraction given as:  $f_l = \Delta H/L$ , where  $\Delta H$  is the latent heat content of a control volume and  $L$  is the latent heat of fusion,  $J$  is the current density and  $B$  is the magnetic field intensity. In Eq. (3.5),  $K_m$  is a large number [12] and  $b$  is a small number to avoid division by zero. The above formulation ensures that the velocity becomes zero in the solid region and increases continuously into the liquid region. The details of the formulation of the above term have been reported by Brent et al. [23]. The calculation of the Lorentz force term is presented in the literature [10], and is not repeated here.

The pressure field was obtained by solving the following continuity equation simultaneously with the momentum equation [12,17]:

$$\frac{\partial u_i}{\partial x_i} = 0 \quad (3.6)$$

The total enthalpy,  $H$ , is represented by a sum of sensible heat,  $h$ , and latent heat content,  $\Delta H$ , i.e.,  $H = h + \Delta H$ , where  $h = \int C_p dT$ ,  $C_p$  is the specific heat,  $T$  is the temperature,  $\Delta H = f_l L$ ,  $L$  is the latent heat of fusion, and the liquid fraction,  $f_l$ , is assumed to vary linearly with temperature in the mushy zone [12,17]:

$$f_l = \begin{cases} 1 & T > T_L \\ \frac{T - T_S}{T_L - T_S} & T_S \leq T \leq T_L \\ 0 & T < T_S \end{cases} \quad (3.7)$$

where  $T_L$  and  $T_S$  are the liquidus and the solidus temperature, respectively. The thermal energy transport in the weld workpiece can be expressed by the following modified energy equation [12,17]:

$$\rho \frac{\partial h}{\partial t} + \rho \frac{\partial (u_i h)}{\partial x_i} = \frac{\partial}{\partial x_i} \left( \frac{k}{C_p} \frac{\partial h}{\partial x_i} \right) - \rho \frac{\partial \Delta H}{\partial t} - \rho \frac{\partial (u_i \Delta H)}{\partial x_i} - \rho U \frac{\partial h}{\partial x_i} - \rho U \frac{\partial \Delta H}{\partial x_i} \quad (3.8)$$

where  $k$  is the effective thermal conductivity. In the liquid region, the value of the thermal conductivity in Eq. (3.8) is taken as the effective thermal conductivity, which is a

property of the specific welding system and not an inherent property of the liquid metal. Typical values of effective thermal conductivity are much higher than that of the thermal conductivity of the liquid. The higher value is important because it allows accurate modeling of the high rates of transport of heat in systems with strong fluctuating velocities that are inevitable in small weld pools with very strong convection currents [23].

The species conservation equation is given by:

$$\frac{\partial(\rho C)}{\partial t} + \frac{\partial(\rho u_i C)}{\partial x_i} = \frac{\partial}{\partial x_i} \left( \rho D \frac{\partial C}{\partial x_i} \right) - \rho U \frac{\partial C}{\partial x_i} \quad (3.9)$$

where  $C$  is the solute concentration and  $D$  is the effective mass diffusivity of the solute. The incorporation of solute conservation equation in the numerical model developed in the present study facilitates the calculation of solute distribution in the weld and its influence on weld properties.

### 3.1.1.2 Boundary conditions

The weld top surface is assumed to be flat. The velocity boundary condition is given by [12,17]:

$$\begin{aligned} \mu \frac{\partial u}{\partial z} &= f_L \left( \frac{\partial \gamma}{\partial T} \frac{\partial T}{\partial x} + \frac{\partial \gamma}{\partial C} \frac{\partial C}{\partial x} \right) \\ \mu \frac{\partial v}{\partial z} &= f_L \left( \frac{\partial \gamma}{\partial T} \frac{\partial T}{\partial y} + \frac{\partial \gamma}{\partial C} \frac{\partial C}{\partial y} \right) \\ w &= 0 \end{aligned} \quad (3.10)$$

where  $u$ ,  $v$  and  $w$  are the velocity components along the  $x$ ,  $y$  and  $z$  directions, respectively,  $d\gamma/dC$  is the concentration coefficient of surface tension and  $d\gamma/dT$  is the temperature coefficient of surface tension. The  $\partial\gamma/\partial C$  term has been incorporated in Eq. (3.10) in the present study because the distribution of solute in the weld pool is not necessarily uniform and therefore  $\partial C/\partial x$  and  $\partial C/\partial y$  have finite values. As shown in Eq. (3.10), the  $u$  and  $v$  velocities at the surface are determined from the Marangoni effect [12]. The  $w$  velocity is zero since there is no flow of liquid metal perpendicular to the pool top surface. The heat flux at the top surface is given by [12,17]:

$$k \frac{\partial T}{\partial z} = \frac{dQ\eta}{\pi r_b^2} \exp\left(-\frac{d(x^2 + y^2)}{r_b^2}\right) - \sigma\varepsilon(T^4 - T_a^4) - h_c(T - T_a) \quad (3.11)$$

where  $r_b$  is the arc radius of a circular region within which the arc power is focused,  $d$  is the dimensionless arc power distribution factor, which determines the nature of distribution of the power density of the arc,  $Q$  is the total arc power,  $\eta$  is the arc efficiency,  $\sigma$  is the Stefan–Boltzmann constant,  $h_c$  is the heat transfer coefficient, and  $T_a$  is the ambient temperature. The first term on the right hand side of Eq. (3.11) is the heat input from the heat source, defined by a Gaussian heat distribution. The arc power distribution factor,  $d$ , determines the nature of the Gaussian heat distribution pattern. The distribution is rather diffused for low values of  $d$  such as 0.5 and more focused for higher values of  $d$  such as 3.0. The second and third terms represent the heat loss by radiation and convection, respectively. At all other surfaces, temperatures are taken as ambient temperature and the velocities are set to zero.

### 3.1.2 Genetic algorithm as an optimization model

A real number based genetic algorithm (GA) is used to enhance the reliability of the output of the numerical transport phenomena based model by estimating an optimum set of uncertain input parameters for the model, i.e., arc efficiency ( $\eta$ ), arc radius ( $r_b$ ), arc power distribution factor ( $d$ ), effective thermal conductivity ( $k_{\text{eff}}$ ) and effective viscosity ( $\mu_{\text{eff}}$ ). To start with, many initial sets of randomly chosen values of these unknown input parameters are created. A systematic global search is next undertaken to find the most optimum set of values of these unknown input parameters that lead to the least error between the calculated and the experimental weld pool dimensions, i.e., weld pool penetration and width. The experimental data consists of sets of five welding conditions and the corresponding measured weld pool dimensions for the GTA welding of stainless steels, as given in Table 3.1. The calculated weld pool penetration and width for each set of input welding variables are obtained from the numerical transport phenomena based model. The randomly chosen values of unknown input parameters do not always produce the desired weld dimensions. The resulting mismatch between the computed and the desired weld dimensions is expressed by the following objective function,  $O1(f)$ :

$$O1(f) = \sum_{m=1}^5 \left[ \left( \frac{p_m^c}{p_m^e} - 1 \right)^2 + \left( \frac{w_m^c}{w_m^e} - 1 \right)^2 \right] \quad (3.12)$$

where  $m$  is the index that identifies the specific set of welding conditions given in Table 3.1,  $p_m^c$  and  $w_m^c$  are the computed weld pool penetration and width, respectively, and,  $p_m^e$  and  $w_m^e$  are the corresponding experimental or desired values of these two weld attributes for the set of welding conditions with index  $m$ .

Table 3.1. Welding variables and experimentally measured weld pool penetration and width. The experimental data was provided by Dr. T. J. Lienert and Dr. M. Johnson of Los Alamos National Laboratory.

Data set	Current (A)	Voltage (V)	Welding speed (mm/s)	Sulfur (wt%)	Weld pool penetration (mm)	Weld pool width (mm)
1	101	9.6	1.7	0.003	1.37	4.83
2	150	9.9	1.7	0.003	2.18	6.80
3	150	10.5	1.7	0.293	3.12	5.91
4	100	10.0	3.4	0.024	1.22	4.15
5	101	9.9	3.4	0.293	1.39	4.05

The objective function,  $O1(f)$ , depends on the five unknown input parameters:

$$O1(f) = O1(f_1, f_2, f_3, f_4, f_5) = O1\left(\eta, \frac{r_b}{e_r}, d, \frac{k_{eff}}{k_s}, \frac{\mu_{eff}}{\mu_{fl}}\right) \quad (3.13)$$

In Eq. (3.13),  $e_r$  is the radius of the electrode,  $k_s$  is the thermal conductivity of the solid metal at room temperature,  $\mu_{fl}$  is the viscosity of molten steel,  $k_{eff}$  is the effective thermal conductivity of liquid metal, and  $\mu_{eff}$  is the effective viscosity of liquid metal. These are reference values that represent the order of magnitude of the unknown input parameters. These reference values and other data needed for the calculations are given in Table 3.2. Note that Eq. (3.13) has been made non-dimensional in order to preserve the importance

of all five unknown input parameters, making their non-dimensional values comparable in magnitude. The GA produces new individuals, or sets of unknown input parameters, with iterations based on the evolutionary principles [21,22]. **Error! Reference source not found.** provides explanations of various terms used in GA as related to welding. The GA used in the present study is a parent centric recombination (PCX) operator based generalized generation gap (G3) model [21,22]. This model was chosen because it has been shown to have a faster convergence rate on standard test functions as compared to other evolutionary algorithms [21,22]. The specific application of this model for obtaining the optimum set of values of the five unknown input parameters of the numerical transport phenomena based model for GTA welding is described as follows.

A population is a collection of many individuals and each individual represents a set of randomly chosen values of the five non-dimensionalized unknown input parameters. A parent refers to an individual in the current population. The best parent is the individual that has the best fitness, i.e., gives the minimum value of the objective function, defined by Eq. (3.12), in the entire population.

Table 3.2. Data used in the calculations [5].

Physical property	Value
Liquidus Temperature, $T_l$ (K)	1785.0
Solidus temperature, $T_s$ (K)	1745.0
Density of metal, $\rho$ (kg/m <sup>3</sup> )	7200.0
Thermal conductivity of solid, $k_s$ (J/m-s-K)	25.08
Specific heat of solid, $C_{ps}$ (J/kg-K)	702.24
Specific heat of liquid, $C_{pl}$ (J/kg-K)	806.74
Temperature coefficient of surface tension, $d\gamma/dT$ (N/m-K)	$-0.47 \times 10^{-3}$
Coefficient of thermal expansion, $\beta$ (K <sup>-1</sup> )	$1.5 \times 10^{-6}$
Viscosity of molten iron, $\mu_{fl}$ (kg/m-s)	$6.7 \times 10^{-3}$
Radius of the electrode, $e_r$ (mm)	1.0

The algorithm for the model is as follows:

1. The best parent and two other randomly selected parents are chosen from the population.
2. From the three chosen parents, two offsprings or new individuals are generated using a recombination scheme. PCX based G3 models are known to converge rapidly when three parents and two offsprings are selected [22]. A recombination scheme is a process for creating new individuals from the parents.
3. Two new parents are randomly chosen from the current population.
4. A subpopulation of four individuals that includes the two randomly chosen parents in step 3 and two new offsprings generated in step 2 is formed.
5. The two best solutions, i.e., the solutions having the least values of the objective function, are chosen from the subpopulation of four members created in step 4. These two individuals replace the two parents randomly chosen in step 3.
6. The calculations are repeated from step 1 again until convergence is achieved.

The above steps, as applied to the present study, are shown in Fig. 3.1. The working of the model to find the unknown input variables by minimizing the objective function is illustrated in Fig. 3.2. The recombination scheme (step 2) used in the present model is based on the PCX operator. A brief description of the PCX operator, as applied to the present problem of five unknown input parameters, is presented below.

First three parents, i.e.,  $(f_1^0, f_2^0, f_3^0, f_4^0, f_5^0)$ ,  $(f_1^1, f_2^1, f_3^1, f_4^1, f_5^1)$ ,  $(f_1^2, f_2^2, f_3^2, f_4^2, f_5^2)$  are randomly selected from the current population. Here, the subscripts represent the five unknown input parameters, while the superscripts denote the parent identification

number. 
$$\bar{g} = \left( \frac{f_1^0 + f_1^1 + f_1^2}{3}, \frac{f_2^0 + f_2^1 + f_2^2}{3}, \frac{f_3^0 + f_3^1 + f_3^2}{3}, \frac{f_4^0 + f_4^1 + f_4^2}{3}, \frac{f_5^0 + f_5^1 + f_5^2}{3} \right), \text{ i.e.,}$$

the mean vector, or centroid, of the three chosen parents is computed. To create an offspring, one of the parents, say  $\bar{x}^{(p)} = (f_1^0, f_2^0, f_3^0, f_4^0, f_5^0)$  is chosen randomly. The direction vector,  $\bar{d}^{(p)} = \bar{x}^{(p)} - \bar{g}$ , is next calculated from the selected parent to the mean vector or centroid. Thereafter, from each of the other two parents, i.e.,  $(f_1^1, f_2^1, f_3^1, f_4^1, f_5^1)$

and  $(f_1^2, f_2^2, f_3^2, f_4^2, f_5^2)$ , perpendicular distances,  $D_i$ , to the direction vector,  $\bar{d}^{(p)}$ , are computed and their average,  $\bar{D}$ , is found.

Table 3.3: Terminology used in genetic algorithm.

Biological terms	Equivalent welding variables and representation in genetic algorithm
Genes: Units containing hereditary information	In the form of non-dimensional variables, $f_1, f_2, f_3, f_4$ and $f_5$ . Eg. $f_1 = 1.10$ ; $f_2 = 1.70$ ; $f_3 = 1.56$ ; $f_4 = 1.85$ ; $f_5 = 1.21$ .
Chromosome/Individual: A number of genes folded together	A set of input variable values taken together, i.e., (1.10, 1.70, 1.56, 1.85, 1.21)
Population: Collection of many chromosomes/individuals	Collection of multiple sets: (1.10, 1.70, 1.56, 1.85, 1.21), (1.20, 1.54, 1.65, 1.91, 1.17), ..... (1.23, 1.65, 1.75, 1.68, 1.35)
Parents: Chromosomes/individuals participating for creating new individuals (or offsprings)	Parents: Eg. (1.10, 1.70, 1.56, 1.85, 1.21), (1.23, 1.65, 1.75, 1.68, 1.35)
Objective function value: Value of objective function determines if a chromosome/individual survives or dies	Objective function: Calculated for each set of input variables using Eq. (3.12)

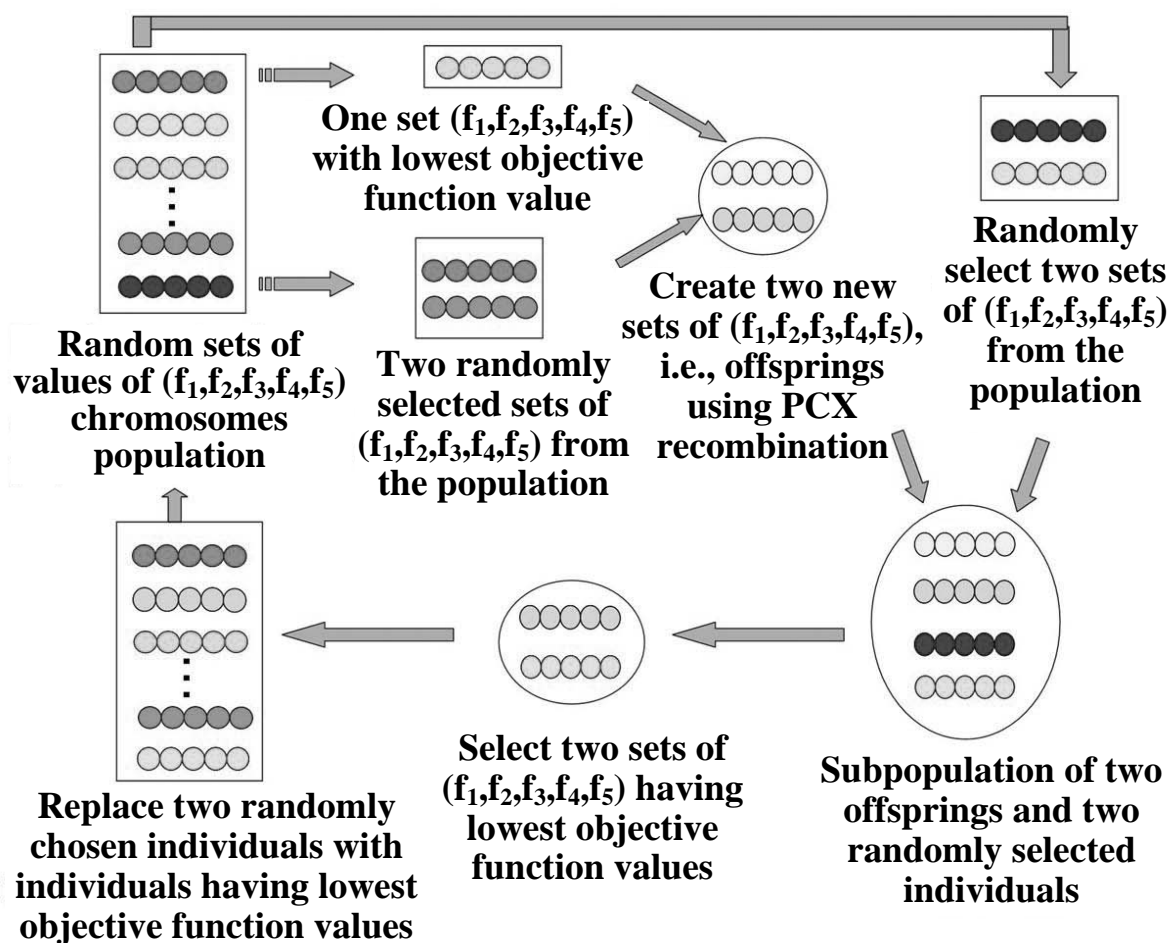


Fig. 3.1. Generalized generation gap (G3) genetic algorithm using parent centric recombination (PCX) operator [24].

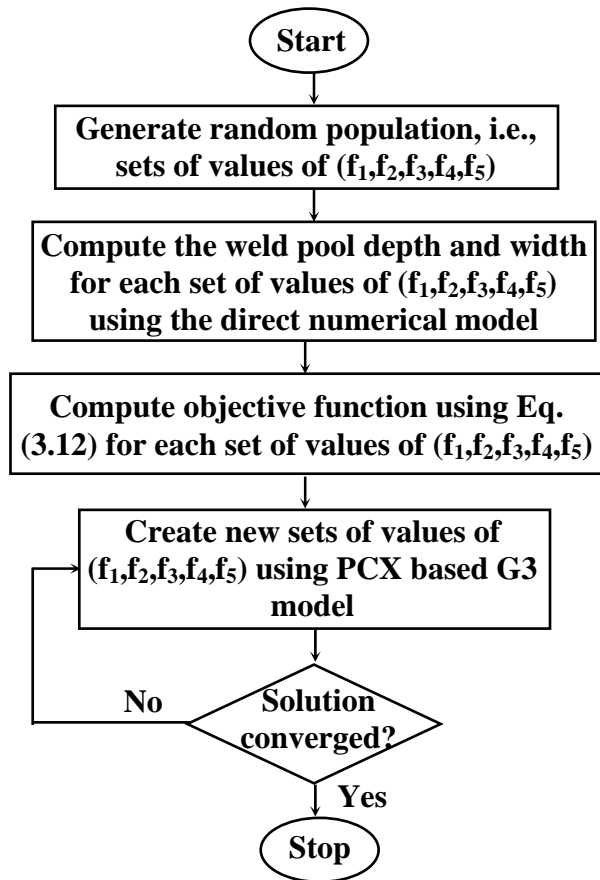


Fig. 3.2. Flow chart of the generalized generation gap (G3) model.

Finally, the offspring, i.e.,  $\bar{y} = (f'_1, f'_2, f'_3, f'_4, f'_5)$ , is created as follows:

$$\bar{y} = \bar{x}^{(p)} + w_\zeta |\bar{d}^{(p)}| + \sum_{i=1, i \neq p}^5 w_\eta \bar{Dh}^{(i)} \quad (3.14)$$

where  $\bar{h}^{(i)}$  are the orthonormal bases that span the subspace perpendicular to  $\bar{d}^{(p)}$ , and  $w_\zeta$  and  $w_\eta$  are randomly calculated zero-mean normally distributed variables. The values of the variables that characterize the offspring,  $\bar{y} = (f'_1, f'_2, f'_3, f'_4, f'_5)$ , are calculated as follows:

$$f'_1 = f_1^0 + f_{11} + f_{12} \quad (3.15)$$

$$f'_2 = f_2^0 + f_{21} + f_{22} \quad (3.16)$$

$$f'_3 = f_3^0 + f_{31} + f_{32} \quad (3.17)$$

$$f'_4 = f_4^0 + f_{41} + f_{42} \quad (3.18)$$

$$f'_5 = f_5^0 + f_{51} + f_{52} \quad (3.19)$$

where,

$$f_{11} = w_\zeta \left( \frac{2f_1^0 - f_1^1 - f_1^2}{3} \right) \quad (3.20)$$

$$f_{21} = w_\zeta \left( \frac{2f_2^0 - f_2^1 - f_2^2}{3} \right) \quad (3.21)$$

$$f_{31} = w_\zeta \left( \frac{2f_3^0 - f_3^1 - f_3^2}{3} \right) \quad (3.22)$$

$$f_{41} = w_\zeta \left( \frac{2f_4^0 - f_4^1 - f_4^2}{3} \right) \quad (3.23)$$

$$f_{51} = w_\zeta \left( \frac{2f_5^0 - f_5^1 - f_5^2}{3} \right) \quad (3.24)$$

$$f_{12} = w_\eta \left( \frac{a_2 + b_2}{2} \right) \left[ 1 - \left( \frac{2f_1^0 - f_1^1 - f_1^2}{3d} \right)^2 \right] \quad (3.25)$$

$$f_{22} = w_{\eta} \left( \frac{a_2 + b_2}{2} \right) \left[ 1 - \left( \frac{2f_2^0 - f_2^1 - f_2^2}{3d} \right)^2 \right] \quad (3.26)$$

$$f_{32} = w_{\eta} \left( \frac{a_2 + b_2}{2} \right) \left[ 1 - \left( \frac{2f_3^0 - f_3^1 - f_3^2}{3d} \right)^2 \right] \quad (3.27)$$

$$f_{42} = w_{\eta} \left( \frac{a_2 + b_2}{2} \right) \left[ 1 - \left( \frac{2f_4^0 - f_4^1 - f_4^2}{3d} \right)^2 \right] \quad (3.28)$$

$$f_{52} = w_{\eta} \left( \frac{a_2 + b_2}{2} \right) \left[ 1 - \left( \frac{2f_5^0 - f_5^1 - f_5^2}{3d} \right)^2 \right] \quad (3.29)$$

The expressions for the variables  $d$ ,  $a_2$ , and  $b_2$ , used in Eqs. (3.25) to (3.29), are as follows:

$$d = \sqrt{\left( \frac{2f_1^0 - f_1^1 - f_1^2}{3} \right)^2 + \left( \frac{2f_2^0 - f_2^1 - f_2^2}{3} \right)^2 + \left( \frac{2f_3^0 - f_3^1 - f_3^2}{3} \right)^2 + \left( \frac{2f_4^0 - f_4^1 - f_4^2}{3} \right)^2 + \left( \frac{2f_5^0 - f_5^1 - f_5^2}{3} \right)^2} \quad (3.30)$$

$$a_2 = e_1 \times \sqrt{1 - (a_1)^2} \quad (3.31)$$

$$b_2 = e_2 \times \sqrt{1 - (b_1)^2} \quad (3.32)$$

$$a_1 = \sum_{i=1}^5 \frac{(f_i^1 - f_i^0) \left( \frac{2f_i^0 - f_i^1 - f_i^2}{3} \right)}{d \times e_1} \quad (3.33)$$

$$e_1 = \sqrt{(f_1^1 - f_1^0)^2 + (f_2^1 - f_2^0)^2 + (f_3^1 - f_3^0)^2 + (f_4^1 - f_4^0)^2 + (f_5^1 - f_5^0)^2} \quad (3.34)$$

$$b_1 = \sum_{i=1}^5 \frac{(f_i^2 - f_i^0) \left( \frac{2f_i^0 - f_i^1 - f_i^2}{3} \right)}{d \times e_2} \quad (3.35)$$

$$e_2 = \sqrt{(f_1^2 - f_1^0)^2 + (f_2^2 - f_2^0)^2 + (f_3^2 - f_3^0)^2 + (f_4^2 - f_4^0)^2 + (f_5^2 - f_5^0)^2} \quad (3.36)$$

## 3.2 Results and Discussion

### 3.2.1 Improving the reliability of the output of the numerical transport phenomena based model

Since the calculations of temperature and velocity fields are based on well established principles of transport phenomena, the lack of reliability of the computed results originate from the uncertain values of the input parameters that cannot be specified from welding conditions. In order to address this problem, values of arc efficiency ( $\eta$ ), arc radius ( $r_b$ ), arc power distribution factor ( $d$ ), effective thermal conductivity of the molten metal ( $k_{\text{eff}}$ ) and effective viscosity of the molten metal ( $\mu_{\text{eff}}$ ) were determined from a limited volume of experimental data using a genetic algorithm based global optimization technique. The experimental data used for this purpose are listed in Table 3.1. The optimized values of the five unknown input parameters are presented in Table 3.4.

Table 3.4. Optimized values of the five unknown input parameters of the numerical transport phenomena based model.

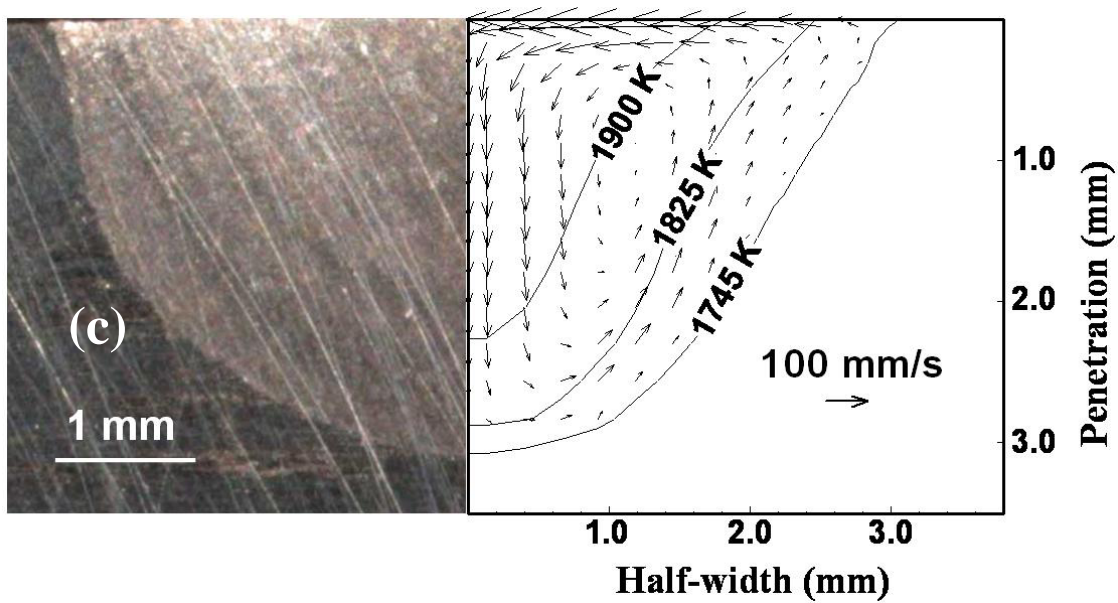
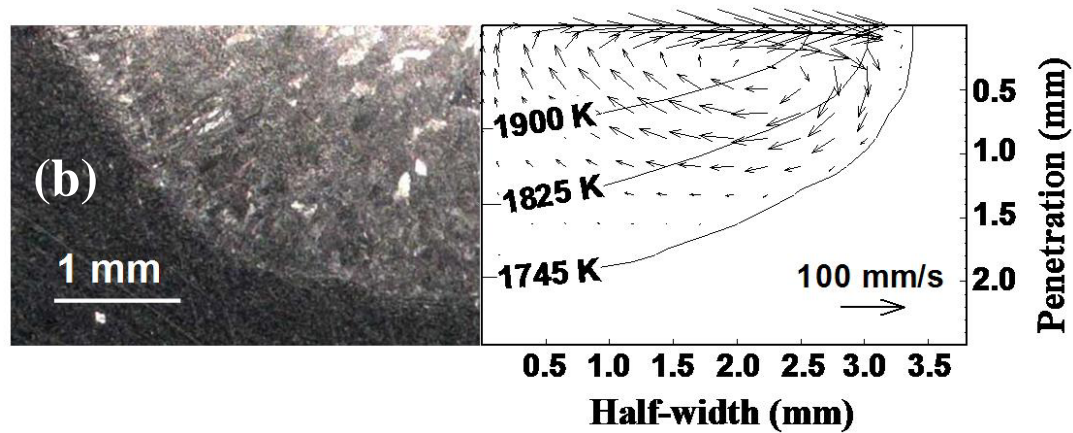
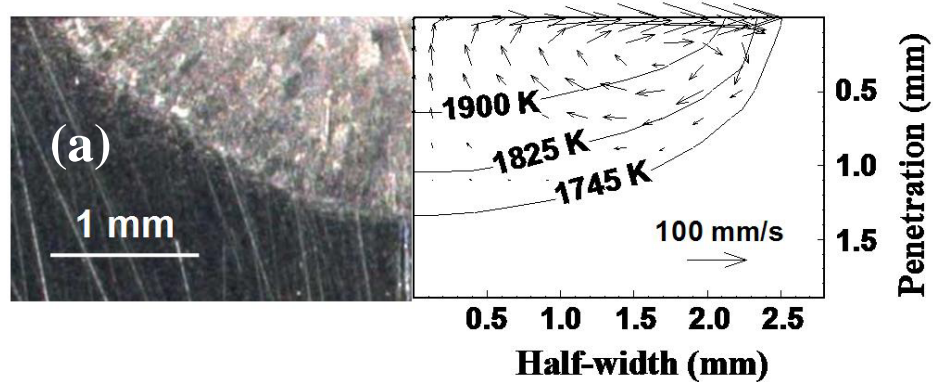
Unknown variable	Value
Arc efficiency, $\eta$	0.66
Arc radius, $r_b$ (mm)	2.8
Arc power distribution factor, $d$	2.0
Effective thermal conductivity of liquid metal, $k_{\text{eff}}$ (J/m-s-K)	125.5
Effective viscosity of liquid metal, $\mu_{\text{eff}}$ (kg/m-s)	0.03

The values of effective thermal conductivity and effective viscosity represent an enhancement of about 5 and 4 times, respectively, over the corresponding values for thermal conductivity and viscosity given in Table 3.2. This behavior is consistent with the presence of turbulent flow in the weld pool during GTA welding, as reported in the

literature [5,25-28]. De and DebRoy [5] reported the enhancement factors for thermal conductivity and viscosity in steel welds to be 4 and 15, respectively, using gradient based optimization techniques. Hong et al. [26] suggested an enhancement factor between 12 and 15 for thermal conductivity and a factor more than 6 for the viscosity while using a 150 A current and 25 V based on peak temperature analysis in the weld pool and k- $\epsilon$  turbulence model calculations. Choo and Szekely [25] suggested an enhancement factor of 8 for thermal conductivity and a factor of 30 for the viscosity at a current of 100 A by matching the calculated weld pool geometry with the experimentally determined geometry. They [25] also verified the weld pool shape and values of enhancement factors using the k- $\epsilon$  turbulence model. Kumar and DebRoy [28] reported enhancement factors in the range of 5 to 9 for gas metal arc (GMA) fillet welding. The estimated values of arc efficiency, arc radius and arc power distribution factor are 0.66, 2.8 mm and 2.0, respectively, as shown in Table 3.4. Choo et al. [29] have reported arc efficiency values higher than 0.68, while Mendez et al. [30] indicated the arc radius to be approximately 1.9 mm for currents of up to 300 A. The power distribution factor depends on the electrode angle and other experimental conditions, and its value varies between 0.5 and 3.0. The differences in the values of the arc radius and the power distribution factor with their values reported in the literature are thought to be due to the differences in the experimental conditions. However, the values available in the literature [5,25-30] are specific to the welded material and welding conditions, and cannot be used in the present study.

The optimized values of the unknown input parameters were used to calculate the weld geometry for the five sets of welding conditions listed in Table 3.1. Fig. 3.3(a) to (e) show good agreement between the calculated and the experimentally measured weld pool geometries indicating the appropriateness of the computed uncertain input parameters. Furthermore, a good agreement between the computed and the experimental weld dimensions indicates that the numerical transport phenomena based model, using the optimized values of the unknown input parameters, can provide both the expected trends and the correct weld pool geometry for various sets of welding conditions. After the values of the uncertain input parameters are determined, the calculation procedure can

serve as a reliable link between the welding variables and the weld attributes such as the weld pool geometry.



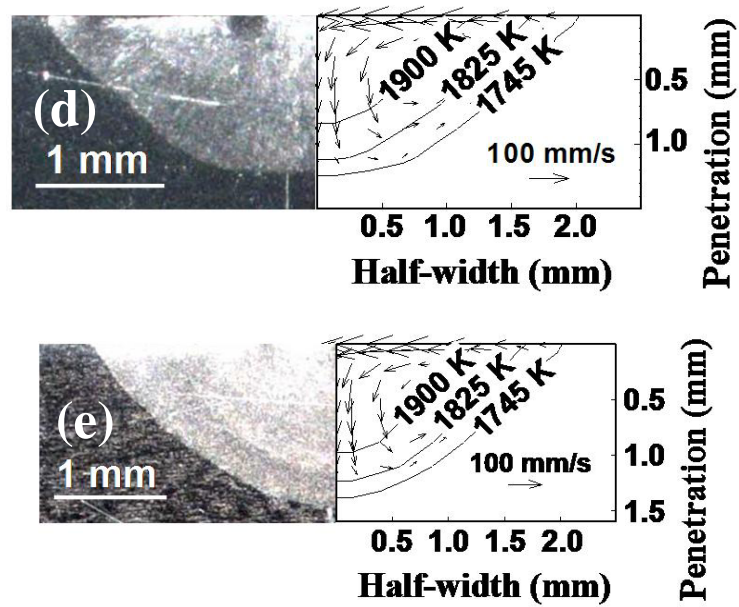


Fig. 3.3. Experimental weld geometry and the calculated weld geometry, (a) to (e), obtained using the optimum set of values of the unknown input parameters for the five sets of welding conditions given in Table 3.1, i.e., 1 to 5, respectively. The 1745 K isotherm is the equilibrium solidus temperature of stainless steel, which marks the weld pool boundary.

### 3.3 Summary and Conclusions

In the present study, solute conservation equations were incorporated into an already existing numerical heat transfer and fluid flow model for gas tungsten arc (GTA) welding to calculate the solute distribution in the weld. The lack of reliability of the results obtained from the current numerical transport phenomena based models of GTA welding in predicting weld pool geometry originate mainly from the uncertainty in the values of several input variables such as arc efficiency, arc radius, arc power distribution factor, effective thermal conductivity and effective viscosity of the molten metal. A transport phenomena based model for GTA welding can be combined with an evolutionary optimization algorithm to enhance the reliability of the computed temperature and velocity fields. By using a real number based GA, the values of these uncertain parameters were determined from a limited volume of experimental data for the GTA welding of stainless steel. The optimized values of the uncertain input parameters lie within the range of their values reported in the literature. The computed weld pool shape and size utilizing the optimized values of the uncertain input parameters agreed well with the corresponding experimentally determined values for various welding conditions indicating the effectiveness of the approach. Once the reliability of output of the transport phenomena based model has been enhanced, it can now be applied to determine the distribution of solutes in the weld, and their impact on the weld pool geometry (Chapter 6) and consumable design to avoid occurrence of weld defects like liquation cracking (Chapter 7) under similar welding conditions.

### 3.4 References

1. H. Zhao, and T. DebRoy, J. Appl. Phys. 93, 10089 (2003).
2. W. Zhang, C.-H. Kim, and T. DebRoy, J. Appl. Phys. 95, 5210 (2004).
3. W. Zhang, C.-H. Kim, and T. DebRoy, J. Appl. Phys. 95, 5220 (2004).
4. A. De, and T. DebRoy, J. Appl. Phys. 95, 5230 (2004).
5. A. De, and T. DebRoy, J. Phys. D: Appl. Phys. 37, 140 (2004).
6. S. Mishra, and T. DebRoy, J. Phys. D: Appl. Phys. 37, 2191 (2004).
7. S. Mishra, and T. DebRoy, Acta Mater. 52, 1183 (2004).
8. X. He, P. Fuerschbach, and T. DebRoy, J. Appl. Phys. 94, 6949 (2003).
9. C.-H. Kim, W. Zhang, and T. DebRoy, J. Appl. Phys. 94, 2667 (2003).
10. A. Kumar, and T. DebRoy, J. Appl. Phys. 94, 1267 (2003).
11. S. A. David, R. Trivedi, M. E. Eshelman, J. M. Vitek, S. S. Babu, T. Hong, and T. DebRoy, J. Appl. Phys. 93, 4885 (2003).
12. W. Zhang, G. G. Roy, J. Elmer, and T. DebRoy, J. Appl. Phys. 93, 3022 (2003).
13. X. He, P. Fuerschbach, and T. DebRoy, J. Phys. D: Appl. Phys. 36, 3079 (2003).
14. X. He, P. W. Fuerschbach, and T. DebRoy, J. Phys. D: Appl. Phys. 36, 1388 (2003).
15. J. W. Elmer, T. A. Palmer, W. Zhang, B. Wood, and T. DebRoy, Acta Mater. 51, 3333 (2003).
16. T. Hong, and T. DebRoy, Metall. Mater. Trans. B 34, 267 (2003).
17. K. Mundra, T. DebRoy, and K. Kelkar, Numerical Heat Transfer A 29, 115 (1996).
18. A. Kumar, and T. DebRoy, Int. J. Heat Mass Transfer. 47, 5793 (2004).
19. D. E. Goldberg, *Genetic Algorithm in Search, Optimization and Machine Learning* (Addison-Wesley, MA, 1989).
20. *Handbook of Evolutionary Computations*, edited by T. Back, D. B. Fogel and Z. Michalewicz (IOP Publishing Ltd., Oxford University Press, 2000).
21. K. Deb, A. Anand, and D. Joshi, Evolutionary Computation 10, 371 (2002).
22. K. Deb, *Multi-objective optimization using evolutionary algorithms – Edition 1* (Wiley, New York, 2001).
23. A. D. Brent, V. R., Voller, and K. J. Reid, Numerical Heat Transfer 13, 297 (1988).

24. A. Kumar, S. Mishra, J. W. Elmer and T. DebRoy, *Metall. Mater. Trans. A* 36, 15 (2005).
25. R. T. C. Choo, and J. Szekely, *Weld. J.* 73, 25s (1994).
26. K. Hong, D. C. Weckmann, A. B. Strong, and W. Zheng, *Sci. Technol. Weld. Joining* 7, 125 (2002).
27. K. Hong, D. C. Weckmann, A. B. Strong, and W. Zheng, *Sci. Technol. Weld. Joining* 8, 313 (2003).
28. A. Kumar and T. DebRoy, *J. Phys. D: Appl. Phys.* 38, 127 (2005).
29. R. T. C. Choo, J. Szekely, and R. C. Westhoff, *Metall. Trans. B* 23, 357 (1992).
30. P. F. Mendez, K. L. Niece and T. W. Eagar, in *Proceedings from Materials Solutions Conference '99 on Joining of Advanced and Speciality Materials II*, edited by M. Singh, J. E. Indacochea, J. N. DuPont, K. Ikeuchi, and J. M. Fernandez (ASM International, Materials Park, OH 2000), pp. 151–158.

## Chapter 4

### **A Genetic Algorithm and Gradient Descent Based Neural Network with the Predictive Power of a Numerical Transport Phenomena Based Model for Welding**

As described in the previous chapters, numerical transport phenomena based models have provided significant quantitative insights into the fusion welding process. However, these powerful tools are not extensively used in the welding industry because they are complex, require specialized training to develop and test, and consume a large amount of computer time. A practical solution to this problem is to develop a neural network that is capable of providing high computational speed.

Neural network models are powerful non-linear regression analysis methods [1-5] that can relate input variables like welding process parameters and material properties with weld characteristics such as weld pool geometry. In recent decades, many researchers have attempted systematic correlations between welding variables and weld characteristics using artificial neural networks [1,2,6-25]. The previous efforts to model the gas tungsten arc (GTA) welding process using neural network were based on training the network with experimental data [11,15,21]. Since the volume of experimental data required to train a neural network depends on the number of input and output variables, most previous efforts considered only few input parameters to keep the necessary volume of experimental data tractable [11,15,21]. For example, Tarng et al. [11], Andersen et al. [15] and Juang et al. [21] developed neural network models of GTA welding process, which considered the effects of process parameters like welding speed, arc current and voltage as inputs. These neural network models were developed using a limited volume of experimental data, and they could not determine the effect of material properties like thermal conductivity, specific heat, etc. on weld pool geometry. Furthermore, the output variables considered in these neural networks were also limited. For example, the existing neural network models do not provide any information about some of the important output parameters such as the cooling rate and peak temperature. A review of previous work indicates that what is needed is a framework for rapid calculation of weld pool geometry, cooling rate and peak temperature for the GTA welding of various materials.

In the present study, six feed forward neural networks have been developed for the GTA welding of stainless steel. Each network provides one of the six output parameters of GTA welds, i.e., depth, width and length of the weld pool, peak temperature, cooling time from 800°C to 500°C, and maximum liquid velocity. The networks require values of seventeen input parameters including the welding variables like current, voltage, welding speed, arc efficiency, arc radius, and power distribution factor, and material properties like thermal conductivity, specific heat and concentration of sulfur in steel. The training data is generated from the numerical transport phenomena based model developed in the present study. Since the training data is made up of results from the numerical transport phenomena based model, the outputs of the trained neural networks will comply with the basic phenomenological laws of welding physics. With the improvements in computational hardware and software in recent years, including faster machines and larger data storage capacity, a large volume of training and testing data can be generated with the numerical transport phenomena based models in a realistic time frame, such as a week or two for 1000 runs of the transport phenomena based model. The weights of the neural networks were calculated using two optimization schemes, first using a gradient descent (GD) method with various sets of randomized initial weights, and then applying a hybrid optimization scheme where a genetic algorithm (GA) is used in combination with the GD method. The neural networks produced by the hybrid optimization approach gave better results than all the networks based on only the GD method. Unlike the GD method alone, the hybrid optimization scheme could find the global optimal weights, which is illustrated by the good agreement between all the outputs from the neural networks and the corresponding results from the transport phenomena based model.

#### **4.1 Neural Network Model**

Six feed forward neural networks have been developed for the gas tungsten arc (GTA) welding of low carbon steel. Each neural network takes 17 input variables that include various welding variables such as arc current, voltage, welding speed, and material properties such as thermal conductivity, specific heat, and provides a single

output, which can be one of the six output parameters, i.e., depth, width and length of the weld pool, peak temperature, cooling time between 800°C and 500°C, and maximum liquid velocity in the weld pool. The cooling time was calculated on the work piece surface along the welding direction. The input variables such as arc efficiency, arc power distribution factor and arc radius determine how heat is absorbed at various locations in the work piece [26]. Since temperature independent thermophysical properties of the solid alloy are used in the model, a question arises as to how to select their values. As the heat flow in the solid region near the weld pool affects both the size and shape of the weld pool as well as the temperature field in the entire work piece, it is appropriate to use thermophysical properties at a temperature closer to the melting point than to the ambient temperature. Effective thermal conductivity and effective viscosity are used as input variables because they allow accurate modeling of the turbulence effect in the weld pool. These two variables are system properties, and their values are obtained by enhancing the molecular values of liquid thermal conductivity and viscosity, respectively. Optimized values for these two variables for GTA welding of stainless steel have been determined in Chapter 3.

The structure of each neural network along with all the input and output variables is shown in Fig. 4.1. Each neural network contains an input layer, a hidden layer and an output layer. The input layer contains all the 17 input variables, which are connected to nodes in the hidden layer, represented by circles in Fig. 4.1, through the weights assigned for each link.

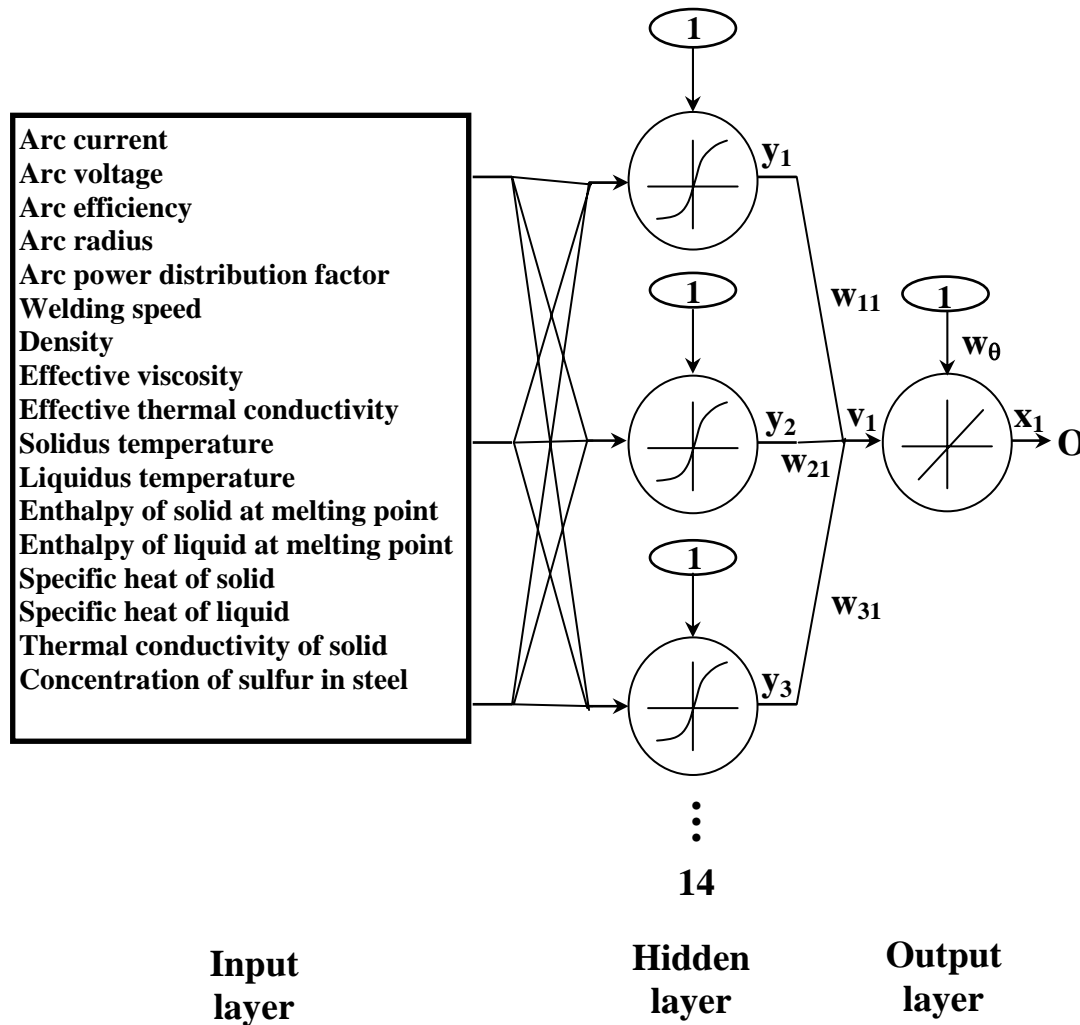


Fig. 4.1. Neural network architecture used in the present study. The input layer has 17 input variables and the output layer has one of the six output variables,  $O$ , i.e., weld pool depth, weld pool width, weld pool length, peak temperature, cooling time from  $800^{\circ}\text{C}$  to  $500^{\circ}\text{C}$  or maximum liquid velocity in the weld pool. Each connection to a node,  $j$ , from a node in the previous layer,  $i$ , has an adjustable weight,  $w_{ij}$ , associated with it. The weights embody the non-linear relationship between the input and the output variables. Each node in the hidden and the output layers is given an extra input, which always has a value of 1. The weight,  $w_0$ , of this extra input is called the bias. The net input,  $v_j$ , for a node,  $j$ , is described in Eq. (4.1) and  $y_i$  is the output of node,  $i$ .

The number of nodes in the hidden layer is found by optimizing the neural network. Each connection to a node,  $j$ , from a node in the previous layer,  $i$ , has an adjustable weight,  $w_{ij}$ , associated with it. The weights,  $w_{ij}$ , embody the non-linear relationship between the input and the output variables. Also, each node in the hidden and the output layers is given an extra input, which always has a value of 1. The weight of this extra input is called the bias. The net input,  $v_j$ , for a node,  $j$ , is given as:

$$v_j = \sum_i w_{ij}y_i + w_0 \quad (4.1)$$

where  $i$  is a node in the previous layer,  $w_{ij}$  is the weight of the connection between nodes  $j$  and  $i$ ,  $y_i$  is the output of node  $i$ , and  $w_0$  is the bias weight. Equation (4.1) is calculated for all the nodes in the hidden layers as well as the output layer.

Now, the output of node  $j$  is calculated by using a transfer function. A hyperbolic tangent function (a symmetric sigmoid function), which is a non-linear function producing output between -1 to +1, is used as transfer function for the nodes in the hidden layer, and a linear transfer function is used for the nodes in the output layer. The use of a non-linear transfer function in the hidden layer allows the network to learn nonlinear and linear relationships between input and output vectors [20], while the use of a linear transfer function in the output layer allows the network to produce values outside the range of -1 to +1. Thus, the output,  $x_j$ , of a node  $j$  in the hidden layer is given by:

$$x_j = \tanh(a \times v_j) \quad (4.2)$$

where 'a' is the slope of the sigmoid function. By varying the parameter 'a', sigmoid functions of different slopes can be obtained [27]. Increase in the value of 'a' increases the slope of the activation function and vice versa. A very high value of the slope makes the curve close to a step function while a low value retards the convergence rate. Based on the findings of previous works, a value of 1.5 was used to achieve rapid convergence [28,29]. Furthermore, the use of the tanh function in Eq. (4.2) as the activation function helps in keeping the problem reasonably well-conditioned. An attractive feature of the

hyperbolic tangent function is that its derivative does not increase computational volume significantly [27]. The output,  $x_j$ , of a node  $j$  in the output layer is given by:

$$x_j = v_j \quad (4.3)$$

The training of a neural network implies finding a set of weights that minimize error between the desired output and the output calculated by the neural network. A back-propagation algorithm [3] is used for the training of the neural networks. This algorithm tries to minimize the objective function, i.e., the mean square error (MSE) between the desired output and the neural network output. The MSE is defined as [3]:

$$\text{MSE} = \frac{\sum_p \sum_k (d_{pk} - o_{pk})^2}{p \times k} \quad (4.4)$$

where  $p$  is the number of training datasets,  $k$  represents the number of output nodes, which is one in this work,  $d_{pk}$  is the desired output and  $o_{pk}$  is the output produced by the neural network. The desired outputs of the neural network such as weld pool depth, width, and length, cooling rate, peak temperature and maximum liquid velocity are dependent on input welding conditions, material properties and the network parameters such as the weights.

The back-propagation algorithm adjusts the weights in the steepest descent direction (negative of the gradient) [3]. This is the direction in which the error,  $E$ , decreases most rapidly. For a given set of input-output training data, the partial derivatives of the error with respect to each weight,  $\partial E/\partial w$ , are calculated in two passes [3]. The forward pass calculates the output of each node in the hidden layers and the output layer, based on the inputs from the previous layers, as described by Eqs. (4.1) to (4.3). The backward pass propagates the derivatives from the output layer back to the input layer, and updates the weights [3]. The backward pass is well documented in the literature [3,30] and is not described here. Once  $\partial E/\partial w$  are calculated, the weights are changed by an amount proportional to  $\partial E/\partial w$  as:

$$\Delta w = -\varepsilon \frac{\partial E}{\partial w} \quad (4.5)$$

where  $\varepsilon$  is called the learning rate. A large learning rate enables quick convergence, but it can also lead to overstepping of the solution and oscillation of the error [8]. On the other hand, small learning rate may prevent oscillation of the error, but it requires much more time to reach the solution [8]. Therefore, in the present study  $\varepsilon$  was taken as 0.1 during initial iterations, and reduced to 0.01 once the error became very small. A simple method for increasing the rate of learning without oscillation is to include a momentum term in Eq. (4.5) as follows [3]:

$$\Delta w(n) = -\varepsilon \frac{\partial E}{\partial w} + \alpha \Delta w(n-1) \quad (4.6)$$

where  $n$  is the number of iterations, an iteration being defined as a single sweep through all the input-output pairs in the training dataset, and  $\alpha$  is an exponential decay factor between 0 and 1 that determines the relative contribution of the current gradient,  $\Delta w(n)$ , and the earlier gradients,  $\Delta w(n-1)$ , to the weight change. The value of  $\alpha$  is set to 0.9 in the present study, based on guidance from previous research [20,30].

The training of the neural network was started with random small weights. It was observed that after the initial rapid decrease in error, further descent became very sluggish, and the result depended on the initial random weights, which are common problems with gradient descent algorithms [4,31,32]. Furthermore, for simple two-layer networks (without a hidden layer), the error surface is bowl shaped and using gradient-descent techniques to minimize objective function is not a problem. However, the addition of a hidden layer, used to solve more difficult problems like GTA welding process, increases the possibility for complex error surfaces which contain many minima. The gradient based methods can easily get trapped in such local minima. Stochastic optimization techniques are capable of finding the global minima and avoiding local minima [33-35]. Therefore, a genetic algorithm [33-35] is used along with the gradient descent method to find the optimal global weights in the present work. But, if the genetic algorithm is such a powerful technique in finding the global minima, then why should one even care about using the gradient based methods? Why not use only the genetic algorithm? The answer to this question again lies in the fact that genetic algorithm is a stochastic optimization method [33-35]. It tends to explore a wide search space using

evolutionary principles [33-35]. As a result, if only genetic algorithm is used in the present problem, it will take much longer than the hybrid scheme to reach global minima. The validity of the above argument is illustrated by Fig. 4.2, which shows the performance of genetic algorithm for the generalized Rosenbrock function,  $F_{Ros}$ , which is a standard test function, given by [34]:

$$F_{Ros} = \sum_{i=1}^{n-1} \left( 100(x_i^2 - x_{i+1})^2 + (x_i - 1)^2 \right) \quad (4.7)$$

where  $i$  is the index for the number of variables,  $n$  is the number of variables considered ( $n=5$  for the present example) and  $x_i$  are the value of variables. The function  $F_{Ros}$  has minimum at  $x_i = 1$  with  $F_{Ros} = 0$ . Fig. 4.2 shows the minimization of  $F_{Ros}$  with iterations for two cases, (i) when a random search was conducted with the initially guessed values of  $x_i$  lying in the range  $[-5,5]$ , and (ii) when some guidance was provided to the genetic algorithm by introducing an initially guessed value of  $x_i = 0.7$ , which is close to the actual solution of  $x_i = 1$ . It can be seen in Fig. 4.2 that the guided search converges much faster than the random search. Therefore, in the present study, if some initial guidance is provided to the genetic algorithm by using the gradient based techniques, which rapidly decrease the error in the beginning, then the genetic algorithm can search for the global minima in much less time. Thus, a hybrid optimization scheme is adopted in the present study.

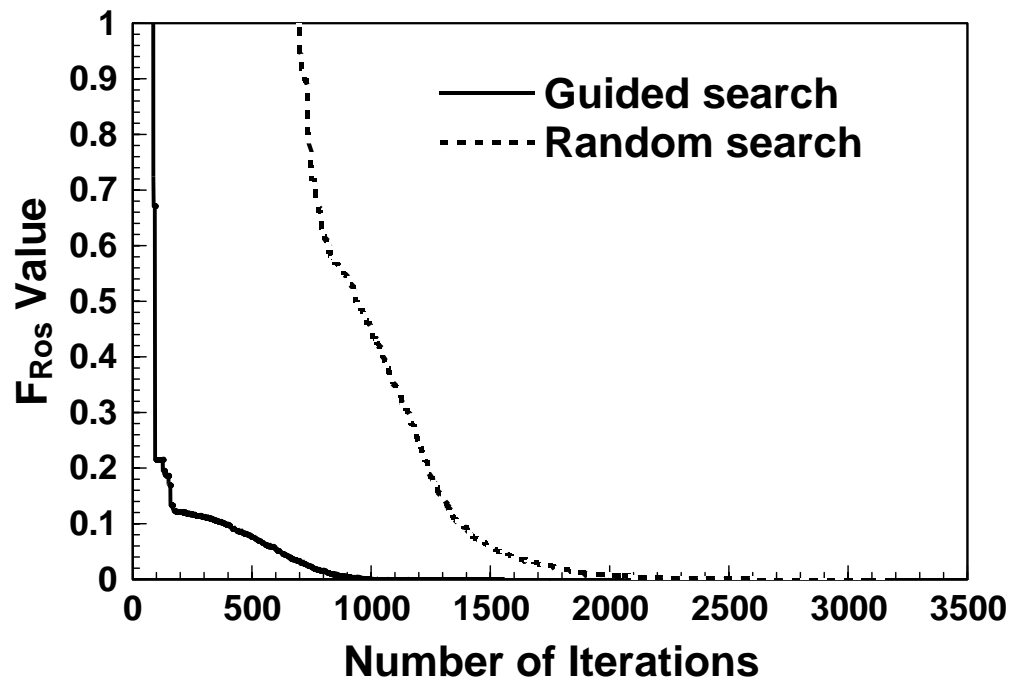


Fig. 4.2. The minimization of the generalized Rosenbrock function,  $F_{Ros}$ , given in Eq. (4.7), with iterations. Random search involved random initial guess, while guided search included an initial guess, which was close to the actual solution.

The genetic algorithm (GA) used in the present study is a parent centric recombination (PCX) operator based generalized generation gap (G3) model [33-35]. This model was chosen because it has been shown to have a faster convergence rate on standard test functions as compared to other evolutionary algorithms and classical optimization algorithms [34]. Detailed description of this model is available in the literature [33-38] and is not repeated here. To start with, many initial sets of randomly chosen values of weights were created. Five of these initial sets of weights were made equal to five different sets of weights calculated by the gradient descent algorithm. A systematic global search was next undertaken to find the most optimum set of weights that leads to the least mean square error (MSE), given in Eq. (4.4). The mean square error depends on the values of weights:

$$\text{MSE}(w) = \text{MSE}(w_1, w_2, \dots, w_q) \quad (4.8)$$

where  $q$  is the number of weights in the network. The GA produced new individuals, or sets of weights, with iterations based on evolutionary principles [34,35]. The specific application of G3-PCX model for obtaining the optimum set of weights is described as follows.

The algorithm for the model is as follows:

1. A population is a collection of many individuals and each individual represents a set of randomly chosen weights. A parent refers to an individual in the current population. The best parent is the individual that has the best fitness, i.e., gives the minimum value of the mean square error, defined by Eq. (4.4), in the entire population. The best parent and two other randomly selected parents are chosen from the population.
2. From the three chosen parents, two offsprings or new individuals are generated using a recombination scheme. PCX based G3 models are known to converge rapidly when three parents and two offsprings are selected [35]. A recombination scheme is a process for creating new individuals from the parents.
3. Two new parents are randomly chosen from the current population.
4. A subpopulation of four individuals that includes the two randomly chosen parents in step 3 and two new offsprings generated in step 2 is formed.

5. The two best solutions, i.e., the solutions having the least values of the mean square error, are chosen from the subpopulation of four members created in step 4. These two individuals replace the two parents randomly chosen in step 3.

6. The calculations are repeated from step 1 again until convergence is achieved.

The above steps, as applied to the present study, are shown in Fig. 4.3. The process of finding the optimum set of weights by minimizing the mean square error is illustrated in

Fig. 4.4. The recombination scheme (step 2) used in the present model is based on the PCX operator. A brief description of the PCX operator, as applied to the present problem of optimum set of weights, is presented below.

First three parents, i.e.,  $(w_1^0, w_2^0, \dots, w_q^0)$ ,  $(w_1^1, w_2^1, \dots, w_q^1)$ ,  $(w_1^2, w_2^2, \dots, w_q^2)$  are randomly selected from the current population. Here, the subscripts represent the  $q$  weights of the neural network, while the superscripts denote the parent identification number. The vector,  $\bar{g} = \left( \frac{w_1^0 + w_1^1 + w_1^2}{3}, \frac{w_2^0 + w_2^1 + w_2^2}{3}, \dots, \frac{w_q^0 + w_q^1 + w_q^2}{3} \right)$ , i.e., the mean vector or centroid of the three chosen parents is computed. To create an offspring, one of the parents, say  $\bar{x}^{(\text{par})} = (w_1^0, w_2^0, \dots, w_q^0)$  is chosen randomly. The direction vector,  $\bar{d}^{(\text{par})} = \bar{x}^{(\text{par})} - \bar{g}$ , is next calculated from the selected parent to the mean vector or centroid. Thereafter, from each of the other two parents, i.e.,  $(w_1^1, w_2^1, \dots, w_q^1)$  and  $(w_1^2, w_2^2, \dots, w_q^2)$ , perpendicular distances,  $D_i$ , to the direction vector,  $\bar{d}^{(\text{par})}$ , are computed and their average,  $\bar{D}$ , is found. Finally, the offspring, i.e.,  $\bar{y} = (w_1', w_2', \dots, w_q')$ , is created as follows:

$$\bar{y} = \bar{x}^{(\text{par})} + v_\zeta \left| \bar{d}^{(\text{par})} \right| + \sum_{i=1, i \neq \text{par}}^q v_\eta \bar{D} \bar{h}^{(i)} \quad (4.9)$$

where  $\bar{h}^{(i)}$  are the orthonormal bases that span the subspace perpendicular to  $\bar{d}^{(\text{par})}$ , and  $v_\zeta$  and  $v_\eta$  are randomly calculated zero-mean normally distributed variables.

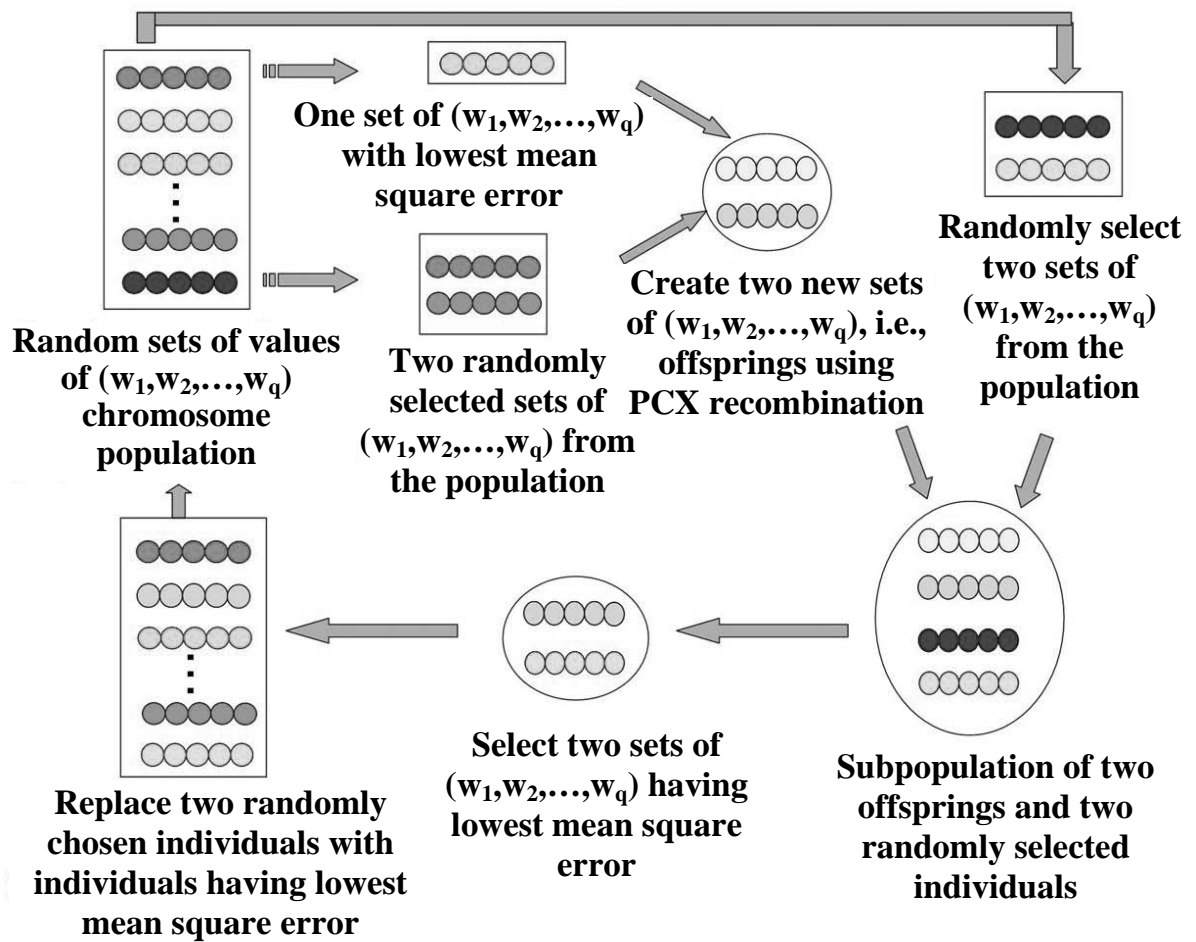


Fig. 4.3. Generalized generation gap (G3) genetic algorithm using parent centric recombination (PCX) operator.

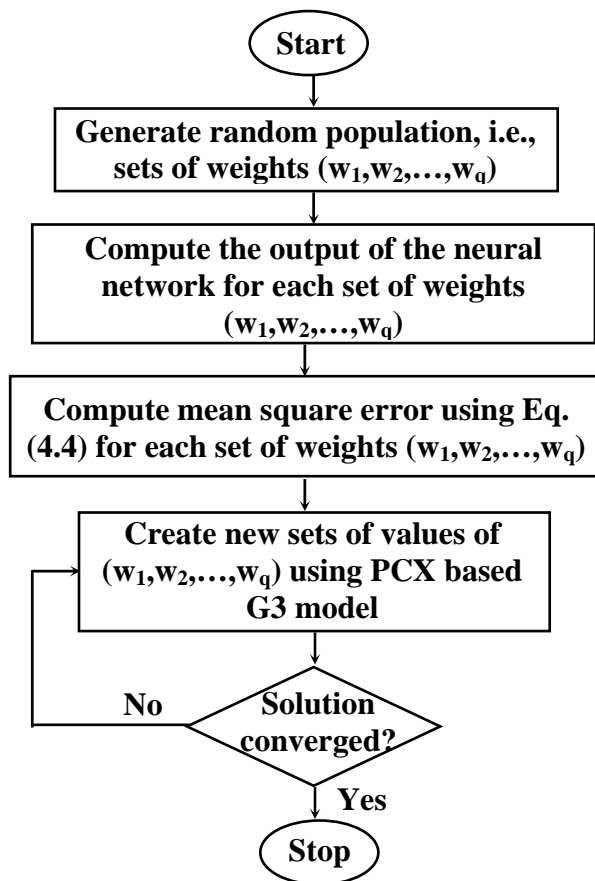


Fig. 4.4. Flow chart of the generalized generation gap (G3) model.

The values of the variables that characterize the offspring,  $\bar{y} = (w'_1, w'_2, \dots, w'_q)$ , are calculated next. As an example, only the calculation of  $w'_1$  and  $w'_2$  will be described here:

$$w'_1 = w_1^0 + w_{11} + w_{12} \quad (4.10)$$

$$w'_2 = w_2^0 + w_{21} + w_{22} \quad (4.11)$$

where,

$$w_{11} = v_\zeta \left( \frac{2w_1^0 - w_1^1 - w_1^2}{3} \right) \quad (4.12)$$

$$w_{21} = v_\zeta \left( \frac{2w_2^0 - w_2^1 - w_2^2}{3} \right) \quad (4.13)$$

$$w_{12} = v_\eta \left( \frac{a_2 + b_2}{2} \right) \left[ 1 - \left( \frac{2w_1^0 - w_1^1 - w_1^2}{3d} \right)^2 \right] \quad (4.14)$$

$$w_{22} = v_\eta \left( \frac{a_2 + b_2}{2} \right) \left[ 1 - \left( \frac{2w_2^0 - w_2^1 - w_2^2}{3d} \right)^2 \right] \quad (4.15)$$

The expressions for the variables  $d$ ,  $a_2$ , and  $b_2$ , used in Eqs. (4.14) and (4.15), are as follows:

$$d = \sqrt{\left( \frac{2w_1^0 - w_1^1 - w_1^2}{3} \right)^2 + \left( \frac{2w_2^0 - w_2^1 - w_2^2}{3} \right)^2 + \dots + \left( \frac{2w_q^0 - w_q^1 - w_q^2}{3} \right)^2} \quad (4.16)$$

$$a_2 = e_1 \times \sqrt{1 - (a_1)^2} \quad (4.17)$$

$$b_2 = e_2 \times \sqrt{1 - (b_1)^2} \quad (4.18)$$

$$a_1 = \sum_{i=1}^q \frac{(w_i^1 - w_i^0) \left( \frac{2w_i^0 - w_i^1 - w_i^2}{3} \right)}{d \times e_1} \quad (4.19)$$

$$e_1 = \sqrt{(w_1^1 - w_1^0)^2 + (w_2^1 - w_2^0)^2 + \dots + (w_q^1 - w_q^0)^2} \quad (4.20)$$

$$b_1 = \sum_{i=1}^q \frac{(w_i^2 - w_i^0) \left( \frac{2w_i^0 - w_i^1 - w_i^2}{3} \right)}{d \times e_2} \quad (4.21)$$

$$e_2 = \sqrt{(w_1^2 - w_1^0)^2 + (w_2^2 - w_2^0)^2 + \dots + (w_q^2 - w_q^0)^2} \quad (4.22)$$

## 4.2 Calculation Procedure

Neural networks require a large database for training and testing. The number of training datasets should be more than the number of weights connecting different nodes. For a single hidden layer network, the number of weights,  $q$ , is given as:

$$q = (n_i + 1) \times n_h + (n_h + 1) \times n_o \quad (4.23)$$

where  $n_i$  is the number of input variables, i.e., 17 in the present work,  $n_h$  is the number of nodes in the hidden layer and  $n_o$  is the number of output variables, i.e., 1. For double hidden layer network:

$$q = (n_i + 1) \times n_h + (n_{h1} + 1) \times n_{h2} + (n_{h2} + 1) \times n_o \quad (4.24)$$

where  $n_{h1}$  and  $n_{h2}$  are the number of nodes in hidden layers 1 and 2, respectively. Since the number of weights increases with the increase in the number of hidden layers, an optimal number of hidden layers are needed.

### 4.2.1 Number of hidden layers in the network

Number of hidden layers in neural network depends on the type of problem and the relationships between the input and the output variables represented through the objective function. Theoretically, any continuous variation of output with respect to input can be represented by a single hidden layer [39,40]. Two hidden layers are needed when the relationship between the input and the output variables are discontinuous [39,40]. The use of more than optimal number of hidden layers in the network may result in undesirable over-fitting of the data [27,39,40]. A single hidden layer was used since the outputs are continuous in nature in the GTA welding.

#### 4.2.2 Database generation

A database for training of the neural networks was generated to capture the effects of all the welding variables and material properties. Out of the 17 input variables in GTA welding, 10 most important variables that affect the output significantly include current, voltage, welding speed, arc radius, arc power distribution factor, arc efficiency, effective thermal conductivity of liquid, effective viscosity of liquid, thermal conductivity of solid, and the concentration of sulfur. The complex interactions between these 10 variables were captured by making 1250 different runs of the three dimensional numerical transport phenomena based model considering about 10 different values of each variable. The effect of the remaining variables such as density, specific heat of the solid, specific heat of the liquid, etc. was captured by making 500 different runs of the numerical transport phenomena based model considering about 6 different values of each variable. Considering sufficient number of different values of the variables increases the degrees of freedom and helps to capture the effect of the variables, which have large influence on the weld geometry and cooling rate. Out of the 1750 total runs conducted, 1250 datasets were included in the training dataset and the remaining 500 datasets formed the testing dataset for the validation of the neural network. Thus, the combinations of the values of variables in the testing datasets were completely different from those in the training datasets. The 17 input variables and their ranges of values used for the generation of datasets are shown in Table 4.1. The ranges of values of the input variables correspond to the GTA welding of stainless steel. Furthermore, Fig. 4.5 shows that the different values considered for each variable are well distributed about the mean value for the variable, which ensures that the effect of almost the entire range of values for each variable can be taken into account in the datasets.

Table 4.1. The input variables and their ranges of values considered in the training datasets.

Variables	Minimum value	Maximum value
Arc current, I (A)	9.00E+01	2.50E+02
Voltage, V (V)	9.60E+00	2.60E+01
Arc efficiency, $\eta$	3.50E-01	8.50E-01
Arc radius, r (m)	1.00E-03	2.90E-03
Arc power distribution factor, d	5.00E-01	3.00E+00
Welding speed, U (m/s)	1.00E-03	1.00E-02
Density of liquid, $\rho$ (kg/m <sup>3</sup> )	6.60E+03	7.80E+03
Effective viscosity of liquid, $\mu$ (kg/m-s)	6.00E-02	1.00E-01
Liquidus temperature, $T_l$ (K)	1.73E+03	1.77E+03
Solidus temperature, $T_s$ (K)	1.785E+03	1.845E+03
Enthalpy of solid at melting point, $H_s$ (J/kg)	1.05E+06	1.15E+06
Enthalpy of liquid at melting point, $H_l$ (J/kg)	1.32E+06	1.42E+06
Specific heat of solid, $C_{ps}$ (J/kg-K)	6.27E+02	7.86E+02
Specific heat of liquid, $C_{pl}$ (J/kg-K)	7.74E+02	8.99E+02
Thermal conductivity of solid, $k_s$ (J/m-s-K)	2.30E+01	3.97E+01
Effective thermal conductivity of liquid, $k_l$ (J/m-s-K)	8.36E+01	5.02E+02
Concentration of sulfur in steel, $C_s$ (wt%)	0.00E+00	3.50E-01

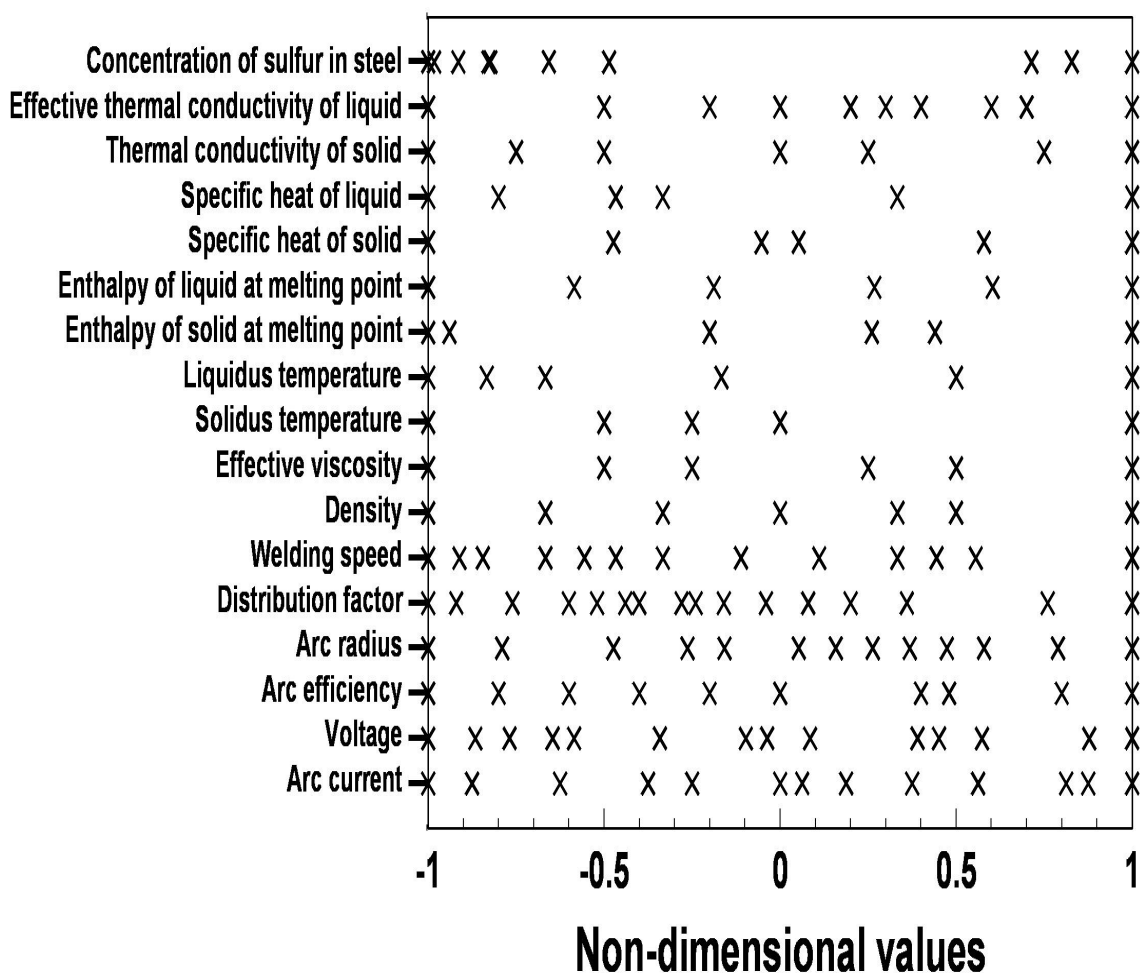


Fig. 4.5. The ranges of values of the input variables in the training and testing datasets. The normalized values of the variables were obtained using Eq. (4.25) and corresponding minimum and maximum values listed in Table 4.1.

### 4.2.3 Normalizing inputs and outputs

There is significant variation in the scales of values of the input and output variables. The vastly different scales of inputs and bias values lead to ill-conditioning of the problem [27,28]. While large inputs cause ill-conditioning by leading to very small weights, large outputs do so by leading to very large weights [27,28]. To eliminate the ill-conditioning problem, the data was normalized using the following formula [27,28]:

$$x' = 2 \times \left( \frac{x - x_{\min}}{x_{\max} - x_{\min}} \right) - 1 \quad (4.25)$$

where  $x$  is the original value of the variable,  $x'$  is the normalized value, while  $x_{\min}$  and  $x_{\max}$  represent the minimum and maximum values of the variable in all the datasets. Equation (4.25) normalizes the data in the range of -1 to 1. The range of values of all input and output parameters from -1 to +1 implies that the standard deviation cannot exceed 1, while its symmetry about zero means that the mean will typically be relatively small. Furthermore, its maximum derivative is also 1.5, so that back-propagated errors will be neither magnified nor attenuated more than necessary [27,28].

### 4.2.4 Selection of initial weights

In the back-propagation algorithm, the magnitude of the error propagated backward through the network is proportional to the value of the weights. If all the weights are the same, the back propagated errors will be the same, and consequently all of the weights will be updated by the same amount [27,28]. To avoid this symmetry problem, the initial weights of the network were selected randomly. Furthermore, to avoid the premature saturation of the network, the initial values of the weights were distributed inside a small range of values, i.e., in the interval [-0.5, 0.5]. When the weights are small, the units operate in the linear regions of the transfer function and consequently the transfer function does not saturate.

The calculation starts with the selection of number of nodes in the hidden layer. The total number of weights in the network depends upon the number of nodes in the hidden layer. The weights are then initialized randomly in the interval [-0.5, 0.5]. In the next step, a back-propagation algorithm is used to minimize the error on the training

dataset. The optimized weights calculated by the gradient descent method are stored as one possible set of weights. This process is repeated 5 times with different randomly selected initial weights for fixed values of nodes in the hidden layer for each output variable. All of these five optimized sets of weight are provided as input to the GA. The final aim of the GA is to find the weights in the network through a systematic global search that will give the least error between the neural network prediction and numerical transport phenomena based calculations. The flowchart of the calculation scheme is presented in Fig. 4.6. The convergence is based on the error in training and testing data. When the error during testing starts increasing, the calculation is stopped to avoid over-fitting even if the error with training dataset decreases with further iterations.

### **4.3 Results and Discussion**

#### **4.3.1 Structure chosen for the neural networks**

The selection of suitable network architecture is important as it affects the network's convergence as well as the accuracy of predictions [6]. The number of nodes in the hidden layer were varied to get an optimum number of nodes that resulted in minimum mean square error (MSE) defined in Eq. (4.4). The average MSE of five runs made with different initial random weights is plotted in Fig. 4.7 for different number of nodes in the hidden layer. The results are for all the six neural networks with different output variables, and the runs were conducted using the gradient descent method. Fig. 4.7 shows that for all the six neural networks the average MSE decreases with increase in the number of hidden nodes. For the neural networks with weld pool depth, width, and length, and cooling time from 800°C to 500°C, the MSE becomes almost constant for more than 14 hidden nodes in the network. Even for the neural networks with peak temperature and maximum velocity as the output variables, the decrease in MSE on increasing the number of hidden nodes above 14 is rather insignificant. Therefore, networks with 14 nodes in the hidden layer were used in the present study.

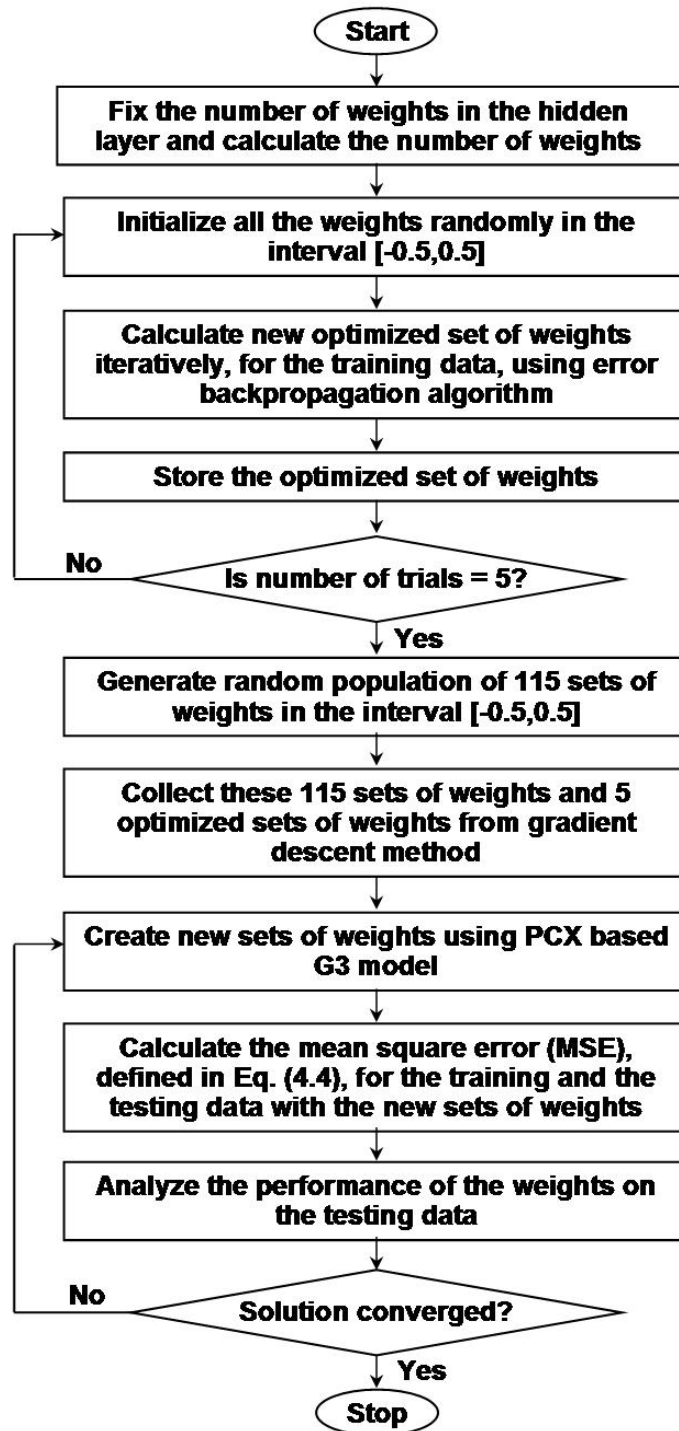


Fig. 4.6. Flowchart for training the neural network.

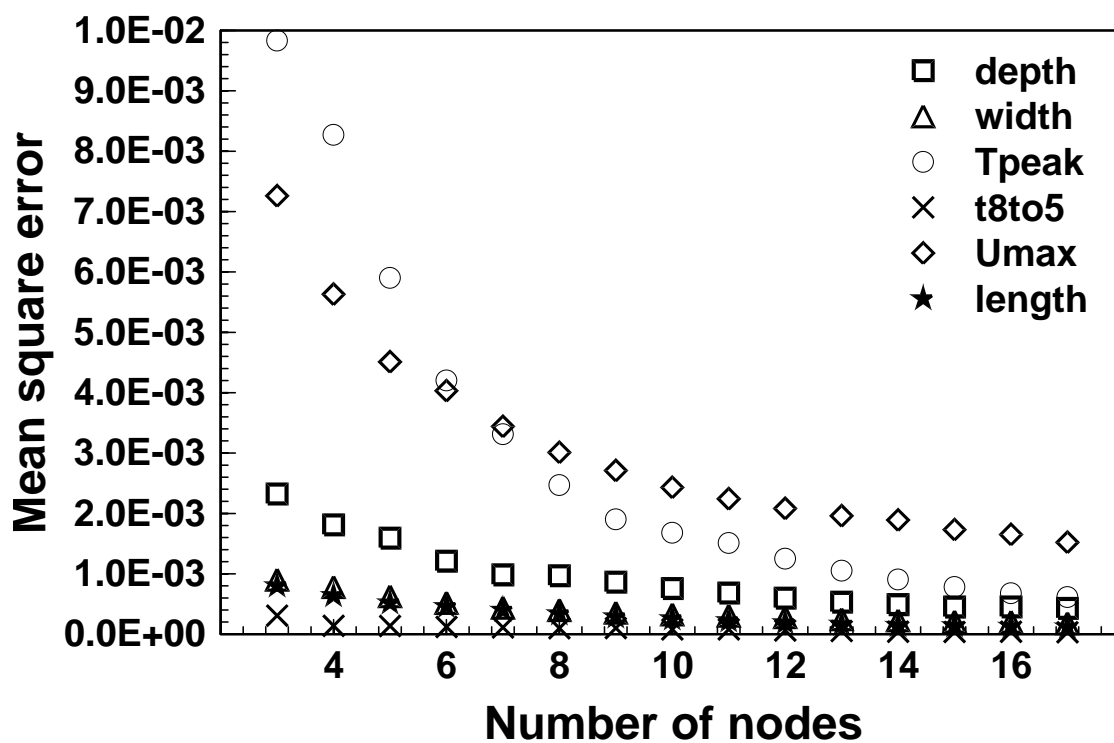


Fig. 4.7. Comparison of mean square error (MSE), defined by Eq. (4.4), for different number of nodes in the hidden layer. For each output variable the results are an average of five runs, with different sets of initial random weights, using the gradient descent training method. The number of iteration for each run were 5000.

### 4.3.2 Gradient descent versus hybrid training approach

As described earlier in the section on mathematical modeling, the neural network model developed in the present study uses a combined gradient descent and genetic algorithm (hybrid) training approach. The initial guidance is provided by gradient descent algorithm and then the GA finds the global minimum of the mean square error (MSE) to provide a well trained network. The neural networks were first trained on the training dataset of 1250 input-output pairs using the gradient descent method. Since the output of this method depends on the initial set of guessed weights, five sets of initial random weights were used. In order to assess the performance of the gradient descent method, the decrease of MSE with iterations is plotted for all the six neural networks in Fig. 4.8. Each plot represents an average of five runs with different random initial weights in order to avoid any local optimal solution. It can be seen that in all the cases the error decreases very rapidly for the first 2000 iterations, but after that further decrease is very slow. Since further improvement in error was very slow and insignificant, the training of the network using the gradient descent method was stopped after 5000 iterations. The MSE values for the six neural networks, after training by the gradient descent method for 5000 iterations, have been listed in Table 4.2.

Table 4.2. Comparison of the mean square error (MSE), defined in Eq. (4.4), for the gradient descent method and the hybrid training approach. The results for the gradient descent method were taken after 5000 iterations.

Output variable	MSE Gradient descent	MSE Hybrid approach
Weld pool depth (mm)	$5.37 \times 10^{-4}$	$1.50 \times 10^{-4}$
Weld pool width (mm)	$3.39 \times 10^{-4}$	$6.77 \times 10^{-5}$
Weld pool length (mm)	$2.80 \times 10^{-4}$	$4.00 \times 10^{-5}$
Peak temperature (K)	$1.17 \times 10^{-3}$	$1.87 \times 10^{-4}$
Cooling time 800°C to 500°C (s)	$1.50 \times 10^{-4}$	$3.89 \times 10^{-6}$
Maximum velocity (mm/s)	$2.69 \times 10^{-3}$	$9.99 \times 10^{-4}$

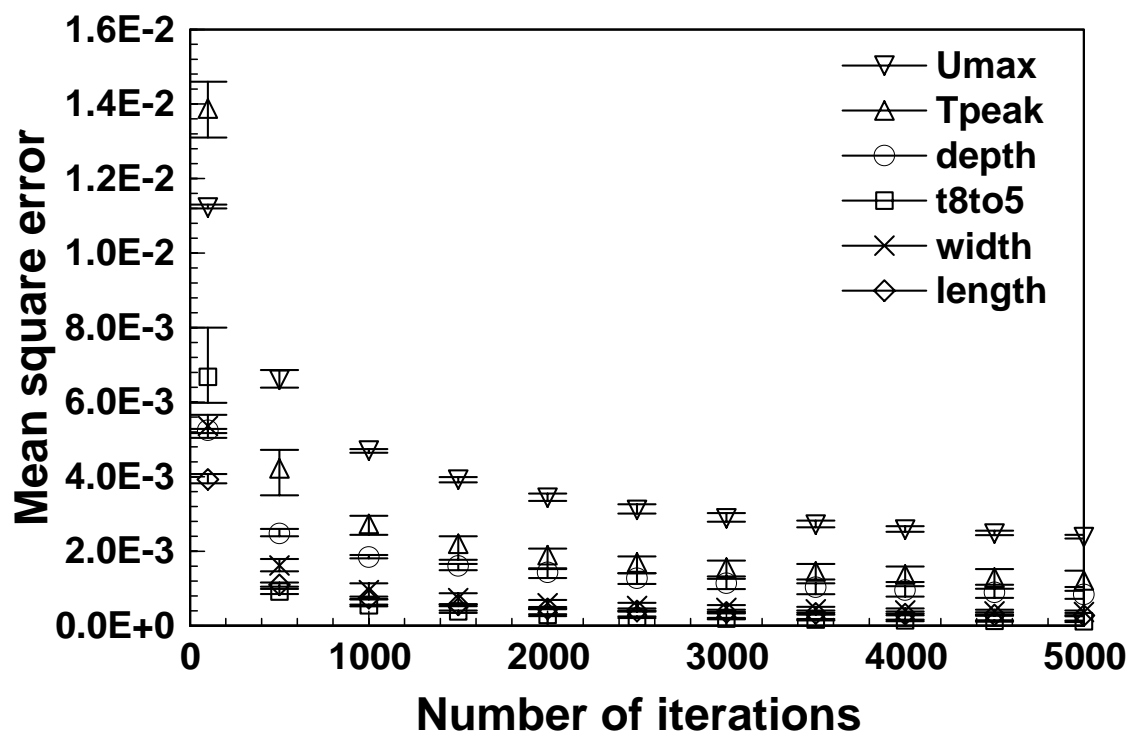


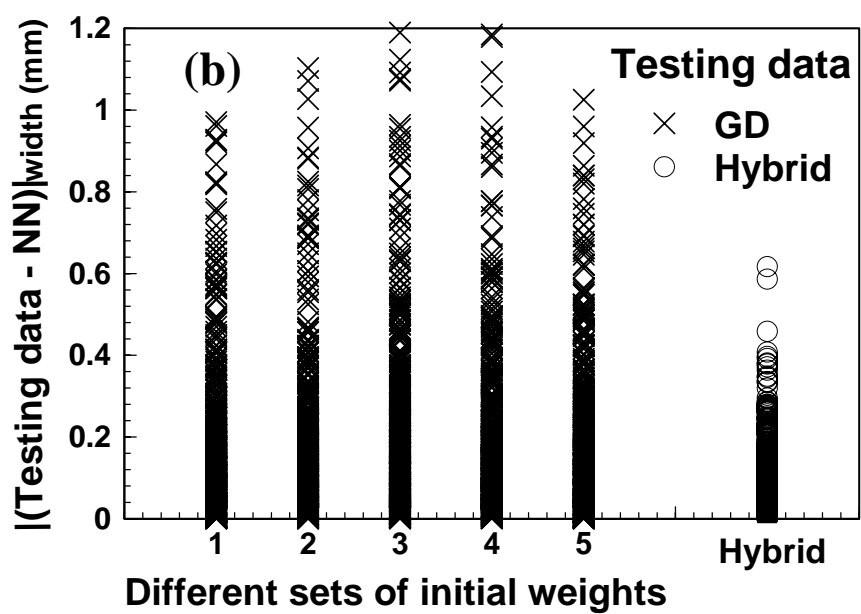
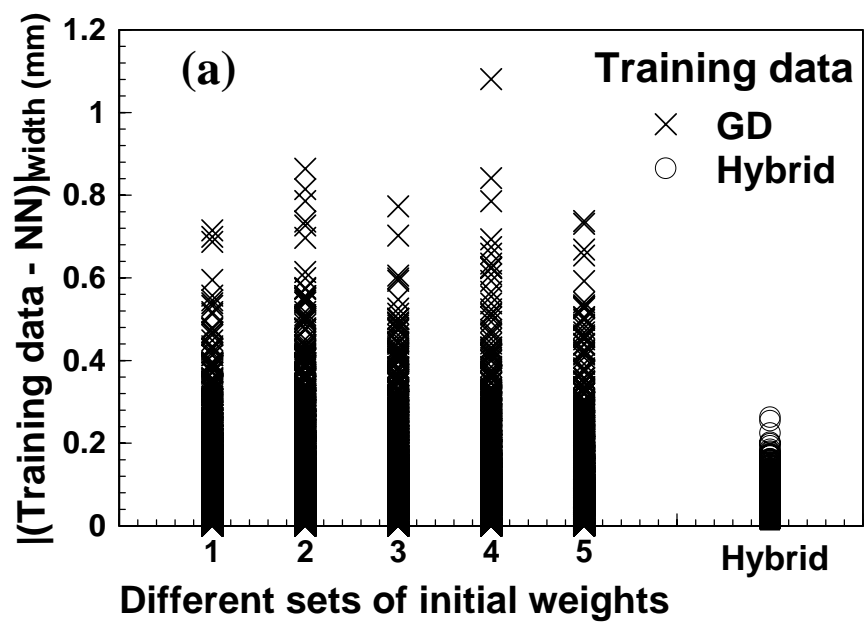
Fig. 4.8. Mean square error (MSE), defined by Eq. (4.4), versus number of iterations for the gradient descent training method. For each output variable five runs were conducted with different sets of initial random weights. The error bars show the variation of MSE values over the five runs.

Now, to test the performance of the hybrid approach, the five sets of weights calculated after 5000 iterations of the gradient descent method, were given as inputs to the genetic algorithm (GA). Adding these sets of weights to the initial population of GA ensures the presence of five sets of near optimum weights within the starting population, and helps in finding the global solutions more efficiently. Two convergence criteria were used. The first criterion required the training to stop if the mean square error (MSE) became less than  $1.0 \times 10^{-6}$ , which is a low enough acceptable error for the problem at hand. For example, for an input depth value of 2.5 mm, the MSE of  $1.0 \times 10^{-6}$  in the non-dimensionalized depth value would correspond to an actual error of 0.004 mm, which is very small. The second criterion was based on the concern of over-fitting of the neural network [4,20,22,27]. During training of the neural network, the error on the training data is driven to a very small value, but when new data are presented to the network, the error is large. This means that the network has memorized the training examples, but it has not learned to generalize to new situations [20]. A common method of avoiding this problem is that while training the network, its performance is simultaneously tested on a set of testing data. The training of the network is stopped as soon as the mean square error in the testing data starts increasing. This was set as the second convergence criterion in the present study in order to avoid over-fitting of the neural network. The testing dataset consists of 500 input-output pairs, and the ranges of values of the input and output parameters lie within their ranges of values given in Table 4.1. The GA found the global set of weights giving much improved mean square errors as listed under hybrid approach in Table 4.2. It can be seen that the MSEs for all the neural networks using the hybrid approach are much better than those obtained using gradient descent method alone.

To further compare the performance of the gradient descent and the hybrid approaches, the five sets of weights provided by the gradient descent approach and the global set of weights provided by the hybrid approach, were used to calculate the respective output variable values from the neural network for the training and the testing datasets. Fig. 4.9(a) shows the absolute value of the difference between the training data and the corresponding results from neural network, for weld pool width as the output variable, while Fig. 4.9(b) shows similar plot for testing data. Fig. 4.9(c) and (d) show

similar plots for peak temperature as the output variable. These plots contain results for the five sets of weights obtained using the gradient descent method and the global set of weights obtained using the hybrid approach. It can be seen that in all the cases the weights from the hybrid approach provide results that fit much better to both the training and the testing data. The results obtained by using the weights from gradient descent method have much more scatter as compared to those obtained from hybrid approach. Similar results were obtained for other output variables as well. Thus, the hybrid approach provides a well trained network with global optimal weights, where the output from the trained neural network can accurately map the inputs to the outputs.

The values of the five set of weights from gradient descent method and those from hybrid approach have been plotted in Fig. 4.10(a) and (b) for output variables of weld pool depth and maximum liquid velocity, respectively. It can be seen that the weights from the gradient descent method are mostly confined to a narrow range of  $[-1.0, 1.0]$ , which is very close to their initial range of  $[-0.5, 0.5]$ , while the weights from the hybrid approach are scattered in a much wider area. For example, the global set of weights for weld pool depth lie in the range of  $[-8.0, 6.0]$  and those for maximum liquid velocity lie in the range of  $[-7.0, 4.0]$ . This means that in the hybrid approach, the genetic algorithm (GA) explored a much wider search area, irrespective of the initial guessed values, and was able to find the global optimal weights. Thus, the hybrid approach conducts a more thorough search of the possible search space, and provides a better trained network.



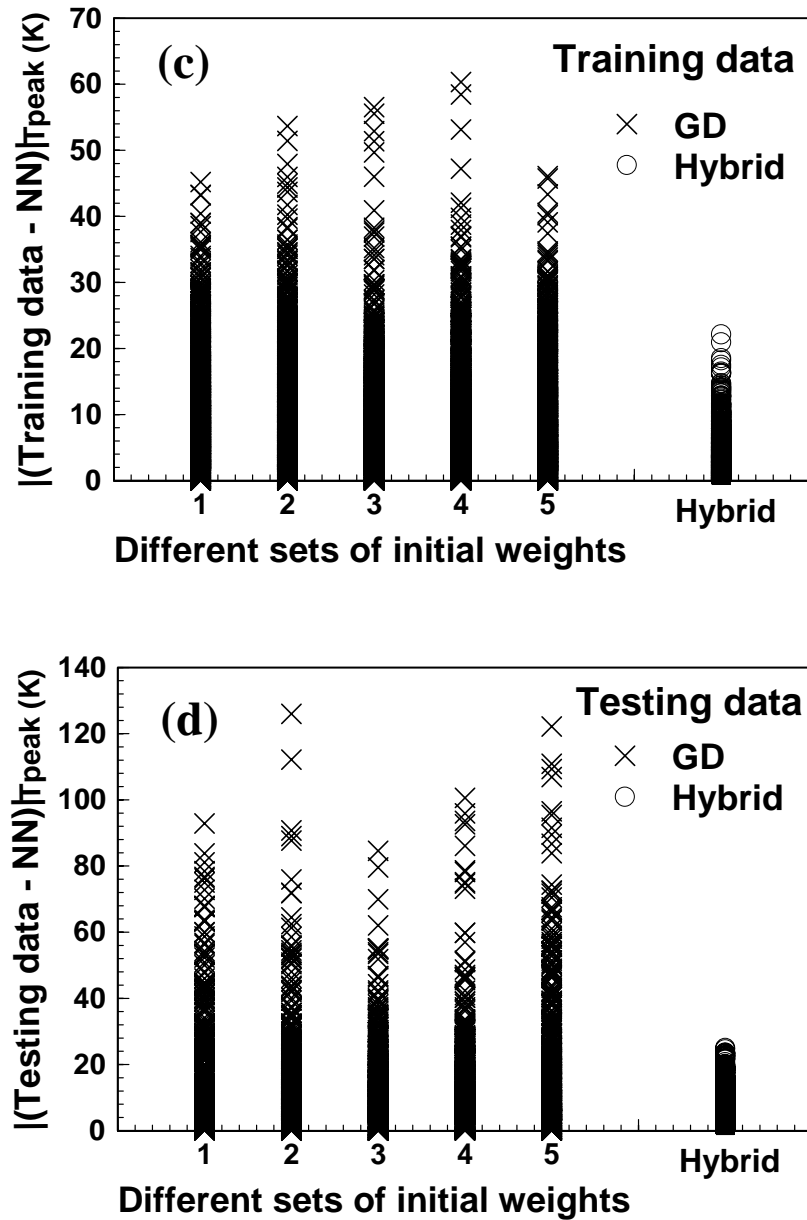


Fig. 4.9. Absolute value of the difference between (a) the weld pool width in the training data and that calculated from neural network (NN); (b) the weld pool width in the testing data and that calculated from neural network (NN); (c) the peak temperature in the training data and that calculated from neural network (NN); and (d) the peak temperature in the testing data and that calculated from neural network (NN). The results are for the five sets of weights calculated by gradient descent (GD) method, and the global set of weight calculated by the hybrid approach.

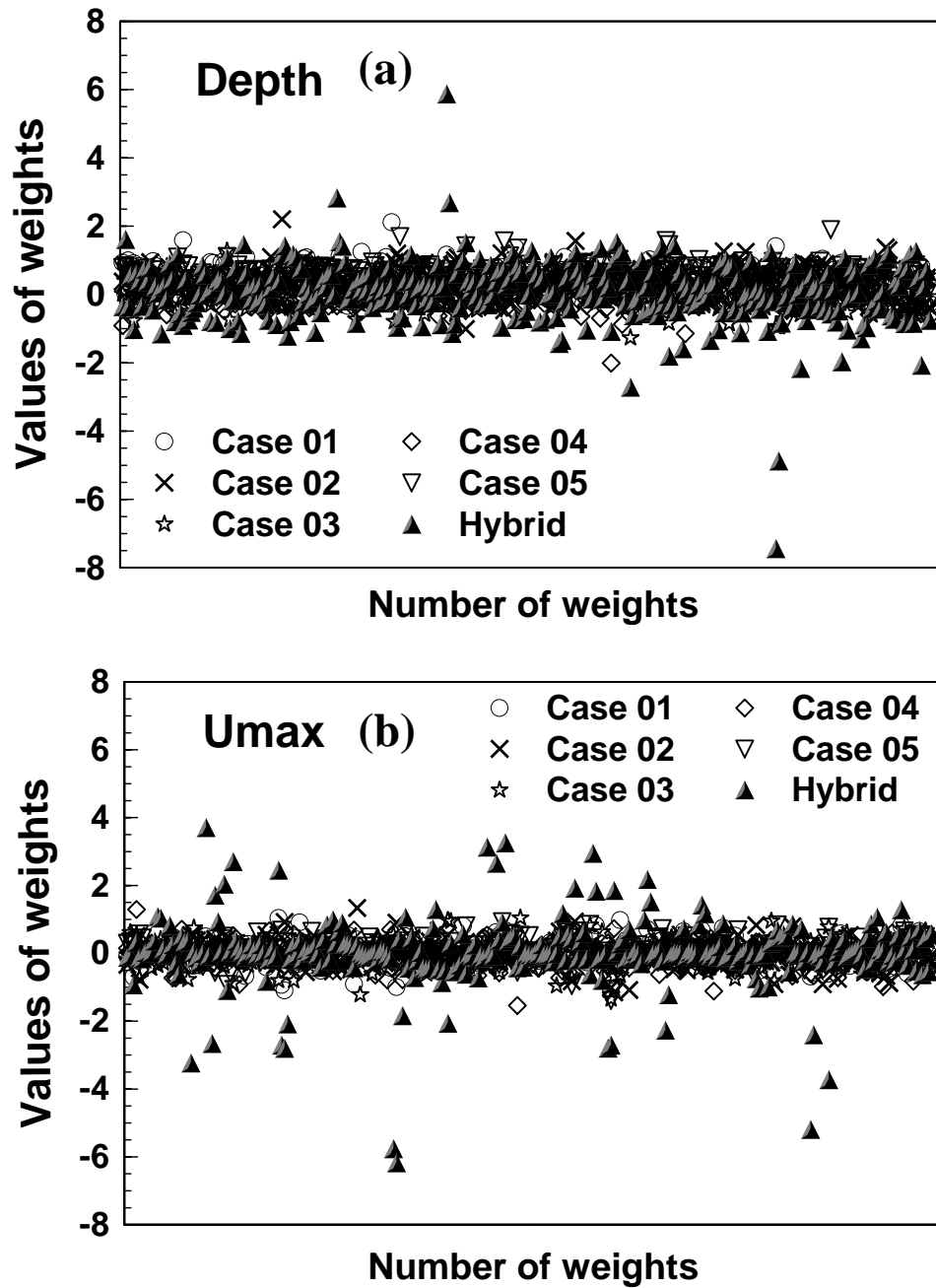


Fig. 4.10. Comparison of the values of weights for the gradient descent and hybrid training approaches for (a) weld pool depth, and (b) maximum liquid velocity in the weld pool. Cases 01 to 05 are for the five sets of weights obtained from gradient descent method when using five different sets of initial random weights.

### 4.3.3 Evaluating the predicting capability of the neural networks

Six neural networks have been developed, each providing a specific output, i.e., depth, width and length of the weld pool, peak temperature, cooling time between 800°C and 500°C or maximum liquid velocity in the weld pool. The predicting capability of the neural networks is illustrated in Fig. 4.11 and Fig. 4.12, which compare the output parameters calculated by the model with their corresponding values provided in the training and the testing datasets. Fig. 4.11(a) and (b) compare the weld pool depth calculated by the neural network with that provided in the training and testing datasets, respectively. All points lie on or very close to the diagonal line and the results obtained from the neural network agree well with the values calculated using numerical transport phenomena based model. The MSE for the training dataset was  $1.5 \times 10^{-4} \text{ mm}^2$  and that for the testing dataset was  $5.0 \times 10^{-4} \text{ mm}^2$ , which was the least error that could be obtained on the testing dataset. To further evaluate the error in the values of weld pool depth provided by the neural network model, the absolute value of mean error, ME, between the target depth, i.e., the one given in the training and the testing datasets, and the depth calculated by the neural network is calculated as:

$$\text{ME} = \frac{1}{p} \sum_{i=1}^p |d_i - o_i| \quad (4.26)$$

where  $i$  is the index for the input dataset,  $p$  is the number of input datasets,  $d_i$  is the desired output and  $o_i$  is the output produced by the neural network. The ME for depth in the training dataset was 0.04 mm and that in the testing dataset was 0.07 mm, where a typical depth value for GTA welding of low carbon steel is 2.3 mm. Thus, the error in depth is well within the error limits for the process being considered.

In Fig. 4.11(a) the depth varies from 0.9 to 8.5 mm, depending on the values of the input process parameters and the material properties. This shows that the process parameters and material properties considered in the present study have a significant impact on the weld pool depth. The fact that the neural network model could accurately predict the depth values for all the cases in Fig. 4.11(a) and (b), indicates that it is capable

of accurately representing the results of the three-dimensional numerical transport phenomena based model for GTA welding.

Fig. 4.11(c) and (d) show similar results for weld pool width, and Fig. 4.11(e) and (f) show similar results for weld pool length. Similarly, the results for peak temperature are presented in Fig. 4.12(a) and (b), those for cooling time between 800°C and 500°C in Fig. 4.12(c) and (d), and those for maximum liquid velocity in the weld pool in Fig. 4.12(e) and (f). The corresponding MSEs and MEs are listed in Table 4.3. The MEs for the training data for weld pool width and length, peak temperature, cooling time between 800°C and 500°C and maximum liquid velocity in the weld pool are 0.05 mm, 0.05 mm, 4 K, 0.01 s and 5 mm/s, respectively. These MEs are quite small compared to the respective magnitudes of these output variables, which are also listed in Table 4.3. Though the MEs for the testing data were slightly higher than those for the training data in all the cases, the difference was not very significant as can be seen from Table 4.3. All the results indicate that the neural networks can accurately predict different features of weld pool geometry as well as the peak temperature and cooling time, and hence can be used for simulations with predetermined good accuracy.

Table 4.3. The mean square error (MSE), defined in Eq. (4.4), and mean error (ME), defined in Eq. (4.26), for the results of the neural network for the weld pool geometry, peak temperature, cooling time between 800°C and 500°C and maximum liquid velocity in the weld pool. The results were obtained using the hybrid training approach.

Output variable	MSE Training data	MSE Testing data	ME Training data	ME Testing data	Typical value in the data
Weld pool depth (mm)	$1.50 \times 10^{-4}$	$5.00 \times 10^{-4}$	0.04	0.07	2.3
Weld pool width (mm)	$6.77 \times 10^{-5}$	$3.24 \times 10^{-4}$	0.05	0.09	6.8
Weld pool length (mm)	$4.00 \times 10^{-5}$	$1.00 \times 10^{-4}$	0.05	0.09	8.7
Peak temperature (K)	$1.87 \times 10^{-4}$	$6.90 \times 10^{-4}$	4	8	2237
Cooling time 800°C to 500°C (s)	$3.89 \times 10^{-6}$	$1.57 \times 10^{-5}$	0.01	0.01	2.0
Maximum velocity (mm/s)	$9.99 \times 10^{-4}$	$3.72 \times 10^{-3}$	5	10	190

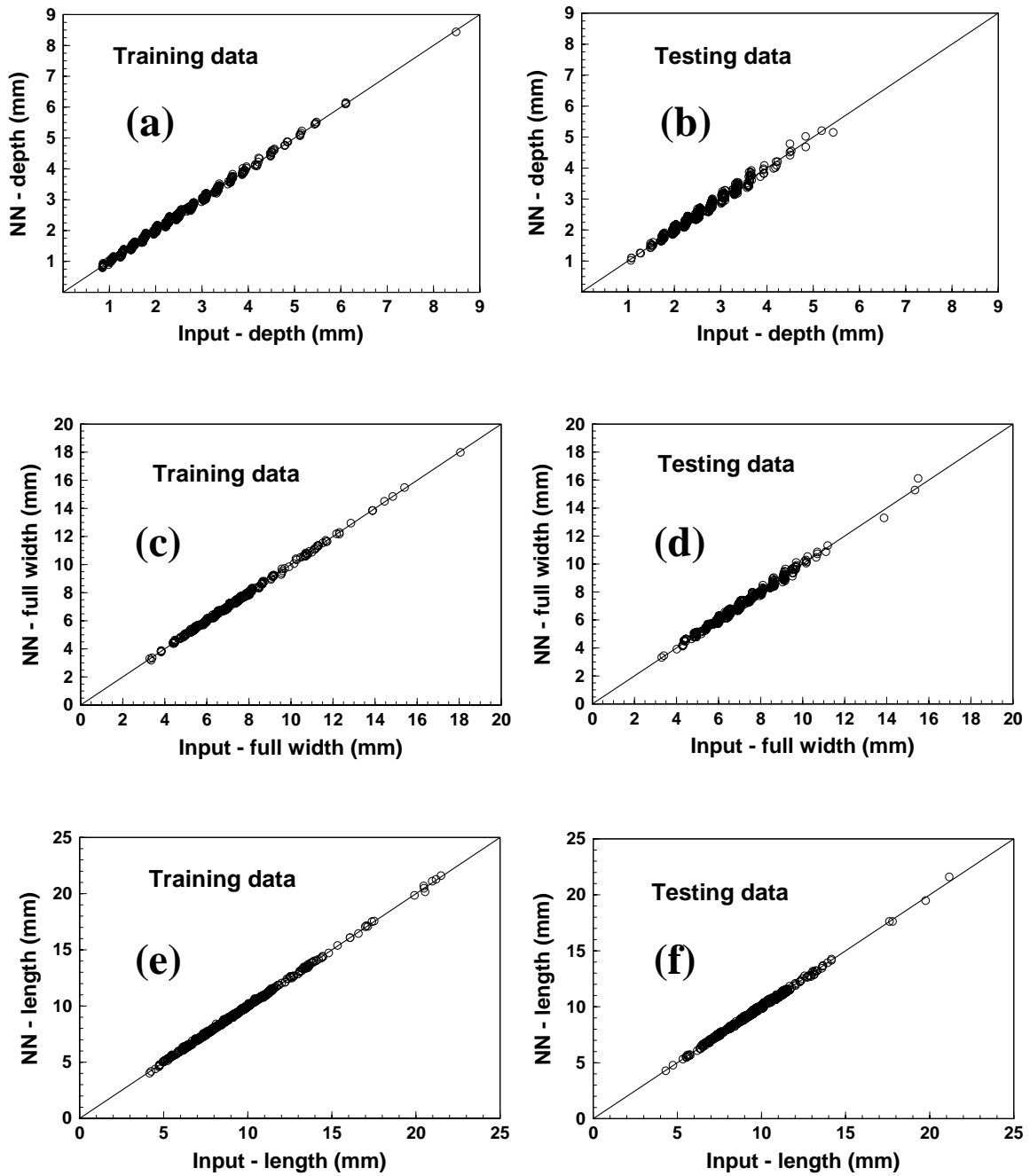


Fig. 4.11. Comparison of weld pool (a) and (b) depth, (c) and (d) width and (e) and (f) length calculated by the respective neural networks and those given in the training and the testing datasets, respectively.

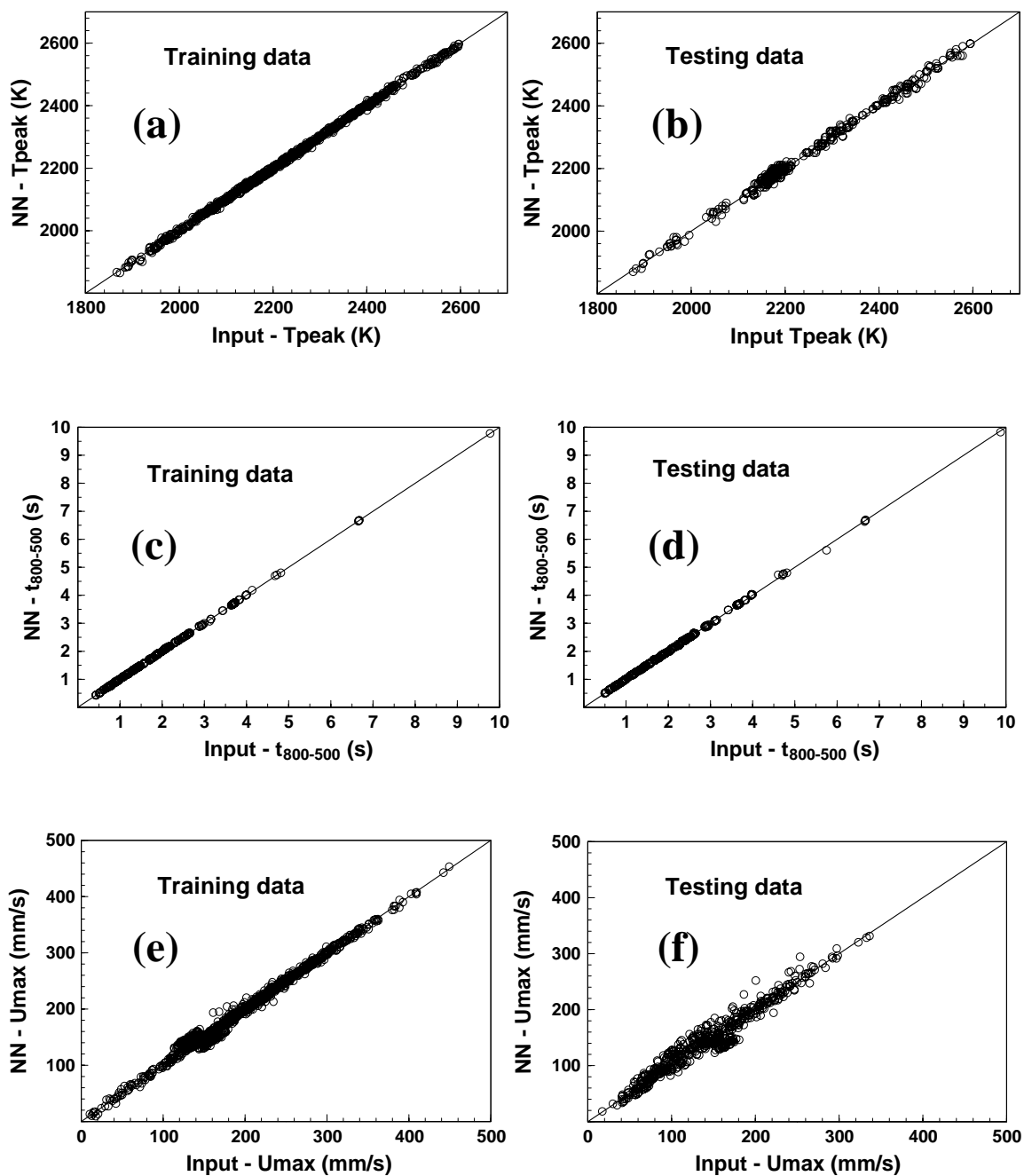


Fig. 4.12. Comparison of (a) and (b) peak temperature, (c) and (d) cooling time between 800°C and 500°C and (e) and (f) maximum liquid velocity in the weld pool calculated by the respective neural networks and those given in the training and the testing datasets, respectively.

#### **4.4 Summary and Conclusions**

Six neural networks have been developed for GTA welding of stainless steel. Each of these neural networks takes 17 input variables, which include welding process parameters and important material properties, and provides one output variable. The output variables include depth, width and length of the weld pool, peak temperature, cooling time from 800°C to 500°C and maximum liquid velocity in the weld pool. The networks were trained using a hybrid optimization scheme including the gradient descent method and a genetic algorithm. The hybrid approach gave lower errors than only the gradient descent method on both training and testing datasets, and the results did not depend on the initial choice of weights. The training and testing datasets contained results from the reliable numerical transport phenomena based model for GTA welding. The accurate prediction of these results by the neural networks ensured that the output of these networks complies with the phenomenological laws of welding physics.

#### 4.5 References

1. J. M. Vitek, Y. S. Iskander and E. M. Oblow, *Weld. J.* 79, 33s (2000).
2. J. M. Vitek, Y. S. Iskander and E. M. Oblow, *Weld. J.* 79, 41s (2000).
3. D. E. Rumelhart, G. E. Hinton and R. J. Williams, *Nature* 323, 533 (1986).
4. L. Burke and J. P. Ignizio, *J. Intelligent Manufacturing* 8, 157 (1997).
5. L. Fausett, *Fundamentals of Neural Networks* (Prentice-Hall, NJ, 1994).
6. I. S. Kim, J. S. Son, S. H. Lee and P. K. D. V. Yarlagadda, *Robotics Computer-Integrated Manufacturing* 20, 57 (2004).
7. I. S. Kim, J. S. Son and P. K. D. V. Yarlagadda, *Robotics Computer-Integrated Manufacturing* 19, 567 (2003).
8. D. S. Nagesh and G. L. Datta, *J. Mat. Process. Technol.* 123, 303 (2002).
9. H. K. D. H. Bhadeshia, D. J. Mackay and L. E. Svensson, *Mat. Sc. Technol.* 11, 1046 (1995).
10. P. Li, M. T. C. Fang and J. Lucas, *J. Mat. Process. Technol.* 71, 288 (1997).
11. Y. S. Tarng, H. L. Tsai and S. S. Yeh, *Int. J. Machine Tools & Manufacture* 39, 1427 (1999).
12. J.-Y. Jeng, T.-F. Mau and S.-M. Leu, *J. Mat. Process. Technol.* 99, 207 (2000).
13. E. A. Metzbower, J. J. Deloach, S. H. Lalam and H. K. D. H. Bhadeshia, *Sc. Technol. Weld. Joining* 6, 116 (2001).
14. I. S. Kim, Y. J. Jeong, C. W. Lee and P. K. D. V. Yarlagadda, *Int. J. Advanced Manufacturing Technol.* 22, 713 (2003).
15. K. Andersen, G. E. Cook, G. Karsai and K. Ramaswamy, *IEEE Trans. Ind. Appl.* 26, 824 (1990).
16. G. E. Cook, R. J. Barnett, K. Andersen and A. M. Strauss, *IEEE Trans. Ind. Appl.* 31, 1484 (1995).
17. H. Tsuei, D. Dunne and H. Li, *Sc. Technol. Weld. Joining* 8, 205 (2003).
18. J. Gao and C. Wu, *Sc. Technol. Weld. Joining* 8, 143 (2003).
19. I. S. Kim, S. H. Lee and P. K. D. V. Yarlagadda, *Sc. Technol. Weld. Join.* 8, 347 (2003).

20. H. Demuth and M. Beale, *Neural network tool box user's guide – Version 3.0* (Mathworks, Inc., MA, 1998).
21. S. C. Juang, Y. S. Tarn and H. R. Lii, *J. Mat. Process. Technol.* 75, 54 (1998).
22. J. M. Vitek, S. A. David, M. W. Richey, J. Biffin, N. Blundell and C. J. Page, *Sc. Technol. Weld. Joining* 6, 305 (2001).
23. K. Eguchi, S. Yamane, H. Sugi, T. Kubota and K. Oshima, *Sc. Technol. Weld. Joining* 4, 327 (1999).
24. X. Li, S. W. Simpson and M. Rados, *Sc. Technol. Weld. Joining* 5, 71 (2000).
25. E. A. Metzbower, J. J. Deloach, S. H. Lalam and H. K. D. H. Bhadeshia, *Sc. Technol. Weld. Joining* 6, 368 (2001).
26. A. Kumar and T. DebRoy, *J. Appl. Phys.* 94(2): 1267-1277 (2003).
27. S. Haykin, *Neural Networks – A Comprehensive Foundation – Edition 2* (Pearson Education, Singapore, 2001).
28. T. Masters, *Practical Neural Network Recipes in C++* (Academic Press, Boston, 1993).
29. B. L. Kalman and S. C. Kwasny, *Proceedings of the International Joint Conference on Neural Networks - Volume 4* (Baltimore, 1992) pp. 578-581.
30. N. K. Bose and P. Liang, *Neural Network Fundamentals with Graphs, Algorithms, and Applications* (McGraw-Hill, New York, 1996).
31. P. K. D. V. Yarlagadda, *Proc. Inst. Mech. Engineers B - J. Engineering Manufacture* 215, 1465 (2001).
32. S. H. Huang and H. C. Zhang, *Computers in Industry* 26, 107 (1995).
33. A. Kumar, S. Mishra, J. W. Elmer and T. DebRoy, *Metall. Mat. Trans. A* 36, 15 (2005).
34. K. Deb, A. Anand and D. Joshi, *Evolutionary Computation* 10, 371 (2002).
35. K. Deb, *Multi-Objective Optimization Using Evolutionary Algorithms - Edition 1* (Wiley, New York, 2001).
36. S. Mishra and T. DebRoy, *J. Phys. D: Appl Phys.* 38, 2977 (2005).
37. S. Mishra and T. DebRoy, *J. Appl. Phys.* 98, 044902 (2005).
38. A. Kumar and T. DebRoy, *Metall. Mat. Trans. A* 36, 2725 (2005).

39. R. P. Lippmann, IEEE Acoustics, Speech, Signal Process. Mag. 3, 4 (1987).
40. J. Makhoul, A. El-Jaroudi and R. Schwartz, *Proc. Int. Joint Conf. Neural Networks - Volume 1* (Washington DC, 1989) pp. 455-460.

## Chapter 5

### **Tailoring Weld Geometry Using a Genetic Algorithm and a Neural Network Trained with Numerical Transport Phenomena Based Calculations**

Weld attributes like geometry and cooling rate are strong functions of the welding process parameters such as arc current, voltage and welding speed. A specific weld pool geometry can be produced using multiple sets of these welding variables, i.e., different combinations of arc current, voltage and welding speed [1]. The available numerical transport phenomena based models are unidirectional in nature, i.e., they are designed to calculate temperature and velocity fields for a given set of welding variables. In other words, they cannot predict the welding variables needed to achieve a target weld geometry [1] or other weld attributes. Furthermore, these models are comprehensive and require significant amount of computer time to run. For example, the computational methodology described in Chapter 3, for finding the optimized values of the uncertain input parameters of the numerical transport phenomena based model, required more than 200 runs of the numerical model, and it took several days to do these many runs. At present, there is no systematic methodology that can determine, in a realistic time frame, such as a few minutes, the multiple sets of welding variables to achieve a specified weld geometry based on scientific principles.

Three main requirements need to be satisfied by a model for systematic tailoring of a weld attribute such as weld geometry based on scientific principles. First, the model should be capable of capturing all the major complex physical processes occurring during the gas tungsten arc (GTA) welding. Second, the model must have a bi-directional capability. In other words, in addition to the capability of the traditional unidirectional, forward models to compute the weld shape and size from a given set of welding variables, it should also have the inverse modeling ability, i.e., it should be able to systematically predict welding variables needed to produce a target weld geometry. Finally, the model must be able to determine various welding variable sets needed to attain a target weld geometry within a reasonable time.

Since multiple combinations of welding variables can lead to a target weld geometry [1], the classical gradient-based search and optimization methods that produce a single optimum solution cannot be used. These methods use a point-by-point approach, where one relatively imperfect solution in each iteration is modified to a different more appropriate solution [2,3]. Therefore, a combination of a classical optimization method with a phenomenological model can provide only a single local optimum solution in situations where multiple solutions exist. In contrast, genetic algorithms (GA) can obtain a population of optimal solutions [2-5]. In the context of welding, a GA can systematically search for multiple combinations of welding variable sets that comply with the phenomenological laws of welding physics and improve with iterations [1].

Recently, Kumar and DebRoy [1] developed bi-directional phenomenological model of gas metal arc (GMA) fillet welding by coupling a genetic algorithm based optimization method with a three-dimensional numerical transport phenomena based model. They [1] showed that the above approach can predict multiple combinations of welding variables to achieve a target geometry. However, this model [1] is unsuitable for practical applications, since it requires several days of computer calculations, even when run on a parallel computing facility, i.e., running the model on multiple processors simultaneously to reduce computational time. Unless a model can do calculations in a reasonable time, it is unlikely to find widespread practical applications.

Neural network models are powerful non-linear regression analysis methods [6-11] that can relate input variables like welding process parameters and material properties with weld characteristics such as weld pool geometry. If a neural network is trained with the data generated from a numerical transport phenomena based model for fusion welding, the output of the trained neural network will comply with the basic phenomenological laws of welding physics. With the improvements in computational hardware in recent years, a large volume of training and testing data can be generated with a well tested numerical transport phenomena based model in a realistic time frame. It is shown in the present study that multiple combinations of welding variables necessary to achieve a target GTA weld geometry can be systematically computed by a real number based genetic algorithm and a neural network that has been trained with the results of the

numerical transport phenomena based model. The neural network has been developed in the present study and is described in the previous chapter. The neural network could accurately predict the results of fusion zone geometry, peak temperature and cooling rate, obtained from the numerical transport phenomena based model, indicating that the output of the network complies with the phenomenological laws of welding physics. A genetic algorithm is used to determine a population of solutions, by minimizing an objective function that represents the difference between the calculated and the desired values of weld pool penetration and width. The use of a neural network in place of the numerical transport phenomena based model significantly expedites the computational task. The desired weld geometry could be obtained with various combinations of welding variable sets.

### **5.1 Mathematical Model**

The main computational engine used here includes two neural network models, which are trained and validated using the results of a well tested numerical transport phenomena based model described in Chapter 3. The details of the neural network models have been described in the previous chapter. The two neural network models considered here relate 17 important input welding variables and material properties to the weld pool penetration and width. The neural networks are computationally more efficient than the numerical transport phenomena based model. Furthermore, the results from the neural networks match accurately with the corresponding results from the numerical transport phenomena based model.

The genetic algorithm (GA) based search for multiple sets of welding variables to achieve a target weld geometry starts with many initial sets of randomly chosen values of the three most important welding variables, i.e., arc current, voltage and welding speed. A systematic global search is next undertaken to find multiple sets of values of these three welding variables that lead to least error between the calculated and the target weld dimensions, i.e., penetration and width. The neural network model calculates the values of these weld dimensions for each set of input welding variables. The chosen values of welding variables do not always produce the desired weld dimensions and the resulting

mismatch between the computed and the desired weld dimensions is expressed by the following objective function,  $O(f)$ :

$$O(f) = \left( \frac{p^c}{p^t} - 1 \right)^2 + \left( \frac{w^c}{w^t} - 1 \right)^2 \quad (5.1)$$

where  $p^c$  and  $w^c$  are the computed penetration and width of the weld bead, respectively and  $p^t$  and  $w^t$  are the corresponding target or desired values of these attributes. The objective function,  $O(f)$ , depends on the three main welding variables, i.e., arc current,  $I$ , voltage,  $V$ , and welding speed,  $U$ .

$$O(f) = O(f_1, f_2, f_3) = O\left(\frac{I}{I_r}, \frac{V}{V_r}, \frac{U}{U_r}\right) \quad (5.2)$$

In Eq. (5.2), the reference values,  $I_r$ ,  $V_r$  and  $U_r$  represent the order of magnitude of the welding variables. Note that Eq. (5.2) is made non-dimensional to preserve the importance of all three welding variables by making their non-dimensional values comparable in magnitude. The GA produces new individuals, or sets of welding conditions, with iterations based on the evolutionary principles [1,3-5]. The GA used in the present study is a parent centric recombination (PCX) operator based generalized generation gap (G3) model [1,3-5]. This model was chosen because it has been shown to have a faster convergence rate on standard test functions as compared to other evolutionary algorithms and classical optimization algorithms [3,4]. The specific application of this model for obtaining the multiple sets of welding variables to achieve a target weld geometry is described as follows. The explanations of various terms used in GA as related to welding are described in Chapter 3 (Table 3.3).

The algorithm for the model is as follows:

1. A population is a collection of many individuals and each individual represents a set of randomly chosen values of the three input variables, i.e., arc current, voltage and welding speed. A parent refers to an individual in the current population. The best parent is the individual that has the best fitness, i.e., gives the minimum value of the objective function, defined by Eq. (5.1), in the entire population. The best parent and two other randomly selected parents are chosen from the population.

2. From the three chosen parents, two offsprings or new individuals are generated using a recombination scheme. PCX based G3 models are known to converge rapidly when three parents and two offsprings are selected [3,4]. A recombination scheme is a process for creating new individuals from the parents.
3. Two new parents are randomly chosen from the current population.
4. A subpopulation of four individuals that includes the two randomly chosen parents in step 3 and two new offsprings generated in step 2 is formed.
5. The two best solutions, i.e., the solutions having the least values of the objective function, are chosen from the subpopulation of four members created in step 4. These two individuals replace the two parents randomly chosen in step 3.
6. The calculations are repeated from step 1 again until convergence is achieved.

The above steps, as applied to the present study, are shown in Fig. 5.1. The working of the model to find the multiple sets of welding variables by minimizing the objective function is illustrated in Fig. 5.2. The recombination scheme (step 2) used in the present model is based on the PCX operator. A brief description of the PCX operator, as applied to the present problem, is presented below.

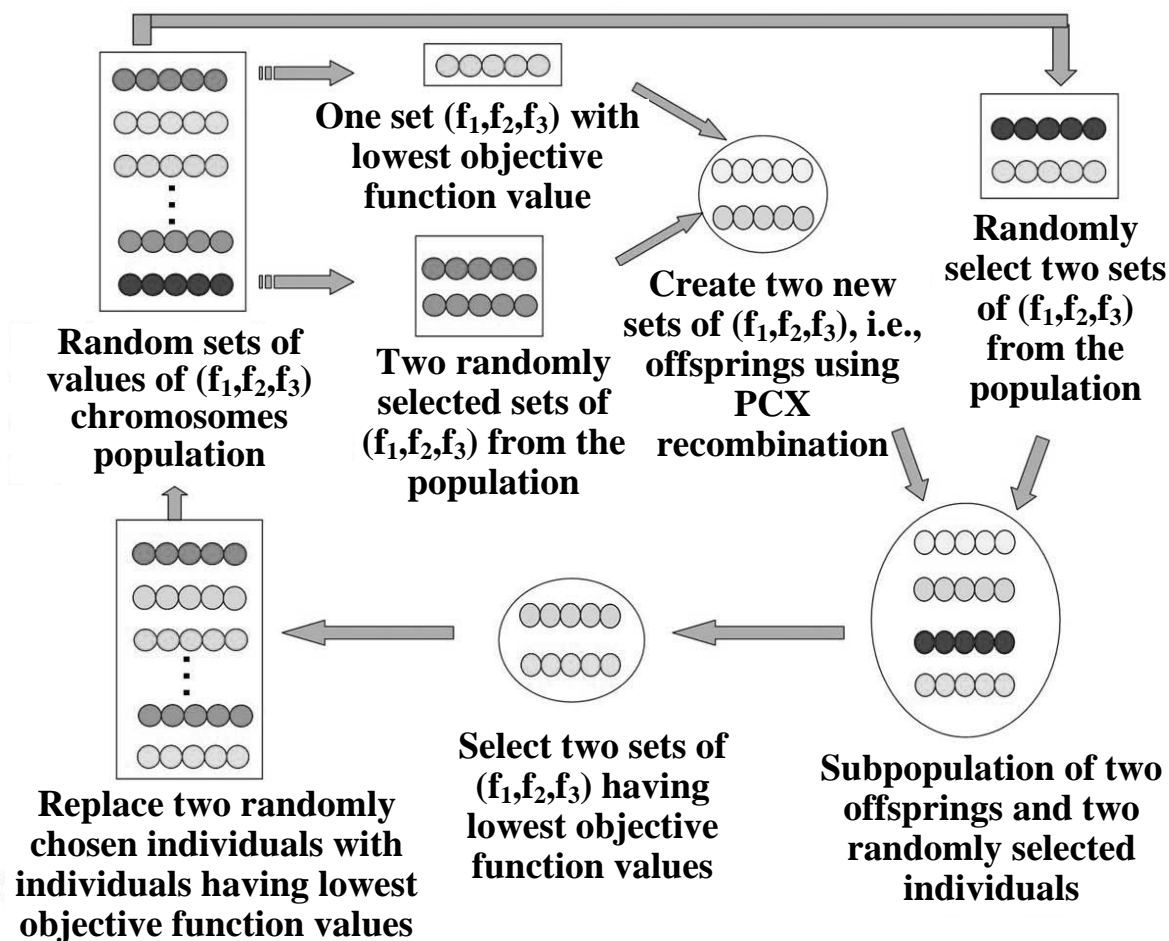


Fig. 5.1. Generalized generation gap (G3) genetic algorithm using parent centric recombination (PCX) operator.

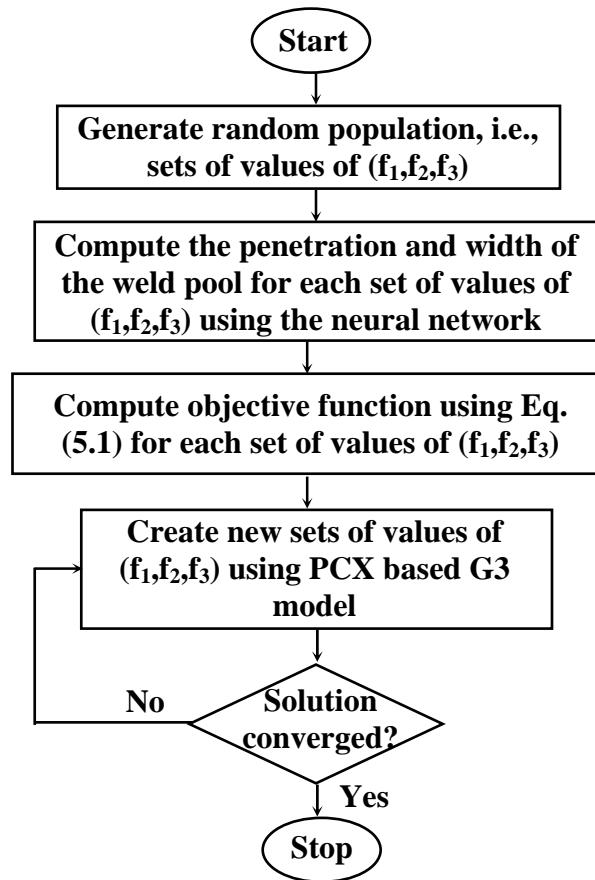


Fig. 5.2. Flow chart of the generalized generation gap (G3) model.

First, three parents, i.e.,  $(f_1^0, f_2^0, f_3^0)$ ,  $(f_1^1, f_2^1, f_3^1)$ ,  $(f_1^2, f_2^2, f_3^2)$  are randomly selected from the current population. Here, the subscripts represent the three input welding variables, while the superscripts denote the parent identification number. The mean vector or centroid,  $\bar{g} = \left( \frac{f_1^0 + f_1^1 + f_1^2}{3}, \frac{f_2^0 + f_2^1 + f_2^2}{3}, \frac{f_3^0 + f_3^1 + f_3^2}{3} \right)$ , of the three chosen parents is computed. To create an offspring, one of the parents, say  $\bar{x}^{(p)} = (f_1^0, f_2^0, f_3^0)$  is chosen randomly. The direction vector,  $\bar{d}^{(p)} = \bar{x}^{(p)} - \bar{g}$ , is next calculated from the selected parent to the mean vector or centroid. Thereafter, from each of the other two parents, i.e.,  $(f_1^1, f_2^1, f_3^1)$  and  $(f_1^2, f_2^2, f_3^2)$ , perpendicular distances,  $D_i$ , to the direction vector,  $\bar{d}^{(p)}$ , are computed and their average,  $\bar{D}$ , is found. Finally, the offspring, i.e.,  $\bar{y} = (f_1', f_2', f_3')$ , is created as follows:

$$\bar{y} = \bar{x}^{(p)} + w_\zeta |\bar{d}^{(p)}| + \sum_{i=1, i \neq p}^3 w_\eta \bar{D} \bar{h}^{(i)} \quad (5.3)$$

where  $\bar{h}^{(i)}$  are the orthonormal bases that span the subspace perpendicular to  $\bar{d}^{(p)}$ , and  $w_\zeta$  and  $w_\eta$  are randomly calculated zero-mean normally distributed variables.

The values of the variables that characterize the offspring,  $\bar{y} = (f_1', f_2', f_3')$ , are calculated as follows:

$$f_1' = f_1^0 + f_{11} + f_{12} \quad (5.4)$$

$$f_2' = f_2^0 + f_{21} + f_{22} \quad (5.5)$$

$$f_3' = f_3^0 + f_{31} + f_{32} \quad (5.6)$$

where,

$$f_{11} = w_\zeta \left( \frac{2f_1^0 - f_1^1 - f_1^2}{3} \right) \quad (5.7)$$

$$f_{21} = w_\zeta \left( \frac{2f_2^0 - f_2^1 - f_2^2}{3} \right) \quad (5.8)$$

$$f_{31} = w_{\zeta} \left( \frac{2f_3^0 - f_3^1 - f_3^2}{3} \right) \quad (5.9)$$

$$f_{12} = w_{\eta} \left( \frac{a_2 + b_2}{2} \right) \left[ 1 - \left( \frac{2f_1^0 - f_1^1 - f_1^2}{3d} \right)^2 \right] \quad (5.10)$$

$$f_{22} = w_{\eta} \left( \frac{a_2 + b_2}{2} \right) \left[ 1 - \left( \frac{2f_2^0 - f_2^1 - f_2^2}{3d} \right)^2 \right] \quad (5.11)$$

$$f_{32} = w_{\eta} \left( \frac{a_2 + b_2}{2} \right) \left[ 1 - \left( \frac{2f_3^0 - f_3^1 - f_3^2}{3d} \right)^2 \right] \quad (5.12)$$

The expressions for the variables  $d$ ,  $a_2$ , and  $b_2$ , used in Eqs. (5.10) to (5.12), are as follows:

$$d = \sqrt{\left( \frac{2f_1^0 - f_1^1 - f_1^2}{3} \right)^2 + \left( \frac{2f_2^0 - f_2^1 - f_2^2}{3} \right)^2 + \left( \frac{2f_3^0 - f_3^1 - f_3^2}{3} \right)^2} \quad (5.13)$$

$$a_2 = e_1 \times \sqrt{1 - (a_1)^2} \quad (5.14)$$

$$b_2 = e_2 \times \sqrt{1 - (b_1)^2} \quad (5.15)$$

$$a_1 = \sum_{i=1}^3 \frac{(f_i^1 - f_i^0) \left( \frac{2f_i^0 - f_i^1 - f_i^2}{3} \right)}{d \times e_1} \quad (5.16)$$

$$e_1 = \sqrt{(f_1^1 - f_1^0)^2 + (f_2^1 - f_2^0)^2 + (f_3^1 - f_3^0)^2} \quad (5.17)$$

$$b_1 = \sum_{i=1}^3 \frac{(f_i^2 - f_i^0) \left( \frac{2f_i^0 - f_i^1 - f_i^2}{3} \right)}{d \times e_2} \quad (5.18)$$

$$e_2 = \sqrt{(f_1^2 - f_1^0)^2 + (f_2^2 - f_2^0)^2 + (f_3^2 - f_3^0)^2} \quad (5.19)$$

## 5.2 Results and Discussion

The neural network used here was trained and validated with results from a well tested three-dimensional numerical transport phenomena based model described in

Chapter 3. As described in the previous chapter, separate feed forward neural networks were developed, one each for predicting penetration and width of GTA butt welds to achieve high accuracies in the calculation of these output parameters. The weights in the neural network models were calculated using a hybrid optimization scheme involving the gradient descent (GD) method and a genetic algorithm (GA). The hybrid optimization scheme helped in finding optimal weights through a global search as evidenced by good agreement between all the outputs from the neural networks and the corresponding results from the numerical transport phenomena based model. The neural network model provided correct values of penetration and width for various combinations of welding variables, i.e., current,  $I$ , voltage,  $V$ , and welding speed,  $U$ .

It has been shown recently [1] that by coupling a GA based optimization method with a three-dimensional numerical transport phenomena based model, multiple combinations of welding variables can be predicted to achieve a target weld geometry. This is possible because GA can provide a population of solutions. In the present study, the neural network model was combined with a real number based GA to tailor weld geometry. The effectiveness of the approach was tested by finding different sets of welding variables, which could provide a specified weld geometry. The computational task involved three steps. First, a target weld geometry was selected by specifying one set of values of penetration and width. Second, the model was run to obtain multiple combinations of welding variable sets each of which could produce the target weld geometry. Third, and final, the results obtained from the model were adequately verified. These three steps are explained in detail in the following discussion.

To start the calculation, the specification of a target weld geometry was necessary. It involved stating realistic combinations of the weld penetration and width. To test the model, these weld dimensions from an actual welding experiment were specified as a target geometry. The target weld geometry was obtained experimentally in the present study using the following welding variables:  $I = 101.0$  A,  $V = 9.9$  V and  $U = 3.4$  mm/s for GTA welding of 303 stainless steel (0.293 wt% sulfur), and the resulting weld dimensions were: penetration = 1.39 mm and width = 4.05 mm. If the model works correctly, the various combinations of welding variables obtained from the model must

include a set of welding variables that are fairly close to the set of variables used in the experiment. It should be noted that the ability of the model to produce this solution is only a necessary, but not sufficient component of the model verification. Since the model produces multiple solutions, other solutions obtained from the model have to be verified by comparing the calculated weld geometry with the experimentally obtained geometry.

In the next step (i.e. second step), a population of 120 individuals was defined to start the operation of GA. This number of variable sets was determined based on how the population size influences the effectiveness of GA using standard test functions [3,4]. Each individual in the population contained a set of randomly chosen welding variables, i.e., arc current, voltage and welding speed. Fig. 5.3(a) shows the initial values of the individuals, i.e., sets of I, V and U.

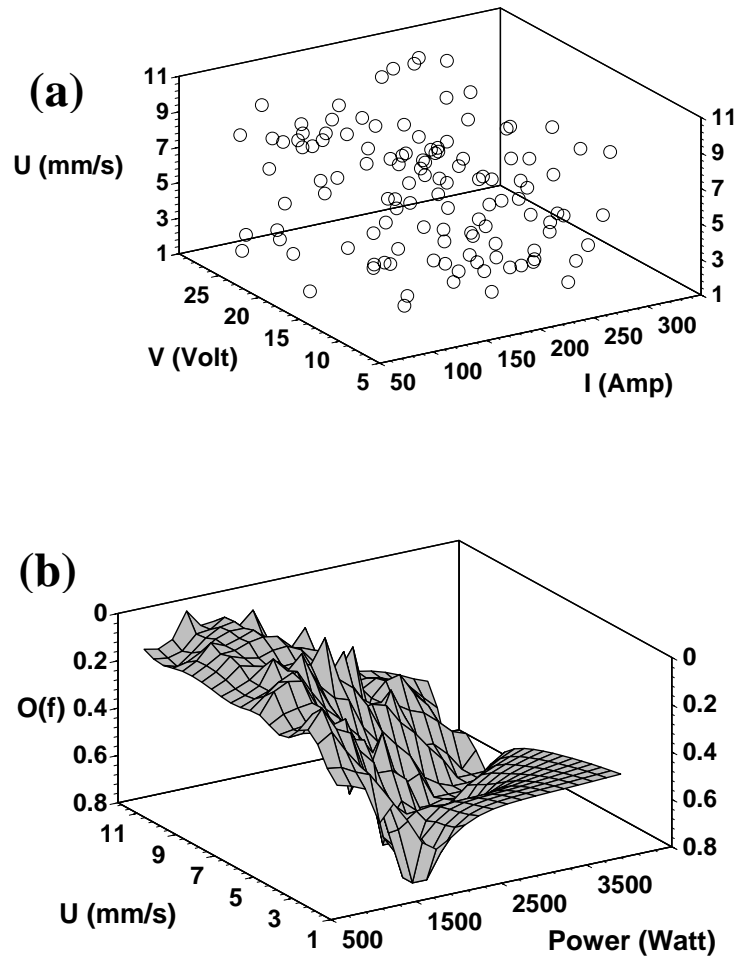


Fig. 5.3: Initial values of individual welding variable sets and their objective functions. (a) A large space of variables was searched to find optimum solutions as shown by 120 randomly selected initial welding variable sets. (b) The low values of the objective functions of several individuals in the initial population indicate the possibility of existence of multiple optimal solutions.

Values of the welding variables I, V and U were chosen randomly in the range of 75-300 A, 8-30 V and 1.7-10.0 mm/s, respectively. Such large ranges of values were chosen for the welding variables in order to explore a large domain of welding variables to include all possible solutions and also to maintain diversity in the solutions. These welding variable sets were then improved iteratively using a combination of GA and the neural network. The progress of the iterations was monitored by calculating the objective function values, defined in Eq. (5.1), for each set of welding variables. An individual with a low objective function value indicates that the I, V and U values it contains result in a small discrepancy between the computed and the target weld geometry. Fig. 5.3(b) shows that for many sets of welding variables, the computed values of the objective function,  $O(f)$ , are fairly low, indicating that each of these variable sets can produce a weld geometry that is close to the target geometry.

Fig. 5.4(a), (b) and (c) indicate several welding variable sets that have progressively lower objective function values. The objective function values are lower than 0.1, 0.01 and 0.001, corresponding to the 1st, 10th and 25th generation of individuals, respectively. It is noteworthy that in Fig. 5.4, the sets of welding variables are distributed throughout the welding variable space, signifying the existence of multiple paths to attain the specified weld geometry. The progressive reduction of the objective function values of the best individuals indicates that the solutions are improved with iterations. The calculation was continued until 5% individuals in the population had the value of objective function less than  $1.0 \times 10^{-5}$ . The chosen value of the objective function ensured sufficient accuracy within the practical limits of experimental errors. The calculated combinations of the welding variables, which constitute the final solutions, are presented in Table 5.1. The calculations required less than one minute in a PC with 3.0 GHz Intel P4 CPU and 1024 MB PC2700 DDR-SDRAM memory. It is useful to recall that several days of computational time was required on similar machines by a model developed by Kumar and DebRoy [1] that used a numerical transport phenomena based model. This time saved by using a neural network justifies its use as a forward model in place of a numerical transport phenomena based model.

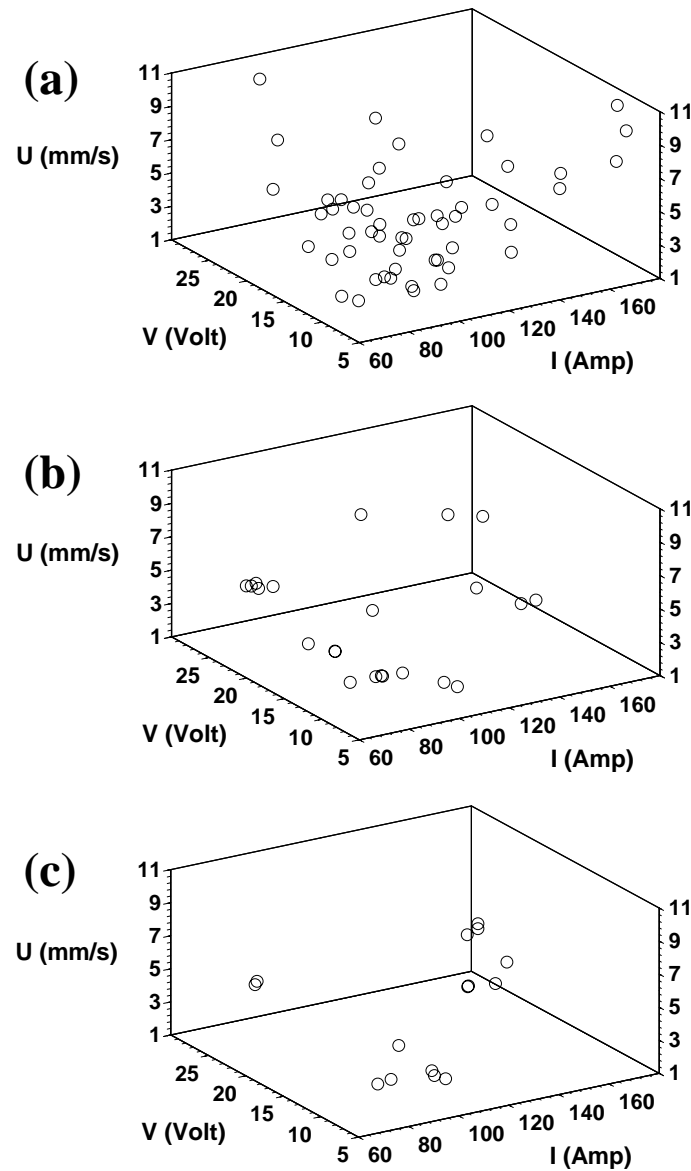


Fig. 5.4: Several fairly diverse welding variable sets could produce low values of the objective function indicating the existence of alternate paths to obtain the target weld geometry. The plots show the welding variable sets that produced low values of the objective function,  $O(f)$ , with iterations. (a) individuals after 1st iteration with  $O(f)$  less than 0.1, (b) individuals after 10th iteration with  $O(f)$  less than 0.01, and (c) individuals after 25th iteration with  $O(f)$  less than 0.001.

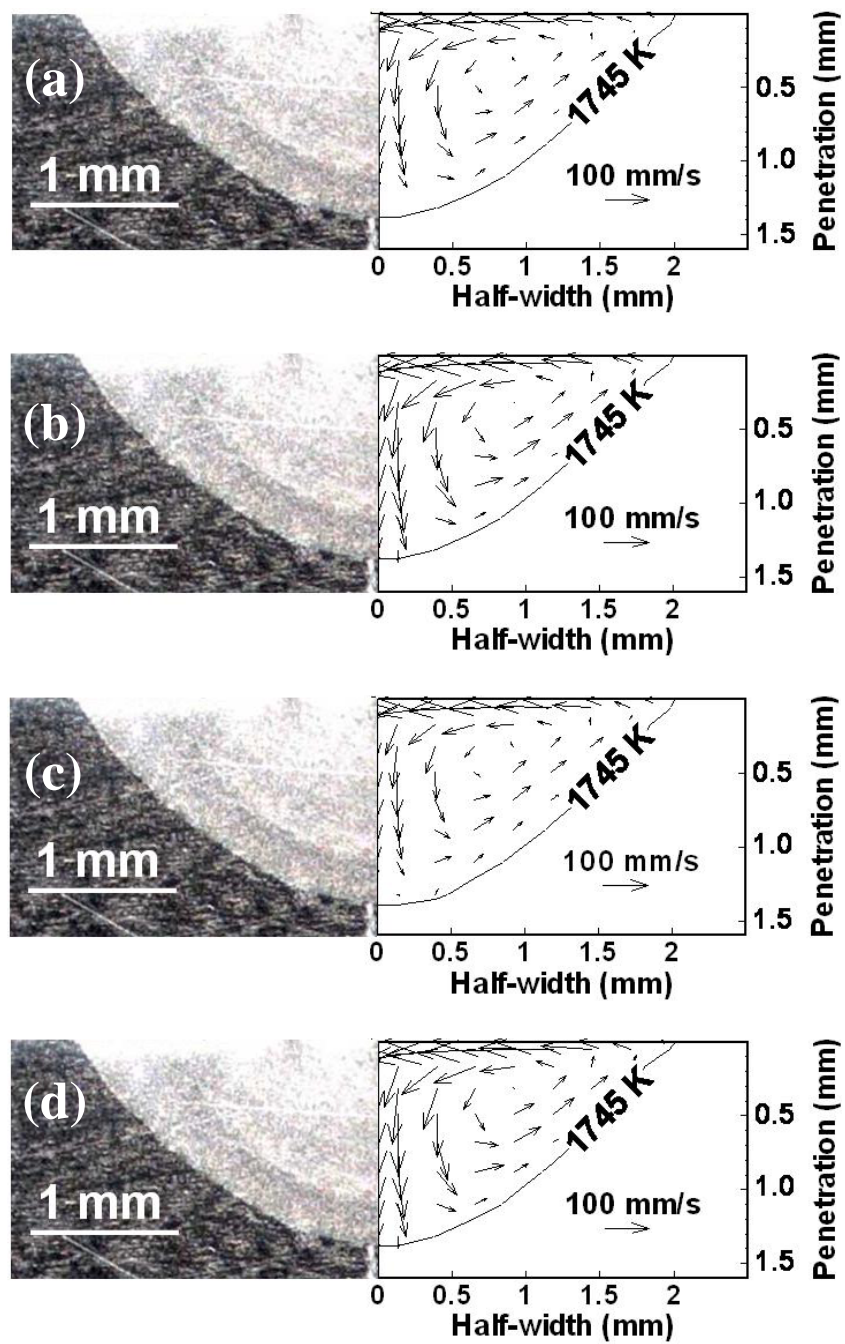
Table 5.1: Various combinations of welding variables, i.e., arc current (I), voltage (V) and welding speed (U) obtained using neural network model to achieve the following target weld dimensions: penetration = 1.39 mm and width = 4.05 mm. The target weld geometry was obtained experimentally using the following welding variables: I = 101.0 A, V= 9.9 V and U = 3.4 mm/s for GTA welding of 303 stainless steel (0.293 wt% sulfur).

<b>Individual Solutions</b>	<b>I (Amp)</b>	<b>V (Volt)</b>	<b>U (mm/s)</b>	<b>Penetration (mm)</b>	<b>Width (mm)</b>
(a)	102.6	9.8	3.4	1.40	4.08
(b)	86.6	23.3	9.0	1.39	4.06
(c)	97.2	10.1	3.2	1.39	4.04
(d)	133.6	11.4	9.6	1.39	4.06
(e)	115.6	10.2	5.1	1.39	4.05
(f)	126.8	10.3	6.7	1.39	4.05
(g)	88.6	9.7	2.2	1.39	4.04
(h)	94.3	9.5	2.6	1.39	4.06

The third step involved verification of the computed solutions. Since the target geometry was produced by conducting an experiment, an initial test is to check if the population of solutions produced by the model includes a set of welding variables that is very close to, if not the same as, that used to produce the weld. Note that the values of arc current, voltage and welding speed in solution (a) of Table 5.1 are almost the same as the corresponding experimental values. Each solution, i.e., a set of current, voltage and welding speed, listed in Table 5.1, was used to calculate the geometric parameters, i.e., penetration and width of the weld using the neural network. The computed geometric parameters were compared with those produced in the experiment. Table 5.1 shows that for each set of computed welding conditions, the corresponding geometric parameters agreed well with the desired experimental values. In order to further test the accuracy of the solutions, i.e., sets of current, voltage and welding speed listed in Table 5.1, the weld geometry for each case was calculated from the numerical transport phenomena based model for GTA welding described in Chapter 3. These calculated weld geometries were

compared with the experimental target weld geometry, as shown in Fig. 5.5(a) to (h). The calculated weld pool boundary is marked by the solidus temperature of stainless steel, i.e., 1745 K. Fig. 5.5 shows that all the optimized solutions listed in Table 5.1 result in the correct prediction of the target weld shape and size. Furthermore, the solutions in Table 5.1 exhibit significantly different values of the welding variables indicating the diversity of the paths through which the specified geometry can be obtained. For example, Table 5.1 shows that the current values ranged from 86.6 to 133.6 A, voltages varied between 9.5 to 23.3 V and welding speed changed from 2.2 to 9.6 mm/s in various sets of optimized values. The fact that all these diverse viable paths can lead to the same weld pool dimensions clearly indicates the complexity and significant non-linearity of the fusion welding system.

A similar exercise was also undertaken where a hypothetical weld geometry represented by a penetration of 1.94 mm and a width of 4.39 mm was produced by a current of 124.3 A, voltage of 9.4 V and welding speed of 3.0 mm/s in 304RL stainless steel (0.024 wt% sulfur). Table 5.2 lists all other combinations of welding variables, i.e., solutions (b) to (h) that can produce this geometry. The values of the welding variables differed considerably from each other. For example, current, voltage and welding speed varied among solutions by 38%, 30% and 55%, respectively. All these differences in the important welding variables indicate significant diversity in the paths, all of which lead to the same set of target weld dimensions.



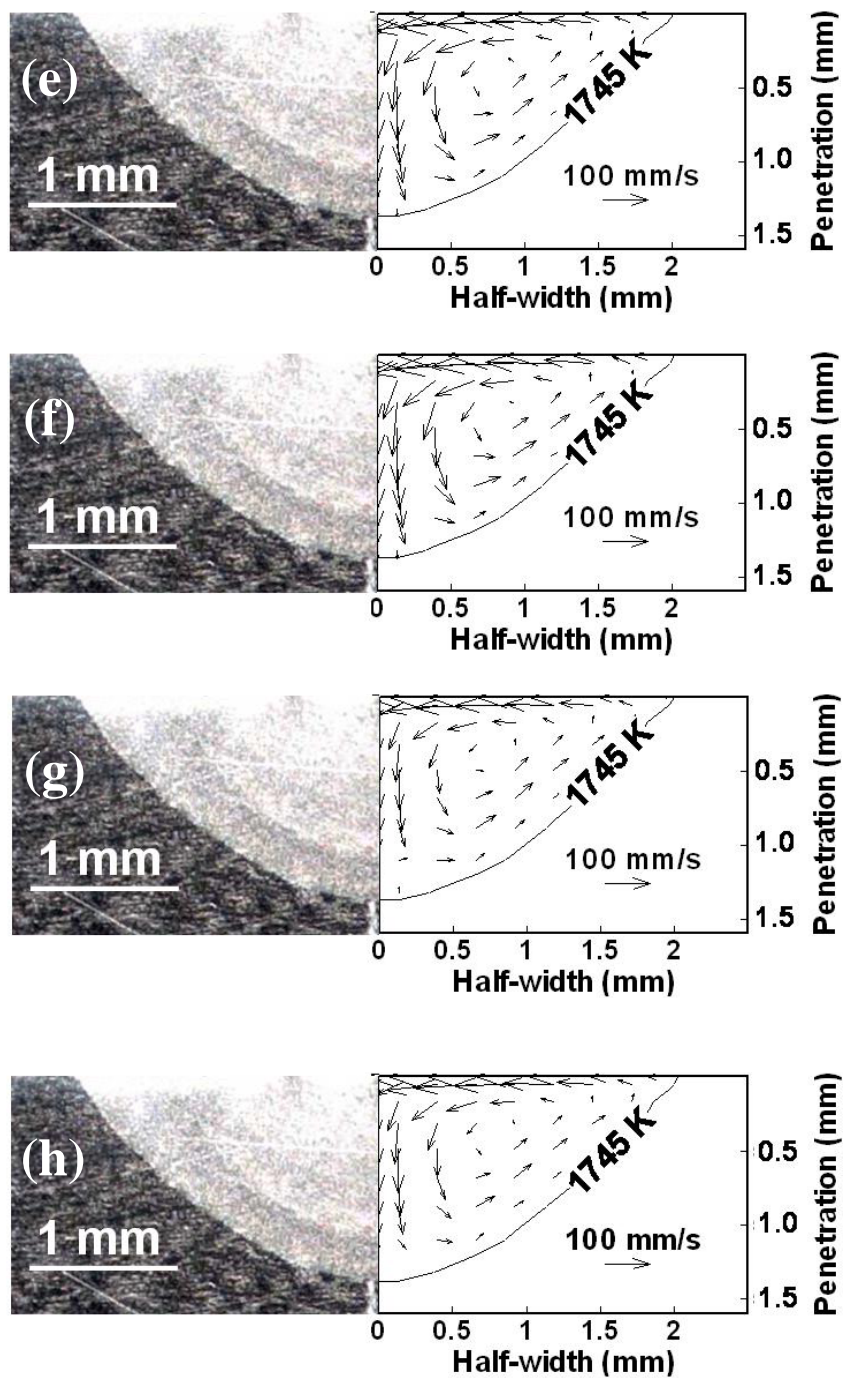


Fig. 5.5: Comparison of the experimental target weld geometry with those calculated from the numerical transport phenomena based model for GTA welding described in Chapter 3. Calculated weld geometries in cases (a) to (h) correspond to the eight solutions, i.e., sets of current, voltage and welding speed listed in Table 5.1. In the calculated results the weld pool boundary is marked by the 1745 K isotherm, which is the solidus temperature of stainless steel.

Table 5.2: Various combinations of welding variables, i.e., arc current (I), voltage (V) and welding speed (U) obtained using neural network model to achieve the following target weld dimensions: penetration = 1.94 mm and width = 4.39 mm. The target weld geometry was obtained using the welding conditions listed in (a).

<b>Individual Solutions</b>	<b>I (Amp)</b>	<b>V (Volt)</b>	<b>U (mm/s)</b>	<b>Penetration (mm)</b>	<b>Width (mm)</b>
(a)	124.3	9.4	3.0	1.94	4.39
(b)	79.3	16.0	3.1	1.94	4.37
(c)	99.9	9.8	1.7	1.94	4.33
(d)	116.4	9.3	2.5	1.94	4.38
(e)	145.7	9.0	4.2	1.94	4.36
(f)	89.3	12.4	2.3	1.94	4.36
(g)	107.0	9.6	2.1	1.94	4.37
(h)	175.9	8.6	6.0	1.94	4.37

### 5.3 Summary and Conclusions

A bidirectional model of gas tungsten arc (GTA) welding was developed by coupling a neural network model with a real number based genetic algorithm to calculate the welding conditions needed to obtain a target weld geometry. Unlike conventional neural network models that are trained with experimental data, which predict weld geometry for a particular set of welding conditions, the proposed model could estimate the welding conditions necessary for obtaining a target weld geometry within the framework of phenomenological laws.

The model was used to determine multiple sets of welding variables, i.e., combinations of arc current, voltage and welding speed to obtain a specified weld geometry. It was found that a specific weld geometry was attainable via multiple pathways involving various sets of welding variables. Furthermore, these sets of welding variables involved significantly different values of current, voltage and welding speed. The use of a neural network model in place of numerical transport phenomena based model reduced the computation time and provided the solution within one minute. The

high speed makes the neural network based model appropriate in various applications where rapid calculations are desired. Good agreement between the model predictions and the experimental data of weld pool penetration and width for various welding conditions shows that this approach is promising.

#### 5.4 References

1. A. Kumar and T. DebRoy, *Metall. Mater. Trans. A* 36, 2725 (2005).
2. D. E. Goldberg, *Genetic Algorithm in Search, Optimization and Machine Learning* (Addison-Wesley, MA, 1989).
3. K. Deb, *Multi-objective Optimization using Evolutionary Algorithms* (Wiley, New York, 2001).
4. K. Deb, A. Anand and D. Joshi, *Evolutionary Computation* 10, 371 (2002).
5. A. Kumar, S. Mishra, J. W. Elmer and T. DebRoy, *Metall. Mater. Trans. A* 36, 15 (2005).
6. J. M. Vitek, Y. S. Iskander and E. M. Oblow, *Weld. J.* 79, 33 (2000).
7. H. K. D. H. Bhadeshia, *ISIJ Int.* 39, 966 (1999).
8. S. Haykin, *Neural Network: A Comprehensive Foundation* (Prentice Hall Pub., NJ, 1999).
9. T. Masters, *Practical Neural Network Recipes in C++* (Academic Press, Boston, 1993).
10. M. T. Hagan, *Neural Network Design* (PWS Pub., Boston, 1996).
11. D. E. Rumelhart, G. E. Hinton and R. J. Williams, *Nature* 323, 533 (1986).

## Chapter 6

### Evolution of Weld Pool Geometry on Welding Plates with Same and Different Sulfur Contents

The solute distribution in a weld has significant impact on its properties such as the evolution of weld pool geometry. For example, when stainless steel containing surface active elements like sulfur is welded, the temperature coefficient of surface tension,  $d\gamma/dT$ , often becomes positive, causing the liquid metal to flow from the periphery to the center of the weld pool. This fluid motion moves hot fluid downwards in the middle of the weld pool resulting in a deep and narrow weld bead. This phenomenon has been well captured both via experiments and mathematical models for welding of two plates with same sulfur content [1-12].

An important question that is related to but different from the above example is what would happen if the two plates being welded have different sulfur contents. The available models cannot address these problems. Such situations are common in the nuclear waste management industry where stabilization, packaging and storage of plutonium-bearing materials involve welding of 316 stainless steel (SS) container (0.03 wt% sulfur) with 416 SS lid (>0.15 wt% sulfur) [13]. The final closure of the container must be leak-tight and structurally sound [13-15]. Another example is the tungsten inert gas (TIG) welding of small diameter stainless steel tubing for instrumentation systems in CANDU (Canadian Deuterium Uranium) nuclear reactors [12]. Experiments have shown that during welding of two stainless steel plates with different sulfur contents the point of maximum penetration shifts towards the plate with lower sulfur content [10,12]. The weld bead shift is sometimes so severe that there is very little melting of the piece with higher sulfur content, i.e., lack-of-fusion defect occurs at the interface, resulting in improper joining of the two pieces [12]. Since many of the instrumentation systems in a nuclear reactor contain the primary coolant, insufficient fusion of the interface is unacceptable [12].

Heiple et al. [5] gave a qualitative explanation for the shifting of the weld bead based on their surface tension driven fluid flow model. They stated that the plate with

lower sulfur content has relatively higher surface tension than the one with higher sulfur content. The result is a net surface tension gradient across the weld pool leading to surface fluid flow toward the low sulfur plate. This flow pattern causes maximum penetration in the plate containing less sulfur. However, once the weld pool is formed, liquid metal in the weld pool circulates vigorously causing mixing of sulfur from the two plates. Actual surface tension gradient should depend on the final sulfur distribution in the weld pool. Also, during a similar experiment, Rollin et al. [10] observed that the welding arc was displaced towards the low sulfur side. They [10] stated that the arc shift should also be a contributing factor to the weld bead shift, along with the surface tension driven fluid flow. A thorough quantitative modeling effort, which can take into account all the factors affecting weld bead shift, and predict the location, size and shape of the weld bead when joining two plates with different sulfur contents, is still lacking in the literature.

In the present study, the evolution of weld pool geometry of GTA welds is examined when welding two stainless steel plates with different sulfur contents. The numerical transport phenomena based model, described in Chapter 3, is used to calculate the sulfur distribution in the weld pool and the resulting weld pool geometry. The modification of weld pool convection pattern due to top surface sulfur distribution, and the shifting of the welding arc towards the low sulfur side are identified as the two main factors contributing to the evolution of weld pool geometry. The experimental results were provided by Dr. T. J. Lienert and Dr. M. Johnson of the Los Alamos National Laboratory. The calculated weld pool geometry is in fair agreement with the corresponding experimental results indicating the validity of the approach.

## 6.1 Experimental Procedure

Three grades of stainless steel (SS), i.e., 303 (0.293 wt% sulfur, S), 304RL (0.024 wt% S) and 304L (0.003 wt% S), were used in the present study. Grade 303 is a high sulfur containing SS while grade 304L has negligible amount of sulfur. The compositions of the three grades of SS are given in Table 6.1. Specimens or plates measuring 50.8 mm (width)  $\times$  254 mm (length)  $\times$  9.5 mm (height) were prepared for each grade of SS. Pairs

of plates containing same and different sulfur contents were welded using gas tungsten arc (GTA) welding. No preheat was used. Argon was used both as the welding and the shielding gas. The welding conditions used in the present study are given in Table 6.2. The first six cases in Table 6.2 correspond to the welding of plates having same sulfur contents, while the rest of the cases are for the welding of plates with different sulfur contents. Two current levels and two welding speeds were employed in the experiments. After welding, conventional polishing and etching techniques were used to reveal the fusion zone boundary, and weld pool width and penetration were measured. The top surface and bulk concentrations of surface active elements, sulfur and phosphorus, were measured by Electron Probe MicroAnalysis (EPMA).

Table 6.1. Compositions of the three grades of stainless steels (SS) used in the present study.

<b>SS</b>	<b>C</b>	<b>P</b>	<b>S</b>	<b>Si</b>	<b>Mn</b>	<b>Cr</b>
<b>304L</b>	0.022	0.028	0.003	0.303	1.811	18.537
<b>304RL</b>	0.019	0.031	0.024	0.322	1.412	18.151
<b>303</b>	0.050	0.027	0.293	0.510	1.620	17.210

<b>SS</b>	<b>Ni</b>	<b>Mo</b>	<b>Ti</b>	<b>N</b>	<b>Cu</b>	<b>Co</b>
<b>304L</b>	8.453	0.296	NA	0.052	0.246	NA
<b>304RL</b>	8.660	0.039	0.003	0.047	0.400	0.101
<b>303</b>	8.720	NA	NA	NA	NA	NA

Table 6.2. Welding conditions used in the present study. Case numbers 1 to 6 list the cases where the two welded specimens contained the same amount of sulfur. The remaining entries are for the cases where the two welded specimens contained different amounts of sulfur.

<b>Case no.</b>	<b>SS (Left)</b>	<b>SS (Right)</b>	<b>Current (A)</b>	<b>Voltage (V)</b>	<b>Welding speed (mm/s)</b>
1	304L	304L	101	9.6	1.7
2	304RL	304RL	100	9.6	1.7
3	304L	304L	150	9.9	1.7
4	303	303	150	10.5	1.7
5	304RL	304RL	100	10.0	3.4
6	303	303	101	9.9	3.4
7	304L	303	150	10.5	1.7
8	304RL	303	150	10.8	1.7
9	304L	304RL	150	10.5	1.7
10	304L	303	150	10.8	3.4
11	304RL	303	150	10.9	3.4
12	304L	304RL	150	10.7	3.4
13	304L	303	100	9.8	1.7
14	304RL	303	100	10.0	1.7
15	304L	304RL	100	9.9	1.7
16	304L	303	100	10.2	3.4
17	304RL	303	100	10.2	3.4
18	304L	304RL	100	10.0	3.4

## 6.2 Mathematical Model

The numerical transport phenomena based model for fusion welding has been described in detail in Chapter 3. Therefore, only the effect of surface active element,

sulfur, on weld pool convection, and the incorporation of this effect in the numerical transport phenomena based model will be described here.

### 6.2.1 The effect of surface active element, sulfur on weld pool convection

The spatial gradient of surface tension ( $\gamma$ ) is a stress, which is known as the Marangoni shear stress. This stress arises due to spatial variation of temperature and composition, which can be expressed as:

$$\tau = \frac{\partial\gamma}{\partial T} \frac{\partial T}{\partial r} + \frac{\partial\gamma}{\partial C} \frac{\partial C}{\partial r} \quad (6.1)$$

where  $\tau$  is the shear stress due to surface tension,  $T$  is the temperature,  $r$  is the distance along the surface from the heat source, and  $C$  is the concentration of surface active element, sulfur. When the materials being welded either have no sulfur or have the same composition of sulfur throughout, then the concentration gradient,  $\partial C/\partial r$ , is zero, and the difference in surface tension is due to the spatial temperature variation alone. In other words, the shear stress depends only on  $\partial\gamma/\partial T$  and the spatial temperature gradient  $\partial T/\partial r$  at the pool surface.

In the absence of sulfur, the temperature coefficient of surface tension ( $\partial\gamma/\partial T$ ) for many materials is less than zero. In other words, the higher the temperature, the lower the surface tension. Hence, at the weld pool top surface, the liquid metal flows radially outward, since the warmer liquid metal of lower surface tension near the center of the pool is pulled outward by the cooler metal of higher surface tension at the pool edge [1-5]. Pushed by the strong outward flow at the top surface, the liquid metal is transported outwards from the middle of the weld pool and rises at the center of the pool, as shown in Fig. 6.1(a).

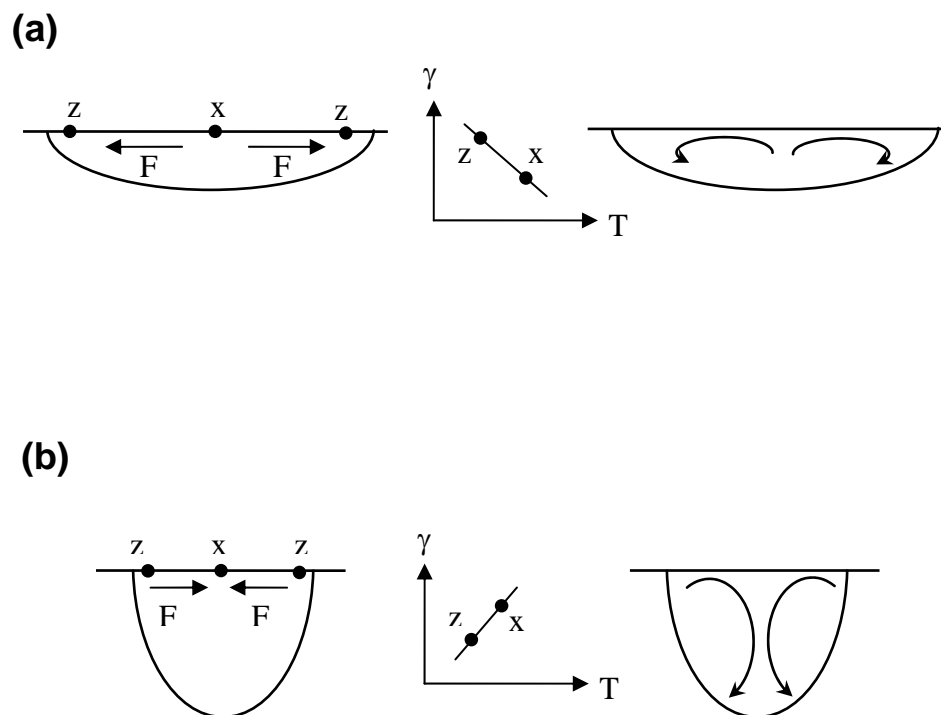


Fig. 6.1. Liquid convection in the weld pool for two cases: (a)  $\partial\gamma/\partial T$  is negative, which is generally the case when surface active element like sulfur is absent. (b)  $\partial\gamma/\partial T$  is positive, which is generally the case when surface active element like sulfur is present. Symbol  $\gamma$  is the surface tension,  $\partial\gamma/\partial T$  is the temperature coefficient of surface tension,  $T$  is the temperature,  $x$  and  $z$  are two locations in the weld pool, and  $F$  is the driving force.

The presence of sulfur in the weld pool can make the value of  $\partial\gamma/\partial T$  positive [1-5], because sulfur tends to preferentially segregate to the surface and change the surface properties. For liquid material with a positive value of  $\partial\gamma/\partial T$ , the direction of the Marangoni shear stress and the resulting flow pattern are shown in Fig. 6.1(b). This flow pattern is expected, since the cooler metal of lower surface tension at the pool edge is pulled inward by the warmer liquid metal of higher surface tension near the center of the pool.

Surface tension for a binary Fe-S alloy is given as a function of both temperature and activity of sulfur as [2]:

$$\gamma = \gamma_m - A[T - T_m] - RT\Gamma_s \ln[1 + Ka_s] \quad (6.2)$$

$$K = k_1 \exp\left(-\frac{\Delta H^0}{RT}\right) \quad (6.3)$$

where  $\gamma_m$  is the surface tension of the pure metal at melting point,  $T_m$  is the melting point of the material,  $a_s$  is the activity of sulfur,  $A$  is negative of  $\partial\gamma/\partial T$  for pure metal,  $\Gamma_s$  is the surface excess at saturation,  $k_1$  is the entropy factor, and  $\Delta H^0$  is the standard enthalpy of adsorption. Since the amount of sulfur in stainless steel is very small (dilute solution), the activity of sulfur in Eq. (6.2) is replaced by concentration of sulfur in wt%,  $C$  [2]. The validity of Eq. (6.2) for application in stainless steel has been demonstrated in reference [16]. By differentiating Eq. (6.2) with respect to temperature the expression for  $\partial\gamma/\partial T$  as a function of both temperature and sulfur concentration can be obtained as [2]:

$$\frac{\partial\gamma}{\partial T} = -A - R\Gamma_s \ln[1 + KC] - \frac{KC}{1 + KC} \Gamma_s (\Delta H^0 - \Delta\bar{H}_s^m) \quad (6.4)$$

where  $\Delta\bar{H}_s^m$  is the partial molar enthalpy of mixing of sulfur in the solution. For dilute solution,  $\Delta\bar{H}_s^m$  is taken as zero [2]. Using Eq. (6.4) and the data given in Table 6.3,  $\partial\gamma/\partial T$  is plotted as a function of temperature for different sulfur concentrations in Fig. 6.2. It can be seen that for low sulfur concentrations such as 0.003 wt%,  $\partial\gamma/\partial T$  is negative over the entire temperature range. Negative  $\partial\gamma/\partial T$  causes the liquid to move from the center to the periphery on the top surface leading to a wide and shallow weld pool. On the other hand, for very high sulfur concentrations such as 0.3 wt%,  $\partial\gamma/\partial T$  is positive over the

entire temperature range. Positive  $\partial\gamma/\partial T$  causes the liquid to move from the periphery to the center on the top surface leading to a narrow and deep weld pool.

When the two plates being welded have different sulfur contents then the value of  $\partial C/\partial r$  in Eq. (6.1) is no longer zero and the value of  $\partial\gamma/\partial C$  must be calculated. Differentiating Eq. (6.2) with respect to sulfur concentration gives:

$$\frac{\partial\gamma}{\partial C} = -\frac{RT\Gamma_s K}{1 + KC} \quad (6.5)$$

The influence of surface active element sulfur is incorporated in the numerical model in the form of surface tension boundary condition on the top surface. The surface tension boundary condition is given as:

$$\begin{aligned} \mu \frac{\partial u}{\partial z} &= f_L \left( \frac{\partial\gamma}{\partial T} \frac{\partial T}{\partial x} + \frac{\partial\gamma}{\partial C} \frac{\partial C}{\partial x} \right) \\ \mu \frac{\partial v}{\partial z} &= f_L \left( \frac{\partial\gamma}{\partial T} \frac{\partial T}{\partial y} + \frac{\partial\gamma}{\partial C} \frac{\partial C}{\partial y} \right) \\ w &= 0 \end{aligned} \quad (6.6)$$

where  $u$ ,  $v$  and  $w$  are the velocity components along the  $x$ ,  $y$  and  $z$  directions, respectively,  $\partial\gamma/\partial C$  is the concentration coefficient of surface tension and  $\partial\gamma/\partial T$  is the temperature coefficient of surface tension. As shown in Eq. (6.6), the  $u$  and  $v$  velocities at the surface are determined from the surface tension gradient effect. The  $w$  velocity is zero since there is no flow of liquid metal perpendicular to the pool top surface.

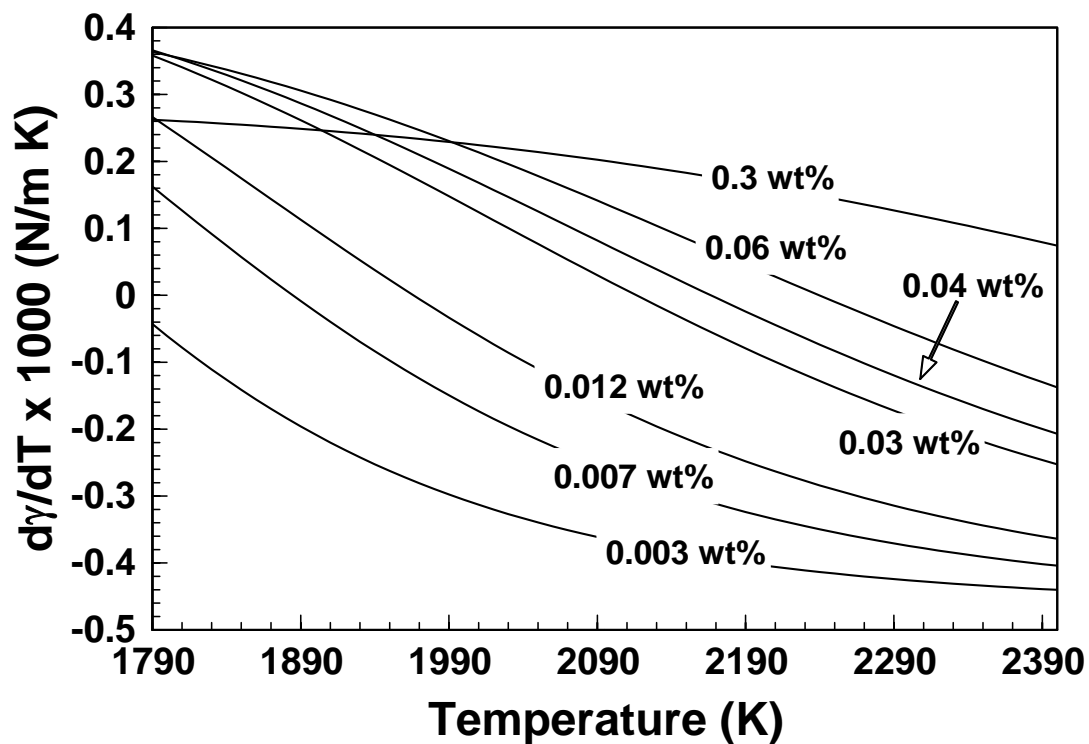


Fig. 6.2. Temperature coefficient of surface tension,  $d\gamma/dT$ , as a function of temperature for stainless steel specimens containing 0.003 wt%, 0.007 wt%, 0.012 wt%, 0.03 wt%, 0.04 wt% , 0.06 wt% and 0.3 wt% sulfur.

### 6.2.2 Loss of sulfur from the top surface

Because of the high temperatures involved during fusion welding vaporization of alloying elements takes place from the top surface. Sulfur is also lost from the surface and this fact is incorporated into the model by applying a mass loss boundary condition at the top surface. The loss of sulfur from the top surface involves two steps: (i) transfer of sulfur from the bulk to the free surface and (ii) vaporization of sulfur from the free surface. The flux of sulfur from the bulk to the free surface,  $J_S$ , is given as [17]:

$$J_S = -D \frac{dC}{dz} = D \frac{C_{\text{sur}} - C_{\text{bulk}}}{\Delta z} \quad (6.7)$$

where  $D$  is the diffusion coefficient of sulfur in molten steel,  $C_{\text{sur}}$  is the concentration of sulfur at the top surface,  $C_{\text{bulk}}$  is the concentration of sulfur in the bulk and  $\Delta z$  is the distance along the  $z$ -direction. The evaporation flux of sulfur vapor,  $J_B$ , is given as [18]:

$$J_B = k_{M,e} (C_{\text{sur}} - C_{\text{amb}}) \quad (6.8)$$

where  $k_{M,e}$  is the evaporation mass transfer coefficient and  $C_{\text{amb}}$  is the concentration of sulfur in the vapor phase. Assuming mass conservation at the top surface,  $J_S$  becomes equal to  $J_B$ . Combining Eqs. (6.7) and (6.8) and assuming  $C_{\text{amb}}$  equal to zero gives the mass loss boundary condition at the top surface as:

$$C_{\text{sur}}(i+1) = C_{\text{bulk}}(i) - \frac{k_{M,e} \times C_{\text{sur}}(i)}{D / \Delta z} \quad (6.9)$$

where  $i$  denotes the current iteration and  $i+1$  denotes the next iteration and  $\Delta z$  is the distance along the  $z$ -direction.

The value of  $K_{M,e}$  was obtained from the study of Ohno and Ishida [19]. They [19] heated iron-sulfur (Fe-S) alloys, containing 0.18 to 0.42 wt% sulfur, to  $1873 \pm 20$  K in a high-frequency induction furnace under 1 atm pressure of argon. Then, maintaining the same temperature, they [19] kept the alloys under vacuum ( $10^{-2} - 10^{-3}$  mm Hg) for 5, 10 and 15 minutes and measured the amount of sulfur loss in each case. They [19] calculated the specific evaporation constant or the evaporation mass transfer coefficient,  $K_i$  (cm/s), for sulfur by using the following expression:

$$-\frac{d[\%i]}{dt} = K_i \frac{A}{V_0 - vt} [\%i] \quad (6.10)$$

where %i is the concentration of sulfur in wt%, t is time in s, A is the surface area of the melt in cm<sup>2</sup>, V<sub>0</sub> is the initial volume of the melt in cm<sup>3</sup> and v is the volume change of the melt in cm<sup>3</sup>/s. Four alloys having different sulfur contents were studied. The value of v was approximately independent of time and was experimentally determined for each alloy. Taking log of Eq. (6.10) and rearranging gave:

$$\log[\%i] = \log[\%i]_0 + \frac{1}{v} K_i A \log\left(\frac{V_0 - vt}{V_0}\right) \quad (6.11)$$

Ohno and Ishida [19] plotted sulfur concentration versus  $\log(V/V_0)$ , as shown in Fig. 6.3, where V is equal to  $V_0 - vt$ . For each alloy, four data points were plotted as shown in Fig. 6.3, which correspond to keeping the heated alloys under vacuum for 0, 5, 10 and 15 minutes, respectively. The initial sulfur content of an alloy corresponds to time,  $t = 0$  in Eq. (6.11). A linear relationship was obtained for each alloy in Fig. 6.3, indicating that first order kinetics was followed. Using Eq. (6.11) and the slopes of the lines in Fig. 6.3, Ohno and Ishida [19] calculated the value of  $K_i$  for each alloy. The values of  $K_i$  for the four alloys were as follows: alloy with 0.18 wt% sulfur -  $K_i = 6.6 \times 10^{-6}$  m/s; alloy with 0.26 wt% sulfur -  $K_i = 6.7 \times 10^{-6}$  m/s; alloy with 0.35 wt% sulfur -  $K_i = 8.4 \times 10^{-6}$  m/s; and alloy with 0.42 wt% sulfur -  $K_i = 7.0 \times 10^{-6}$  m/s. Based on these values of  $K_i$ , an average value of  $7.2 \times 10^{-6}$  m/s has been used for  $K_{M,e}$  in the present study. The data used in the calculations are given in Table 6.3. The same set of data was used for all the three kinds of stainless steels listed in Table 6.1 because the difference in the values of physical properties of these steels was less than 2% [20]. Owing to the low value of  $K_{M,e}$ , the sulfur loss from the top surface was not significant in the present study.

Table 6.3. Data used in the calculations.

Problem data/physical property	Value	Reference
Liquidus Temperature, $T_l$ (K)	1785.0	[21]
Solidus temperature, $T_s$ (K)	1745.0	[21]
Density of metal, $\rho$ (kg/m <sup>3</sup> )	7200.0	[21]
Thermal conductivity of solid, $k_s$ (J/m-s-K)	25.08	[21]
Specific heat of solid, $C_{ps}$ (J/kg-K)	702.24	[21]
Specific heat of liquid, $C_{pl}$ , (J/kg-K)	806.74	[21]
Temperature coefficient of surface tension, $d\gamma/dT$ (N/m-K)	$-0.47 \times 10^{-3}$	[21]
Coefficient of thermal expansion, $\beta$ (K <sup>-1</sup> )	$1.50 \times 10^{-6}$	[21]
Viscosity of molten iron, $\mu_{fl}$ (kg/m-s)	$6.70 \times 10^{-3}$	[21]
Surface excess of sulfur at saturation, $\Gamma_s$ (mol/m <sup>2</sup> )	$1.30 \times 10^{-3}$	[2]
Enthalpy of adsorption for sulfur, $\Delta H^0$ (J/kg-mol)	$-1.66 \times 10^6$	[2]
Entropy factor, $k_1$	$3.18 \times 10^{-3}$	[2]

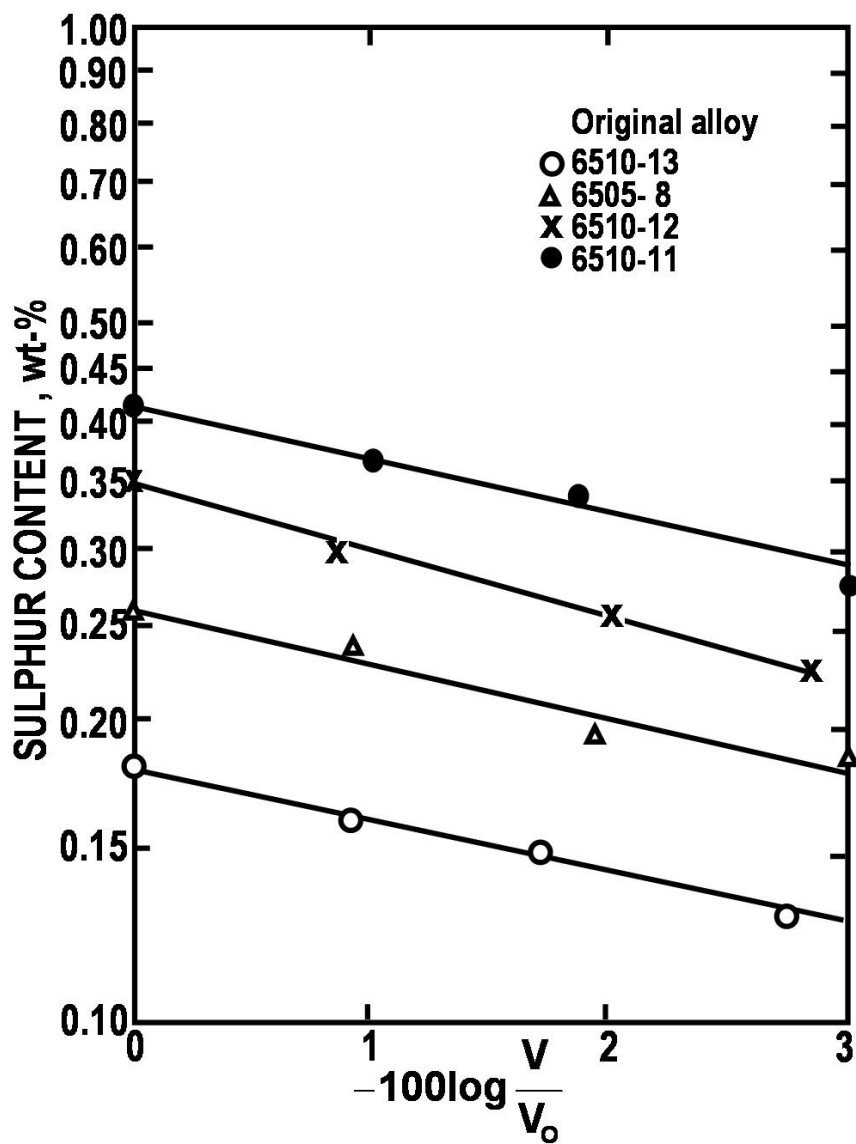


Fig. 6.3. Desulphurization of Fe-S alloys at 1600 °C [19].  $V$  is equal to  $V_0 - vt$ , where  $V_0$  is the initial volume of the melt in  $\text{cm}^3$ ,  $v$  is the volume change of the melt in  $\text{cm}^3/\text{s}$ , and  $t$  is time in s. Initial sulfur contents of the four alloys were: 6510-13 had 0.18 wt%, 6505-8 had 0.26 wt%, 6510-12 had 0.35 wt% and 6510-11 had 0.42 wt%. The data points for each alloy correspond to keeping the heated alloys under vacuum for 0, 5, 10 and 15 minutes, respectively.

## **6.3 Results and Discussion**

### **6.3.1 Role of phosphorus as a surface active element**

Besides sulfur, other elements like oxygen and phosphorus are also surface active in nature and affect the surface tension of molten steel [2,22]. In the three kinds of stainless steels used in the present study, some amount of phosphorus is also present. Fig. 6.4 shows the variation of surface tension of liquid iron with the amount of different surface active elements. It can be seen from this figure that phosphorus has a very small influence on the surface tension of liquid iron. Therefore, the effect of phosphorus as a surface active element was neglected in the present study.

### **6.3.2 Evolution of weld pool geometry on welding two plates with same sulfur contents**

The evolution of weld pool geometry on welding two plates with same sulfur contents has been well understood in the literature [1-12]. Therefore, as a first step, the numerical transport phenomena based model developed in the present study was validated by applying it to gas tungsten arc (GTA) welding of stainless steel plates having same sulfur contents. The calculated weld pool penetration and width are compared with the corresponding experimental results in Table 6.4. The data sets in Table 6.4 are arranged in a manner such that case numbers 1 and 2 have the same energy input but different sulfur contents. Similar argument applies to case numbers 3 and 4, and case numbers 5 and 6 also. Thus, the effect of sulfur on weld pool geometry can be clearly observed. The experimental and calculated weld pool geometries corresponding to cases 1 to 6 in Table 6.4 are shown in Fig. 6.5(a) to (f), respectively.

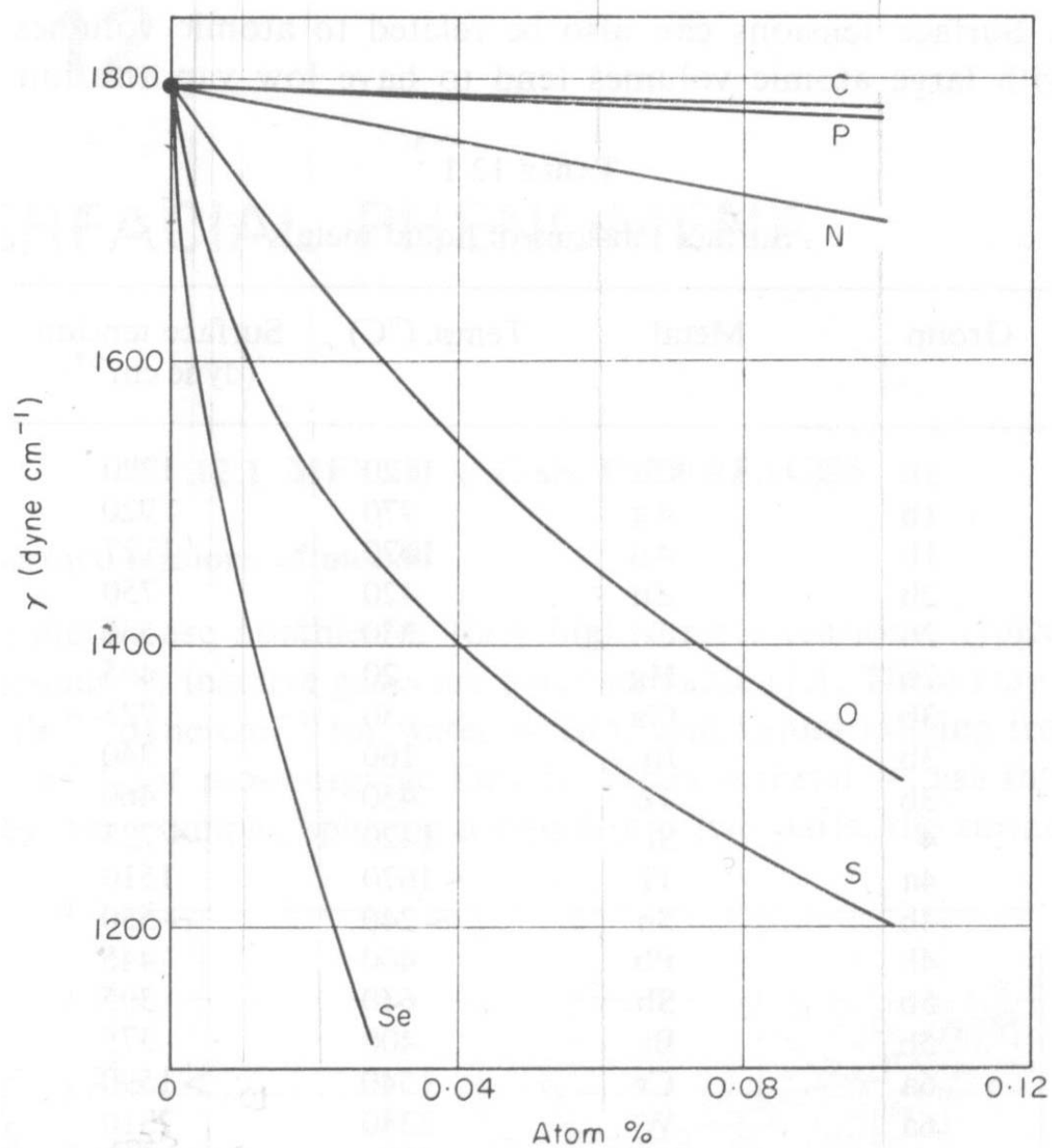


Fig. 6.4. Surface tension versus atom% for solutions of C, P, N, O, S and Se in liquid iron at 1823 K [22]. After P. Kozakevitch, in "Surface Phenomena of Metals", Society of Chemical Industry Monograph 28 (1968) p. 223.

The effect of sulfur on weld pool geometry can be described by comparing one pair in Fig. 6.5 where the energy input was the same but the sulfur contents were different, i.e., Fig. 6.5(c) and (d). These two figures show the experimental and the calculated weld pool geometries for stainless steel welds containing 0.003 wt% and 0.293 wt% sulfur, respectively. It can be seen that the weld containing 0.293 wt% sulfur has a much deeper penetration than that containing 0.003 wt% sulfur. This result can be explained on the basis of the convection dominant heat transport in the weld pool. The relative importance of convection and conduction in the overall transport of heat in the weld pool can be assessed from the value of the Peclet number,  $Pe_h$ , which is given by:

$$Pe_h = \frac{u\rho C_p L}{k} \quad (6.12)$$

where  $u$  is the velocity,  $\rho$  is the density,  $C_p$  is the specific heat at constant pressure,  $L$  is the characteristic length, and  $k$  is the thermal conductivity of the melt. When  $Pe_h$  is large, which in physical terms means large melt velocity, large weld-pool, and poor thermal conductivity, heat is transported primarily by convection. The  $Pe_h$  values for the six cases listed in Table 6.4 and shown in Fig. 6.5(a) to (f) are calculated in Table 6.5. The maximum values of the Peclet number for the two cases being compared, i.e., Fig. 6.5(c) and (d) are 31 and 20, respectively. Such high Peclet numbers indicate that convection is dominant in transporting the heat in the weld pool. As a result, the weld pool geometry is largely determined by the direction of the liquid flow. The direction of liquid flow is in turn governed by the sign of  $\partial\gamma/\partial T$ . For Fig. 6.5(c), the sulfur content is 0.003 wt%. Referring to Fig. 6.2 it can be seen that for 0.003 wt% sulfur,  $\partial\gamma/\partial T$  is negative for the entire temperature range, i.e., the entire weld pool top surface in Fig. 6.5(c). The negative value of  $\partial\gamma/\partial T$  results in an outward flow and consequently a shallow and wide weld pool is formed. In Fig. 6.5(d), the specimen contains 0.293 wt% sulfur, and Fig. 6.2 shows that for such high sulfur contents  $\partial\gamma/\partial T$  is positive over the entire temperature range. Positive  $\partial\gamma/\partial T$  causes the convection pattern to be radially inwards resulting in a deep and narrow weld pool. The directions of the liquid velocities and the weld pool shape and size in Fig. 6.5(c) and (d) are consistent with the above observation. Similar comparison can be made between Fig. 6.5(a) and (b) and Fig. 6.5(e) and (f). Good agreement between the

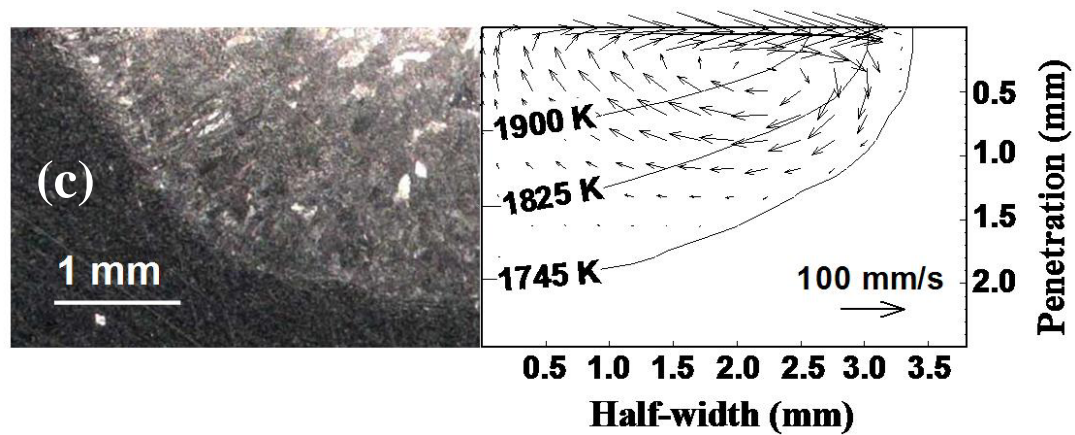
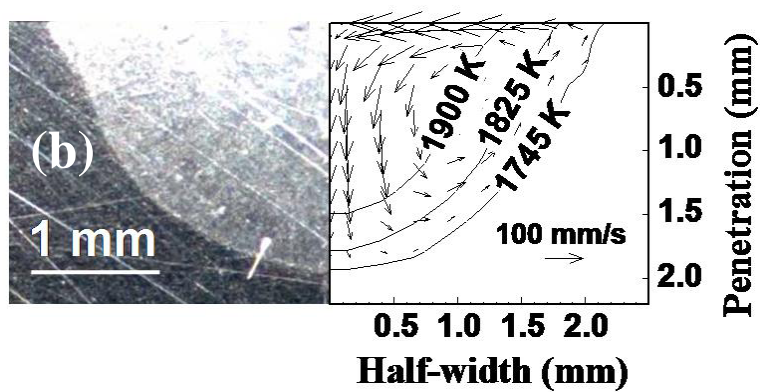
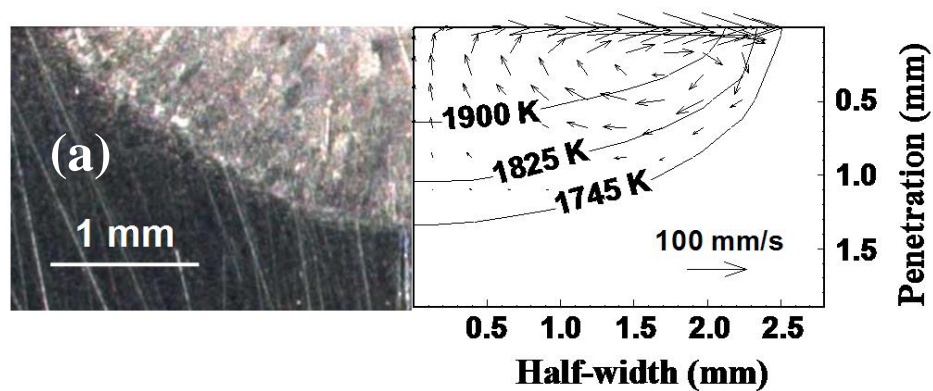
calculated and measured weld pool geometries in all the cases shown in Fig. 6.5(a) to (f), corresponding to cases 1 to 6 in Table 6.4, indicate that the role of sulfur on the weld pool geometry could be reasonably predicted by the numerical transport phenomena based model.

Table 6.4. Welding variables and experimentally measured weld pool penetration and width. The experimental data was provided by Dr. T. J. Lienert and Dr. M. Johnson of Los Alamos National Laboratory. 'Exp' stands for experimental results while 'Cal' stands for calculated results.

Case no.	Current (A)	Voltage (V)	Welding speed (mm/s)	Sulfur (wt%)	Weld pool penetration (mm)		Weld pool width (mm)	
					Exp	Cal	Exp	Cal
1	101	9.6	1.7	0.003	1.37	1.36	4.83	4.93
2	100	9.6	1.7	0.024	1.94	1.97	4.37	4.41
3	150	9.9	1.7	0.003	2.18	2.02	6.80	6.93
4	150	10.5	1.7	0.293	3.12	3.09	5.91	6.07
5	100	10.0	3.4	0.024	1.22	1.27	4.15	4.13
6	101	9.9	3.4	0.293	1.39	1.41	4.05	4.10

Table 6.5. The values of Peclet numbers ( $Pe_h$ ) for heat transfer for the six cases listed in Table 6.4 and shown in Fig. 6.5.

Case no.	Velocity, $u$ (m/s)	Density, $\rho$ ( $\text{kg/m}^3$ )	Specific heat, $C_p$ (J/kg-K)	Length, $L$ (m)	Thermal conductivity, $k$ (W/m-K)	Peclet number, $Pe_h$
1	0.235	7200	807.1	0.0012	125.5	13
2	0.256	7200	807.1	0.0011	125.5	13
3	0.384	7200	807.1	0.0017	125.5	31
4	0.279	7200	807.1	0.0015	125.5	20
5	0.208	7200	807.1	0.0010	125.5	10
6	0.263	7200	807.1	0.0010	125.5	13



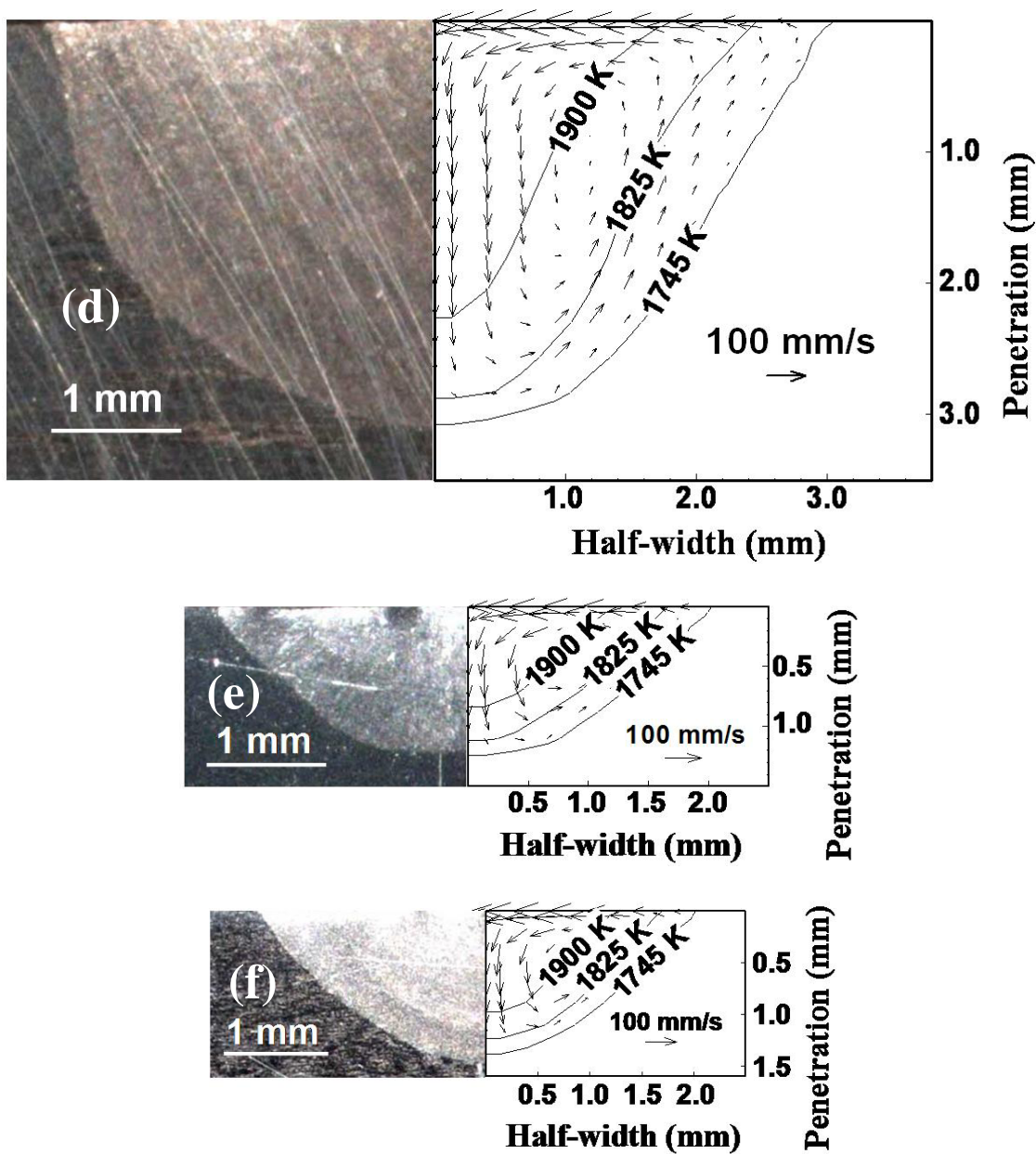


Fig. 6.5. Experimental and calculated weld pool geometry, (a) to (f), for the six sets of welding conditions given in cases 1 to 6 of Table 6.4, respectively. The 1745 K isotherm is the equilibrium solidus temperature of stainless steel, which marks the weld pool boundary.

### 6.3.3 Geometry of weld pool during welding of two plates with different sulfur concentrations

The welding conditions for the experiments where the two welded specimens contained different amounts of sulfur are listed in Table 6.2 in case numbers 7 to 18. The welding cases in Table 6.2 are organized such that sets of three cases, for example, case numbers 7 to 9 have the same energy input but different combinations of the stainless steels (SS) used in the present study. The left plate always has the stainless steel with the lower sulfur content. In case 7, 304L SS is welded to 303 SS, in case 8, 304RL SS is welded to 303 SS, and in case 9, 304L SS is welded to 304RL SS. Case numbers 10 to 12, 13 to 15, and 16 to 18 are organized in the same manner. For the same SS combination, the energy input decreases in the following order:  $7 > 10 > 13 > 16$ . Such an organization of results will facilitate easy analysis of the effect of energy input and SS combination on the weld pool geometry.

First, it is important to analyze the key features of the welded specimens and the welding conditions so that they can be incorporated in the modeling. Fig. 6.6 shows the experimental micrograph for case number 13 of Table 6.2, where a 304L SS plate (left plate) having low sulfur content (0.003 wt%) is welded to a 303 SS plate (right plate) having very high sulfur content (0.293 wt%). The joint of the two plates is denoted by the vertical white line next to location 'A' in Fig. 6.6. Following are some key features associated with this micrograph:

- (a) The weld pool is shifted towards the lower sulfur plate with less melting on the high sulfur side. This is known as the lack-of-fusion defect [12] and it results in improper joining of the two pieces.
- (b) The point of maximum penetration, C, is shifted by a distance AB from the joint of the two plates. The length AB is also known as the center line shift (CLS) [12].
- (c) During experiments, the arc shifted towards the low sulfur side. Similar observation has been reported in the literature [10]. The occurrence of arc shift has been demonstrated in the present study by conducting the following experiment. Looking from the left hand side of the setup shown in Fig. 6.7, in the first half of the setup, a low sulfur plate (304L – 0.003 wt% sulfur) was kept on the right hand side and a high sulfur plate (304RL – 0.024

wt% sulfur) was kept on the left hand side. After half way, the plates were reversed, i.e., the left plate was made the low sulfur plate and the right plate the high sulfur plate as shown in Fig. 6.7. The resulting shift of the weld bead top surface and the arc towards the low sulfur side can be seen in Fig. 6.7 and Fig. 6.8, respectively. Fig. 6.8(a) corresponds to welding of the first half of the setup shown in Fig. 6.7 and therefore, the arc is shifted towards right, i.e., the location of the low sulfur plate (304L). Fig. 6.8(b) corresponds to welding of the latter half of the setup causing the arc to shift towards left, i.e., the new location of the low sulfur plate (304L). The role of arc shift on the formation of the weld pool is examined in this thesis.

(d) An undercut can be seen on the high sulfur side, while an over-fill can be seen on the low sulfur side, indicating a net movement of mass from the high sulfur side to the low sulfur side. Comparison of all the experiments shows that the undercut is more severe in cases involving 303 SS, which has very high sulfur content. The occurrence of undercut can be explained qualitatively by the surface tension driven fluid flow suggested by Heiple et al. [5]. They [5] stated that the plate with lower sulfur content has relatively higher surface tension than the one with higher sulfur content. The result is a net surface tension gradient across the weld pool leading to surface fluid flow toward the side of the plate with less sulfur. This flow pattern should cause the net movement of mass from the high sulfur side to the low sulfur side. However, they [5] did not experimentally determine the flow during welding. They also did not calculate the flow. However, once the weld pool is formed, liquid metal in the weld pool circulates vigorously causing mixing of sulfur from the two plates. Actual surface tension gradient will depend on the sulfur distribution in the weld pool. A proper quantitative understanding of the occurrence and extent of undercut is still lacking. The weld pool surface is assumed to be flat in the present study for the sake of simplicity.

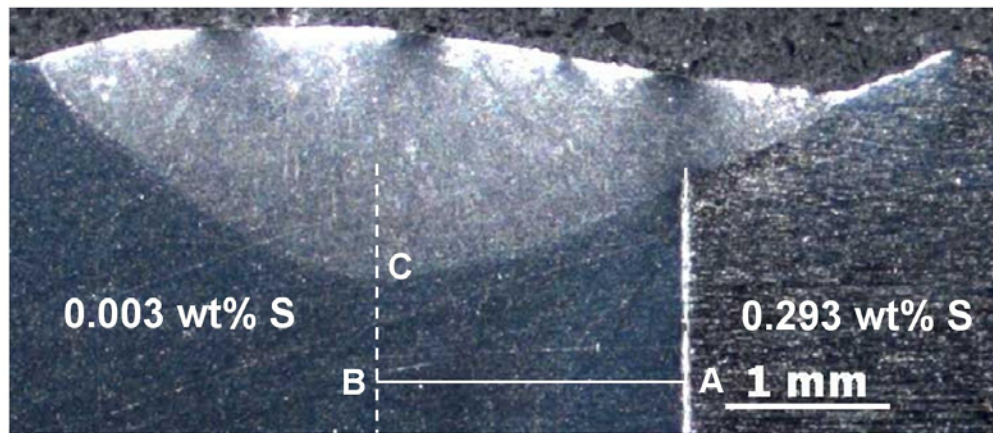


Fig. 6.6. Weld pool geometry when welding a stainless steel plate having low sulfur content (0.003 wt%) with a plate having very high sulfur content (0.293 wt%). The white line at location 'A' indicates the joint of the two plates. Location 'C' indicates the point of maximum penetration. Line 'AB' denotes the shift of the point of maximum penetration from the joint of the two plates. The length of line 'AB' is called the center line shift (CLS). Welding conditions: 100 A, 9.8 V, welding speed is 1.7 mm/s.

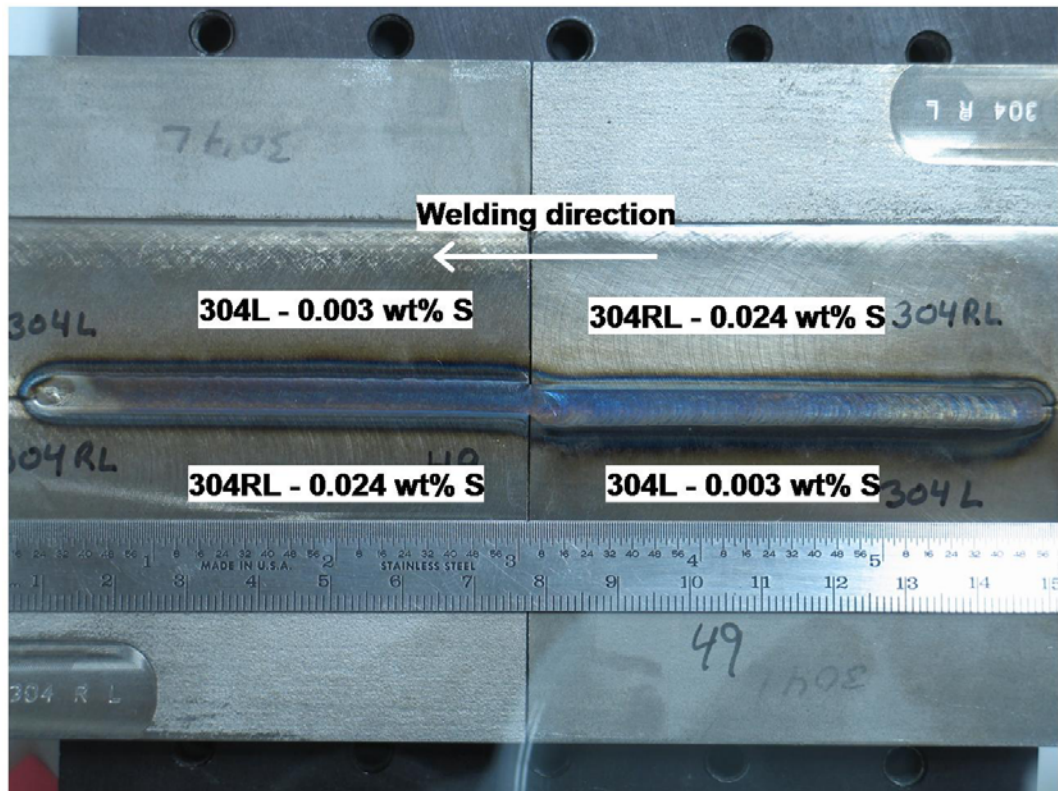


Fig. 6.7. An experiment to demonstrate the shifting of the arc towards the low sulfur side. Looking from the left side of the setup, first a low sulfur plate (304L – 0.003 wt% sulfur) on the right was welded to a high sulfur plate (304RL – 0.024 wt% sulfur) on the left. After half way the plates were reversed as shown in the figure.

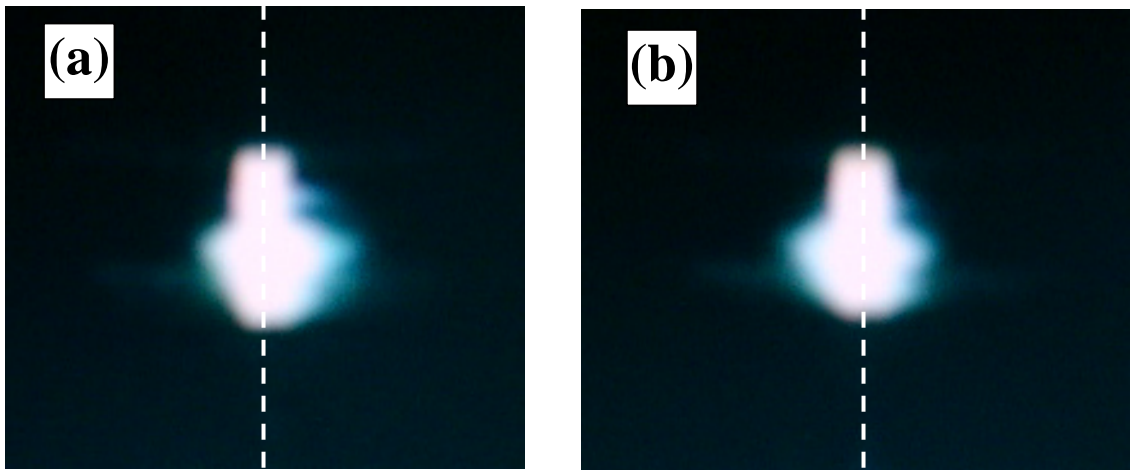


Fig. 6.8. The shifting of the arc towards the low sulfur side. The pictures of the arc were taken from the left side of the setup shown in Fig. 6.7. The vertical dotted line shows the center line of the weld. (a) The arc can be seen shifted towards right, i.e., towards the low sulfur side (304L plate). (b) The arc is seen shifted towards left because after halfway the low sulfur plate (304L) is kept on the left side as shown in Fig. 6.7.

The reasons for the shifting of the arc are not available in the literature. A possible explanation can be the presence of easily ionized metal vapor selectively above the low sulfur containing plate. The resulting improvement in the electrical conductivity of the arc plasma above the low sulfur plate may lead to arc shift. Dunn and Eagar [23] noted that the conductivity of arc plasma can be increased several orders of magnitude even by very small amounts of easily ionized metal vapors. During welding of alloys, metals vaporize from the weld pool surface. Argon is generally used as the shielding gas and most metals have ionization potentials significantly lower than that of argon [23]. As a result, argon plasma contains ionized metal vapors leading to enhanced electrical conductivity of the plasma [23]. Abbaoui et al. [24] calculated the thermal and electrical conductivities of argon plasmas containing a variety of metal vapors, and showed that the ionization potential of the metal contaminant is the predominant criterion in determining the magnitude of the increase in plasma conductivity. Furthermore, the higher the amount of ionized metal vapor, the higher is the electrical conductivity of the plasma [23].

The degree of ionization of different metals with temperature is given in Fig. 6.9 [25]. It can be seen that metals such as potassium, sodium and manganese can be easily ionized at normal arc temperatures, and would be important in enhancing the conductivity of the plasma. When sulfur is present in stainless steel, it has a profound influence on the activity of these metals in steel. For example, the activity of manganese is given by [26]:

$$[a_{\text{Mn}}] = f_{\text{Mn}} [\text{wt\% Mn}] \quad (6.13)$$

where  $f_{\text{Mn}}$  is the activity coefficient of manganese. The expression for  $f_{\text{Mn}}$  is given as [26]:

$$\log[f_{\text{Mn}}] = \log[f_{\text{Mn}}^0] + [\text{wt\% Sulfur}]e_{\text{Mn}}^{\text{S}} + \sum([\text{wt\% } j]e_{\text{Mn}}^j) \quad (6.14)$$

where  $e_{\text{Mn}}^{\text{S}}$  is the interaction parameter of Mn with sulfur,  $j$  represents other elements in the steel and  $e_{\text{Mn}}^j$  is the interaction parameter of Mn with element  $j$ . The value of  $e_{\text{Mn}}^{\text{S}}$  is  $-4.3 \times 10^2$  [26]. A negative value of  $e_{\text{Mn}}^{\text{S}}$  means that with the increase in the sulfur content the value of  $\log(f_{\text{Mn}})$  in Eq. (6.14) decreases and as a result the value of activity of

manganese given by Eq. (6.13) also decreases. Thus, there will be a lower concentration of manganese vapors on the high sulfur side resulting in shifting of the arc towards the low sulfur side.

An important question is how much should the arc be shifted from the joint of the two plates? Experimental measurements of arc shift are too difficult to conduct. Some guideline about the location of the arc can be obtained from the location of maximum weld pool penetration. During welding, the maximum heat is supplied directly below the arc and this leads to the maximum penetration at or very near to that location. Therefore, the location of maximum penetration is assumed to be the location of the arc axis in the present study. The arc shift is quantified by the center line shift (CLS), which is given by the length of line AB in Fig. 6.6. Table 6.6 lists the CLS values for all the dissimilar sulfur specimens. It can be seen from Table 6.6 that energy input is an important factor affecting the CLS. For example, for the same SS combination, the CLS for case 1 having higher energy input is higher than that for case 10 having lower energy input. Furthermore, a comparison of cases 1 to 3 shows that for approximately the same energy input, the difference in the sulfur content of the two plates also affects CLS. It is evident from Table 6.6 that the CLS does not depend linearly on the above mentioned factors. A three parameter optimization was conducted to get the values of a, b and c in the following equation from the experimental data in Table 6.6.

$$\text{CLS} = a \times |C_L - C_R|^b \times \left( \frac{I \times V}{U} \right)^c \quad (6.15)$$

The resulting relation between the CLS and the above mentioned factors, i.e., energy input and the difference in sulfur contents of the two plates is given as follows:

$$\text{CLS} = 0.19 \times |C_L - C_R|^{0.24} \times \left( \frac{I \times V}{U} \right)^{0.42} \quad (6.16)$$

where CLS is the center line shift in mm,  $C_L$  is the sulfur content of the left plate in wt%,  $C_R$  is the sulfur content of the right plate in wt%, I is current in Amp, V is voltage in Volts and U is the welding speed in mm/s. The corresponding plot is shown in Fig. 6.10. The symbols represent the experimental data and the line represents a linear fit to the experimental data. The linear fit passes through the origin so that the CLS is zero when

the two plates have the same sulfur content. Tinkler et al. [12] also explored the link between sulfur content and CLS. They [12] welded several stainless steel tubes containing between 15 ppm (1 ppm =  $10^{-4}$  wt%) and 140 ppm sulfur with standard stainless steel tubes containing 15 ppm or 133 ppm sulfur. Their [12] results for the variation of CLS on welding various stainless steel tubes to low sulfur (15 ppm) standard and high sulfur (133 ppm) standard are shown in Fig. 6.11(a) and (b), respectively. All the experiments were performed using the same energy input. In their [12] experiments, the standard tube was kept on the left hand side and the subject tube was kept on the right hand side. The  $x=0$  location corresponded to the joint of the two plates. Since the weld pool shifts towards the low sulfur side, the CLS values were negative for all the cases involving the low sulfur standard, as shown in Fig. 6.11(a), and positive for majority of cases involving the high sulfur standard as shown in Fig. 6.11(b). In these figures the solid circles represent the results for cases where the two tubes had different sulfur contents, while the crosses represent the cases where the two tubes had the same sulfur contents. When the two tubes had the same sulfur content, the CLS was almost zero. A linear relation was obtained between the CLS and the sulfur content of the subject tubes in both Fig. 6.11(a) and (b). However, the data points were mostly clustered at the two extremes of the sulfur content range considered in the experiments. Furthermore, Tinkler et al. [12] did not take into account the effect of energy input, which is an important factor influencing the CLS, as can be seen from Table 6.6. The empirical relation given in Eq. (6.16) takes into account the effect of both the energy input and the difference in sulfur contents of the two plates, and can be readily used to determine the location of the arc during welding.

Table 6.6. The center line shift (CLS) of all the experimental results for welding of plates with different sulfur contents. SS stands for stainless steel.  $C_L$  is the sulfur concentration in wt% in the left piece while  $C_R$  is the sulfur concentration in wt% in the right piece. The value of energy input (J/mm) is given by (Current×Voltage/Welding speed).

Case no.	SS (Left)	SS (Right)	$ C_L-C_R $ (wt% S)	Current (A)	Voltage (V)	Welding speed (mm/s)	Energy input (J/mm)	CLS (mm)
1	304L	303	0.293	150	10.5	1.7	926.47	2.44
2	304RL	303	0.27	150	10.8	1.7	952.94	2.68
3	304L	304RL	0.023	150	10.5	1.7	926.47	1.77
4	304L	303	0.293	150	10.8	3.4	476.47	2.16
5	304RL	303	0.27	150	10.9	3.4	480.88	2.22
6	304L	304RL	0.023	150	10.7	3.4	472.06	1.32
7	304L	303	0.293	100	9.8	1.7	576.47	1.88
8	304RL	303	0.27	100	10.0	1.7	588.24	1.38
9	304L	304RL	0.023	100	9.9	1.7	582.35	0.8
10	304L	303	0.293	100	10.2	3.4	300.00	1.51
11	304RL	303	0.27	100	10.2	3.4	300.00	1.52
12	304L	304RL	0.023	100	10.0	3.4	294.12	0.8

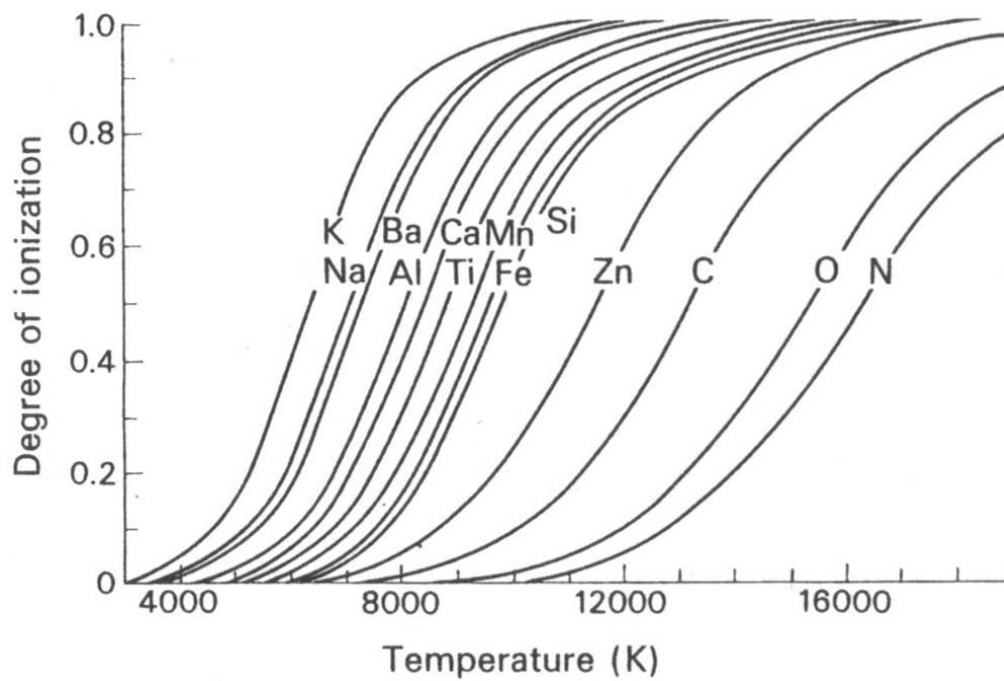


Fig. 6.9. The degree of ionization (logarithmic scale) versus temperature for some gases and metal vapors [25].

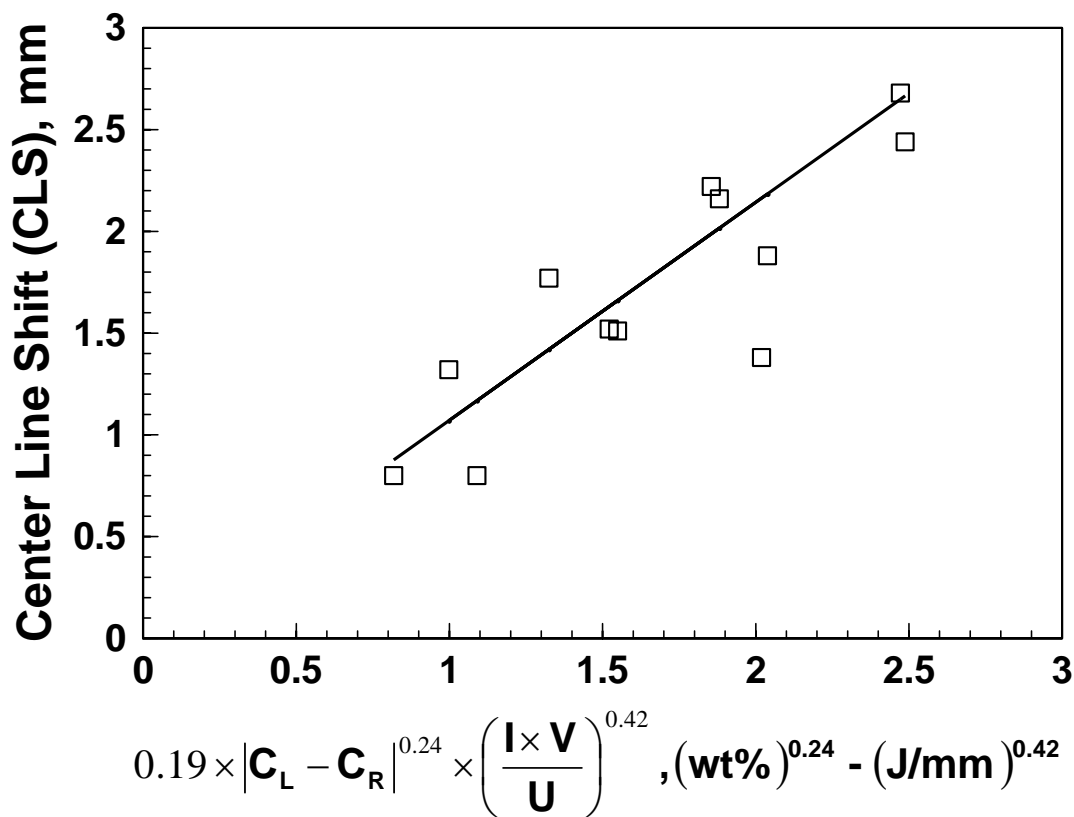


Fig. 6.10. Relation between the center line shift (CLS) and the two factors affecting it, i.e., absolute value of difference in sulfur content of the two plates and the energy input per unit length. The symbols represent the experimentally measured data while the line represents the linear fit to the experimental data. The symbol  $C_L$  is the sulfur content of the left plate (wt%),  $C_R$  is the sulfur content of the right plate (wt%),  $I$  is current (A),  $V$  is voltage (V) and  $U$  is the welding speed (mm/s).

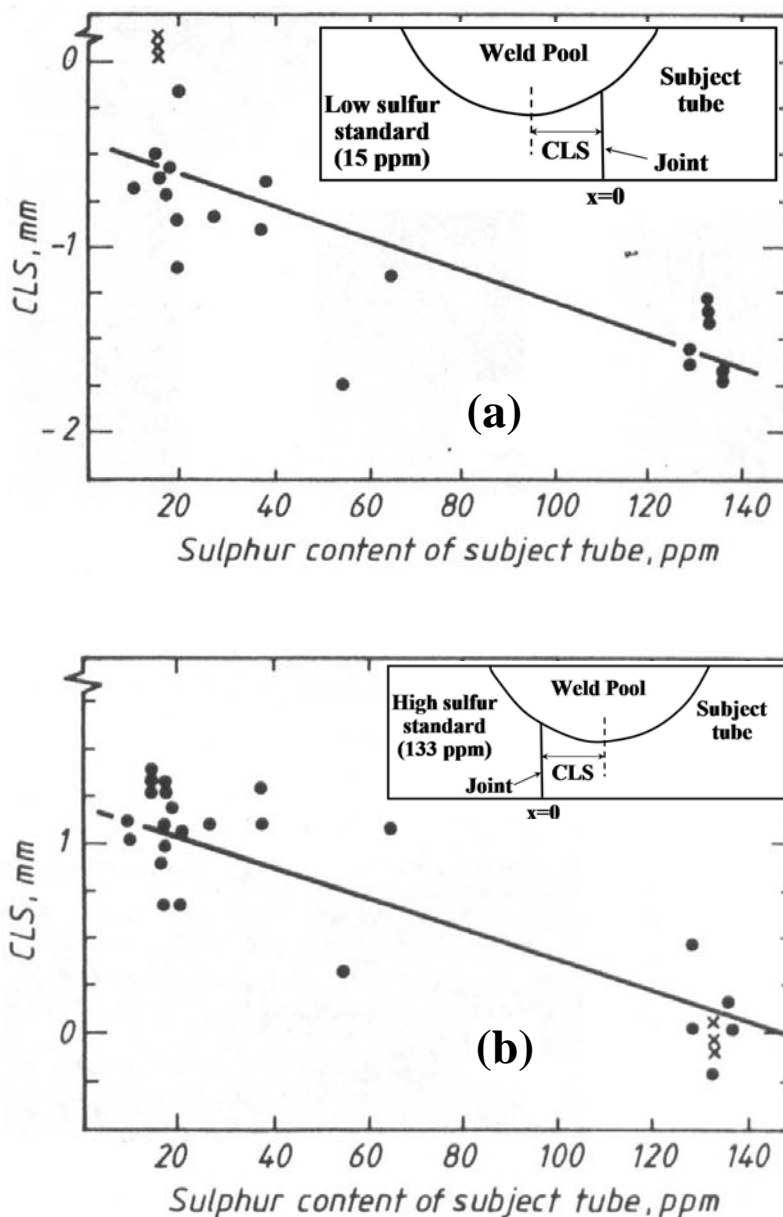


Fig. 6.11. Variation of center line shift (CLS) with sulfur content when subject tubes were welded to: (a) low sulfur standard, i.e., 15 ppm (0.0015 wt%) sulfur, (b) high sulfur standard, i.e., 133 ppm (0.0133 wt%) sulfur [12]. The solid circles represent the results for cases where the two tubes had different sulfur contents. The crosses represent the cases where the two tubes had the same sulfur content. Welding conditions: Start current – 35 A; Finish current – 26 A; Fixture rotation speed – 4.6 revolutions/min, Outer diameter of tubing – 9.5 mm. Unit conversion: 1 ppm =  $10^{-4}$  wt%.

Next, the numerical transport phenomena based model developed in the present study is used to calculate the evolution of weld pool geometry for all the cases listed in Table 6.6. The arc is shifted by a distance equal to the experimentally measured value of CLS in each case. The loss of sulfur from the top surface is taken into account through Eq. (6.9). The calculated weld pool geometries for cases 1 to 12 listed in Table 6.6 are compared with the corresponding experimental micrographs in Fig. 6.12 to Fig. 6.23, respectively. In each figure, part (a) shows the experimental weld pool geometry, part (b) shows the temperature and velocity fields, where the contours show the temperature in degree Kelvin and the vectors show the liquid velocity, and part (c) shows the distribution of sulfur in the weld pool, where the contours show the sulfur concentration in wt% and the vectors show the liquid velocity. The solid vertical line shows the joint of the two plates being welded. The concentration of sulfur in wt% is also marked in the base metal on either side of the joint in part (c) of each figure.

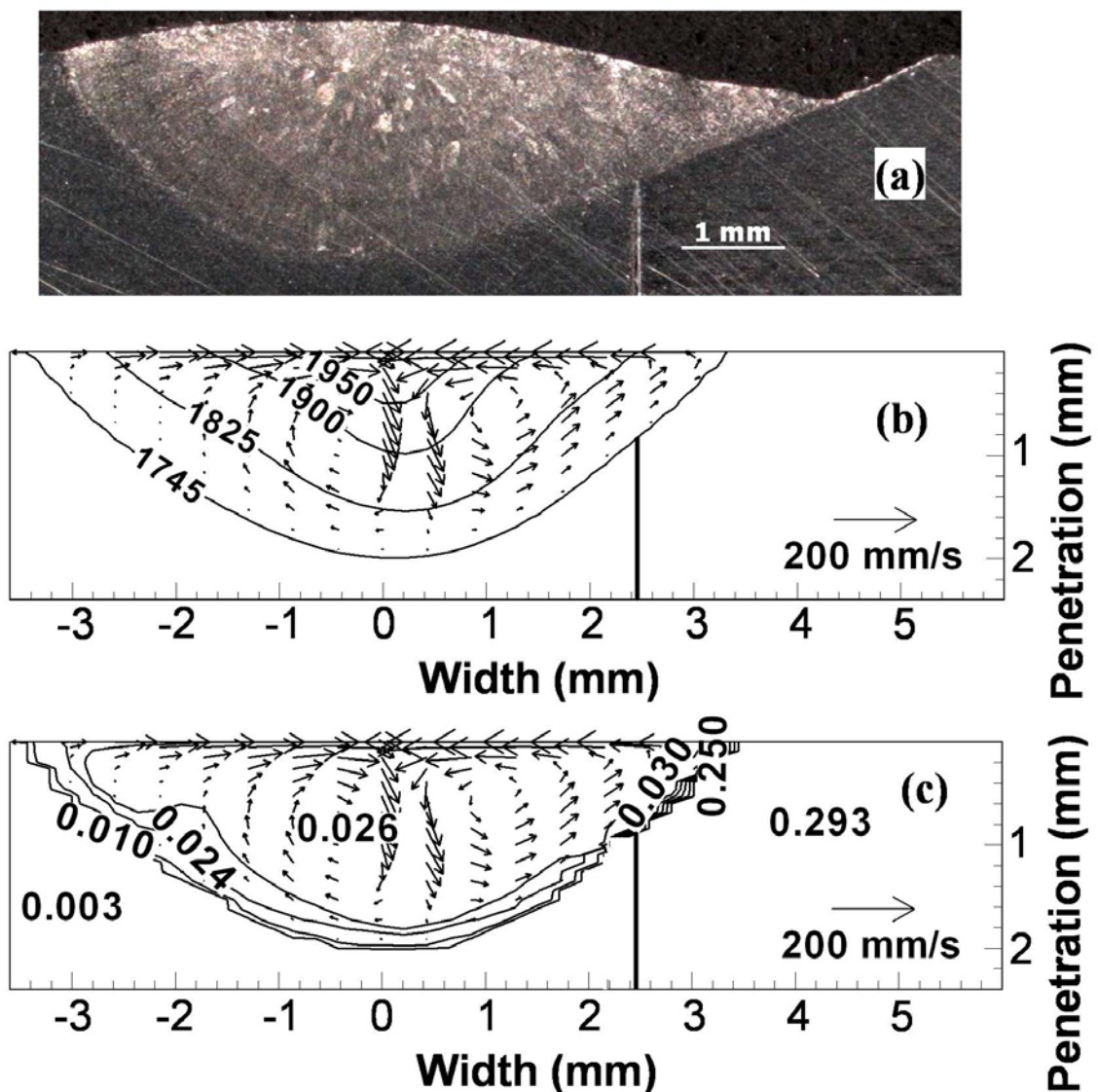


Fig. 6.12. Results for case 1 in Table 6.6. (a) Experimental weld pool geometry. The vertical line shows the joint of the two plates. (b) Calculated temperature and velocity fields in the weld pool. The contours represent the temperatures in degree Kelvin and the vectors represent the liquid velocity. The 1745 K isotherm is the solidus temperature of stainless steel used and marks the weld pool boundary. (c) Calculated concentration of sulfur in the weld pool. The contours represent sulfur concentration in wt%. The sulfur concentration on the top surface and the bulk of the weld pool was about 0.026 wt%. Welding conditions: 150 A, 10.5 V, welding speed is 1.7 mm/s.

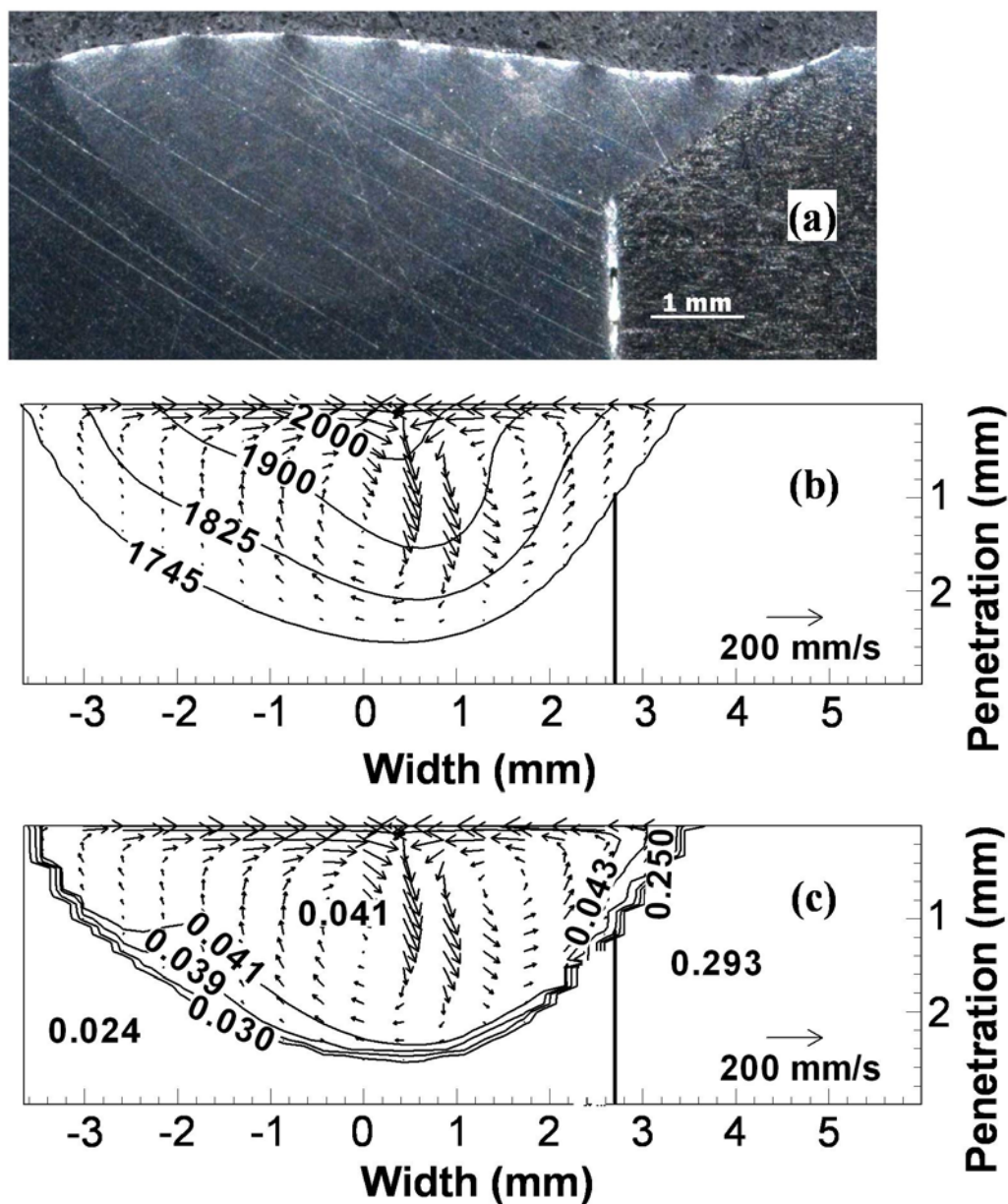


Fig. 6.13. Results for case 2 in Table 6.6. (a) Experimental weld pool geometry. The vertical line shows the joint of the two plates. (b) Calculated temperature and velocity fields in the weld pool. The contours represent the temperatures in degree Kelvin and the vectors represent the liquid velocity. The 1745 K isotherm is the solidus temperature of stainless steel used and marks the weld pool boundary. (c) Calculated concentration of sulfur in the weld pool. The contours represent sulfur concentration in wt%. The sulfur concentration on the top surface and the bulk of the weld pool was about 0.041 wt%. Welding conditions: 150 A, 10.8 V, welding speed is 1.7 mm/s.

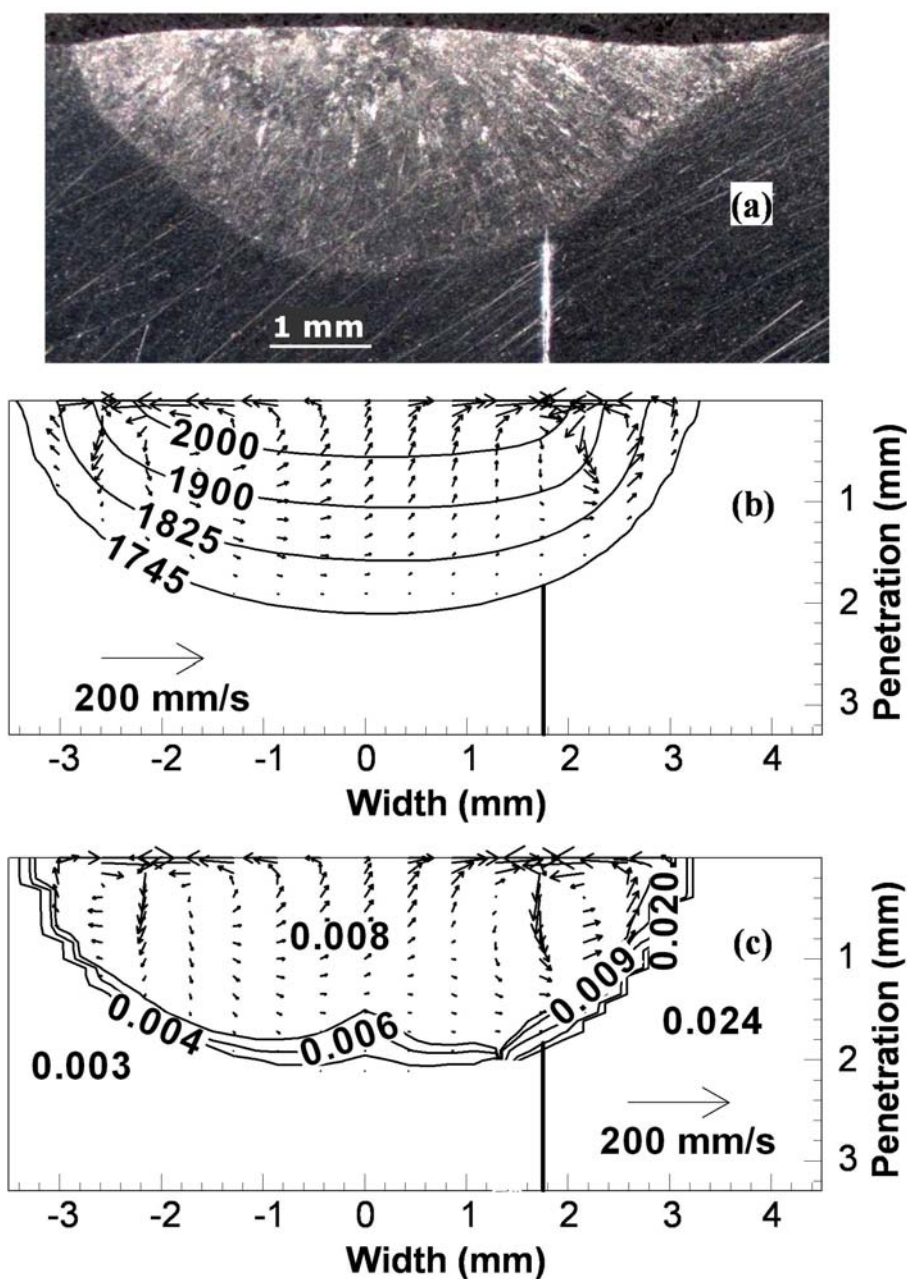


Fig. 6.14. Results for case 3 in Table 6.6. (a) Experimental weld pool geometry. The vertical line shows the joint of the two plates. (b) Calculated temperature and velocity fields in the weld pool. The contours represent the temperatures in degree Kelvin and the vectors represent the liquid velocity. The 1745 K isotherm is the solidus temperature of stainless steel used and marks the weld pool boundary. (c) Calculated concentration of sulfur in the weld pool. The contours represent sulfur concentration in wt%. The sulfur concentration on the top surface and the bulk of the weld pool was about 0.008 wt%. Welding conditions: 150 A, 10.5 V, welding speed is 1.7 mm/s.

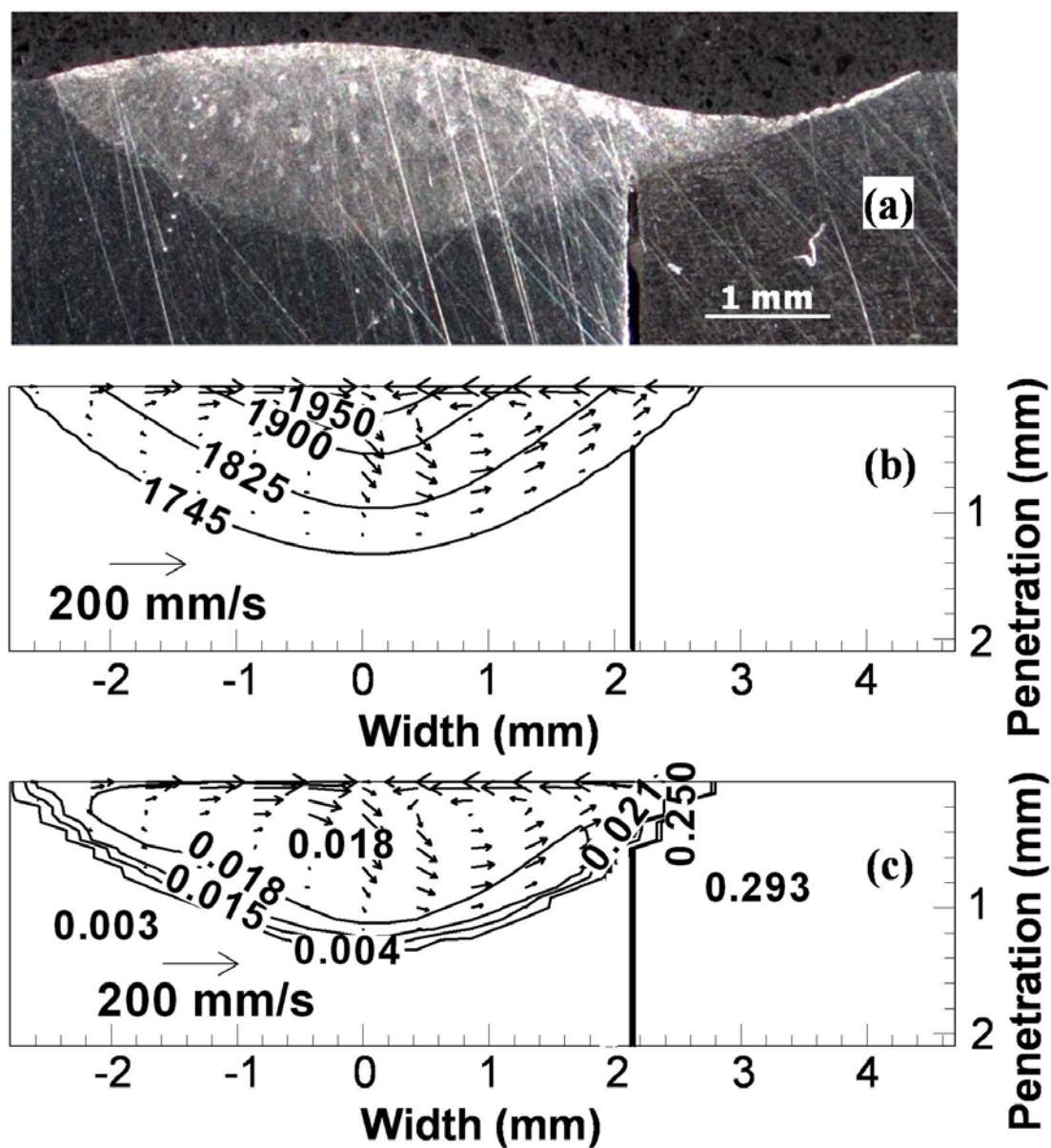


Fig. 6.15. Results for case 4 in Table 6.6. (a) Experimental weld pool geometry. The vertical line shows the joint of the two plates. (b) Calculated temperature and velocity fields in the weld pool. The contours represent the temperatures in degree Kelvin and the vectors represent the liquid velocity. The 1745 K isotherm is the solidus temperature of stainless steel used and marks the weld pool boundary. (c) Calculated concentration of sulfur in the weld pool. The contours represent sulfur concentration in wt%. The sulfur concentration on the top surface and the bulk of the weld pool was about 0.018 wt%. Welding conditions: 150 A, 10.8 V, welding speed is 3.4 mm/s.

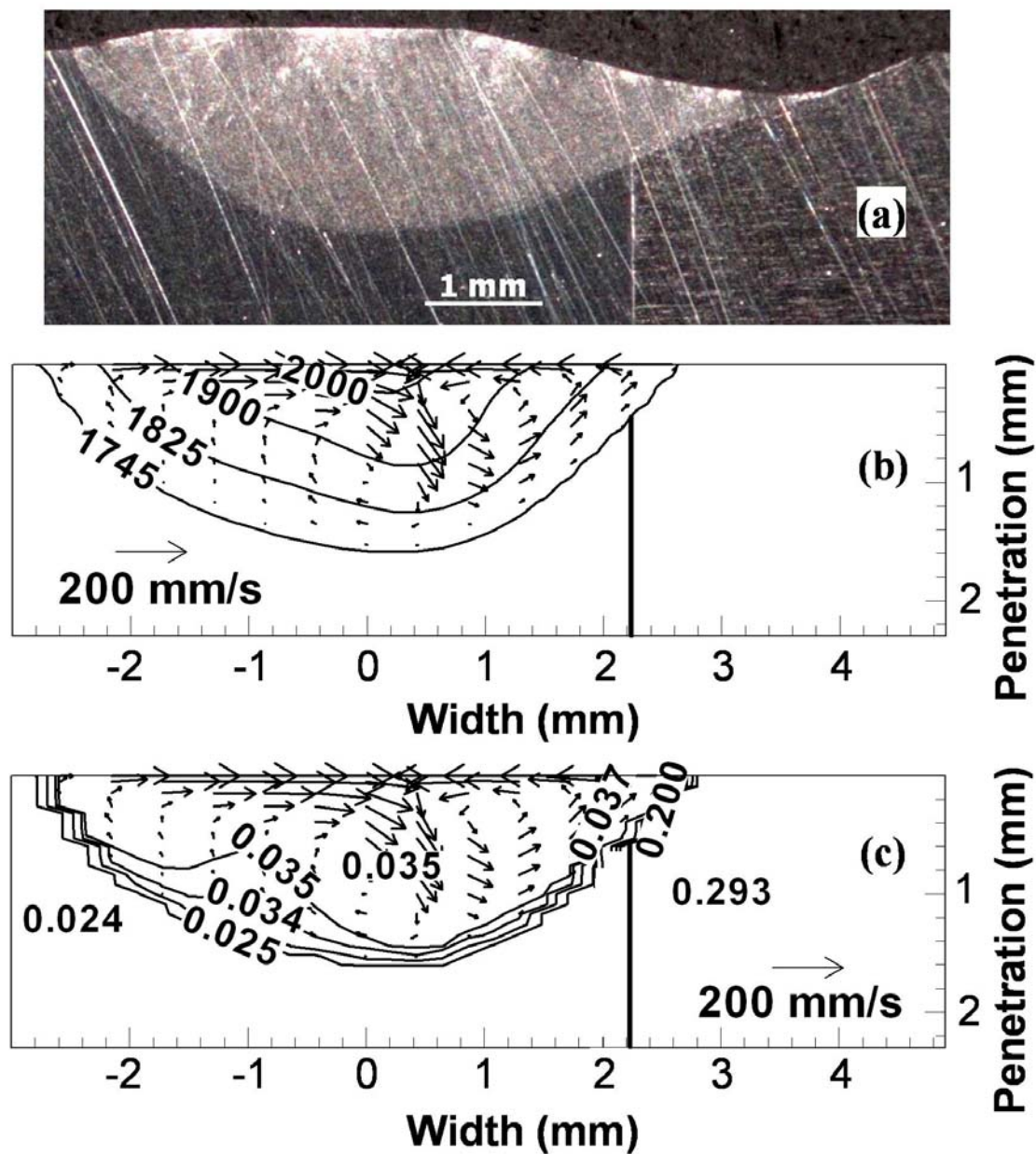


Fig. 6.16. Results for case 5 in Table 6.6. (a) Experimental weld pool geometry. The vertical line shows the joint of the two plates. (b) Calculated temperature and velocity fields in the weld pool. The contours represent the temperatures in degree Kelvin and the vectors represent the liquid velocity. The 1745 K isotherm is the solidus temperature of stainless steel used and marks the weld pool boundary. (c) Calculated concentration of sulfur in the weld pool. The contours represent sulfur concentration in wt%. The sulfur concentration on the top surface and the bulk of the weld pool was about 0.035 wt%. Welding conditions: 150 A, 10.9 V, welding speed is 3.4 mm/s.

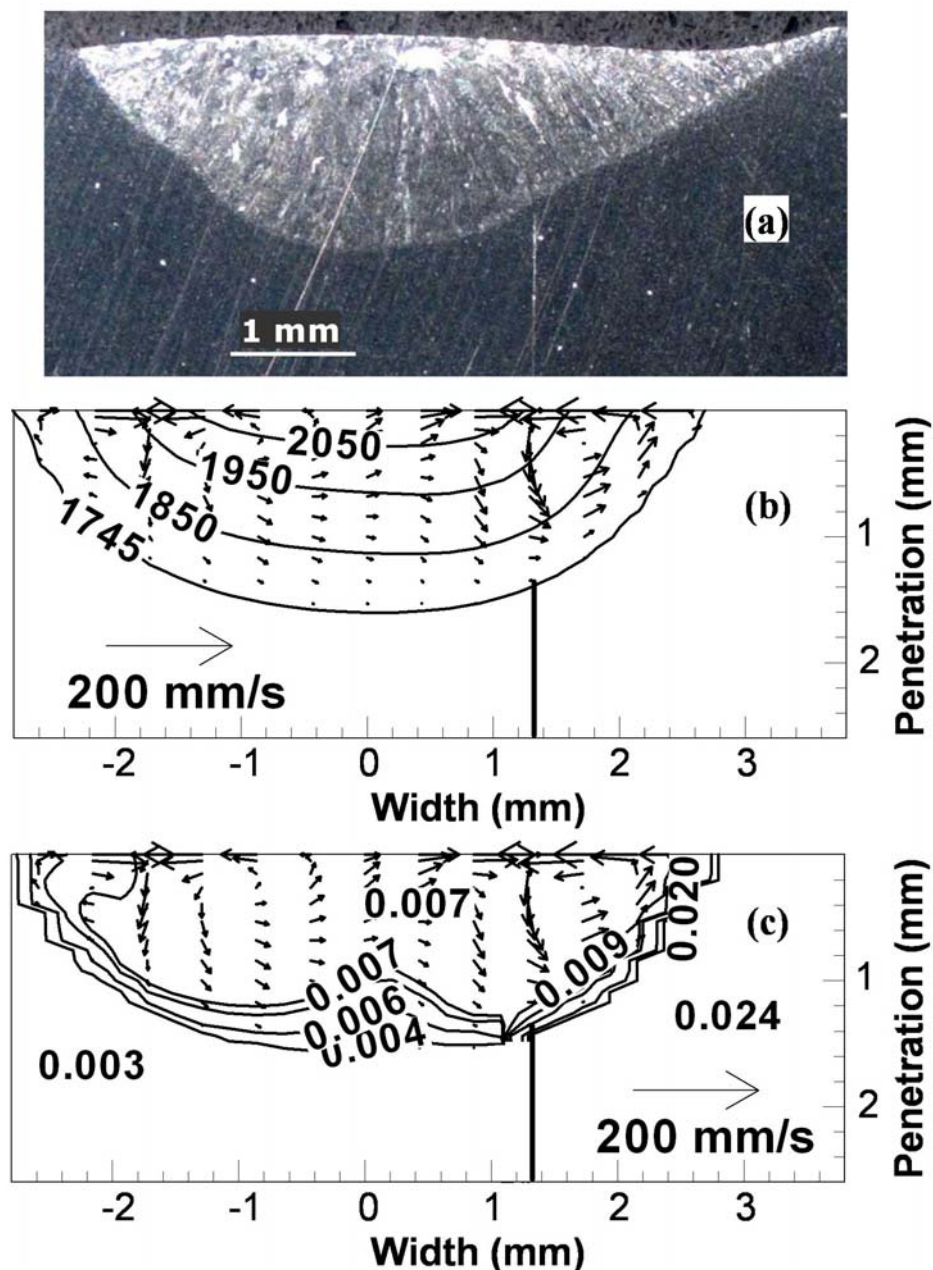


Fig. 6.17. Results for case 6 in Table 6.6. (a) Experimental weld pool geometry. The vertical line shows the joint of the two plates. (b) Calculated temperature and velocity fields in the weld pool. The contours represent the temperatures in degree Kelvin and the vectors represent the liquid velocity. The 1745 K isotherm is the solidus temperature of stainless steel used and marks the weld pool boundary. (c) Calculated concentration of sulfur in the weld pool. The contours represent sulfur concentration in wt%. The sulfur concentration on the top surface and the bulk of the weld pool was about 0.007 wt%. Welding conditions: 150 A, 10.7 V, welding speed is 3.4 mm/s.

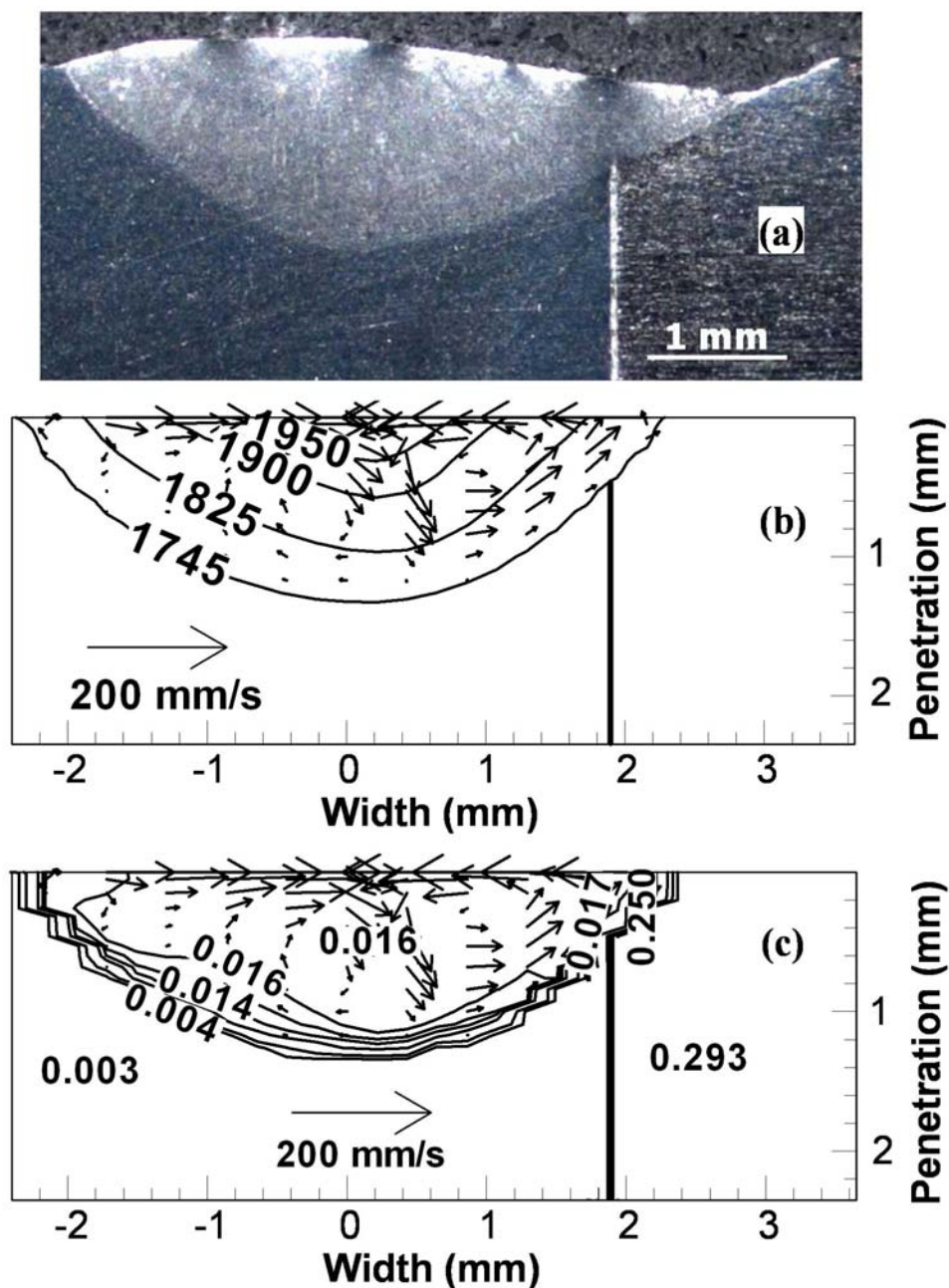


Fig. 6.18. Results for case 7 in Table 6.6. (a) Experimental weld pool geometry. The vertical line shows the joint of the two plates. (b) Calculated temperature and velocity fields in the weld pool. The contours represent the temperatures in degree Kelvin and the vectors represent the liquid velocity. The 1745 K isotherm is the solidus temperature of stainless steel used and marks the weld pool boundary. (c) Calculated concentration of sulfur in the weld pool. The contours represent sulfur concentration in wt%. The sulfur concentration on the top surface and the bulk of the weld pool was about 0.016 wt%. Welding conditions: 100 A, 9.8 V, welding speed is 1.7 mm/s.

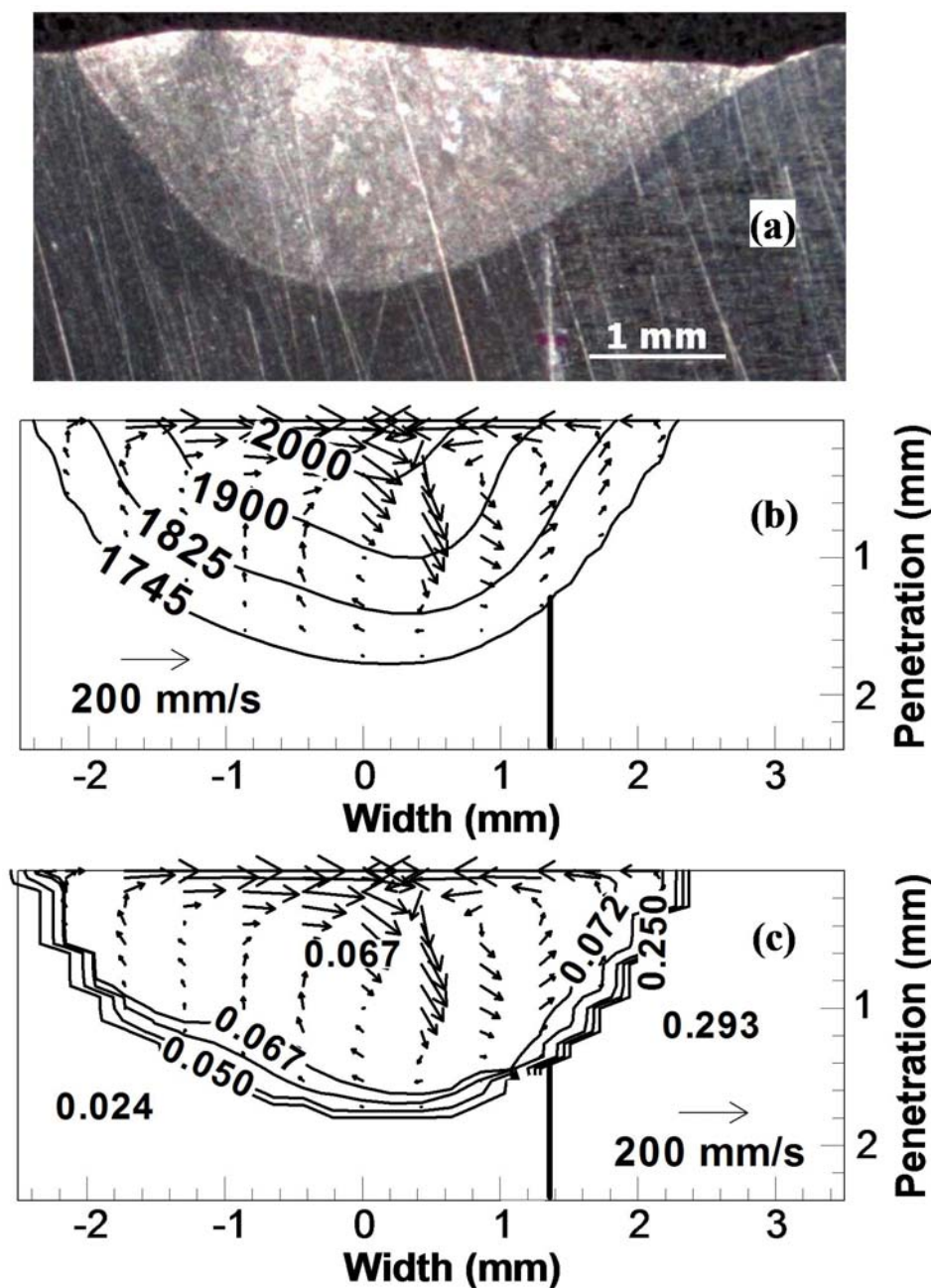


Fig. 6.19. Results for case 8 in Table 6.6. (a) Experimental weld pool geometry. The vertical line shows the joint of the two plates. (b) Calculated temperature and velocity fields in the weld pool. The contours represent the temperatures in degree Kelvin and the vectors represent the liquid velocity. The 1745 K isotherm is the solidus temperature of stainless steel used and marks the weld pool boundary. (c) Calculated concentration of sulfur in the weld pool. The contours represent sulfur concentration in wt%. The sulfur concentration on the top surface and the bulk of the weld pool was about 0.067 wt%. Welding conditions: 100 A, 10.0 V, welding speed is 1.7 mm/s.

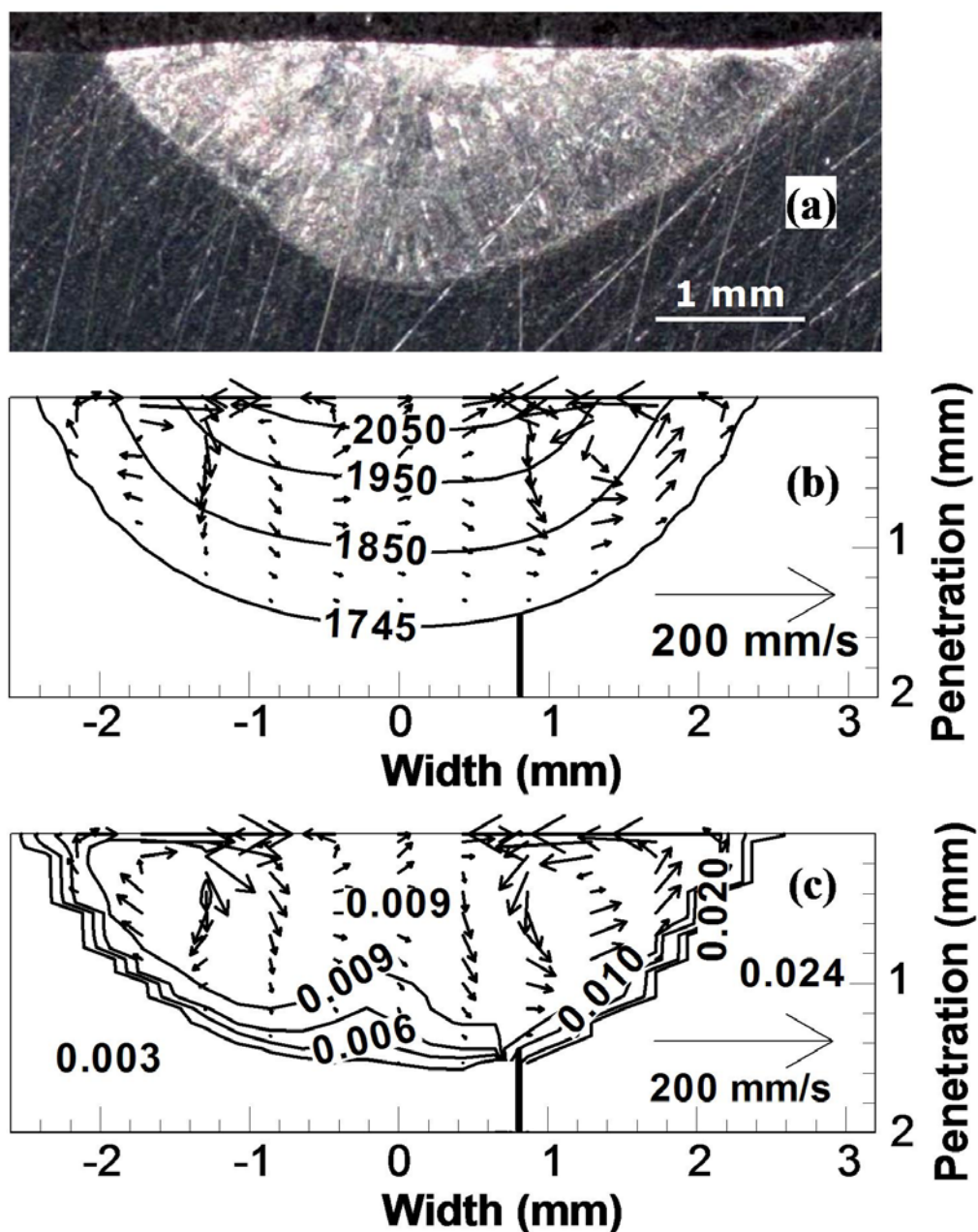


Fig. 6.20. Results for case 9 in Table 6.6. (a) Experimental weld pool geometry. The vertical line shows the joint of the two plates. (b) Calculated temperature and velocity fields in the weld pool. The contours represent the temperatures in degree Kelvin and the vectors represent the liquid velocity. The 1745 K isotherm is the solidus temperature of stainless steel used and marks the weld pool boundary. (c) Calculated concentration of sulfur in the weld pool. The contours represent sulfur concentration in wt%. The sulfur concentration on the top surface and the bulk of the weld pool was about 0.009 wt%. Welding conditions: 100 A, 9.9 V, welding speed is 1.7 mm/s.

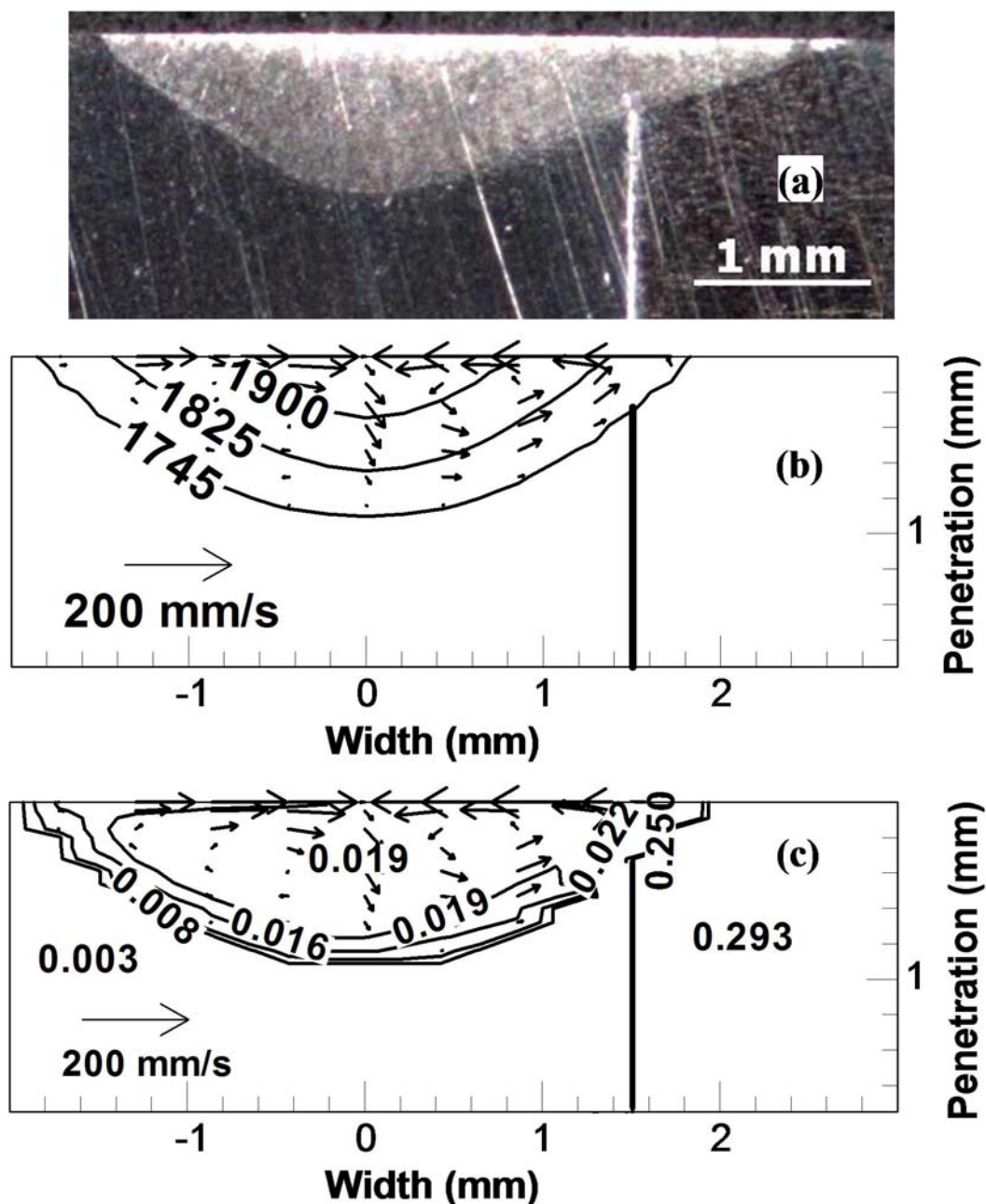


Fig. 6.21. Results for case 10 in Table 6.6. (a) Experimental weld pool geometry. The vertical line shows the joint of the two plates. (b) Calculated temperature and velocity fields in the weld pool. The contours represent the temperatures in degree Kelvin and the vectors represent the liquid velocity. The 1745 K isotherm is the solidus temperature of stainless steel used and marks the weld pool boundary. (c) Calculated concentration of sulfur in the weld pool. The contours represent sulfur concentration in wt%. The sulfur concentration on the top surface and the bulk of the weld pool was about 0.019 wt%. Welding conditions: 100 A, 10.2 V, welding speed is 3.4 mm/s.

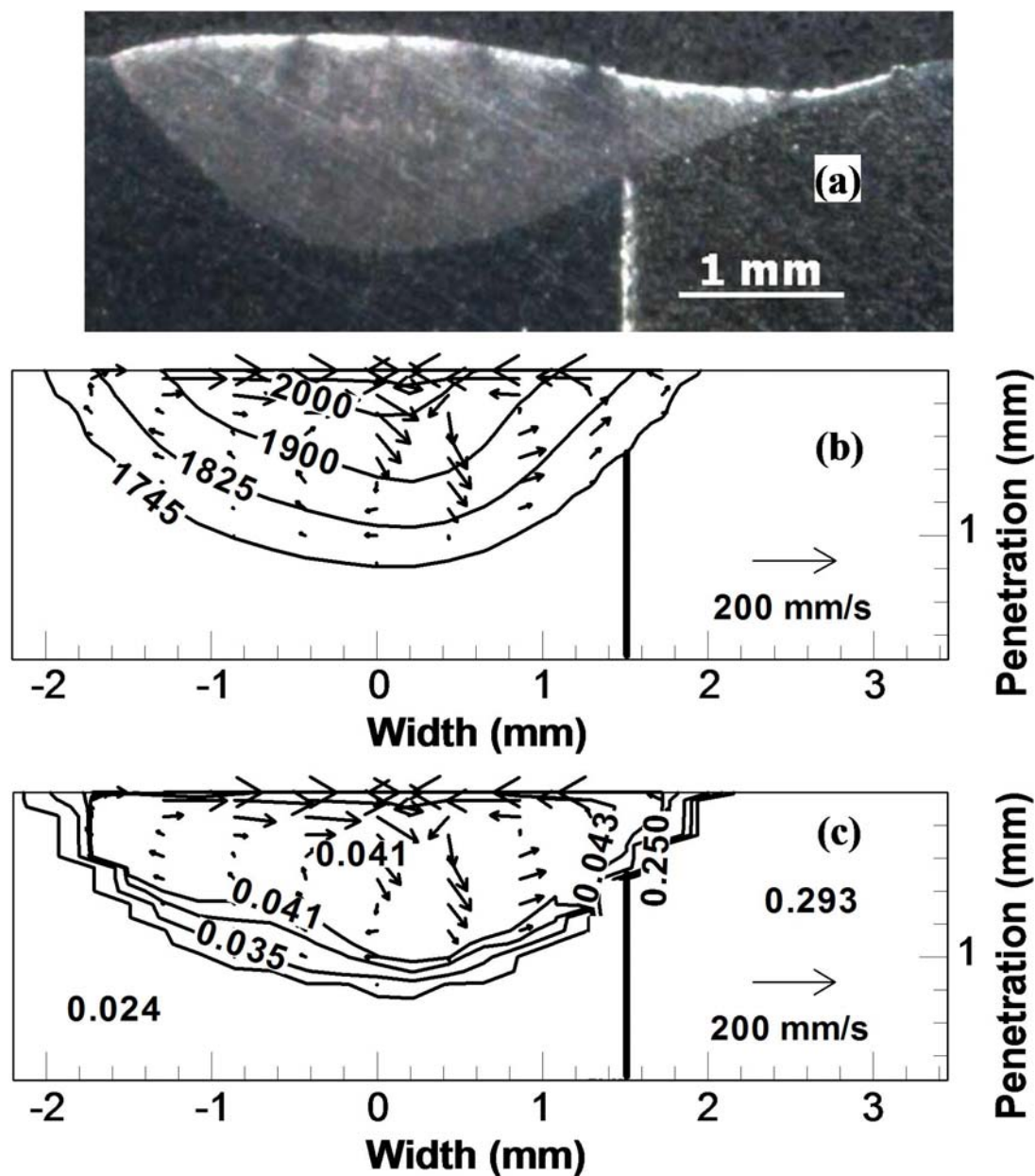


Fig. 6.22. Results for case 11 in Table 6.6. (a) Experimental weld pool geometry. The vertical line shows the joint of the two plates. (b) Calculated temperature and velocity fields in the weld pool. The contours represent the temperatures in degree Kelvin and the vectors represent the liquid velocity. The 1745 K isotherm is the solidus temperature of stainless steel used and marks the weld pool boundary. (c) Calculated concentration of sulfur in the weld pool. The contours represent sulfur concentration in wt%. The sulfur concentration on the top surface and the bulk of the weld pool was about 0.041 wt%. Welding conditions: 100 A, 10.2 V, welding speed is 3.4 mm/s.

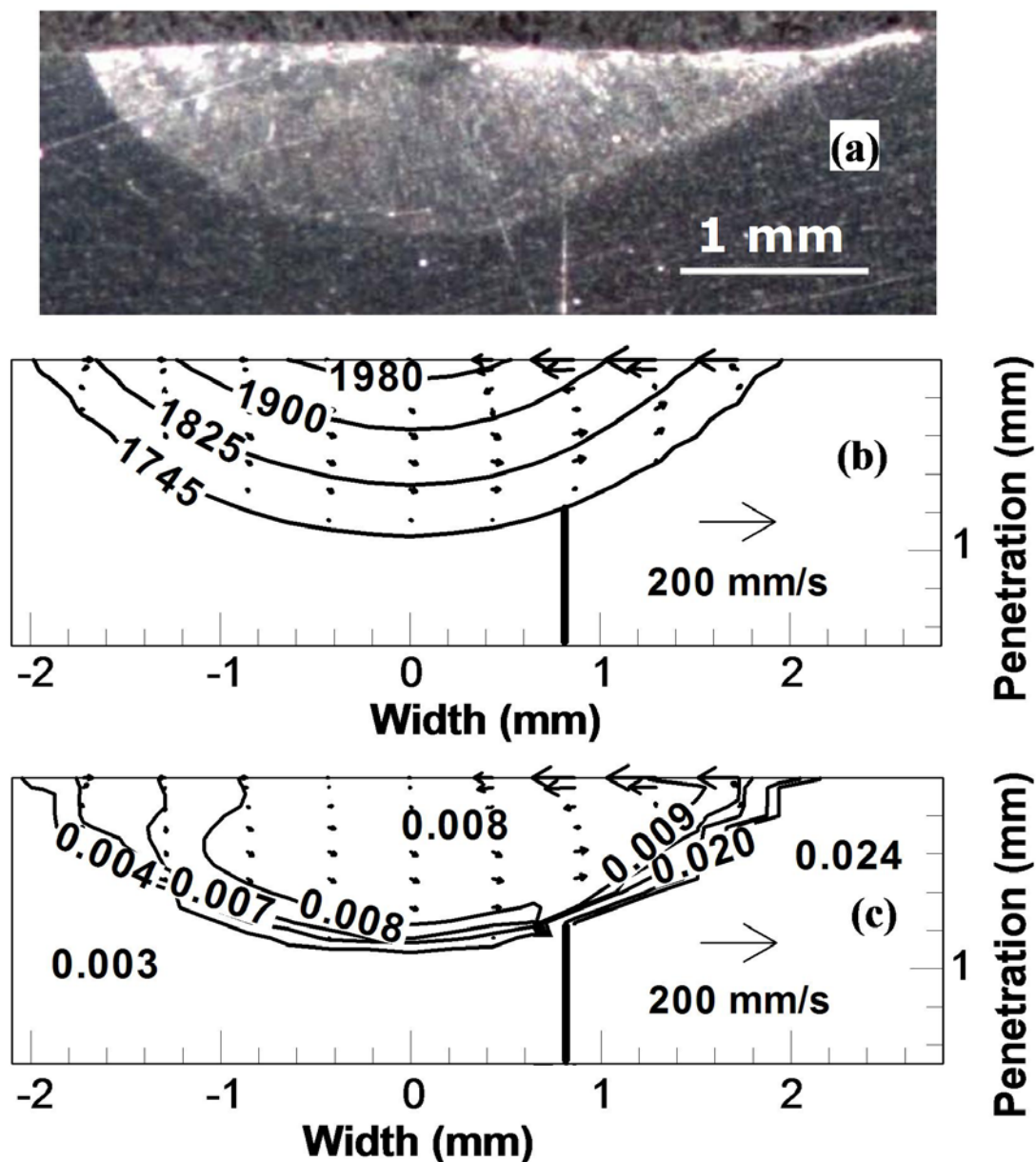


Fig. 6.23. Results for case 12 in Table 6.6. (a) Experimental weld pool geometry. The vertical line shows the joint of the two plates. (b) Calculated temperature and velocity fields in the weld pool. The contours represent the temperatures in degree Kelvin and the vectors represent the liquid velocity. The 1745 K isotherm is the solidus temperature of stainless steel used and marks the weld pool boundary. (c) Calculated concentration of sulfur in the weld pool. The contours represent sulfur concentration in wt%. The sulfur concentration on the top surface and the bulk of the weld pool was about 0.008 wt%. Welding conditions: 100 A, 10.0 V, welding speed is 3.4 mm/s.

Parts (c) of Fig. 6.12 to Fig. 6.23 show the following features about sulfur distribution in the weld pool. On the surface of the weld pool, significant concentration gradient is observed only in small areas near the edges of the weld pool, while in most of the central region of the weld pool surface and the bulk of the weld pool the concentration gradient is fairly small. This is contrary to the earlier [5] belief that when two plates having different sulfur contents are welded, a gradient of sulfur concentration exists on the top surface from the high sulfur to the low sulfur side, which results in a net surface tension gradient across the weld pool top surface leading to surface fluid flow toward the low sulfur side. This flow pattern was believed to cause the shifting of the weld bead towards the low sulfur side. Of all the results presented in parts (c) of Fig. 6.12 to Fig. 6.23, only Fig. 6.23(c) seems to follow the flow pattern as per the earlier belief [5], i.e., the entire liquid is flowing from the high sulfur to the low sulfur side. However, a more careful observation reveals that the strong anticlockwise circulation loop at the right edge does not span the entire weld pool and there is a small clockwise circulation loop at the center of the weld pool. The anticlockwise circulation loop at the right edge is caused by the localized concentration gradient at that edge. The concentration gradient in the center of the weld pool is still very small. Owing to the low concentration of sulfur in the central region of the weld pool top surface, two circulation loops going radially outwards are formed in the center.

To check the validity of the calculated sulfur concentration, Electron Probe Micro-Analysis (EPMA) was used to measure the sulfur concentration on the top surface of the weld pool in cases 1 to 3 in Table 6.6 corresponding to Fig. 6.12 to Fig. 6.14, respectively. Since phosphorus is also present in the specimens, its concentration was also measured. However, the following problem was faced while doing EPMA. Even though EPMA can provide concentration data for a surface area as small as  $1 \mu\text{m}^2$ , such high precision could not be used for the present case. This is because stainless steels containing high amount of sulfur have a tendency to precipitate out sulfides shown by dark spots and discs of manganese-sulfide (MnS) in Fig. 6.24 to Fig. 6.27. Fig. 6.24 shows the distribution of MnS precipitates in 303 SS (0.293 wt% Sulfur), Fig. 6.25 shows the distribution of MnS precipitates in 304RL SS (0.024 wt% Sulfur), Fig. 6.26 shows the

distribution of MnS precipitates in 304 L SS ( 0.003 wt% Sulfur) and Fig. 6.27 shows the distribution of MnS precipitates in the weld pool for case 2 of Table 6.6 where 304RL SS is welded to 303 SS. Fig. 6.27 corresponds to a location in the center of the weld pool. For the base metals, Fig. 6.24 to Fig. 6.26 show that the size and density of MnS precipitates decreases from 303 SS to 304L SS, which is consistent with the amount of sulfur contained by these stainless steels. It is noteworthy that the distribution of MnS precipitates in the base metals is not very uniform, which might lead to variations in sulfur content measurements in different regions of the base metal when EPMA is used. Fig. 6.27 shows that in the weld pool the size and distribution of MnS precipitates is more or less uniform, which indicates the absence of any steep sulfur concentration gradient in the weld pool. Because of the precipitation of MnS, the matrix has a much lower concentration of sulfur than that in the precipitates. Therefore, if EPMA is done at a high precision, the data will show random distribution of sulfur, with low concentration in the matrix and a high value whenever a MnS precipitate is encountered. In order to avoid this problem, EPMA data was averaged over spot sizes of  $50 \times 50 \mu\text{m}^2$ . Both the sulfur and phosphorus concentrations were measured at each spot in wt%.

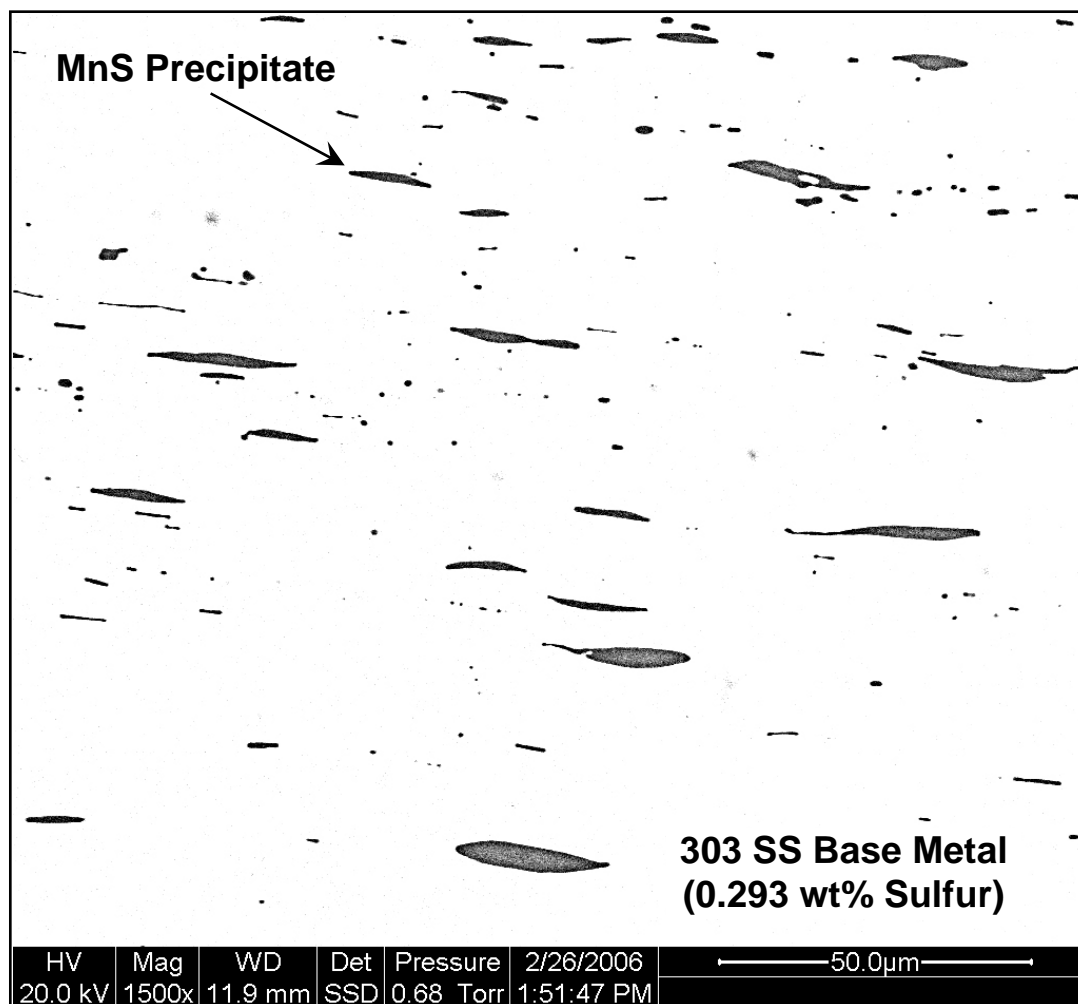


Fig. 6.24. Distribution of manganese-sulfide (MnS) precipitates (dark spots and discs) in 303 stainless steel (SS) base metal.

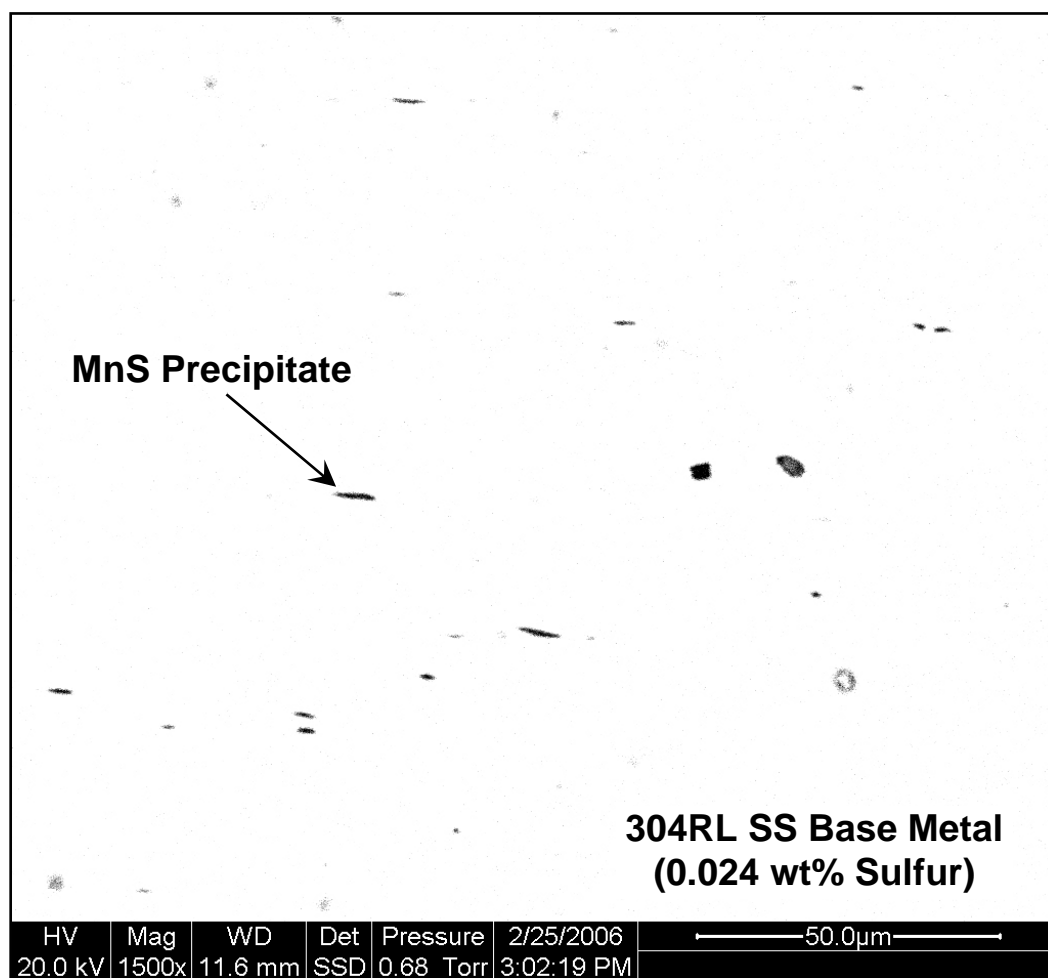


Fig. 6.25. Distribution of manganese-sulfide (MnS) precipitates (dark spots and discs) in 304RL stainless steel (SS) base metal.

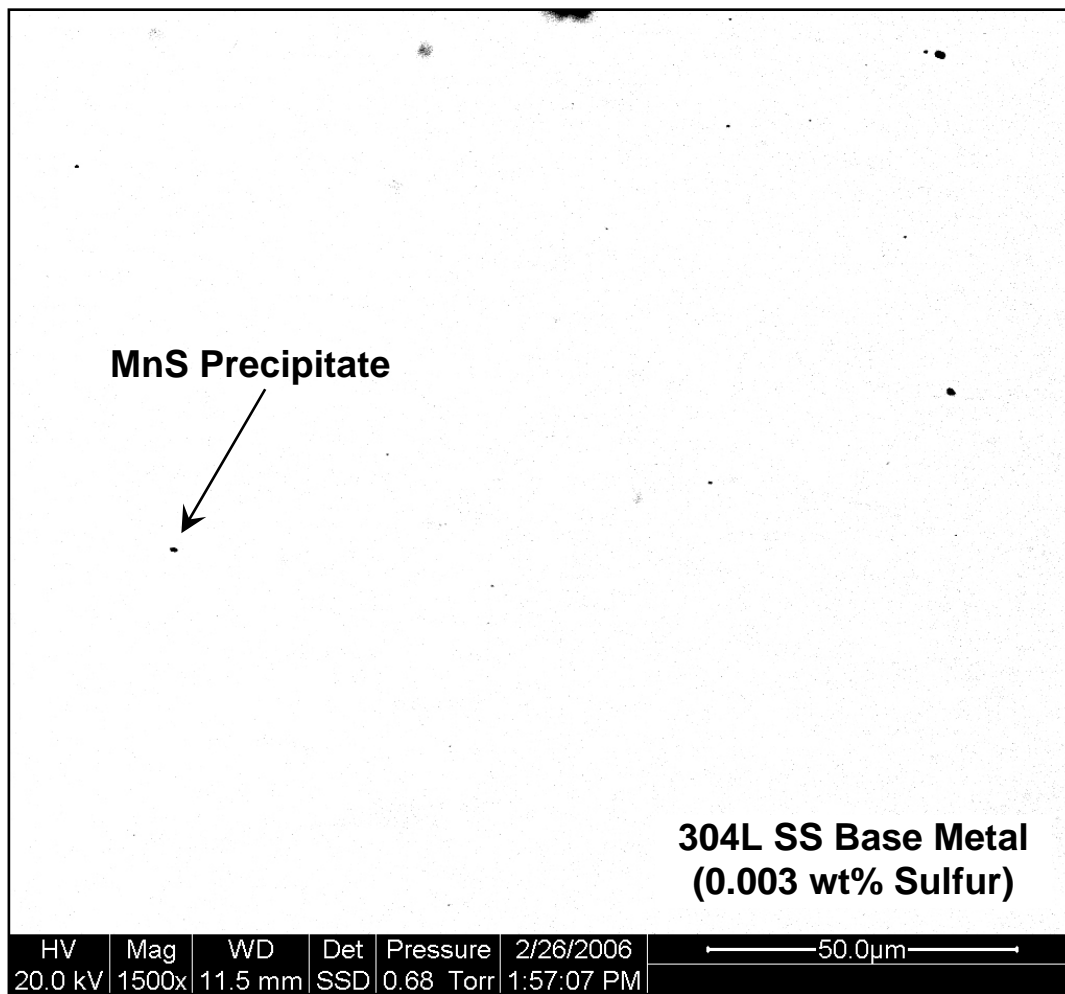


Fig. 6.26. Distribution of manganese-sulfide (MnS) precipitates (dark spots) in 304L stainless steel (SS) base metal.

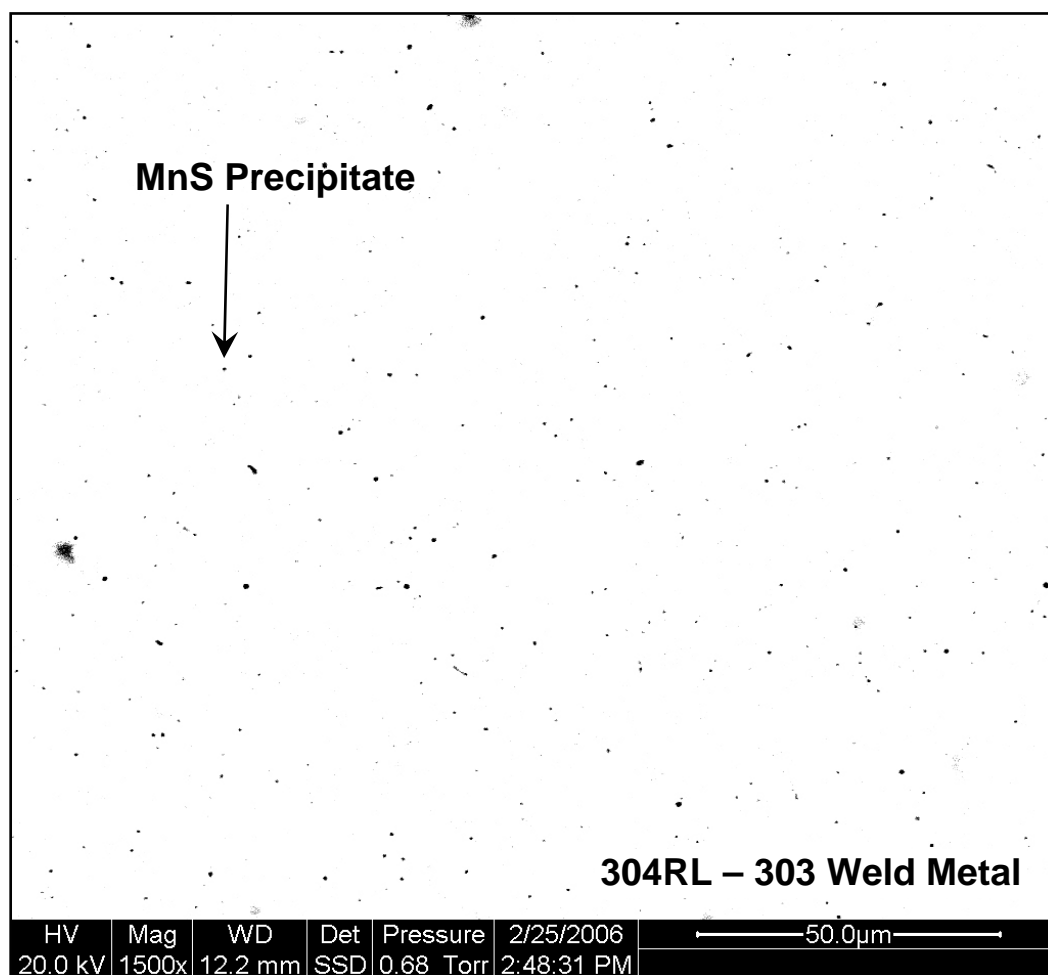


Fig. 6.27. Distribution of manganese-sulfide (MnS) precipitates (dark spots) in the weld pool for case 2 of Table 6.6. Welding conditions: 150 A, 10.8 V, welding speed is 1.7 mm/s. 304RL stainless steel has 0.024 wt% sulfur while 303 stainless steel has 0.293 wt% sulfur.

For each weld, the sulfur and phosphorus concentrations were measured using EPMA at the weld pool top surface along the y-direction, as well as along a vertical line starting from the top surface of the weld, as shown by the dotted lines in Fig. 6.28. Fig. 6.29(a), (b) and (c) show the sulfur distribution on the top surface for the welds given in cases 1, 2 and 3 of Table 6.6, respectively and Fig. 6.30(a), (b) and (c) show the sulfur distribution along the weld pool penetration for the same cases. Fig. 6.31(a), (b) and (c) show the phosphorus distribution on the top surface for the welds given in cases 1, 2 and 3 of Table 6.6, respectively and Fig. 6.32(a), (b) and (c) show the phosphorus distribution along the weld pool penetration for the same cases. Fig. 6.29 shows that there is no significant concentration gradient of sulfur on the top surface of the welds except very close to the edges. This negates the possibility of a concentration gradient induced net surface tension gradient that can lead to surface fluid flow toward the low sulfur side. Therefore, surface concentration gradient does not play a major role in shifting of the weld bead towards the low sulfur side as was believed in earlier studies [5]. The shifting of the arc towards the low sulfur side turns out to be the main factor governing the weld bead shift. Along the vertical direction also there is not much variation in sulfur concentration as shown by Fig. 6.30. The calculated results shown in Fig. 6.29 and Fig. 6.30 are in fair agreement with the experimental measurements indicating the validity of the present approach in calculating sulfur distribution in the weld pool on welding two plates having different sulfur contents. It is noteworthy that in Fig. 6.29 the measured sulfur concentration at several locations in the base metal is either much higher or much lower than the average concentration of the stainless steels used in the calculations. This discrepancy might be attributed to the non-uniform distribution of manganese sulfide precipitates in the base metal. Where the scanned area has less precipitates, the sulfur concentration is low and vice versa. Fig. 6.31 and Fig. 6.32 show that the phosphorus concentration also does not vary much on the top surface as well as in the bulk of the weld pool, which is expected as the phosphorus concentrations of the three stainless steels considered in the present study, are almost the same as shown in Table 6.1.

What causes the absence of any significant sulfur concentration gradient in the weld pool when welding two plates having very different sulfur contents? This question can be answered on the basis of the sulfur transport in the weld pool driven mainly by convection in the weld pool. The relative importance of convection and conduction in the overall transport of sulfur in the weld pool is given by the Peclet number for mass transfer,  $Pe_m$ , which is determined as:

$$Pe_m = \frac{uL}{D} \quad (6.17)$$

where  $D$  is the mass diffusivity of sulfur. The exact value of mass diffusivity is not available in the literature. An order of magnitude value of the mass diffusivity of sulfur in molten stainless steel is given by Luo as [27]  $1.0 \times 10^{-8} \text{ m}^2/\text{s}$ . This value of  $D$  was used in the present study. The value of  $u$  for case 1 of Table 6.6 is 0.235 m/s and the value of  $L$  is 0.0012 m. The corresponding value of  $Pe_m$  is calculated to be  $2.8 \times 10^4$ , which indicates that convection is the primary mode of solute transport in the weld pool. High fluid velocities, sometimes more than 200 mm/s can be seen in Fig. 6.12 to Fig. 6.23. For example, in Fig. 6.12, which corresponds to case 1 in Table 6.6, the length of the weld pool is approximately 7 mm and the welding speed is 1.7 mm/s. Therefore, the characteristic time for which a location on the top surface remains liquid is approximately equal to 4 s. The average fluid velocity on the top surface is more than 100 mm/s at most of the locations. Thus, the fluid at a given location on the top surface can cover a distance equal to half the length, i.e., 3.5 mm in 0.035 s, and a semicircular loop of diameter 3.5 mm in 0.05 s. Such a fast moving fluid can circulate through the weld pool more than 50 times in 4 s, i.e., the time for which any location remains liquid. The fast re-circulating flow will ensure rapid mixing of sulfur in the weld pool. The rapid mixing and convection dominant solute transport prevents any significant sulfur concentration gradient on the weld pool top surface as well as the bulk. Furthermore, the aforementioned discussion illustrates that it is necessary to consider convective mass transport in order to accurately predict the sulfur concentration distribution in the weld pool.



Fig. 6.28. The EPMA measurements of sulfur and phosphorus concentrations were done along the dotted lines.

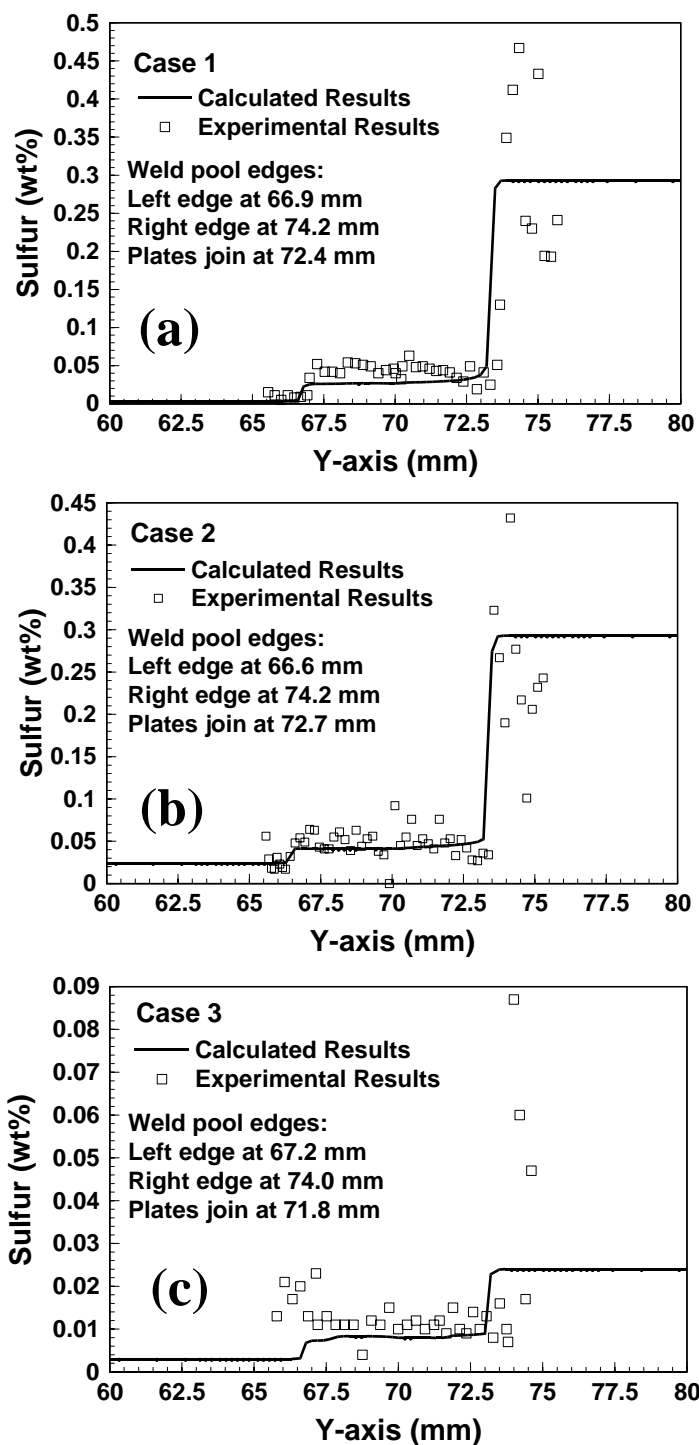


Fig. 6.29. Experimental and calculated sulfur concentrations along the horizontal dotted line shown in Fig. 6.28 for (a) case 1, (b) case 2, and (c) case 3 of Table 6.6. The symbols represent the experimental data and the solid line represents the calculated results.

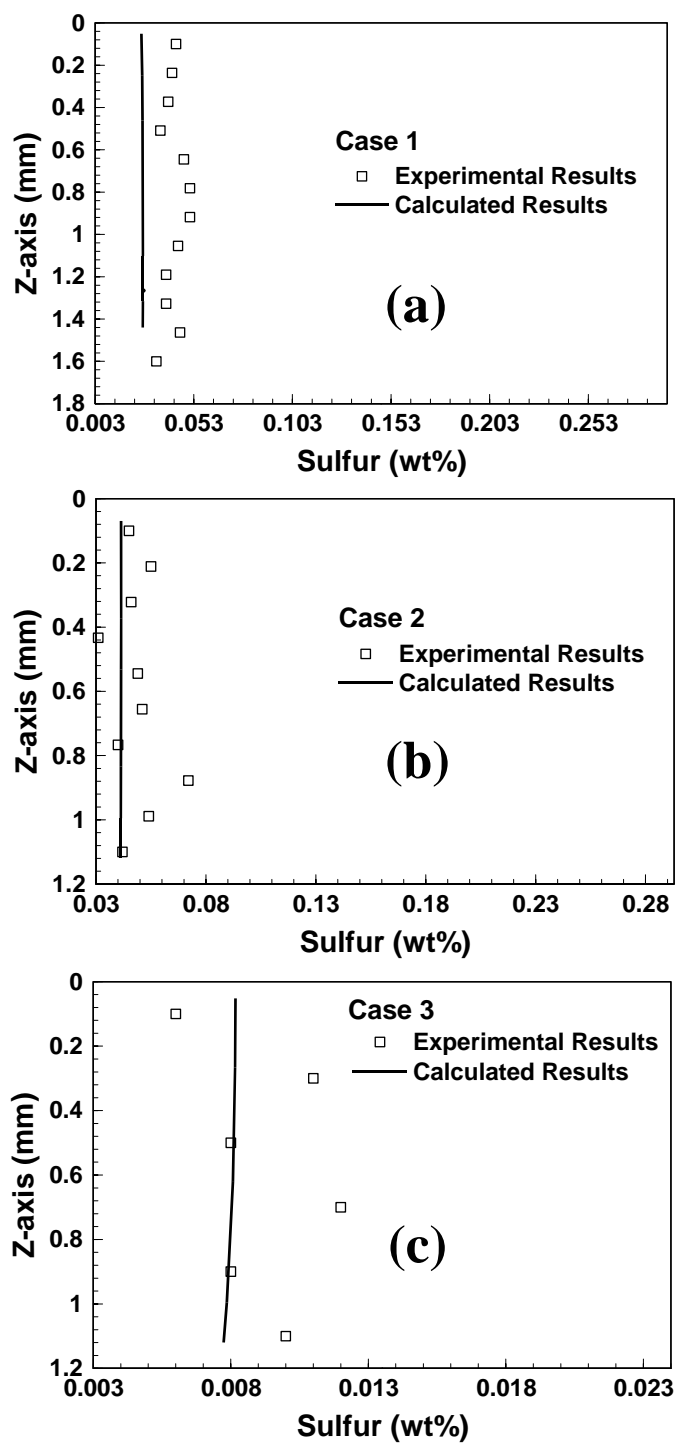


Fig. 6.30. Experimental and calculated sulfur concentrations along the vertical dotted line shown in Fig. 6.28 for (a) case 1, (b) case 2, and (c) case 3 of Table 6.6. The symbols represent the experimental data and the solid line represents the calculated results.

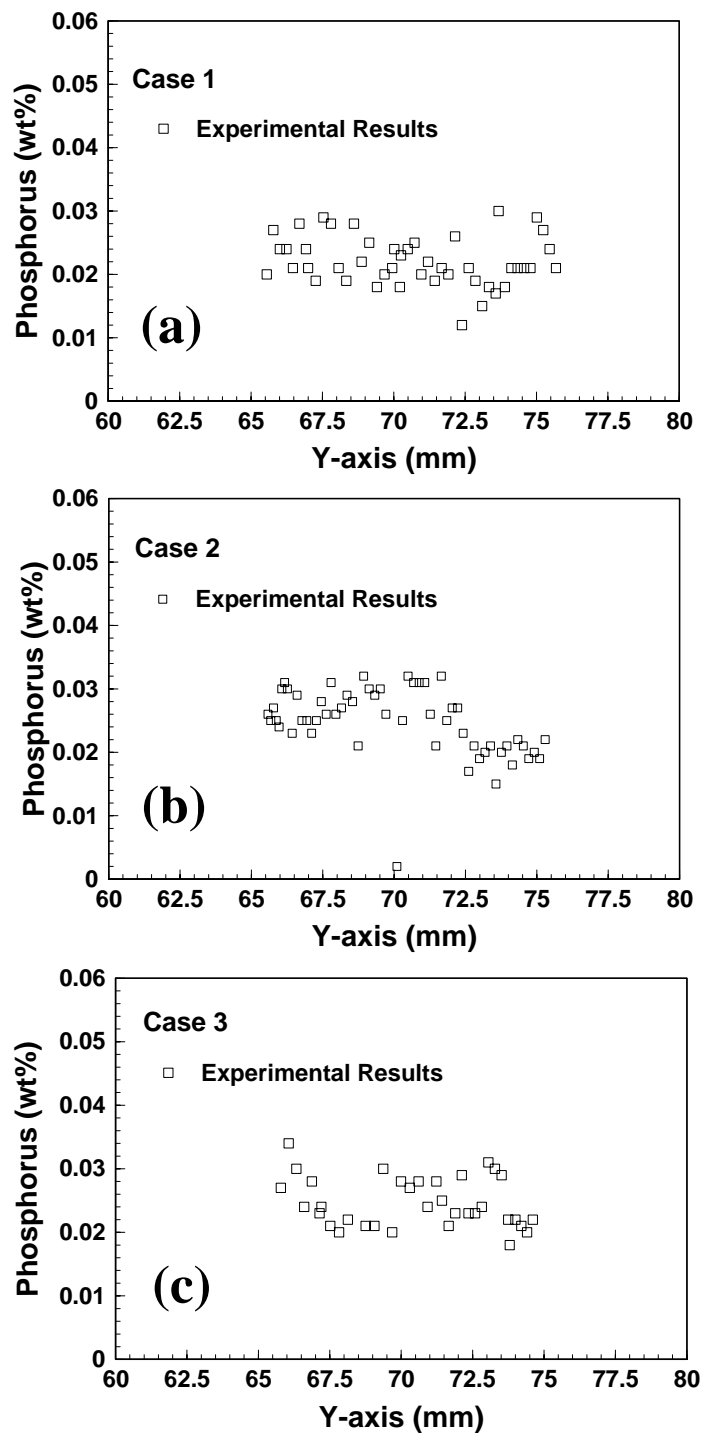


Fig. 6.31. Experimentally measured phosphorus concentrations along the horizontal dotted line shown in Fig. 6.28 for (a) case 1, (b) case 2, and (c) case 3 of Table 6.6.

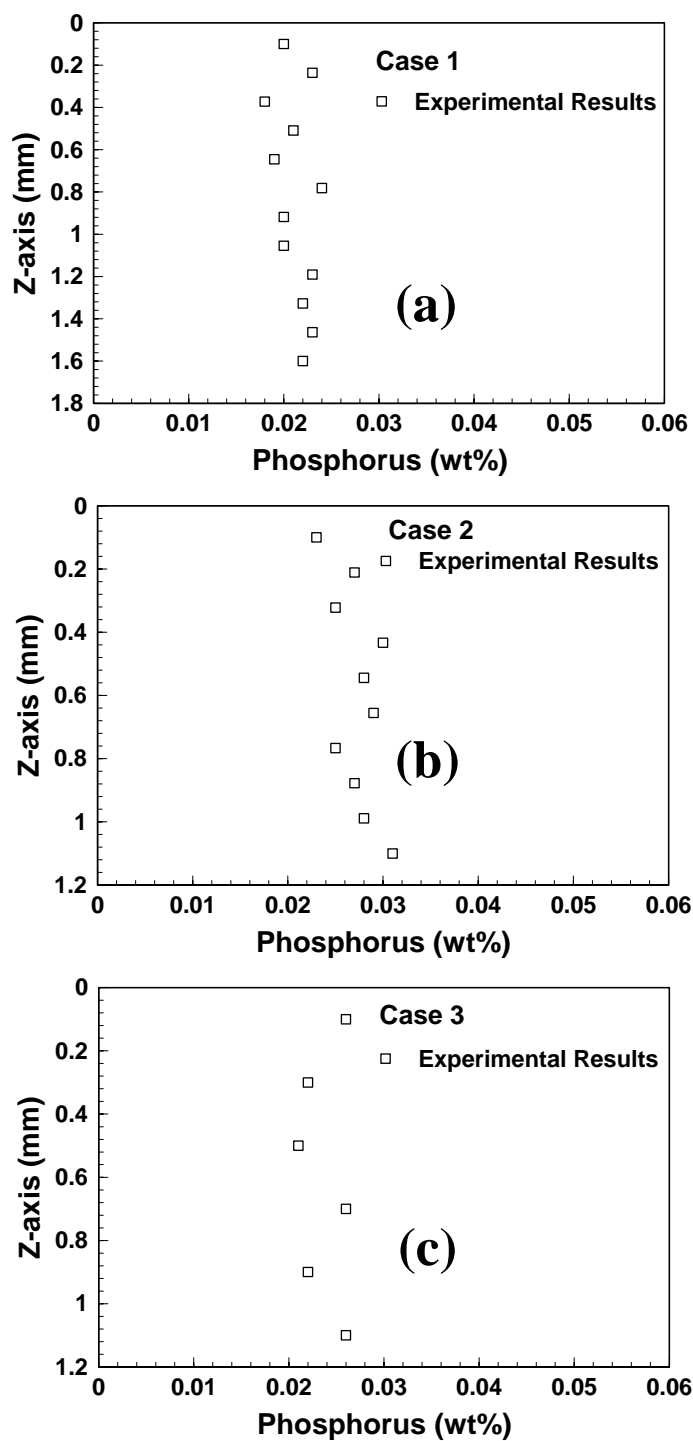


Fig. 6.32. Experimentally measured phosphorus concentrations along the vertical dotted line shown in Fig. 6.28 for (a) case 1, (b) case 2, and (c) case 3 of Table 6.6.

Fig. 6.33 shows the variation of weld pool penetration with energy input per unit length for the 12 cases listed in Table 6.6. For a given energy input, say 930 J/mm, the weld pool penetration for 304RL-303 weld is higher than that for 304L-304RL weld. The Peclet number for heat transfer, given by Eq. (6.12), is 17 for 304L-304RL weld and 29 for 304RL-303 weld for this heat input. Such high values of Peclet number indicate that convection is the primary mode of heat transfer in the weld pool and the effect of sulfur as a surface active element will be important. The calculated sulfur concentration on the top surface of 304RL-303 weld, corresponding to Fig. 6.13(c), is 0.041 wt%. Fig. 6.2 shows that for 0.041 wt% sulfur,  $\partial\gamma/\partial T$  is positive for temperatures lower than approximately 2130 K, i.e., entire weld pool top surface in Fig. 6.13(b). Positive  $\partial\gamma/\partial T$  causes the convection pattern to be radially inwards, as can be seen in Fig. 6.13(b), resulting in a deep weld pool. The calculated sulfur concentration on the top surface of 304L-304RL weld, corresponding to Fig. 6.14(c), is 0.008 wt%. Fig. 6.2 shows that for 0.008 wt% sulfur,  $\partial\gamma/\partial T$  is positive for temperatures lower than 1890 K and negative for higher temperatures. Negative  $\partial\gamma/\partial T$  results in a radially outward flow making the weld pool shallow. Therefore, two circulation loops can be seen in Fig. 6.14(b), the inner circulation loop going radially outwards because of negative  $\partial\gamma/\partial T$  at high temperatures, and the outer circulation loop going radially inwards because of positive  $\partial\gamma/\partial T$  at lower temperatures near the periphery of the weld. As a result, for an energy input of 930 J/mm, the maximum penetration for 304L-304RL weld is 2.27 mm, which is smaller than that for 304L-304RL weld, i.e., 2.57 mm.

The effect of energy input on weld pool penetration and width can be observed from Fig. 6.33 and Fig. 6.34, respectively. It can be seen that for a given stainless steel pair, say 304RL-303, the weld pool penetration and width are higher for higher energy input, which is consistent with the basic principles of transport phenomena.

It can be seen that in all the cases from Fig. 6.12 to Fig. 6.23, the calculated weld pool geometry is in fair agreement with the corresponding experimental results. This shows the validity of the present calculation procedure in predicting the weld pool geometry on welding plates with different sulfur contents. Furthermore, the calculations need to incorporate the effect of both the sulfur distribution in the weld pool and the

shifting of the arc on the weld pool geometry on joining plates with different sulfur contents.

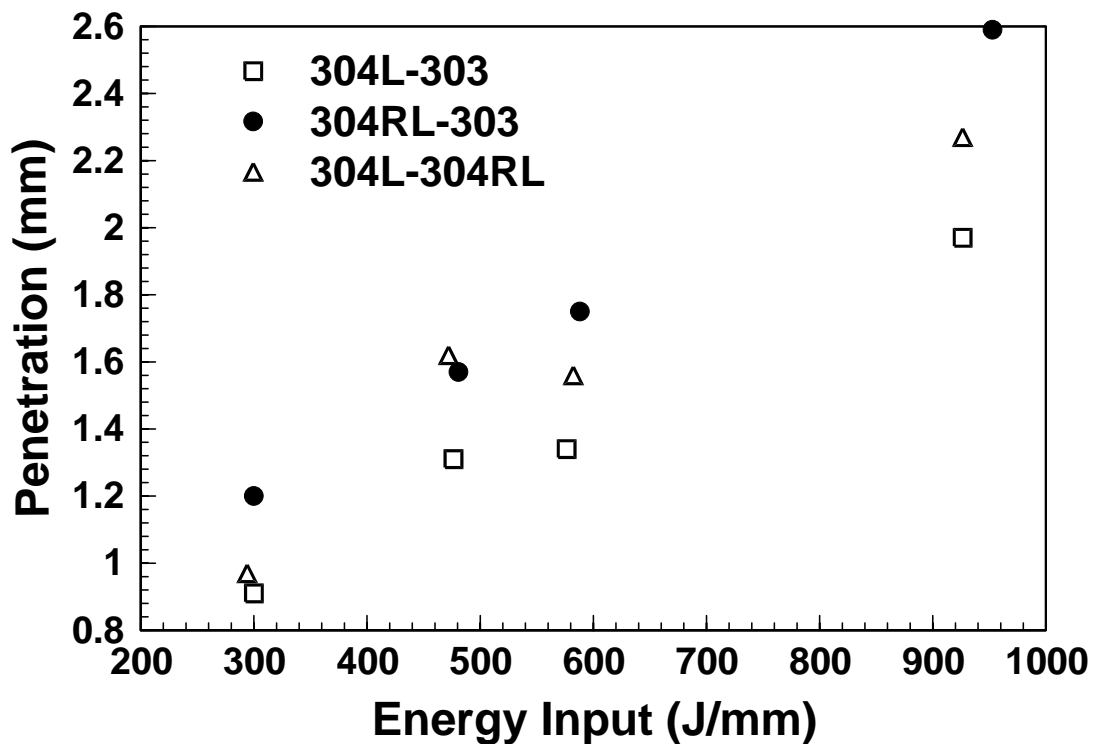


Fig. 6.33. Variation of weld pool penetration with energy input per unit length for 12 cases given in Table 6.6. The three stainless steel combinations welded together are: 304L welded to 303, 304RL welded to 303, and 304L welded to 304RL. The sulfur contents of the three kinds of stainless steels used are: 304L (0.003 wt%), 304RL (0.024 wt%) and 303 (0.293 wt%).

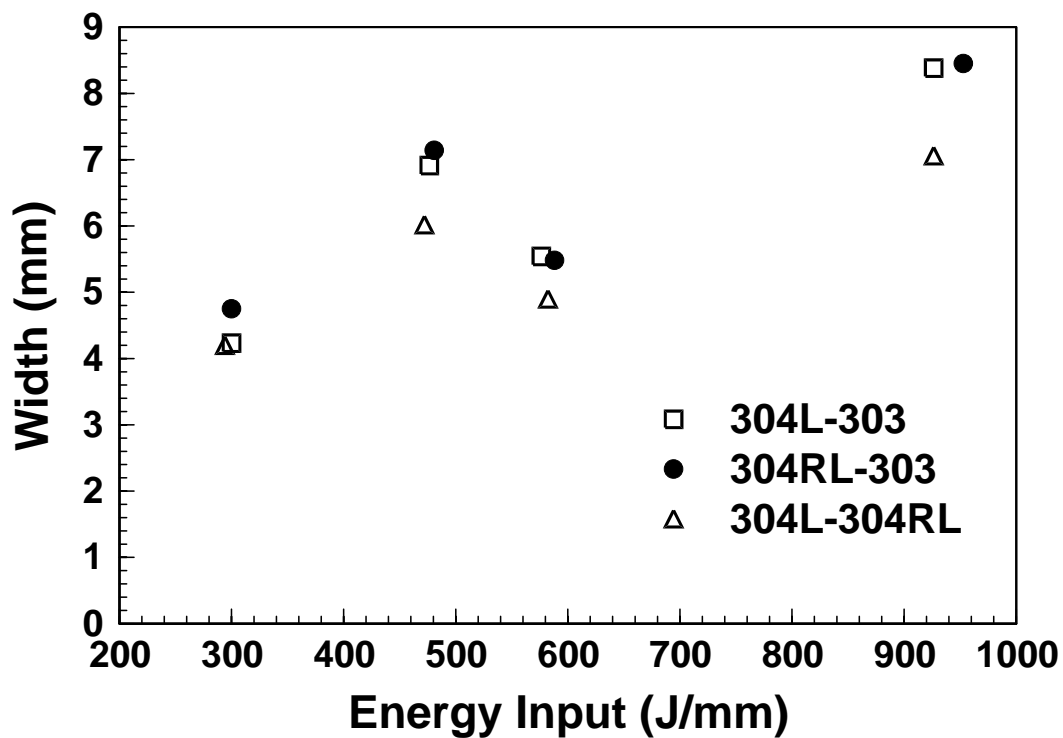


Fig. 6.34. Variation of weld pool width with energy input per unit length for 12 cases given in Table 6.6. The three stainless steel combinations welded together are: 304L welded to 303, 304RL welded to 303, and 304L welded to 304RL. The sulfur contents of the three kinds of stainless steels used are: 304L (0.003 wt%), 304RL (0.024 wt%) and 303 (0.293 wt%).

## 6.4 Summary and Conclusions

A numerical transport phenomena based model has been developed to calculate the solute distribution in the weld pool. The model was applied to calculate the sulfur distribution within the weld pool and the evolution of weld pool geometry.

(a) The calculated results for the cases where the two plates had the same sulfur content were in good agreement with the corresponding experimental results. A high value of Peclet number was observed, which indicated that convection is the primary mode of heat transport within the weld pool. High sulfur content lead to a positive value of temperature coefficient of surface tension,  $\partial\gamma/\partial T$ , resulting in radially inward fluid flow in the weld pool, and enhanced weld pool penetration. In contrast, for steels with very low sulfur content the value of  $\partial\gamma/\partial T$  was negative resulting in radially outward fluid flow and a shallow and wide weld pool.

(b) When two plates having different sulfur contents were welded, the weld pool shifted towards the low sulfur side. Two possible factors, which might contribute to the weld pool shift, were investigated, i.e., shifting of the arc towards the low sulfur side and the gradient of sulfur concentration on the weld pool top surface. It was found that due to the dominant role of convection in solute transport in the weld pool, there was no significant gradient of sulfur concentration on the top surface except very close to the edges. This observation was validated by sulfur concentration measurements using EPMA. Thus, the shifting of the arc towards the low sulfur side was identified as the main factor governing the shifting of the weld pool.

(c) The effect of arc shift on the heat and solute transport has been considered for the first time in the present study, and consequently the major shift in the weld pool could be explained. The amount of arc shift was approximated by the center line shift (CLS), i.e., the distance by which the maximum weld pool penetration was shifted from the plate joint. The CLS was found to be a function of the difference in the sulfur content of the two plates and the energy input.

(d) It was observed that on welding plates with different sulfur contents, sulfur distribution in the weld pool is not the only factor governing the weld pool penetration. The change in heat distribution on the top surface due to the shifting of the arc was

proposed as a competing factor versus sulfur concentration in determining the weld pool penetration.

(e) The weld pool penetration and width increased with the increase in energy input.

(f) The calculated weld pool geometry and the sulfur concentration in the weld pool were in fair agreement with the corresponding experimental results for welding of plates having different sulfur contents, indicating the validity of the present approach.

## 6.5 References

1. W. Pitscheneder, T. DebRoy, K. Mundra and R. Ebner, *Weld. J.* 75, 71s (1996).
2. P. Sahoo, T. DebRoy and M. J. McNallan, *Met. Trans. B* 19, 483 (1988).
3. C. R. Heiple and J. R. Roper, *Weld. J.* 61, 97s (1982).
4. C. R. Heiple, J. R. Roper, R. T. Stagner and J. J. Alden, *Weld. J.* 62, 72s (1983).
5. C. R. Heiple, P. Burgardt, J. R. Roper, J. L. Long: *Proc. Int. Conf. on the Effects of Residual, Trace and Micro-alloying Elements on Weldability and Weld Properties*, TWI, Cambridge, 1984, 36.
6. S. W. Pierce, P. Purgardt and D. L. Olson, *Weld. J.* 78, 45s (1999).
7. B. J. Keene, K. C. Mills, J. L. Robinson and M. H. Rodwell: *Proc. Int. Conf. on the Effects of Residual, Trace and Micro-alloying Elements on Weldability and Weld Properties*, TWI, Cambridge, 1984, 45.
8. J. Leinonen and L. P. Karjalainen: *Proc. Int. Conf. on the Effects of Residual, Trace and Micro-alloying Elements on Weldability and Weld Properties*, TWI, Cambridge, 1984, 4.
9. J. Autio, J. Makio, K. Makela, E. Minni and P. Kettunen: *Proc. Int. Conf. on the Effects of Residual, Trace and Micro-alloying Elements on Weldability and Weld Properties*, TWI, Cambridge, 1984, 18.
10. A. F. Rollin and M. J. Bentley: *Proc. Int. Conf. on the Effects of Residual, Trace and Micro-alloying Elements on Weldability and Weld Properties*, TWI, Cambridge, 1984, 9.
11. K. J. Rodgers: *Proc. Int. Conf. on the Effects of Residual, Trace and Micro-alloying Elements on Weldability and Weld Properties*, TWI, Cambridge, 1984, 2.
12. M. J. Tinkler, I. Grant, G. Mizuno and C. Gluck: *Proc. Int. Conf. on the Effects of Residual, Trace and Micro-alloying Elements on Weldability and Weld Properties*, TWI, Cambridge, 1984, 29.
13. D. G. Kolman, Report on 'Assessment of the corrosion, stress corrosion cracking and embrittlement susceptibility of 30313 storage containers' available at <http://public.lanl.gov/MCEL/PDF-Publications/CorrSCC3013.pdf>.

14. G. R. Cannell, W. L. Daugherty and M. W. Stokes, Report on 'Closure welding of plutonium bearing storage containers' available at <http://sti.srs.gov/fulltext/ms2002053/ms2002053.pdf>.
15. DOE-STD-3013-96, 'Criteria for preparing and packaging plutonium metals and oxides for long-term storage' available at <http://www.eh.doe.gov/techstds/standard/std3013/s963013.pdf>.
16. M. J. McNallan and T. DebRoy, *Met. Trans. B* 22, 557 (1991).
17. R. B. Bird, W. E. Stewart and E. N. Lightfoot, *Transport Phenomena* (John Wiley & Sons, Inc., New York, 1960).
18. G. H. Geiger and D. R. Poirier, *Transport Phenomena in Metallurgy* (Addison-Wesley, MA, 1973).
19. R. Ohno and T. Ishida, *J. Iron Steel Institute* 206, 904 (1968).
20. *Smithells Metals Reference Book – 7th Edition*, Editors - E. A. Brandes and G. B. Brook (Butterworth-Heinemann, Oxford, 1992).
21. A. De, and T. DebRoy, *J. Phys. D: Appl. Phys.* 37, 140 (2004).
22. F. D. Richardson, *Physical Chemistry of Melts in Metallurgy – Vol. 2* (Academic Press, London, 1974).
23. G. J. Dunn and T. W. Eagar, *Welding Research Council Bulletin* 357, 22 (1990).
24. M. Abbaoui, B. Cheminat and P. J. Andanson, *J. Phys. D: Appl. Phys.* 18, L159 (1985).
25. J. F. Lancaster, *The Physics of Welding - 2nd Edition* (Pergamon, Oxford, 1986).
26. L. Coudurier, D. W. Hopkins and I. Wilkomirsky, *Fundamentals of Metallurgical Processes – 2nd Edition* (Pergamon, Oxford, 1985).
27. H. Luo, *Scand. J. Metall.* 30, 212 (2001).

## Chapter 7

### **Probing Liquation Cracking Through Modeling of Momentum, Heat and Solute Transport during Gas Metal Arc Welding of Aluminum Alloys**

Liquation cracking, also known as heat-affected zone (HAZ) cracking, is a common problem in the gas metal arc (GMA) welding of aluminum alloys. It occurs in the HAZ when low melting point region, i.e., partially melted zone (PMZ), is formed during welding. Cracks form when the PMZ cannot withstand the tensile stresses generated during solidification [1]. The occurrence of liquation cracking in aluminum alloys have been confirmed by experiments [1-11]. Huang and Kou [1] found that the partially molten zone (PMZ) becomes prone to liquation cracking when the solid fraction in the PMZ becomes lower than that in the aluminum alloy weld metal. They [1] argued that lower solid fraction in the PMZ makes this region weaker than the weld metal, making the PMZ vulnerable to liquation cracking. The solid fraction of the solidifying weld metal is decided by the solute distribution in the weld pool. Therefore, accurate predictions of liquation cracking susceptibility in aluminum-copper alloys require thorough investigations of non-equilibrium solute distribution during GMA welding.

Composition of the weld metal results from the mixing of the base metal with the filler metal. Solute distribution within the weld pool is by convection and diffusion. Furthermore, both the thermodynamics and the kinetics of solidification affect the solute partitioning during solidification. Both the partitioning of the solute and the mixing of the filler metal with the base metal need to be considered to understand the solute distribution in the weld. However, many previous attempts to understand weld pool solidification considered thermal field alone [12,13] and ignored the convective solute transport in the weld pool. Chakraborty and Dutta [14] developed a solidification model for studying heat and mass transfer in a single-pass laser surface alloying process. However, they [14] assumed equilibrium at the solid-liquid interface that may not be attained when the interface speed is comparable with or faster than the diffusion speed. Both the velocity of solidification front and the undercooling must be considered to accurately represent solidification during welding. The complex coupling of momentum, heat and solute

transport under non-equilibrium conditions during fusion welding have not been investigated. Such an approach is desirable for accurate prediction of the evolution of solute distribution in the weld.

In the present study, the transport phenomena based model developed in Chapter 3 has been adapted to the gas metal arc (GMA) welding process, by considering heat and solute intake due to filler metal addition, and integrating a non-equilibrium solidification model. An effective partition coefficient that considers the local interface velocity and the undercooling is used to simulate solidification during welding. The calculations show that convection plays a dominant role in the solute transport inside the weld pool. The predicted weld metal solute content agrees well with the independent experimental observations. The model provides non-equilibrium solute distribution in the solidifying weld metal, which is used for the design of consumables to avoid liquation cracking, during GMA welding of Al-Cu alloys, using filler metals with different copper contents.

## **7.1 Mathematical model**

The numerical transport phenomena based model, developed in the present study, has been described in Chapter 3. In the present chapter, we will discuss the modifications and additions to this model to adapt it to the gas metal arc (GMA) welding process. During the GMA welding process the filler metal melts and mixes with the molten base metal by convection and diffusion, adding both heat and solute to the molten pool. As the heat source moves, solidification of the molten zone leads to solute rejection in the weld pool and formation of solidified weld metal structure. Furthermore, the base metal melts and mixes with the molten pool, contributing to its solute content. All these factors have been incorporated in the model.

The following major assumptions are made in the model:

- (i) Momentum transfer into the molten pool due to filler material addition is neglected for simplicity.
- (ii) Also, for simplicity, a pseudo-binary equivalent of the multi-component alloy is considered for solidification modeling.

### 7.1.1 Thermal energy conservation equation

For modeling the GMA welding process, the modified thermal energy conservation equation is given as:

$$\rho \frac{\partial h}{\partial t} + \rho \frac{\partial(u_i h)}{\partial x_i} = \frac{\partial}{\partial x_i} \left( K \frac{\partial T}{\partial x_i} \right) - \rho \frac{\partial(\Delta H)}{\partial t} - \rho \frac{\partial(u_i \Delta H)}{\partial x_i} - S_d - \rho U \frac{\partial h}{\partial x_i} - \rho U \frac{\partial \Delta H}{\partial x_i} \quad (7.1)$$

where  $K$  is the thermal conductivity, and  $\Delta H$  is the latent enthalpy content of the computational cell under consideration given by the following expression:

$$\begin{aligned} \Delta H &= L && \text{if } T > T_l \\ &= f_l L && \text{if } T_s \leq T < T_l \\ &= 0 && \text{if } T < T_s \end{aligned} \quad (7.2)$$

where  $T_s$  and  $T_l$  are the solidus and liquidus temperatures, respectively. In Eq. (7.1), the term  $S_d$  represents a volumetric heat source term due to the addition of hot metal droplets from the melting filler metal. Calculation of this term will be described in a following section.

### 7.1.2 Solute conservation equation

The general form of species conservation equation is given by:

$$\frac{\partial(\rho C)}{\partial t} + \frac{\partial(\rho u_i C)}{\partial x_i} = \frac{\partial}{\partial x_i} \left( \rho D \frac{\partial C}{\partial x_i} \right) - \rho U \frac{\partial C}{\partial x_i} \quad (7.3)$$

where  $C$  is the solute concentration and  $D$  is the effective mass diffusivity of the solute. The variable  $C$  embodies components from both solid and liquid phases. Voller et al. [15] have shown that Eq. (7.3) may be rewritten in terms of liquid phase concentration,  $C_l$ , and non-equilibrium partition coefficient. Following their approach and neglecting diffusion in solid, Eq. (7.3) may be rewritten as [15]:

$$\frac{\partial}{\partial t} (\rho C_l) + \frac{\partial(\rho u_i C_l)}{\partial x_i} = \frac{\partial}{\partial x_i} \left( \rho f_l D_l \frac{\partial C_l}{\partial x_i} \right) + \frac{\partial}{\partial t} (\rho f_s C_l) - k_p C_l \frac{\partial}{\partial t} (\rho f_s) - \rho U \frac{\partial C_l}{\partial x_i} - S_m \quad (7.4)$$

where  $k_p$  is the partition coefficient. In Eq. (7.4),  $D_l$  is an effective diffusion coefficient, which will be described in a subsequent section,  $f$  denotes the appropriate phase fraction with subscripts  $l$  and  $s$  referring to liquid and solid phases, respectively, and  $S_m$  is a time-

averaged volumetric mass source term to incorporate the filler metal addition. The calculation of  $S_m$  is discussed in the next section.

Since the solute partitioning at the solid-liquid interface may not reach thermodynamic equilibrium, calculations of  $f_s$  and  $f_l$  and the prescription of an appropriate partition coefficient in Eq. (7.4) requires a rigorous non-equilibrium solidification model. Equation (7.4) also indicates a strong coupling between the thermal, solutal and velocity fields. A key factor in this coupling is the appropriate modeling of the liquid fraction that affects the orientation and location of the pool boundaries. The iterative updating of liquid fraction (or, equivalently, nodal enthalpy) is done in the entire concentration field, since the enthalpy and concentration fields are coupled through the non-equilibrium solidification kinetics at the interface.

### 7.1.3 Filler metal addition

Filler metal addition to the weld pool is considered by incorporating time-averaged volumetric heat and mass sources in the enthalpy and solute conservation equations. The volumetric heat source is described in detail in Chapter 2, Section 2.2.1.1. The volumetric heat source is characterized by its radius ( $R_v$ ), height ( $d$ ) and power density ( $S_v$ ) and considers the interaction between metal droplets and weld pool for various welding conditions [16,17]. The radius of the volumetric heat source is assumed to be 2.7 times the droplet radius [18], and the height ( $d$ ) is calculated from the following equation based on energy balance:

$$d = h_v - x_v + D_d \quad (7.5)$$

where  $h_v$  is the estimated height of cavity by the impact of metal droplets,  $x_v$  is the distance traveled by the center of the slug between the impingement of two successive droplets, and  $D_d$  is the droplet diameter. The total sensible heat input from the metal droplets,  $Q_t$ , is given as:

$$Q_t = \rho \pi r_w^2 w_f H_d \quad (7.6)$$

where  $\rho$  is the density,  $r_w$  is the radius of the wire,  $w_f$  is the wire feeding rate, and  $H_d$  is the total enthalpy of the droplets. It should be noted that a portion of  $Q_t$  is used to heat the

additional metal from the droplets up to liquidus temperature. Therefore, the effective heat of droplets ( $Q_d$ ) carried into the weld pool is given as:

$$Q_d = \rho \pi r_w^2 w_f C_{pl} (T_d - T_l) \quad (7.7)$$

where  $C_{pl}$  is the specific heat of the liquid metal,  $T_d$  is the droplet temperature, and  $T_l$  is the liquidus temperature.

The values of  $h_v$  and  $x_v$  in Eq. (7.5) are calculated based on energy balance as:

$$h_v = \left( -\frac{2\gamma}{D_d \rho g} + \sqrt{\left[ \left( \frac{2\gamma}{D_d \rho g} \right)^2 + \frac{D_d v_d^2}{6g} \right]} \right) \quad (7.8)$$

$$x_v = \left( h_v + \frac{2\gamma}{D_d \rho g} \right) \left\{ 1 - \cos \left[ \left( \frac{g}{h_v} \right)^{1/2} \Delta t \right] \right\} \quad (7.9)$$

where  $\gamma$  is the surface tension of the molten metal,  $g$  is the acceleration due to gravity,  $v_d$  is the droplet impingement velocity and  $\Delta t$  is the interval between two successive drops ( $\Delta t = 1/f$ , where  $f$  is the droplet transfer frequency). As shown in Eqs. (7.5) to (7.9), the calculation of the dimensions of the volumetric heat source requires the knowledge of the droplet transfer frequency, radius and impingement velocity. These parameters are determined from the correlations available in the literature [16]. From the computed values of  $Q_d$ ,  $D_d$  and  $d$ , the time-averaged power density for grid points within the volumetric heat source,  $S_d$ , is calculated as:

$$S_d = \frac{Q_d}{\pi D_d^2 d} \quad (7.10)$$

Solute addition from the filler metal is considered by incorporating a time-averaged volumetric mass source term,  $S_m$ , in the solute conservation equation, Eq. (7.4). The dimensions of the volumetric mass source are assumed to be the same as the volumetric heat source. The net mass of solute from the metal droplets,  $Q_t$ , is given as:

$$Q_t = \rho \pi r_w^2 w_f (C_f - C) \quad (7.11)$$

where  $\rho$  is the density,  $r_w$  is the radius of the wire,  $w_f$  is the wire feeding rate,  $C_f$  is the concentration of solute in the filler metal drops, and  $C$  is the local solute concentration.

The time-averaged volumetric mass source,  $S_m$ , for grid points within the mass source region is given by:

$$S_m = \frac{Q_t}{\pi D_d^2 d} \quad (7.12)$$

#### 7.1.4 Thermo-solutal-flow coupling - enthalpy updating

The following iterative enthalpy updating scheme proposed by Brent et al. [19] is chosen in the present study for its adaptability in a fixed-grid enthalpy based framework:

$$[\Delta H_p]_{n+1} = [\Delta H_p]_n + \frac{a_p}{a_p^0} \lambda \left[ \{h_p\}_n - F^{-1} \{ \Delta H_p \}_n \right] \quad (7.13)$$

where  $a_p$  and  $a_p^0$  are the coefficients of enthalpy for the nodal point P in the discretized energy equation for the current and the previous time steps [20], respectively,  $\Delta H_p$  is the latent heat content and  $h_p$  is the sensible enthalpy associated with the nodal point P,  $n$  is the number of iterations,  $\lambda$  is a relaxation factor, and  $F^{-1}$  is a suitable function that relates local enthalpy with temperature and liquid fraction. In order to include the appropriate thermo-solutal effects [21] in  $F^{-1}$ , the interfacial temperature,  $T$ , is represented as a function of local liquidus composition,  $C_l$ , as [22]:

$$T = T_m + m_L C_l - V / \beta_0 - \Gamma \kappa \quad (7.14)$$

where  $T_m$  is the melting point of the solvent,  $m_L$  is the non-equilibrium liquidus-line slope described by Eq. (7.15),  $V$  is the normal interface velocity,  $\beta_0$  is a kinetic coefficient of interface motion,  $\Gamma$  is a capillary constant calculated as  $\Gamma = T_m \gamma / L \rho$ ,  $\gamma$  is the surface tension,  $L$  is the latent heat of freezing,  $\rho$  is the density, and  $\kappa$  is the mean curvature of the solid-liquid interface. Equation (7.14) represents a deviation of the interfacial temperature from its local equilibrium value due to motion of the interface, the local interfacial curvature-undercooling effect and the non-equilibrium partitioning of the solute. The partitioning effect is considered by relating the non-equilibrium liquidus-line slope ( $m_L$ ) in Eq. (7.14) with its equilibrium value ( $m_L^*$ ) as [22,23]:

$$m_L = m_L^* \left\{ 1 + \frac{1}{1 - k_p^*} \left[ k_p^* - k_p (1 - \ln(k_p / k_p^*)) \right] \right\} \quad (7.15)$$

where  $k_p$  is the modified partition coefficient that can be expressed in terms of equilibrium partition coefficient,  $k_p^*$ , as [22]:

$$k_p = \begin{cases} \frac{k_p^* [1 - (V / V_D^L)^2] + V / V_D^L}{1 - (V / V_D^L)^2 + V / V_D^L} & \dots \text{for } V < V_D^L \\ = 1 & \dots \text{for } V \geq V_D^L \end{cases} \quad (7.16)$$

In Eq. (7.16),  $V_D^L$  is the diffusive speed in the liquid, which can be calculated as [22]:

$$V_D^L = (D_1^* / \tau_D^L)^{0.5} \quad (7.17)$$

where  $\tau_D^L$  refers to the time of diffusional relaxation of collective atoms (molecules, particles) to their equilibrium state in a local volume of alloy [22]. The diffusive speed at which a solute atom diffuses through the interfacial region can be approximated by the ratio of diffusivity of the solute atoms at the interface and a length scale characterizing the interface width. Furthermore, the interface velocity ( $V$ ) in Eq. (7.16) can be calculated in an iterative manner using the following equation [12]:

$$V = \frac{k_s G_s - k_l G_l}{f_l L} \quad (7.18)$$

where  $G_s$  and  $G_l$  are the temperature gradients in solid and mushy zone at the mushy zone/solid interface, respectively,  $k_s$  and  $k_l$  are thermal conductivities of the solid and liquid phases, respectively,  $f_l$  is the liquid fraction, and  $L$  is the latent heat of freezing. For a known interface velocity, the diffusion coefficient appearing in Eq. (7.4) can be prescribed as [22]:

$$D_1 = \begin{cases} D_1^* [1 - (V / V_D^L)^2] & \dots \text{for } V < V_D^L \\ = 0 & \dots \text{for } V \geq V_D^L \end{cases} \quad (7.19)$$

where  $D_1^*$  is the diffusion coefficient in the liquid under the conditions of interfacial equilibrium.

The impact of high solidification rate on local interfacial temperature, as indicated by Eqs. (7.15) and (7.16) is worth examining at this point. From Fig. 7.1, it can be observed that the difference between solidus and liquidus compositions progressively

diminishes with increase of interface velocity due to lack of time available for atomistic rearrangements. Ultimately, as the interface velocity approaches the diffusive speed, the partition coefficient tends to unity. The resulting effect on solidus and liquidus line slopes is depicted in Fig. 7.2. It can be observed from this figure that with an increase in the interface speed, the difference between the liquidus and solidus line slopes decreases rapidly. Thus, the effective solidification range becomes progressively smaller at faster solidification rates. The solidus and liquidus temperatures tend to coincide as the diffusive speed limit is approached. The mushy zone virtually disappears and the liquid instantaneously freezes to form solid crystals without passing through a freezing range. At high solidification rates, the solid fraction cannot be calculated based on equilibrium considerations.

Equations (7.15) to (7.18) can be effectively used to complete the iteration cycle involving updating of enthalpy using Eq. (7.13). The calculations require an appropriate functional relation between liquid composition,  $C_l$ , and liquid fraction,  $f_l$ , consistent with the local solute balance:

$$(C_l - C_s)df_s = (1 - f_s)dC_l \quad (7.20)$$

where  $f_s$  is the mass fraction of the solid and  $C_s$  is the solid phase composition. Replacing  $f_s$  by  $(1-f_l)$  in Eq. (7.20), where  $f_l$  is the mass fraction of the liquid, and integrating,  $f_l$  is obtained as:

$$f_l = \exp\left\{-\int_{C_0}^{C_l} \frac{dC_l}{C_l(1-k_p)}\right\} \quad (7.21)$$

where  $k_p$ , which replaces  $C_s/C_l$ , is a convection-corrected partition-coefficient representing the non-equilibrium effects (given by Eq. (7.16)). Equation (7.21) can be integrated if the variation of  $k_p$  with  $C_l$  is known.

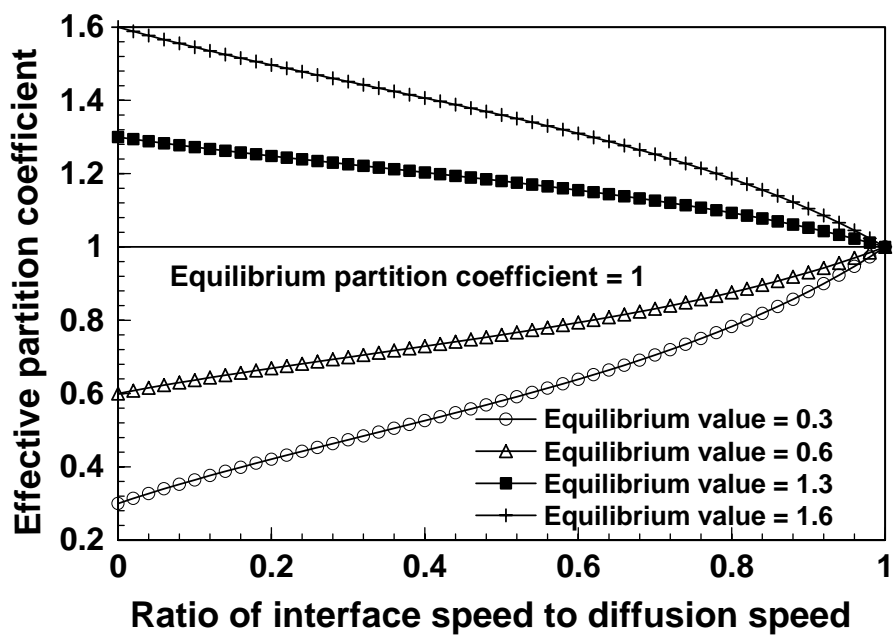


Fig. 7.1. Effect of interface speed on local interfacial partitioning.

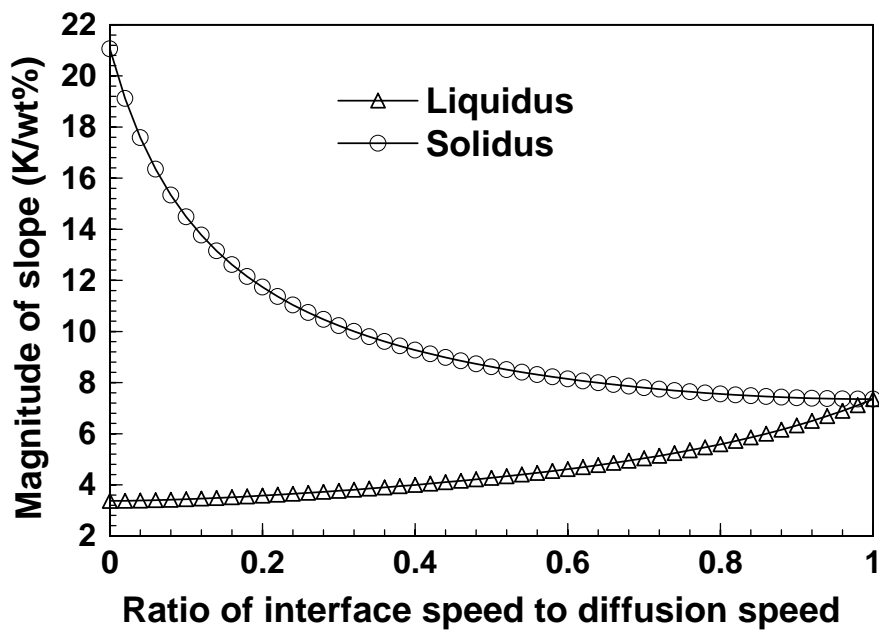


Fig. 7.2. Effect of interface speed on solidus and liquidus line slopes (an equilibrium liquidus slope of  $-3.37$  K/wt%, and an equilibrium partition coefficient of  $0.16$  were chosen for this specific demonstration).

For the specific case of a composition independent partition coefficient, integration of Eq. (7.21) gives [24]:

$$C_1 = C_0 f_1^{k_p-1} \quad (7.22)$$

where  $C_0$  is the initial composition of liquid. Although Eq. (7.22) appears similar in form to the well-known Scheil's equation [24], a key difference lies in the fact that the partition coefficient in Eq. (7.22) is a strong function of the interface growth rate governed by Eq. (7.18) and not a constant.

With the aid of Eqs. (7.14) and (7.22), a final form of the enthalpy updating function appearing in Eq. (7.13) can now be obtained as:

$$F^{-1}(\Delta H) = c_p \left[ T_m + m_L C_0 \left( \frac{\Delta H}{L} \right)^{(k_p-1)} - V/\beta_0 - \Gamma\kappa \right] \quad (7.23)$$

Finally, the liquid fraction is calculated by using Eq. (7.13) as:

$$f_1 = \frac{\Delta H}{L} \quad (7.24)$$

Possible unrealistic intermediate estimates predicted by Eq. (7.24) during iterations can be avoided by imposing the following constraints:

$$\begin{aligned} f_1 &= 0 \quad \text{if } f_1 < 0 \\ &= 1 \quad \text{if } f_1 > 1 \end{aligned} \quad (7.25)$$

Steps of enthalpy updating include:

Step 1: Initialize the velocity, temperature, concentration and liquid fraction field.

Step 2: Form coefficients of the discretization equations for fluid flow, heat transfer and mass transfer, and solve the resultant system of linear algebraic equations.

Step 3: Calculate the ratio of interface speed to diffusive speed (using Eqs. (7.17) and (7.18)).

Step 4: Calculate the non-equilibrium partition coefficient at nodal points (using Eq. (7.16)).

Step 5: Calculate the non-equilibrium liquidus slope (using Eq. (7.15)).

Step 6: Update nodal latent enthalpy, and hence liquid fraction, as per Eqs. (7.13) and (7.24), respectively. This step leads to a corrected weld pool geometry based on the phase fraction evolution through appropriate non-equilibrium thermo-solutal coupling.

Step 7: Go back to Step 2, and iterate until convergence.

### 7.1.5 Boundary conditions

The temperature and velocity boundary conditions have been described in Chapter 3 and are not repeated here. The boundary conditions for solute transport at the solidification interface needs to consider non-equilibrium partitioning of solute at the solidification front:

$$C_l = \frac{C_w}{k_p} \quad (7.26)$$

where  $C_l$  is the local solute concentration in the liquid and  $C_w$  is the solute concentration in the solidified weld metal. Similarly, the boundary condition at the melting front can be written as:

$$C_l = C_b \quad (7.27)$$

where  $C_b$  is the concentration of the solute in the base metal.

## 7.2 Results and Discussion

GMA welding of 2219 aluminum-copper alloy containing 6.3 wt% Cu was simulated. The filler metal compositions varied from 0.08 wt% Cu to 9.0 wt% Cu. The data used in the calculations are summarized in Table 7.1. Fig. 7.3 shows the computed velocity and temperature fields in the weld pool of 2219 alloy with the filler metal composition of 0.08 wt% Cu. The weld pool is wide and shallow because the aluminum alloy has a negative temperature coefficient of surface tension ( $d\gamma/dT$ ), which causes the liquid metal to move from the middle to the periphery on the weld pool surface. The relative importance of convection and conduction in the overall transport of heat in the weld pool can be assessed from the value of the Peclet number,  $Pe_h$ , which is given by:

$$Pe_h = \frac{u\rho C_p L}{k} \quad (7.28)$$

where  $u$  is the velocity,  $\rho$  is the density,  $C_p$  is the specific heat at constant pressure,  $L$  is the characteristic length, and  $k$  is the thermal conductivity of the melt. When  $Pe_h$  is large, which in physical terms means large melt velocity, large weld-pool, and poor thermal conductivity, heat is transported primarily by convection. In the aluminum alloy welds, typical velocity in the pool is 0.2 m/s, density is 2400 kg/m<sup>3</sup>, specific heat is 1060 J/kg-K, characteristic length is 0.0044 m, and thermal conductivity is 192 W/m-K. The corresponding value of  $Pe_h$  is found to be 12, which is much larger than unity. This value of  $Pe_h$  indicates that heat is transported mainly by convection in the weld pool. Therefore, accurate calculations of temperature field can only be done by considering convective heat transport.

Table 7.1. Data used in the calculations [25].

Problem data/physical property	Value
Arc current (amp)	140
Arc voltage (volt)	22
Welding speed (m s <sup>-1</sup> )	4.2 × 10 <sup>-3</sup>
Wire feeding rate (m s <sup>-1</sup> )	9.31 × 10 <sup>-2</sup>
Density (kg m <sup>-3</sup> )	2400
Viscosity of liquid (kg m <sup>-1</sup> s <sup>-1</sup> )	0.3 × 10 <sup>-3</sup>
Specific heat (J kg <sup>-1</sup> K <sup>-1</sup> )	1.06 × 10 <sup>3</sup>
Mass diffusivity of copper in liquid aluminum (m <sup>2</sup> s <sup>-1</sup> ) under interfacial equilibrium conditions	3.0×10 <sup>-9</sup>
Thermal conductivity (W m <sup>-1</sup> K <sup>-1</sup> )	192
Equilibrium partition coefficient	0.16
Equilibrium slope of liquidus line (K/wt%)	-3.37
Solidus temperature of alloy 2219 (K)	821
Liquidus temperature of alloy 2219 (K)	911

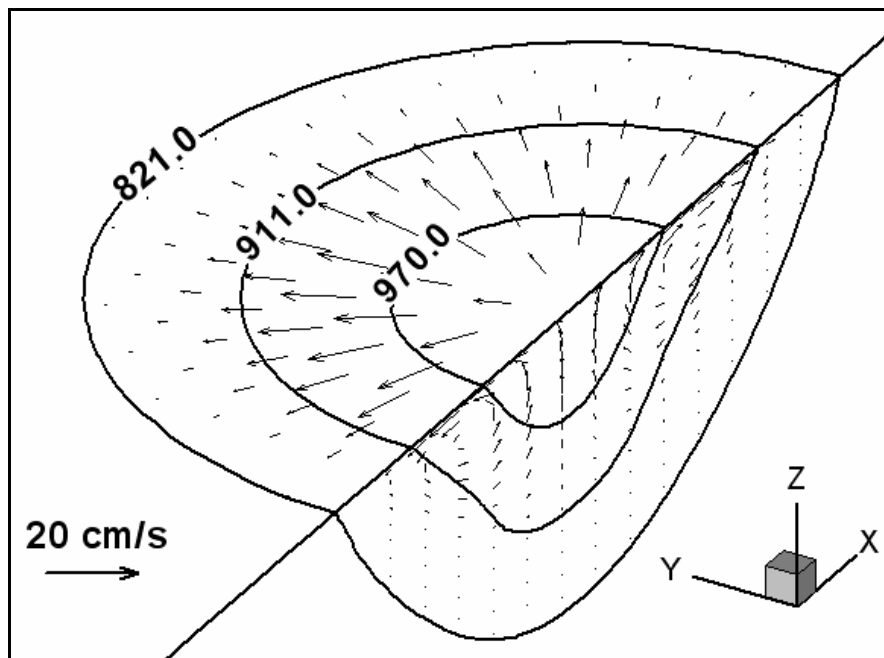


Fig. 7.3. Velocity and temperature fields in the weld pool for the welding conditions indicated in Table 7.1. The filler metal composition was 0.08 wt% copper. All the temperatures are in degree Kelvin.

The Peclet number for mass transfer,  $Pe_m$ , indicates the relative importance of convection and conduction in the overall transport of solute in the weld pool.

$$Pe_m = \frac{uL}{D} \quad (7.29)$$

where  $D$  is the mass diffusivity. The mass diffusivity of aluminum alloy is  $3.0 \times 10^{-9} \text{ m}^2/\text{s}$ . The corresponding value of  $Pe_m$  is calculated to be  $2.9 \times 10^5$ , which indicates that convection is the primary mode of mass transport in the weld pool. Therefore, it is necessary to consider convective mass transport in order to accurately predict the solute concentration distribution in the weld pool.

Fig. 7.4(a) to (d) show the computed solute concentration distributions within the weld pool for four filler metal compositions: 0.08 wt% Cu, 2.0 wt% Cu, 4.0 wt% Cu, and 9.0 wt% Cu. It can be observed that convection plays a dominant role in solute distribution in the weld pool causing efficient mixing of the base metal with the filler metal. At the melting front, in front of the pool, the base metal melts and forms a liquid of the same composition. The filler metal then mixes with the liquid from the base metal resulting in a weld metal composition that lies between the filler metal and the base metal compositions. At the solidification front, the solute is rejected from the solidified material into the molten pool. As a result, high solute concentration is observed at the solidification front in Fig. 7.4(a) to (d). Similarly, in the transverse sections ahead of the heat source, the composition near the melting front is same as that of the base metal. However, in transverse sections behind the heat source, segregation of the solute is observed near the solidification front. In the middle of the weld pool, a large amount of filler metal is added and the solute concentration is fairly close to the filler metal composition. It is noteworthy that the high solute content at the solidification front does not have as much influence on the overall concentration distribution as the mixing of the filler metal with the base metal. This behavior can be attributed to very low mass diffusivity of copper in the alloy and very low liquid velocities in the two phase region adjacent to the solidification front. The rejected solute is confined to a very small region and the low velocities in the two phase region prevent rapid mixing of the rejected solute into the weld pool. It should also be noted that the high solute value depicted in Fig.

7.4(a) to (d) at the rear end of the pool is not observed in real welds. In real welds, because of local redistribution of the solute at the microscopic level, the concentration gradient at the rear end is much less steep. The high solute content value observed in Fig. 7.4(a) to (d) is an artifact of the calculation because of the simplified local equilibrium boundary condition assumption given in Eq. (7.26). However, this assumption would not affect the overall calculation of solute distribution in the weld because the rejected solute is confined to a very small region as mentioned above.

Since the composition of a single-pass GMA aluminum weld is essentially uniform [1], the solidified weld metal solute concentration was assumed to be equal to the average concentration of the solute in the molten weld pool. As shown in Fig. 7.4, the concentration of solute in the solidified weld metal depends on the filler metal composition. The accuracy of the calculated weld metal composition can be examined by comparing the computed weld metal composition for 0.08 wt% filler metal addition with the corresponding independent experimental result of Huang and Kou [1]. For a GMA weld of 2219 alloy using a filler metal containing 0.08 wt% copper, Huang and Kou [1] measured the weld metal composition to be 3.43 wt% copper. For the same welding conditions, the computed weld metal composition was equal to 3.17 wt% copper as shown in Fig. 7.4(a), thus confirming the accuracy of the calculations. The results also indicate the importance of solute transport by convection. Accurate solute concentration distribution cannot be calculated by considering only the diffusive transport.

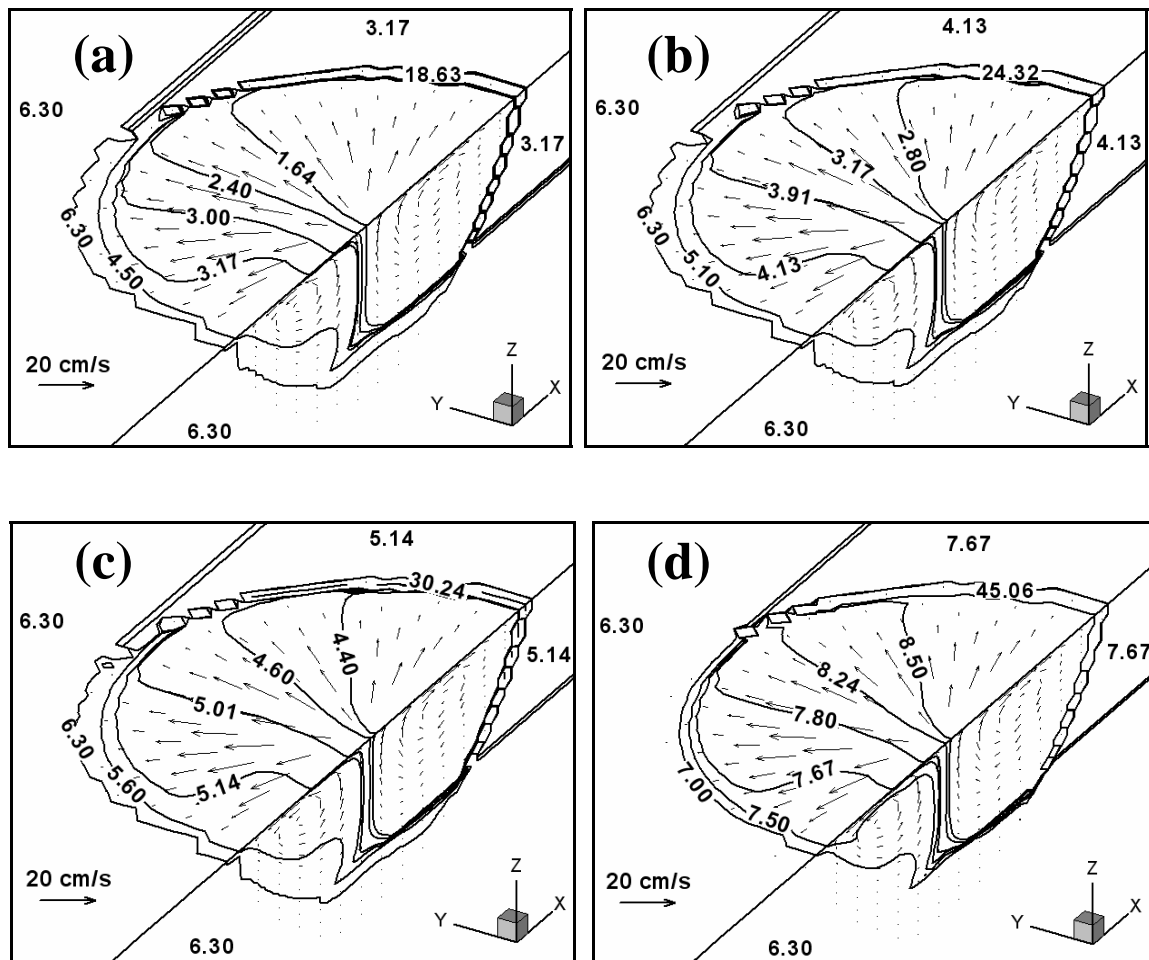


Fig. 7.4. Concentration field (wt% Cu) in the weld pool. The filler metal compositions were (a) 0.08 wt% Cu, (b) 2.0 wt% Cu, (c) 4.0 wt% Cu, and (d) 9.0 wt% Cu.

Gittos and Scott [26] proposed that liquation cracking occurs when the base metal solidus temperature is below the weld-metal solidus temperature. In other words, if the base metal solute content is higher than that of the weld metal, then the PMZ is susceptible to liquation cracking. Fig. 7.5 is a plot of the computed wt% Cu in the weld metal versus the wt% Cu in the filler metal. The concentration of Cu in the base metal was 6.3 wt%. Thus, based on the criterion proposed by Gittos and Scott [26], the PMZ becomes susceptible to liquation cracking when the weld metal concentration is lower than 6.3 wt% Cu. However, Huang and Kou [1] argued that the cooling rate during welding may be too high for equilibrium solidification to occur, and solidification can continue far below the equilibrium solidus temperature. They [1] proposed the criterion that the PMZ becomes prone to liquation cracking when the solid fraction in the PMZ becomes lower than that of the weld metal. A weaker PMZ with lower solid fraction makes this region vulnerable to liquation cracking. Calculation of the solid fraction in the solidifying region requires the computed values of non-equilibrium partition coefficient, which is shown in Fig. 7.6. It should be noted that the value of the non-equilibrium partition coefficient is higher than that of the equilibrium value. The higher value is consistent with the shrinking of the two phase region at high solidification rates. Once  $k_p^*$  and  $k_p$  were obtained for each temperature, Eq. (7.15) was used to get the slope of the liquidus line ( $m_l$ ) at these temperatures. Next, the modified liquidus composition ( $C_l$ ) at each temperature was calculated using  $k_p$ ,  $m_l$ , and the melting point of pure aluminum, 933 K. The corresponding values of the modified solidus compositions,  $C_s$ , at each temperature could be obtained from the values of  $k_p$  and  $C_l$  at these temperatures. The modified  $C_s$  and  $C_l$  were then used to calculate the non-equilibrium solid fractions. The computed solid fraction for the 2219 alloy, having 6.3 wt% Cu taking into account the non-equilibrium solidification is shown in Fig. 7.7. The solid line curve in Fig. 7.7 was calculated from the equilibrium phase diagram using the equilibrium  $C_s$  and  $C_l$  values. The non-equilibrium solid fraction is lower than the corresponding equilibrium value because of undercooling, which prevents solidification to occur at equilibrium temperature at high solidification rates.

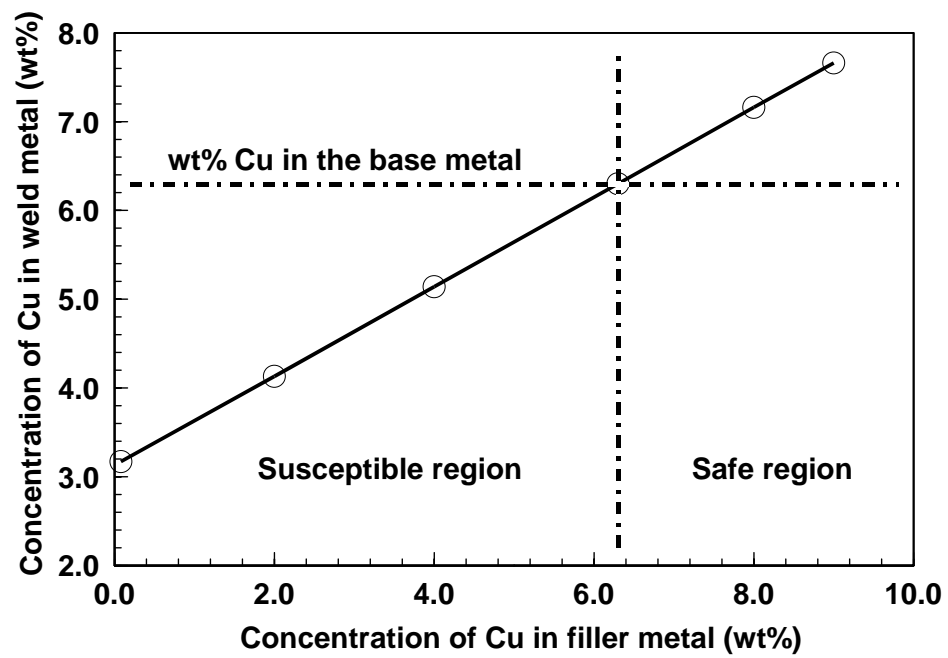


Fig. 7.5. The concentration of copper in the weld metal for different filler metal compositions. The concentration of copper in the base metal was 6.3 wt%. The safe and susceptible regions are indicated for equilibrium solidification.

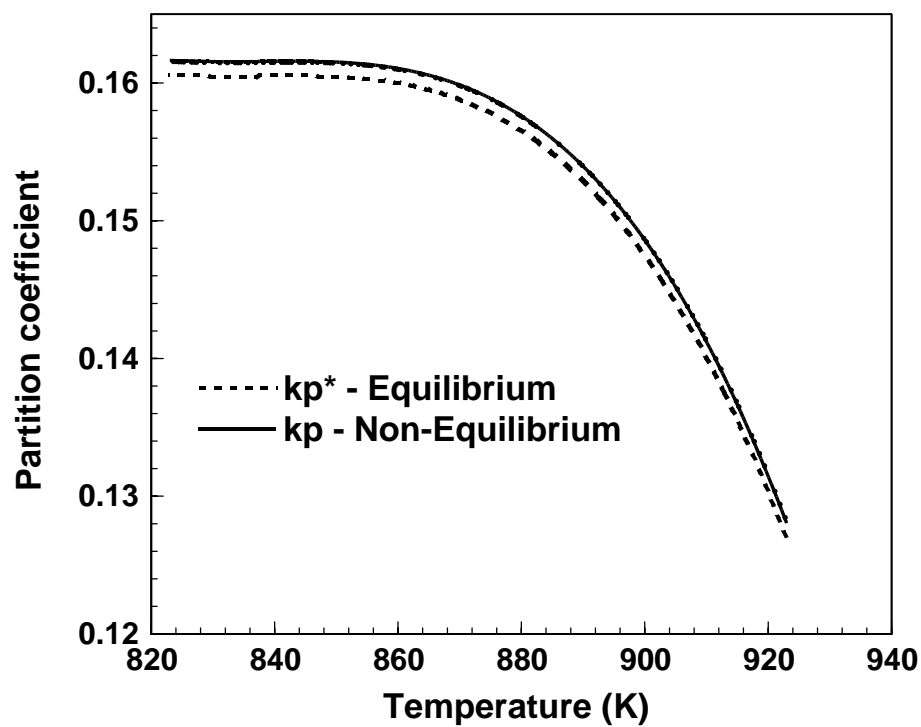


Fig. 7.6. Variation of equilibrium partition coefficient ( $k_p^*$ ) (dotted line) and non-equilibrium partition coefficient ( $k_p$ ) (solid line) with temperature.

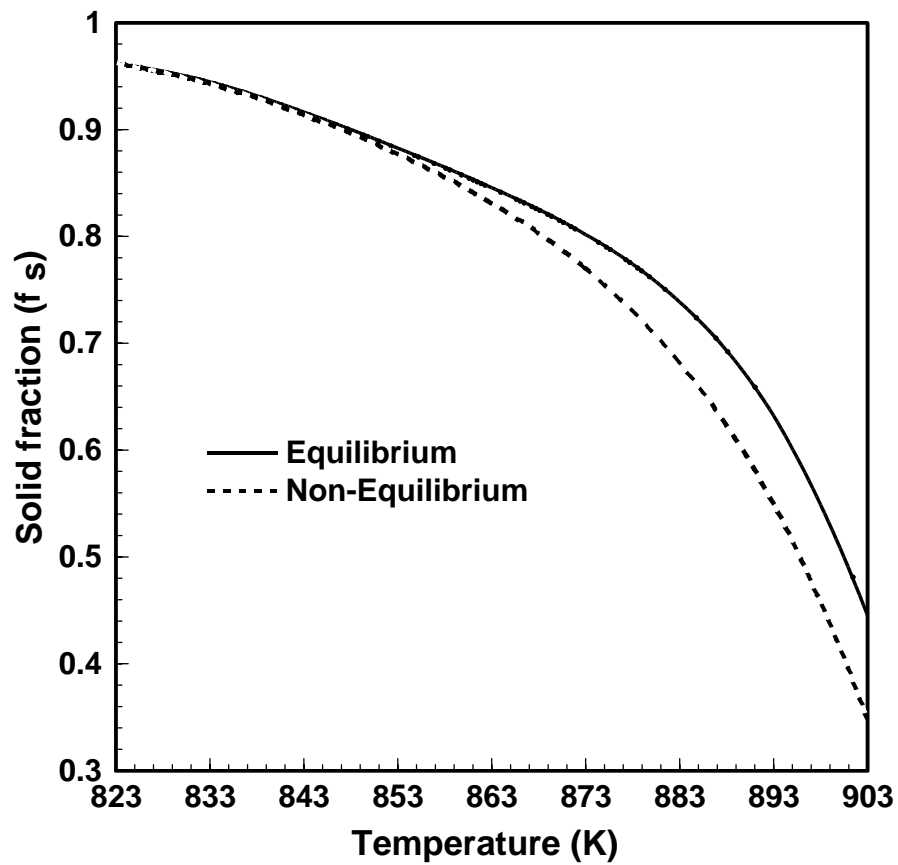


Fig. 7.7. Solid fraction versus temperature for alloy composition of 6.3 wt% copper. The solid line curve was obtained from the equilibrium phase diagram and the dotted line curve was obtained using the modified non-equilibrium solidus and liquidus lines.

The variation of non-equilibrium solid fraction with temperature for three cases has been plotted in Fig. 7.8. One plot is for the base metal or the PMZ composition, i.e., 6.3 wt% Cu, and the other two are for the solidifying weld metal compositions in the mushy region computed from the solute transport model for two welding conditions. The lower plot represents welding of 2219 alloy using a filler metal with 9.0 wt% Cu that leads to a mushy zone composition of 8.91 wt% Cu for the wire feeding rate and other parameters indicated in Table 7.1. Similarly, the upper plot indicates the use of a filler metal of 2.0 wt% Cu, for the same welding conditions, that leads to a mushy zone composition of 2.16 wt% Cu. The solid fraction in the PMZ can be compared with that in the solidifying region, i.e., the mushy zone. The lower graph, representing 9.0 wt% Cu containing filler metal, has lower solid fraction in the mushy zone than that in the PMZ. Therefore, the solidifying weld metal has lower strength than the PMZ and the PMZ is not susceptible to liquation cracking. In contrast, when the 2.0 wt% Cu containing filler metal is used, the solid fraction in the solidifying weld metal is higher than that in the PMZ. Consequently, the solidifying weld metal is stronger than the PMZ making the PMZ susceptible to liquation cracking. The above observations are in agreement with the independent experimental observations of Huang and Kou [1]. Thus, the present calculations considering convective solute transport, non-equilibrium solidification and filler metal addition can be used to predict liquation cracking susceptibility in aluminum alloy welds.

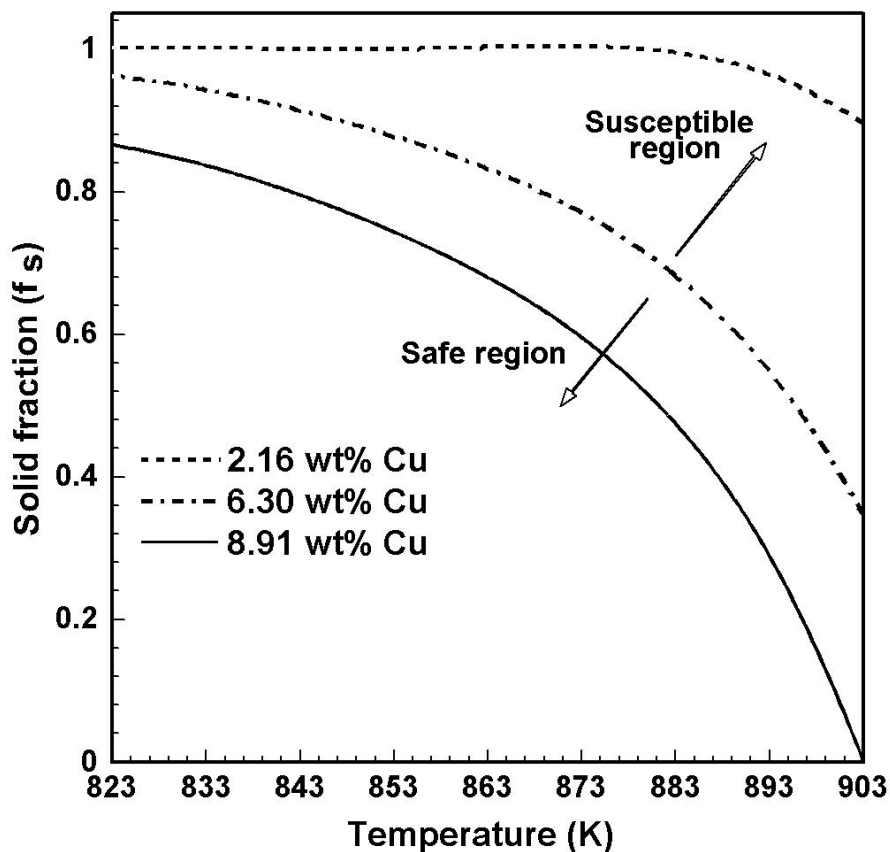


Fig. 7.8. Solid fraction versus temperature calculated using modified non-equilibrium solidus and liquidus lines for different alloy compositions. The PMZ composition was 6.3 wt% Cu (dash-dot line in the center). The calculated mushy zone compositions, or the solidifying weld metal compositions, of 2.16 wt% Cu (dotted line above the central line) and 8.91 wt% Cu (solid line below the central line) correspond to the filler metal compositions of 2.0 wt% Cu and 9.0 wt% Cu, respectively.

### 7.3 Summary and Conclusions

A numerical model that considers momentum, heat and solute transport has been developed to calculate non-equilibrium solute distribution in gas metal arc (GMA) welds. The model uses an effective partition coefficient that considers both the local interface velocity and the undercooling to simulate non-equilibrium solidification during welding. The computed concentration profiles reflect the dissolution of the base metal at the melting front, the strong convection in the weld pool, mixing of the filler metal with the base metal and solute rejection at the solidifying interface. The calculations showed that convection plays a dominant role in solute transport in the weld pool and diffusion calculations alone are insufficient. The predicted weld metal solute content agreed well with the independent experimental observations. Using the computed average composition in the two phase mushy region, the solid fraction in the solidifying weld metal was compared with that in the PMZ for various filler metal compositions. In each case, the susceptibility of liquation cracking was determined by Huang and Kou's criterion, i.e., by comparing the solid fraction in the solidifying weld metal with the corresponding value in the PMZ. The model predictions of liquation cracking susceptibility in Al-Cu alloy weldments were confirmed by independent experiments for various filler metal compositions.

## 7.4 References

1. C. Huang, and S. Kou, *Weld. J.* 83, 50s (2004).
2. H. Zhao and T. DebRoy, *Metall. Mater. Trans. B* 32, 163 (2001).
3. H. W. Kerr, and M. Katoh, *Weld. J.* 66, 251s (1987).
4. M. Miyazaki, K. Nishio, M. Katoh, S. Mukae, and H. W. Kerr, *Weld. J.* 69, 362s (1990).
5. C. Huang, and S. Kou, *Weld. J.* 79, 113s (2000).
6. C. Huang, and S. Kou, *Weld. J.* 80, 9s (2001).
7. C. Huang, and S. Kou, *Weld. J.* 80, 46s (2001).
8. C. Huang, and S. Kou, *Weld. J.* 81, 211s (2002).
9. C. Huang, and S. Kou, *Weld. J.* 82, 184s (2003).
10. C. Huang, and S. Kou, *Weld. J.* 83, 111s (2004).
11. S. Kou, and Y. H. Wang, *Metall. Trans. A* 17, 2271 (1986).
12. W. Zhang, G. G. Roy, J. Elmer, and T. DebRoy, *J. Appl. Phys.* 93, 3022 (2003).
13. X. He, P. W. Fuerschbach, and T. DebRoy, *J. Phys. D: Appl. Phys.* 36, 1388 (2003).
14. S. Chakraborty, and P. Dutta, *Materials and Manufacturing Processes* 17, 455 (2002).
15. V. R. Voller, A. D. Brent, and C. Prakash, *Int. J. Heat Mass Transfer* 32, 1719 (1989).
16. W. Zhang, C.-H. Kim, and T. DebRoy, *J. Appl. Phys.* 95, 5210 (2004).
17. W. Zhang, C.-H. Kim, and T. DebRoy, *J. Appl. Phys.* 95, 5220 (2004).
18. A. Kumar, and T. DebRoy, *Int. J. Heat Mass Transfer.* 47, 5793 (2004).
19. A. D. Brent, V. R., Voller, and K. J. Reid, *Numerical Heat Transfer* 13, 297 (1988).
20. S. V. Patankar, *Numerical Heat Transfer and Fluid Flow* (Hemisphere/McGraw-Hill, Washington DC, 1980).
21. S. Chakraborty, and P. Dutta, *Metall. Mater. Trans. B* 32, 562 (2001).
22. P. Galenko, and S. Sobolev, *Phys. Rev. E* 55, 343 (1997).
23. W. Kurz, and D. J. Fisher, *Fundamentals of Solidification* (3<sup>rd</sup> Edition, Trans. Tech. Publications, Switzerland, 1992).
24. M. C. Flemings, *Solidification Processing* (McGraw Hill, New York, 1974).
25. Q. Z. Diao, and H. L. Tsai, *Metall. Trans. A* 24, 963 (1993).
26. N. F. Gittos, and M. H. Scott, *Weld. J.* 60, 95s (1981).

## Chapter 8

### Concluding Remarks

#### 8.1 Summary

The following problems were addressed in this thesis.

1. Most of the previous work on the applications of numerical transport phenomena to fusion welding was focused on heat transfer and fluid flow. In contrast, the focus of the present thesis is on mass transport during welding where the mixing of the solutes in weld consumables and base metal is studied. A three-dimensional numerical heat, momentum and solute transport model is developed to calculate the temperature and velocity fields and solute distribution in the welds.

2. The lack of reliability of the output of the numerical heat, momentum and solute transport models originates from the uncertainty in the values of some of the input parameters such as arc efficiency, arc radius, arc power distribution factor, and effective thermal conductivity and effective viscosity of the liquid metal. A methodology has been developed and tested to improve the reliability of output of the numerical transport phenomena based model by combining it with a real number based genetic algorithm and a limited volume of experimental data to estimate the values of the five uncertain input parameters.

3. Numerical transport phenomena based models are computationally intensive and require considerable computer time often of the order of 10 to 30 min for a single run. Many computational procedures require repetitive runs of these models. In order to expedite the calculation, a neural network was trained with the data from the numerical heat, momentum and solute transport model. The resulting neural network had the predictive power of the three-dimensional numerical transport phenomena based model but could do the calculations in less than a second.

4. In many real world situations it is desirable to know the input process parameters to obtain a specific output. For example, during welding it would be very useful if some computational procedure could predict the input parameters such as arc current, voltage and welding speed to obtain a specific weld attribute such as weld pool

geometry. The numerical transport phenomena based models lack this bi-directional capability. A methodology has been developed and tested in the present study to tailor fusion weld geometry by combining the neural network, having the predictive power of the numerical transport phenomena based model, with genetic algorithm.

5. The numerical heat, momentum and solute transport calculations were applied to two examples, (a) understanding mixing of consumables with base metal during gas metal arc (GMA) welding of aluminum-copper alloys so that liquation cracking could be predicted, and (b) improved understanding of the role of surface active elements such as sulfur where two plates having different concentrations of sulfur are joined using gas tungsten arc (GTA) welding.

## 8.2 Conclusions

The following are some of the important conclusions of the present thesis research.

1. The reliability of output of the numerical heat, momentum and solute transport model was improved by finding optimized values of uncertain input parameters. (a) The optimized values of the uncertain input parameters lie within the ranges of their values reported in the literature. (b) The computed weld pool shape and size utilizing the optimized values of the uncertain input parameters agreed well with the corresponding experimentally determined values for various welding conditions indicating the effectiveness of the approach. (c) Although the procedure to determine the values of the uncertain input parameters is computationally intensive, taking about 3 days in a 2.8 GHz Pentium 4 PC, the recent improvements in computational hardware and software have made the calculations tractable.

2. Six neural networks, trained by data generated from the numerical heat, momentum and solute transport model were developed for the GTA welding of stainless steel to improve computational efficiency. (a) Each neural network takes 17 input variables, which include welding process parameters and important material properties, and provides one output variable. The output variables include depth, width and length of

the weld pool, peak temperature, cooling time from 800°C to 500°C and maximum liquid velocity in the weld pool. (b) A hybrid optimization scheme, including a gradient descent method and a genetic algorithm, was used to train the networks. The hybrid approach gave lower errors than only the gradient descent method. (c) The results provided by the neural networks agreed well with the corresponding results obtained from the numerical transport phenomena based model, indicating the accuracy of its predictions. (d) Although, significant amount of time was spent in making a number of runs of the numerical transport phenomena based model to generate the data for training the neural networks, the effort was worthwhile as the resulting neural network could be run in less than 1 sec.

3. A bi-directional methodology was developed by combining the neural networks with a genetic algorithm to obtain multiple combinations of welding process parameters such as arc current, voltage and welding speed to obtain a specific weld pool geometry. (a) Because of the use of neural networks in place of the numerical transport phenomena based model, the calculations could be done in a few minutes. (b) Fairly diverse combinations of welding process parameters could be obtained, each of which gave the same weld pool geometry. (c) This accomplishment is a milestone in the tailoring of weld geometry and other attributes based on scientific principles.

4. (a) The reliable numerical heat, momentum and solute transport model could predict the consumable composition for a given base metal composition to avoid liquation cracking in aluminum alloy GMA welds. (b) During GTA welding of stainless steel plates having different sulfur contents, the shifting of the weld bead towards the low sulfur side could be predicted by the numerical transport phenomena based model. The effect of arc shift on the heat and solute transport was considered for the first time in the present study, and this was identified as the main factor governing the weld pool shift.

### **8.3 Future Work**

Several areas were identified during the present thesis research, which needed further investigation.

First, as described in Chapter 6, on GTA welding of stainless steel plates with different sulfur contents the arc shifts towards the low sulfur side. Furthermore, significant undercut is seen in the welds where one of the plates contains very high sulfur. No quantitative explanation is available for the reason and the amount of arc shift as well as the undercut. The arc shifts towards the side where easily ionized metal ions are present in higher amount because these enhance the electrical conductivity of the plasma. Emission Spectroscopy of plasma can identify the metal ions and their amount in the plasma, and thus, shed some light on the origin of arc shift. Therefore, it would be worthwhile to do such measurements in future. Also, to check the validity of the concept that the enhancement of conductivity of the plasma by metal ions causes arc shift, similar welds can be made by laser welding and compared. Furthermore, the weld pool surface was assumed to be flat in the present study. In the future work, more rigorous free surface calculations can be conducted to study the undercut in the welds.

Second, the numerical transport phenomena based model developed in the present study was adapted to calculate the non-equilibrium solute distribution during GMA welding in Chapter 7, by considering heat and solute intake due to filler metal addition, and integrating a non-equilibrium solidification model. For the sake of simplicity, the model was applied to study the susceptibility to liquation cracking in a simple system, i.e., Al-6.3wt%Cu alloy using different compositions of filler metals. Once the capability of the model is demonstrated, in future it can be applied to investigate the susceptibility to liquation cracking of other aluminum alloys as well.

Third, in Chapter 7, an unrealistically high solute content value was calculated at the rear end of the GMA weld pool because of a simplifying local equilibrium assumption at the boundary. In real welds, because of local redistribution of the solute at the microscopic level, the concentration gradient at the rear end is much less steep. The local redistribution of solute can be incorporated by using a more rigorous micro-scale model as against a macro-scale model in future study.

Hopefully, various areas for further investigation mentioned above can be studied in future work to better understand the influence of solute distribution on the evolution of weld pool geometry and the occurrence of weld defects.

## VITA

### Saurabh Mishra

Saurabh Mishra was born in Kanpur (Uttar Pradesh), India on August 6, 1977. In August 1996, he enrolled in the Department of Ceramic Engineering, Institute of Technology, Banaras Hindu University, Varanasi, India where he was awarded the degree of Bachelor of Technology in May 2000. In the fall of 2000, he joined The Pennsylvania State University to pursue graduate study in the Department of Materials Science and Engineering under the guidance of Professor T. DebRoy. He was awarded the degree of Master of Science in May 2003. After that he continued to pursue doctoral study in the same department.

The author is a member of American Welding Society (AWS) and American Society for Metals (ASM-International).

A list of the author's publications during his Ph.D. study at Penn State is as follows.

1. S. Mishra, S. Chakraborty and T. DebRoy, "Probing liquation cracking and solidification through modeling of momentum, heat and solute transport during welding of aluminum alloys", *Journal of Applied Physics* 97, 94912 (2005).
2. S. Mishra and T. DebRoy, "A heat transfer and fluid flow based model to obtain a specific weld geometry through multiple paths", *Journal of Applied Physics* 98, 044902-1 (2005).
3. S. Mishra and T. DebRoy, "A computational procedure for finding multiple solutions of convective heat transfer equations", *Journal of Physics D* 38, 2977 (2005).
4. A. Kumar, S. Mishra, J. W. Elmer and T. DebRoy, "Optimization of Johnson Mehl Avrami equation parameters for  $\alpha$ -ferrite to  $\gamma$ -austenite transformation in steel welds using a genetic algorithm", *Metallurgical and Materials Transactions A* 36, 15 (2005).